TURBULENT EXCHANGE OF MOMENTUM AND CARBON DIOXIDE OF A SITKA SPRUCE PLANTATION

Peter J. McCracken

A thesis submitted for the degree of Doctor of Philosophy to the University of Edinburgh.

Declaration

This thesis has not been submitted in any other application for a degree and is the result of my own work and composition

February, 1993

ABSTRACT

Our knowledge of the global carbon budget is at present insufficient to predict reliably the possible consequences of rising CO_2 levels on the climate and on ecosystems. Attempts to close the global carbon budget have indicated that a major sink for CO_2 may exist in the boreal forests of the northern hemisphere, (Tans *et al.*, 1990). This thesis reports on field experiments which were undertaken to investigate the turbulent exchange of mass, energy and momentum in a northern hemisphere coniferous forest, with special attention to the exchange of carbon dioxide.

The eddy covariance technique was used to measure mass, energy and momentum fluxes above and within a Sitka spruce, (*Picea sitchensis* (Bong.) Carr.), plantation in South West Scotland. The forest had a mean height, h, of 15 m, was densely planted and unthinned. Measurements were made at heights of $1.2h$, $0.7h$ and $0.1h$, where the heights within the canopy corresponded to the lower canopy crown and the dead branch trunkspace, respectively.

The upper canopy was found to be efficient at attenuating momentum, with momentum fluxes at $0.7h$ being only 2 - 3 % of those at $1.2h$. Spectral slopes of velocity and scalar quantities were considerably steeper than expected from Similarity theory indicating a more rapid dissipation of larger scale motions than above the canopy. Evidence was found to support the existence of large, intermittent and energetic structures dominating the turbulent exchange in the forest. Eularian integral length scales for streamwise (L_u) and vertical (L_w) velocities were calculated at $1.2h$ as ~ h and ~ $0.2h$, respectively. A momentum quadrant analysis indicated that ~ 50 % of momentum flux, 21 - 47 % of CO_2 flux and 23 - 44 % of sensible heat flux at $1.2h$ was accounted for by events with instantaneous momentum fluxes greater than four times the mean value, which occurred only 5 - 12 % of the time.

Diurnal cycles of CO_2, heat and radiation fluxes are presented for the forest system. The dependence of CO_2 flux into the forest system on photosynthetically active photon flux, I_P, vapour pressure deficit and air temperature was examined for a warm, sunny day and an overcast day. The main controlling environmental variable during the warm sunny period was found to be I_P, no strong dependence with vapour pressure deficit or air temperature was found. The response of net CO_2 flux into the forest system to I_P, for both data sets, was found to be well represented by a rectangular hyperbola. Curves fitted to the data predicted quantum requirements of 43 and 23 photons (molecule CO_2 fixed)$^{-1}$, dark respiration fluxes of 0.12 and 0.17 mg m^{-2} s^{-1}, saturation net influxes of 1.3 and 1.2 mg m^{-2} s^{-1} and compensation points of 130 and 104 μmol m^{-2} s^{-1} for sunny and overcast periods, respectively.

Corrections required to be made to CO_2 fluxes as a result of density effects (Webb *et al.*, 1980) and system frequency losses are discussed. The co-spectral response of CO_2 at $1.2h$ in unstable conditions was found to be quite different to the Kaimal *et al.* (1972) co-spectral model for sensible heat flux. A CO_2 co-spectral response function at $1.2h$ was obtained by fitting curves of a similar form to the model of Kaimal *et al.* (1972) to calculated CO_2 co-spectral densities.

At $0.1h$ the calculated CO_2 co-spectral densities showed much scatter and had mixed positive and negative components. Consequently the CO_2 fluxes at $0.1h$ could not be corrected for system frequency losses and had little reliability.

The use of the eddy covariance technique above and within a dense forest canopy is discussed and recommendations are made for future work.

ACKNOWLEDGEMENTS

This study was conducted at the Institute of Ecology and Resource management, Edinburgh University. I would like to thank my colleagues Jon Massheder, Chang Ming Fang, Frank Kelliher, John Moncrieff and Dominic McCafferty for their assistance and enthusiasm during the field experiments reported on in this thesis. I would especially like to thank my supervisors John Moncrieff and Paul Jarvis for their guidance and support during the period of this research and for the useful comments and suggestions made on drafts of this thesis.

I would also like to acknowledge Kim Martin for giving freely of his time to proof read this text; hopefully, someday I can return the favour when he finally writes his novel.

Financial support for my research studentship came from the Department of Education Northern Ireland.

TABLE OF CONTENTS

LIST OF SYMBOLS

ROMAN SYMBOLS

a	a constant.
A	the assimilation rate of the trees in a forest, (kg m^{-2} s^{-1}).
$A_{w\alpha}$	stability dependant term related to the peak co-spectral frequency of the sensible heat co-spectral model for thermally stable conditions of Kaimal *et al.* (1972).
$a_{w\rho_c}$	a parameter in the equation of a CO_2 co-spectral response model.
b	a constant.
$B_{w\alpha}$	stability dependant term related to the peak co-spectral frequency of the sensible heat co-spectral model for thermally stable conditions of Kaimal *et al.* (1972).
$b_{w\rho_c}$	a parameter in the equation of a CO_2 co-spectral response model.
c	volume fraction of a scalar gas, (μmol mol^{-1}).
c_k	a constant.
c_s	speed of sound in air, (m s^{-1}).
C	represents a scalar gas, i.e. CO_2.
$C(x, t)$	mean gas concentration at time t at position x along a tube,(kg m^{-3}).
C_0	amplitude of the harmonically varying mean gas concentration $C(x, t)$ at a tube entrance, (kg m^{-3}).
$C_{gh}(n)$	co-spectrum of the two real, continuous series $g(t)$ and $h(t)$.
C_{in}	mean gas concentration at the inlet of a tube, (kg m^{-3}).
$\overline{c_i}$	digital recursive mean (running mean) at the ith time series point.
C_{out}	mean gas concentration at the outlet of a tube, (kg m^{-3}).
c_p	heat capacity of air, (J kg^{-1} K^{-1}).
c_q	heat capacity of water, (J kg^{-1} K^{-1}).
$c_{w\rho_c}$	a parameter in the equation of a CO_2 co-spectral response model.
d	zero plane displacement, (m).
D	vapour pressure deficit, (Pa).
D_c	molecular diffusion coefficient for CO_2 in air, (m^2 s^{-1}).
D_F	a fractional normalised flux density.
D_v	virtual diffusion coefficient of a gas in a tube, (m^2 s^{-1}).
e	vapour pressure of water in air, (Pa).

E	vertical flux of water vapour at a given height, (kg m^{-2} s^{-1}).
f	frequency, where $f = 2\pi/T$, (rad s^{-1}).
f_k	normalised frequency given by $f_k = n(z-d)/\overline{U}$, at height z above a canopy with zero plane displacement d and mean horizontal wind speed $\overline{U}$.
f_0	stability dependant function relating to the sensible heat co-spectral model for thermally stable conditions of Kaimal *et al.* (1972).
f_p	normalised frequency used to describe the averaging loss of measurement over a sensor path length, p, where $f_p = np/\overline{U}$.
f_s	normalised frequency used to describe the frequency loss due to the separation of eddy covariance sensors by distance s, where $f_s = ns/\overline{U}$.
F_a	net CO_2 flux into a forest system, (kg m^{-2} s^{-1}).
$F_{A/R}$	assimilation/respiration CO_2 flux from the trees in a forest where $-F_{A/R} = A$ and $+F_{A/R} = R$, (kg m^{-2} s^{-1}).
F_c	flux of a mass scalar gas, (kg m^{-2} s^{-1}).
F_G	CO_2 flux from the soil and roots of a forest floor, (kg m^{-2} s^{-1}).
F_{RAW}	CO_2 flux uncorrected for the WPL density effect, (kg m^{-2} s^{-1}).
F_W	CO_2 flux from the wood of a forest, (kg m^{-2} s^{-1}).
g	gravitational acceleration, (m^2 s^{-2}).
G	soil heat flux (W m^{-2}).
$G(n)$	frequency series forming a Fourier transform pair with the real, continuous time series $g(t)$, with real component $G_r(n)$ and imaginary component $G_i(n)$.
$g(t)$	real, continuous time series forming a Fourier transform pair with $G(n)$, represented by $g(t) \Leftrightarrow G(n)$.
h	mean height of canopy, (m).
H	sensible heat flux, (W m^{-2}).
H	hole size, defined as the ratio of an instantaneous Reynolds stress with a time mean Reynold's stress.
$H(n)$	frequency series forming a Fourier transform pair with the real, continuous time series $h(t)$, with real component $H_r(n)$ and imaginary component $H_i(n)$.
$h(t)$	real, continuous time series forming a Fourier transform pair with $H(n)$, represented by $h(t) \Leftrightarrow H(n)$.
$H_d(n)$	digital recursive filter response function.

$H\left(\frac{(z-d)}{L}\right)$	stability function relating to the sensible heat co-spectral model for thermally stable conditions of Kaimal *et al.* (1972).
i	imaginary number equal to $\sqrt{-1}$.
I_i	dimensionless turbulence intensity of a Cartesian velocity component, i = 1, 2 and 3 corresponds to I_u, I_v and I_w.
I_P	photosynthetically active photon flux, (μmol m^{-2} s^{-1}).
$I_{Q,H}$	indicator function for conditionally sampling velocity data.
IRGA	an infrared gas analyser.
k	von Karman constant (k = 0.41).
k	wavenumber vector with components k_1, k_2 and k_3 in the three Cartesian directions.
$K_{5/6}$	modified Bessel function of the second kind.
K	a general turbulent eddy diffusivity, (m^2 s^{-1}).
K_c	turbulent eddy diffusivity for a gaseous scalar i.e. CO_2, (m^2 s^{-1}).
K_e	turbulent eddy diffusivity for water vapour e, (m^2 s^{-1}).
K_H	turbulent eddy diffusivity for sensible heat, (m^2 s^{-1}).
K_i	kurtosis of a Cartesian velocity component, i = 1, 2 and 3 corresponds to K_u, K_v and K_w.
K_M	turbulent eddy diffusivity for momentum, (m^2 s^{-1}).
l	transverse length scale, (m).
L	Monin-Obukhov length, (m).
LAI	leaf area index, i.e. the area of leaves per unit area of ground, taking one side of the leaf into account.
LE	latent heat flux, (W m^{-2}).
L_u	Eularian integral length scale of streamwise velocity, (m).
L_w	Eularian integral length scale of vertical velocity, (m).
m	integer, where $2m$ represents the number of points in an FFT block.
m_a	the molecular mass of dry air, (kg).
m_c	the molecular mass of a scalar gas C, (kg).
m_v	the molecular mass of water, (kg).
N	integer number, i.e. the length of a discrete series.
n	natural frequency, (Hz).

n_c	upper limit of natural frequency with contributions to a natural signal such as wind speed or momentum, (Hz).
n_j	discrete series of frequencies, length m, corresponding to the fast Fourier transform of a time series sample at a rate n_s, where $j = 1$ to $(m - 1)$, (Hz).
n_o	Nyquist frequency for a time series and is equal to half the sample frequency, (Hz).
n_p	peak natural frequency for velocity power spectra, (Hz).
n_s	frequency at which a time series has been sampled, (Hz).
p	atmospheric pressure (Pa).
p_l	path length of a sonic anemometer or IRGA, (m).
$\mathbf{p}$	path vector of a sonic anemometer.
$P_g(n)$	frequency series power spectrum of a discrete time series g_k.
p_i	total pressure within a closed path IRGA, (Pa).
p_{stp}	standard pressure of 101.3 kPa.
$Q_{gh}(n)$	quadrature spectrum of the two real, continuous series $g(t)$ and $h(t)$.
Q_j	quadrant in the uw plane, where $j = 1 - 4$.
r_{ab}	cross-correlation coefficient between a and b at a single point.
R	respiration rate of the trees in a forest, (kg m^{-2} s^{-1}).
$\Re$	universal gas constant, $\Re = 8.314$ J mol^{-1} K^{-1}.
Re	Reynold's number.
Re_c	critical Reynold's number for the onset of turbulent flow, $Re_c \cong 2300$.
$R_{gh}(\tau)$	cross-correlation function between two real time series $g(t)$ and $h(t)$ with lag τ, if $g \equiv h$ then the function is the autocorrelation function.
R_n	net radiation, (W m^{-2}).
$R_{Q,H}$	scalar flux fraction containing conditionally sampled scalar fluxes where u and w simultaneously lie in quadrant Q with hole size h in the range H.
s	eddy covariance sensor separation, (m).
S	total solar radiation (W m^{-2}).
$S(\kappa)$	power spectral density function in wavenumber κ for a continuous function.
S_{air}	flux of sensible and latent heat into storage in the air of a forest system, (W m^{-2}).

S_{bm} flux of sensible and latent heat into storage in the biomass of a forest system, (W m^{-2}).

$S_g(n)$ power spectral density function in natural frequency for a continuous function $g(t)$.

S_{LE_a} flux of latent heat into storage in the air of a forest system,(W m^{-2}).

S_{H_a} flux of sensible heat into storage in the air of a forest system, (W m^{-2}).

Sk_i skewness of a Cartesian velocity component, i = 1, 2 and 3 corresponds to Sk_u, Sk_v and Sk_w.

$S_{Q,H}$ momentum stress fraction containing conditionally sampled momentum stresses with u and w lying in quadrant Q with hole size h in the range H.

S_T total flux of sensible and latent heat into storage in the air and biomass of a forest system, (W m^{-2}).

t_t time taken for a fluid parcel to travel through a tube with length X and a discharge velocity U, i.e. $t_t = X/U$, (s).

t_r response time of a sensor, (s).

t_{avg} average transit time between a pair of sonic transducers, (s).

T absolute temperature, (K).

T_{air} absolute air temperature, (K).

$T_B(n)$ transfer function for electronic Butterworth low pass filters.

$T_{d(IRGA)}(n)$ transfer function for an infrared gas analyser dynamic frequency response.

$T_d(n)$ transfer function for the dynamic frequency response of a sensor.

$T_{d(sonic)}(n)$ transfer function for a sonic anemometers dynamic frequency response.

T_i absolute temperature of a sample air stream within a closed path IRGA, (K).

$T_m(n)$ transfer function for the mismatching of eddy covariance instruments dynamic frequency responses.

T_P averaging or sampling time of a time series such as $\alpha(t)$.

$T_p(f)$ transfer function with normalised frequency for the averaging of a scalar gas measurement over an IRGAs path length.

$T_p(n)$ transfer function with natural frequency for the averaging of a scalar gas measurement over an IRGAs path length.

$T_{Q,H}$ time fraction indicating the occurrence of conditionally sampled momentum stresses with u and w lying in quadrant Q with hole size h in the range H.

$T_r(n)$	transfer function for a digital recursive (running mean) filter.
T_{stp}	standard temperature of 273.2 K.
T_s	temperature measured with a sonic thermometer, (K).
$T_s(f)$	transfer function with normalised frequency describing the flux loss of two eddy covariance sensors separated by distance s.
$T_s(n)$	transfer function with natural frequency describing the flux loss of two eddy covariance sensors separated by distance s.
$T_t(n)$	transfer function with natural frequency for a gas sampled through a tube.
T_u	Eularian integral time scale of streamwise velocity, (s).
$T_{w\rho_c}(n)$	total transfer function with frequency for the flux $\overline{w'\rho_c'}$.
T_w	Eularian integral time scale of vertical velocity, (s).
$T_w(f)$	transfer function with normalised frequency for the averaging of a wind speed measurement over a sonic anemometers path length.
$T_w(n)$	transfer function with natural frequency for the averaging of a wind speed measurement over a sonic anemometers path length.
U	discharge velocity of air flowing through a tube, (m s^{-1}).
$\overline{U}$	mean horizontal wind speed, where $\overline{U} = \left(\overline{u}^2 + \overline{v}^2\right)^{1/2}$, (m s^{-1}).
U_*	friction velocity, (m s^{-1}).
U_c	constant wind speed in a uniform wind field, (m s^{-1}).
U_i	velocity vector, where $U_1 = u$, $U_2 = v$ and $U_3 = w$, (m s^{-1}).
$\overline{u}$	mean streamwise velocity over a period, (m s^{-1}).
u'	velocity fluctuation from the mean $\overline{u}$, (m s^{-1}).
u_k	discrete streamwise velocity time series with length N where $k = 0$ to $(N - 1)$, which forms a Fourier transform pair with the series U_k, $(w_k \Leftrightarrow U_k)$.
u_t^*	friction velocity at a tube wall, (m s^{-1}).
$\overline{v}$	mean lateral velocity over a period, (m s^{-1}).
v'	velocity fluctuation from the mean $\overline{v}$, (m s^{-1}).
V	voltage signal from an IRGA, (V).
V_o	reference voltage signal from an IRGA obtained under standard conditions, (V).
$\overline{w}$	mean vertical velocity over a period, (m s^{-1}).

w_j	discrete window function with length N, where $j = 1$ to N.
w_k	discrete vertical velocity time series with length N where $k = 0$ to $(N - 1)$, which forms a Fourier transform pair with the series W_k, $(w_k \Leftrightarrow W_k)$.
W_{ss}	sum of the squared amplitudes of the window function elements w_j.
w'	vertical velocity fluctuation from the mean $\overline{w}$, (m s^{-1}).
x	distance along a tube relative to a co-ordinate system moving in the direction of the fluid discharge velocity U, (m).
x	distance upwind from an instrument tower, (m).
X	length of a tube, (m).
x_i	position vector, where $x_1 = x$, $x_2 = y$ and $x_3 = z$, (m).
z	height above the ground, (m).
z_0	roughness length derived from the logarithmic wind profile, (m).

GREEK SYMBOLS

α	subscript denoting either T for temperature, ρ_c for CO_2 or u for streamwise velocity.
α	IRGA sensitivity to CO_2, (V (kg m^{-3})$^{-1}$).
$\alpha(t)$	time series with a measured time mean $\overline{\alpha}$.
α_1	attenuation coefficient.
β	the Bowen ratio of sensible to latent heat flux, $\beta = H/LE$.
β	IRGA sensitivity to water vapour, (V (kg m^{-3})$^{-1}$).
δ_{ij}	Kronecker delta, where $\delta_{ij} = 1$ if $i \equiv j$ and $\delta_{ij} = 0$ if $i \neq j$.
ΔF_E	water vapour flux correction term of a CO_2 flux for WPL and cross sensitivity effects, (kg m^{-2} s^{-1}).
ΔF_H	sensible heat flux correction term of a CO_2 flux for WPL and cross sensitivity effects, (kg m^{-2} s^{-1}).
$\overline{\Delta q}$	change in specific humidity of the air with time, (g kg^{-1} s^{-1}).
Δt	time interval between samples in a time series.
$\overline{\Delta T}$	average change in air temperature with time, (K s^{-1}).
Δz	vertical height separation between two cross-correlated sensors, (m).
ε	fractional error.
ε_{ab}	fractional error in the covariance of a time series.
ε_v	fractional error in the variance of a time series.

Φ_c	dimensionless stability function for a gaseous scalar i.e. CO_2.
Φ_H	dimensionless stability function for sensible heat *H*.
$\Phi_{ii}(\mathbf{k})$	spectral density tensor of a velocity field.
Φ_M	dimensionless stability function for momentum.
γ	is the psychrometer constant, $\gamma = 1.61 c_p p/\lambda$.
Γ	time constant of a digital recursive filter, (s).
η	a constant given by $\eta = e^{-\Delta t/\Gamma}$, where Γ is the time constant of a digital recursive filter and Δt is the time interval between samples in the time series.
φ_i	phase shifts introduced into measurements made from a sensor due to finite dynamic frequency responses, (rad).
κ	wave number, $\kappa = 2\pi/\lambda$, (rad m^{-1}).
κ_c	molecular diffusivity of a scalar with density in air of ρ_c, (m^2 s^{-1}).
λ	wavelength, (m).
λ_q	latent heat of vaporisation of water, (J kg^{-1}).
μ	ratio of the molecular masses of dry air and water, i.e. $\mu = m_a/m_v$.
υ	kinematic viscosity of a fluid, (m^2 s^{-1}).
θ	angle of the mean wind vector to the measurement path of an open path IRGA.
θ_v	virtual or potential temperature of the air, (K).
ρ	density of moist air, (kg m^{-3}).
ρ_a	density of dry air, (kg m^{-3}).
ρ_c	mass concentration or density of a scalar in air, i.e. CO_2 (kg m^{-3}).
ρ_{ci}	density of CO_2 in air in the sample cell of a closed path IRGA, (kg m^{-3}).
ρ_q	mass of water in the forest biomass per unit area of forest, (kg m^{-2}).
ρ_{stp}	air density at standard temperature and pressure, (kg m^{-3}).
ρ_v	density of water vapour in air, (kg m^{-3}).
ρ_{vi}	density of H_2O in air in the sample cell of a closed path IRGA, (kg m^{-3}).
σ	ratio of the mean density of water vapour in air and dry air, i.e. $\overline{\rho}_v/\overline{\rho}_a$.
σ_α^2	ensemble variance of time series $\alpha(t)$.

$\sigma^2_{\overline{\alpha}}$ variance of the measure time mean $\overline{\alpha}$ about the ensemble mean of the time series $\alpha(t)$.

σ^2_{horiz} total horizontal variance of wind speed, ($m^2\ s^{-2}$).

σ_i standard deviation of a velocity time series, i = 1, 2 and 3 corresponds to σ_u, σ_v and σ_w, ($m\ s^{-1}$).

σ^2_i variance of a velocity time series, i = 1, 2 and 3 corresponds to σ^2_u, σ^2_v and σ^2_w, ($m^2\ s^{-2}$).

τ time lag, (s).

τ_α integral time scale for the time series $\alpha(t)$, (s).

τ_e time when a velocity autocorrelation function equals $1/e$, (s).

τ_s Reynold's stress or momentum flux, ($m^2\ s^{-2}$).

τ_0 time of the first zero crossing of a velocity autocorrelation function, (s).

τ_r effective time constant of a digital recursive (running mean) filter, where $\tau_r = \eta\left(n_s(1-\eta)\right)^{-1}$, (s).

ξ any quantity advecting past a sensor in a turbulent flow.

CHAPTER 1
INTRODUCTION AND AIMS

1.1 INTRODUCTION

In recent years, the vegetation/atmosphere exchange has been a subject of great interest and a popular area of study. With improvements to micrometeorological instrumentation this field provides many opportunities to advance our understanding of the terrestrial environment. In addition to gaining knowledge about the functioning of the ecosystems of the Earth, specific areas of concern are also being addressed. Climate change postulated to result from emission of carbon dioxide from industrial and domestic activities, may have consequences for many of the ecosystems on Earth. Our knowledge of global carbon budgets is at present insufficient to predict reliably the possible consequences of rising CO_2 levels on the climate and on ecosystems. The cycles of carbon between the atmosphere, oceans and terrestrial biota are being examined both with measurements (at the surface and from space) and by general circulation models (GCMs). Major international field experiments have been carried out in different biomes in recent years in an attempt to relate space and surface measurements, and to calibrate GCMs for different land surfaces (Shuttleworth, 1991).

Attempts to close the global carbon budget with GCM have indicated that a major sink for CO_2 may exist in the boreal forests of the northern hemisphere (D'Arrigo *et al.*, 1987; Tans *et al.*, 1990). It is postulated that this sink may be increasing in strength as rising atmospheric CO_2 levels 'fertilise' the forests. Direct measurements of carbon fluxes in these forests to both calibrate GCMs and to obtain estimates of the size of the sink are consequently of vital interest. Few studies of CO_2 exchange between coniferous forests and the atmosphere have been published, Denmead (1969) reported three days of CO_2 fluxes above a *Pinus Radiata* stand and Jarvis *et al.* (1976) reviewed results from the International Biological Program (IBP). More recently Price and Black (1990, 1991) reported comprehensive measurements over a Douglas-fir (*Pseudotsuga menziesii*) forest and Jarvis (1993) reports on measurements from a *Picea Sitchensis* stand in the forest of Mearns, North East Scotland.

Possibly the best surface measurement technique currently available to examine the vegetation/atmosphere exchange in field experiments, is the eddy covariance technique. The use of this technique has increased in recent years with improved designs of sensor and acquisition systems. These advances have improved the accuracy, speed of response and reliability of turbulence measurements. However,

as a result of limitations in sensor size and response, the physical siting of experimental instrument arrays and data analysis techniques, measurements are susceptible to frequency band-limitation and result in a systematic underestimation of measured fluxes. To maximise the reliability of our measurements these limitations must be considered when planning experiments and accounted for in the resulting data. Methods for analysing the potential errors for eddy covariance systems are available and the application of corrections has been reviewed by Moore (1986). These methods have been applied successfully to fluxes measured above field crops (Leuning and King, 1992; Suyker and Verma, 1993) and deciduous forests (Hollinger *et al.*, 1993) but no reports of their application over coniferous forest have been published.

The necessity for further measurements of CO_2 exchanges in coniferous forests is clear. Additionally a careful evaluation of the use of the technique above and within coniferous forest is required. The reliability of eddy covariance measurements depends on our knowledge of the turbulent flow regime in which they are made.

This thesis reports eddy covariance measurements of CO_2, and supporting heat and momentum fluxes, above and within a coniferous forest canopy in south west Scotland. The nature of the turbulent flow regimes at each measurement height are also examined. The correction to fluxes for frequency-limited losses are estimated and the eddy covariance technique evaluated in the different regimes above and below the canopy. The examination of the flow regimes tells us much about the transport processes which dominate exchanges within and above the forest. This information will aid the planning, implementation and interpretation of future eddy covariance experiments.

In this introduction I will discuss some of the basic concepts and techniques employed in this thesis. I will evaluate the various methods of scalar flux measurement , demonstrating that eddy covariance is the most suitable for the purpose, and finally I will state the aims of this research and present the layout of this thesis.

1.2 BASIC CONCEPTS

1.2.1 Micrometeorological Concepts

When a fluid flows over a surface a boundary layer forms as the flow works against the friction of the surface. The velocity of the fluid flow decreases as it approaches the surface where it is zero. The boundary layer above a uniform extensive

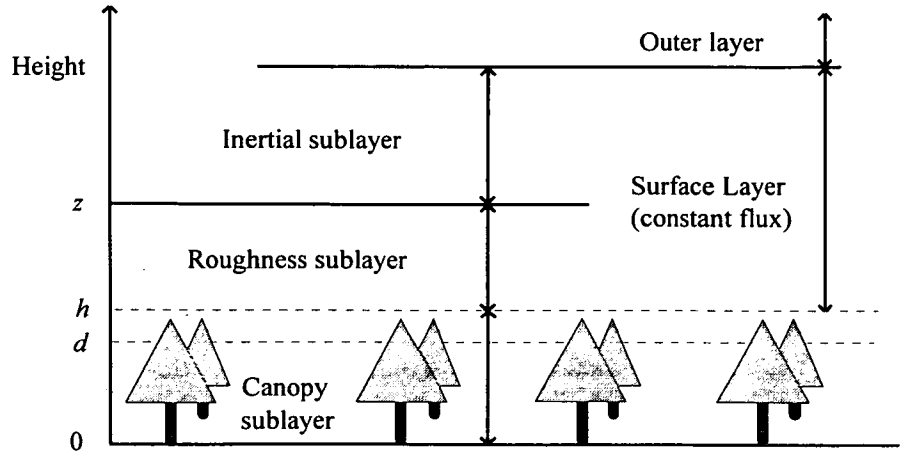

Fig. 1.2.1 Schematic diagram of the lower boundary layer above an extensive homogeneous forest, (after Raupach and Legg, 1984).

surface in neutral steady state conditions can be considered as having an outer layer and a surface layer, Figure 1.2.1.

In the surface layer, the fluxes of momentum and scalars change little with height, (the surface layer is also called the 'constant flux' layer). At the top of the surface layer is the inertial sublayer, where the following relationship describes the flux of momentum or shearing stress, τ_s at a height z with the mean horizontal wind speed $\overline{U}$:

$$\tau_s(z) = \bar{\rho} K_M \frac{d\overline{U}}{dz} = \bar{\rho} U_*^2, \qquad (1.2.1)$$

where ρ is air density, K_M is a turbulent diffusivity for momentum at height z defined:

$$K_M = \frac{kU_*(z-d)}{\Phi_M}, \qquad (1.2.2)$$

where Φ_M is an empirical estimated correction for effects of non-neutral stabilities, k is von Karman's constant (k = 0.41) and d is the zero plane displacement. The velocity, U_*, is the 'friction' or 'eddy rotation' velocity at height z and can be defined as the product of a mean eddy size, or mixing length, with the gradient of mean wind speed with height, i.e. the mean wind speed change over one vertical mixing length. Friction velocity is a useful scaling parameter and is related to the shearing stress, τ_s, as in equation 1.2.1.

In neutral conditions the function Φ_M is equal to 1 and equation 1.2.2 integrates to a semi-logarithmic mean wind speed profile as:

$$\overline{U}(z) = \frac{U_*}{k} \ln\left(\frac{z-d}{z_0}\right), \qquad (1.2.3)$$

where z_0 is the roughness length characteristic of the surface. The two properties that arise from this wind profile and describe the aerodynamics of the surface are d and z_0, and they must be obtained from wind profiles measured in the inertial sublayer. The zero plane displacement d is the height within the canopy at which the wind speed predicted by the wind profile above the canopy approaches zero. The roughness length z_0 is related to the height of a uniform canopy and is as measure of the aerodynamic roughness of the surface.

In the inertial sublayer the boundary layer structure depends only on scales such as U_* and the canopy height, h. Close to the top of the canopy, plant elements interact with the flow and generate turbulent wakes establishing a roughness sublayer (Raupach and Legg, 1984). Within the roughness sublayer the turbulent structure is influenced by the distribution and spatial structure of the canopy and foliage. In a wind tunnel study, the roughness sublayer was found to have an estimated depth of $(h + 1.5l)$, where l is a transverse length scale, often taken as the distance between plants (Raupach *et al.*, 1980). Below the canopy top there is the canopy layer where the dominant turbulent events are large excursions from above with a length scale of order h (Raupach, 1988; Raupach *et al.*, 1989).

1.2.1.1 Measurement Fetch

By placing instruments on a tower at different heights within these sublayers we can measure the exchanges, or fluxes, of mass, energy and momentum. Calculated fluxes in the inertial sublayer will be effectively constant with height whilst in the roughness and canopy sublayers, flux directions and magnitudes will vary with height. For momentum fluxes we might expect to see fluxes decreasing with height through the canopy as momentum is absorbed by the trees. Sources and sinks in the canopy determine the direction and magnitude of the heat and mass fluxes. When solar radiation is strong the canopy is heated and there would be a flux of sensible heat away from the forest. Similarly for CO_2 the flux direction and magnitude will depend on the relative positions and strengths of sources and sinks such as respiration and photosynthesis.

Instruments placed on a tower above a surface are effectively making spatially averaged measurements of a region upwind of the tower. The 'fetch' from a tower is the distance upwind of a change in the surface characteristics. If we are measuring

above a forest we need to be sure that all air flowing through our instrument array lies in the boundary layer affected only by the forest surface.

Recent modelling efforts have estimated the area, or 'flux footprint', over which flux measurements from a tower are representative (Schuepp *et al.* 1990; Leclerc and Thurtell, 1990; Wilson and Swaters, 1991; Horst and Weil, 1992). A schematic representation of the flux footprint upwind of a tower is shown in Figure 1.2.2.

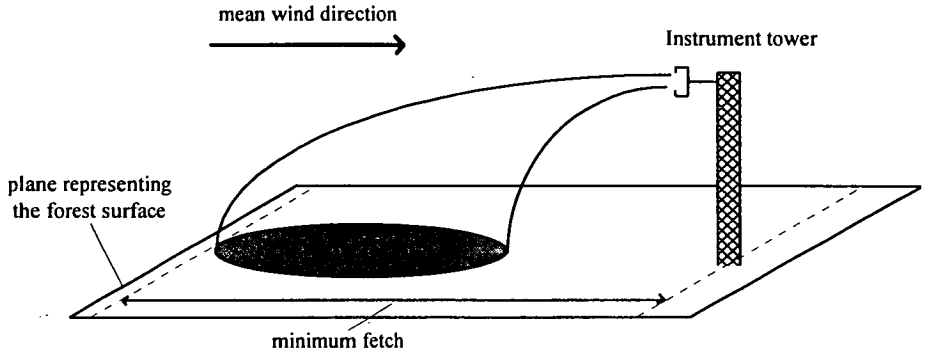

Fig. 1.2.2 Schematic representation of a flux footprint for a tower measuring over a uniform surface. The required fetch of uniform surface is shown for the prevailing conditions.

The size and distance of the footprint from the tower depends on thermal stability, wind speed, the height of the tower and the roughness of the surface. Following the analysis of Schuepp *et al.* (1990), we can obtain an estimate of the footprint by adopting approximate solutions for neutral stability. If we define x as distance upwind from the tower and z as the measurement height, then these solutions give the concentration of the measured quantity at point (x, z) resulting from an infinite crosswind line source in a uniform wind field with constant wind speed, U_c, and constant eddy diffusivity. In this way the concentration gradient with z can be derived and flux estimates arrived at by making use of the scalar diffusivity. The fractional normalised flux density (D_F) of a measured flux is thus estimated as:

$$D_F = \frac{U_c(z-d)}{U_* k x^2} \exp\left(-\frac{U_c(z-d)}{U_* k x}\right), \qquad (1.2.4)$$

where a value of U_c can be estimated as the average wind speed between the surface (at height $d + z_0$) and the measurement height z assuming a logarithmic wind profile, as:

$$U_c = \int_{d+z_0}^{z} \overline{U}(z)\,dz \Big/ \int_{d+z_0}^{z} dz = \frac{U_*\left[\ln\left((z-d)/z_0\right)-1+\left(z_0/(z-d)\right)\right]}{k\left(1-z_0/(z-d)\right)} \qquad (1.2.5)$$

Values of U_* can either be assumed for a particular site or calculated from equation 1.2.3 at height z, similarly for z_0.

An example of the fractional normalised flux density (D_F) for a forest site is shown in Figure 1.2.3 for assumed conditions similar to those expected at our site. The integral of equation 1.2.4 from $x = 0$ to a distance upwind gives the cumulative flux fraction, i.e. is a test of the effective fetch, this fraction is also shown in Figure 1.2.3. The peak contribution to the measured flux comes from ~ 50 m upwind with very small contributions up to 1600 m indicating a required fetch of about 2 km in this example.

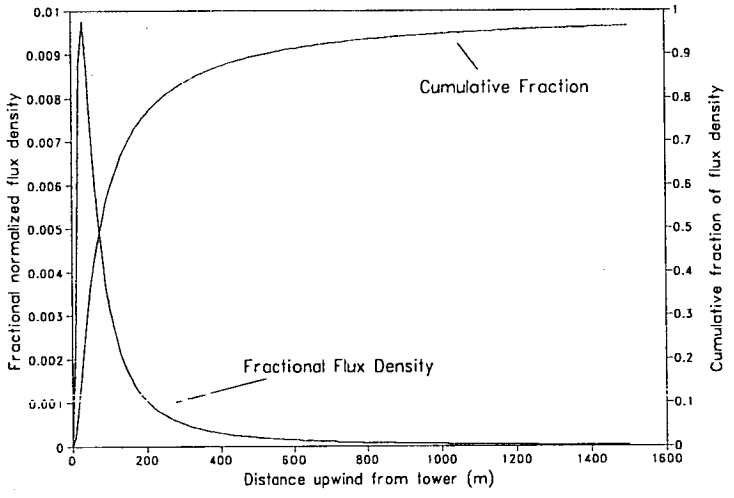

Fig. 1.2.3 Estimated flux footprint upwind from a tower following Schuepp *et al.* (1990). The measurement height z is 18 m, $\overline{U}(z)$ is 4 m s^{-1}, U_* is 0.4 m s^{-1}, d is 12.4 m, z_0, is 0.5 m and air temperature is 20 °C.

1.2.2 Governing Equations For Momentum and Mass Exchanges

The fluxes of momentum, heat and scalars can be calculated indirectly by assuming eddy diffusivities, K, as in equation 1.2.1 for momentum and measuring profiles of mean wind speed and the quantity of interest (see section 1.3.1). However direct expressions for these fluxes can be obtained from the governing equations of turbulent flow above and within plant canopies. These flux equations can be

formulated in terms that can be directly measured by a technique such as eddy covariance.

A useful notation for formulating these equations in three Cartesian dimensions is Einstein's notation (Stull, 1988). In this notation, x_j denotes x, y and z and U_j denotes u, v and w (the velocities in the x, y and z directions) for values of j of 1, 2 and 3, respectively. Above an homogeneous surface in stationary conditions the governing equations for the turbulent flow are (Stull, 1988):

The continuity equation

$$\frac{\partial U_j}{\partial x_j} = 0 \qquad (1.2.6)$$

Newton's 2nd law (conservation of momentum)

$$\frac{\partial U_i}{\partial t} + U_j \frac{\partial U_i}{\partial x_j} + \delta_{i3} g + \frac{1}{\rho}\frac{\partial p}{\partial x_i} - \nu \frac{\partial^2 U_i}{\partial x_j \partial x_j} = 0 \qquad (1.2.7)$$

Scalar conservation equation

$$\frac{\partial \rho_c}{\partial t} + U_j \frac{\partial \rho_c}{\partial x_j} - \kappa_c \frac{\partial^2 \rho_c}{\partial x_j \partial x_j} = 0 \qquad (1.2.8)$$

Where t is time, δ_{i3} is the Kronecker delta, ρ is air density, p is pressure, ν is the kinematic viscosity of air, ρ_c is the density of a passive scalar in air, g is the acceleration due to gravity, and κ_c is the molecular diffusivity of the scalar. (The Coriolis force term in equation 1.2.7 has been omitted as it is generally assumed negligible in the surface layer). Conservation equations can also be written explicitly for conservation of heat and moisture in the turbulent flow, (Stull, 1988).

To obtain equations which are useful in practice and which relate to quantities that we can measure, we must apply Reynolds averaging to the equations. Reynolds averaging is the process of decomposition of instantaneous values of any quantity into the mean value over a period of time and the fluctuation from that mean. Time averages are denoted by an overbar and fluctuations from the time average by a prime, i.e. for velocity and scalar concentration:

$$U_j = \overline{U_j} + U_j' \quad \text{and} \quad \rho_c = \overline{\rho_c} + \rho_c' \qquad (1.2.9)$$

This is shown schematically for streamwise velocity u in Figure 1.2.4 where the time trace varies about its mean, $\bar{u}$, over a time period T_P and each instantaneous deviation from the mean value is given by the fluctuation $u'(t)$; thus at any given time t the streamwise velocity $u(t)$ is given by $u(t) = \bar{u} + u'(t)$.

Thus, the three conservation equations become, (Stull, 1988; Raupach and Thom, 1981):

The continuity equation

$$\frac{\partial \overline{U_j}}{\partial x_j} = 0 \qquad (1.2.10)$$

Newton's 2nd law

$$\frac{\partial \overline{U_i}}{\partial t} + \overline{U_j}\frac{\partial \overline{U_i}}{\partial x_j} = -\delta_{i3} g - \frac{1}{\overline{\rho}}\frac{\partial \overline{p}}{\partial x_i} + \nu \frac{\partial^2 \overline{U_i}}{\partial x_j \partial x_j} - \frac{\partial \overline{\left(U_i' U_j'\right)}}{\partial x_j} \qquad (1.2.11)$$

I II III V VI X

where: Term I represents storage of mean momentum.
Term II describes advection of mean momentum by the mean wind.
Term III allows gravity, to act downwards.
Term V describes the mean pressure-gradient forces.
Term VI represents the influence of viscous stress on the mean motions.
Term X represents the influence of Reynolds stress on the mean motion, or divergence of turbulent momentum flux.

Scalar conservation equation

$$\frac{\partial \overline{\rho}_c}{\partial t} + \overline{U_j}\frac{\partial \overline{\rho}_c}{\partial x_j} = \kappa_c \frac{\partial^2 \overline{\rho}_c}{\partial x_i \partial x_i} - \frac{\partial \overline{\left(U_j' \rho_c'\right)}}{\partial x_j} \qquad (1.2.12)$$

I II VI X

where: Term I represents storage of the scalar.
Term II describes advection of the scalar by the mean wind.
Term VI represents the mean molecular diffusion of the scalar.
Term X represents the divergence of the turbulent scalar flux.

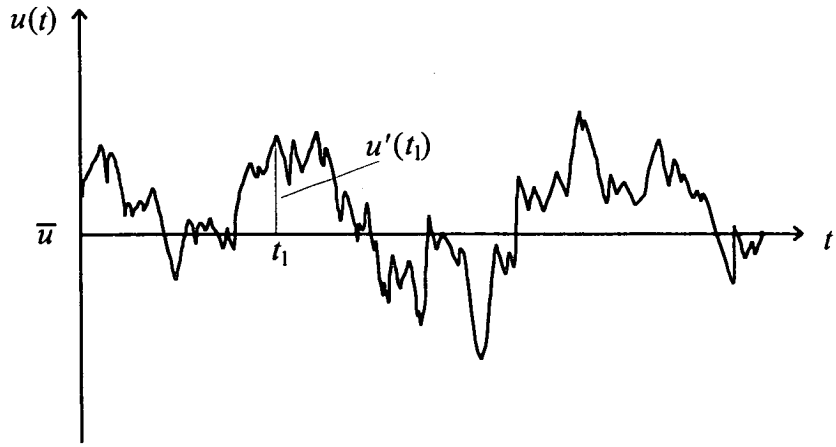

Fig 1.2.4 Schematic time trace of streamwise velocity u about a mean value $\overline{u}$ with deviations from the mean being the fluctuations $u'(t)$.

The complex form of a plant canopy results in a flow which has a large spatial variability so, to consider the canopy as a whole, we must spatially average over a thin volume (Raupach and Thom, 1981; Finnigan, 1985). The resulting conservation equations apply only to the air spaces between plant elements. We will adopt the nomenclature from Raupach and Thom (1981) that angle brackets denote a volume average and double primes a departure from the volume average, i.e.:

$$\overline{U_j} = \langle \overline{U_j} \rangle + \overline{U_j}'' \quad \text{and} \quad \overline{\rho}_c = \langle \overline{\rho}_c \rangle + \overline{\rho}_c'' . \tag{1.2.13}$$

Assuming no mean streamwise pressure gradient and negligible vertical molecular transport compared to vertical turbulent transport, the conservation equations become, in Cartesian notation (Raupach and Thom, 1981):

Momentum conservation equation

$$\frac{\partial}{\partial z}\langle \overline{u}''\overline{w}'' \rangle + \frac{\partial}{\partial z}\langle \overline{u'w'} \rangle = -\frac{1}{\rho}\left\langle \frac{\partial \overline{p}''}{\partial x} \right\rangle + \nu \langle \nabla^2 \overline{u}'' \rangle \tag{1.2.14}$$

I II

Scalar conservation equation

$$\frac{\partial}{\partial z}\langle \overline{w}''\overline{\rho}_c'' \rangle + \frac{\partial}{\partial z}\langle \overline{w'\rho_c'} \rangle = \kappa_c \langle \nabla^2 \overline{\rho}_c'' \rangle \tag{1.2.15}$$

On the *r.h.s.* of equation 1.2.14, term (I) represents form drag and term (II) represents viscous drag per unit mass of air, (Raupach and Thom, 1981). The term on the *r.h.s.* of equation 1.2.15 represents the specific creation density or emission rate per unit mass of air of the scalar with density ρ_c, (Raupach and Thom, 1981). (A rigorous development of the time and volume averaging of the equations is given in Raupach and Shaw (1982) and Finnigan (1985)).

The first terms on the left hand side of equations 1.2.14 and 1.2.15 are dispersive fluxes arising from spatial correlation of mean updraft/downdraft regions, where $\overline{u}$ or $\overline{\rho}_c$ differs from their spatial means $\langle \overline{u} \rangle$ and $\langle \overline{\rho}_c \rangle$. These terms were found to be negligible in the inertial flux layer above an artificial canopy in a wind tunnel, (Raupach *et al.*, 1986). We have now identified quantities which are measurable and will give us the net exchange, or flux, at any height z of either momentum or a scalar. The time and volume averaged momentum flux which describes the drag on the canopy at height z is, from equation 1.2.14, $\rho\langle \overline{u'w'} \rangle$. Similarly, a flux of a scalar with concentration ρ_c is given by equation 1.2.15 as $\langle \overline{w'\rho_c'} \rangle$.

In practice, large time series of velocity and scalar measurements are collected and are averaged over a sampling period, T_P, of around 30 minutes to one hour, giving a time average and a time series of fluctuations about that mean. The volume average is assumed to be inherent to the measurement as parcels of air from many spatial sources are sampled by the instruments, as discussed earlier in relation to the flux footprint. Throughout the thesis, fluxes will be referred to without the angle brackets but the volume average will be implicitly assumed.

1.3 TECHNIQUES FOR MEASURING MASS FLUXES

Techniques for measuring mass fluxes fall into the two categories of direct and indirect methods as discussed previously. Indirect methods are founded on the assumption that mass, heat and momentum exchanges between a plant canopy and the atmosphere occur by a steady turbulent diffusion along mean concentration gradients. A direct method measures fluctuations of the quantity of interest, and of wind speed, calculating the fluxes as discussed in section 1.2.2.

Both direct and indirect methods of measurement of mass and energy fluxes are subject to corrections due to density effects (Webb *et al.*, 1980). Thus for CO_2 flux measurements simultaneous measurements are required of sensible and latent heat.

I will now discuss the techniques in general terms, indicating their advantages and disadvantages in relation to measurement of mass and energy exchanges between forest canopies and the atmosphere.

1.3.1 Flux/Gradient Techniques

Flux/gradient techniques are based on 'K-theory', or first order closure theory, whereby K is a turbulent eddy diffusivity. Exchanges of mass, heat and momentum between a plant canopy and the atmosphere are assumed to occur as a steady turbulent diffusion along mean concentration gradients. The two most widely used experimental flux/gradient methods are the Aerodynamic and Bowen ratio techniques and these are discussed individually below.

No method based on K-theory can be used to measure fluxes within plant canopies. The assumption of steady diffusion along mean gradients implies that the length scale of the turbulence at any height is smaller than the distance over which mean gradients change. This is often not the case within canopies. The study in a *Pinus Radiata* forest of Denmead and Bradley (1985) demonstrated that counter

gradient fluxes of heat, water vapour and CO_2 occurred within the canopy indicating the invalidity of K-theory within canopies.

1.3.1.1 Aerodynamic technique

The flux gradient relationships in neutral conditions for fluxes of momentum, τ_s, sensible heat, H and a gaseous scalar, F_c, with concentration ρ_c (i.e. H_2O or CO_2) are, (Monteith and Unsworth, 1990):

$$\tau_s(z) = K_M \frac{\partial(\rho \overline{U})}{\partial z}, \tag{1.3.1}$$

$$H(z) = -K_H \frac{\partial(\rho c_p T)}{\partial z}, \tag{1.3.2}$$

$$F_c(z) = -K_c \frac{\partial(\rho_c)}{\partial z}, \tag{1.3.3}$$

where c_p is the specific heat capacity of air, and K_M, K_H and K_c are turbulent eddy diffusivities for momentum, sensible heat and a scalar, respectively. From similarity arguments in neutral stability,

$$K_M = K_H = K_c. \tag{1.3.4}$$

Thus by rearranging equations 1.3.1, 1.3.2 and 1.3.3 and taking $\tau_s = \rho U_*^2$, equations for all the fluxes can be obtained in terms of the velocity gradients and U_*, for a scalar gas as:

$$F_c(z) = -U_*^2 \frac{\partial(\rho_c)}{\partial \overline{U}}. \tag{1.3.5}$$

In the aerodynamic method, fluxes are calculated for an entity, as in equation 1.3.5, from measured profiles of wind speed and the entity itself. The turbulent eddy diffusivities are stability dependent, with the general form as shown in equation 1.2.2.

The relationships between K_M, K_H and K_c and between Φ_M, Φ_H and Φ_c have been intensely studied in different stability conditions (Dyer and Hicks, 1970; Webb, 1970; Businger *et al.*, 1971; Pruitt *et al.*, 1973). In neutral stability all entities are transported equally (equation 1.3.4) and $\Phi_M = \Phi_H = \Phi_c = 1$. In unstable conditions Dyer and Hicks (1970) concluded that :

$$\Phi_M^2 = \Phi_H = \Phi_V = \left[1 - 16(z-d)/L\right]^{-0.5}, \tag{1.3.6}$$

where L is the Monin-Obukhov length which is a function of heat and momentum fluxes:

$$L = \frac{-\rho c_p T_{air} U_*^3}{kgH}. \qquad (1.3.7)$$

For stable and slightly unstable conditions, Webb (1970) deduced the slightly different relation:

$$\Phi_M = \Phi_H = \Phi_V = [1 + 5(z-d)/L]. \qquad (1.3.8)$$

The aerodynamic technique suffers from errors due to the uncertainties in these empirical stability formulae. Errors are greatest in strongly stable conditions such as still nights with low wind speed, (Verma and Rosenberg, 1975). The technique is consequently of limited use at night or in highly stable conditions. Errors are also larger above tall canopies compared to field crops, where fluxes are underestimated unless measurements can be made well above the roughness sublayer but still within the inertial sublayer. Additionally gradients are difficult to measure above tall, rough forest because of the enhanced turbulence of the boundary layer.

1.3.1.2 Bowen ratio technique

The Bowen ratio technique uses the energy balance of a surface to develop flux equations. The energy balance of a surface can be written in terms of the net radiation flux (R_n), the sensible and latent heat fluxes, (H and LE, respectively), change in storage of heat in the canopy, S_T, and the soil or ground heat flux, G:

$$R_n = H + LE + S_T + G \qquad (1.3.9)$$

The Bowen ratio, β, is the ratio of sensible to latent heat fluxes and it can be shown that (Thom, 1975):

$$\beta = \frac{H}{LE} = \gamma \frac{\partial T_{air}}{\partial e}, \qquad (1.3.10)$$

where γ is the psychrometer constant,e is the vapour pressure of water vapour in air. Thus β can be found from measurements of T_{air} and e at a series of heights in the constant flux layer. The fluxes of H and LE can be written in the form of equation 1.3.3:

$$H = -K_H \rho c_p \frac{\partial T_{air}}{\partial z}, \qquad (1.3.11)$$

$$LE = -K_e \lambda \frac{\partial e}{\partial z}, \qquad (1.3.12)$$

where K_H and K_e are the diffusivities for sensible heat and water vapour and λ is the latent heat of vaporisation of water. The diffusivities of sensible heat and latent heat

and any quantity other than momentum can be treated as equal in neutral conditions, (Thom, 1975) and thus equation 1.3.9 can be written:

$$R_n - S_T - G = -K\rho c_p \frac{\partial T_{air}}{\partial z} - K\rho c_p \frac{\partial e}{\partial \gamma z} \quad \gamma \frac{\partial e}{\partial z}$$
$$= K\rho c_p \frac{\partial T_e}{\partial z} \qquad (1.3.13)$$

where T_e is the equivalent temperature equal to $T_{air} + (e/\gamma)$. Thus by substituting the diffusivities for the flux profile relationships for other quantities such as CO_2 into equation 1.3.13, flux equations can be obtained in terms of gradients of the scalar concentration with effective temperature. Thus for CO_2:

$$F_c = \frac{(R_n - S_T - G)}{\rho c_p} \frac{\partial \rho_c}{\partial T_e}. \qquad (1.3.14)$$

Errors can occur in Bowen ratio calculated fluxes when R_n is small, i.e. when R_n is of the order of $(S_T + G)$, similarly large errors occur when the $(S_T + G)$ is large as these terms are hard to measure. Errors arising in these circumstances were estimated to be as large as 40 % by Verma and Rosenberg (1975). Clearly the Bowen ratio technique has a large uncertainty at night or in other conditions where R_n is difficult to measure.

1.3.2 The Eddy Covariance Technique

The eddy covariance technique directly measures the covariance between vertical velocity and the quantity of interest, i.e. $\overline{u'w'}$ or $\overline{w'\rho_c'}$ as given in equations 1.2.14 and 1.2.15 for momentum and a scalar with concentration ρ_c. Thus the mean flux of an entity is obtained by averaging the instantaneous covariance of vertical velocity with the entity of interest over a suitable time period. The scale of eddies contributing to the turbulent transport necessitates sampling at rates of at least 1 - 5 Hz, and often even faster. The instruments for eddy covariance require much shorter response times than those used to measure mean concentration profiles in the flux/gradient methods. The main sources of error in eddy covariance measurements arise from imperfect sensor arrays or acquisition system response, which cause a loss of calculated flux. The corrections required for eddy covariance flux measurements have been reviewed by Moore (1986).

The great advantage of the eddy covariance method is that flux measurements can be made at a single point in space rather than by a vertical profile of instruments.

The technique also applies in all stabilities and radiation conditions (i.e. it operates successfully throughout the diurnal cycle) and above and within canopy in the roughness and canopy sublayers.

The requirement for sensors with adequate response times has resulted in the technique becoming widely used only in recent years. The use of the eddy covariance theory for measurement of mass and energy fluxes was first proposed by Swinbank in 1951 and in 1955, Swinbank demonstrated the technique by making field measurements of w, e and T_{air} which were subsequently analysed with a mechanical computer (Dyer, 1961). The fluxes calculated, however, were underestimated due to the poor response of his sensors and acquisition system. The analysis of the data with a mechanical integrator was extremely cumbersome, an obstacle that has been removed by the development of the micro-computer. Further field measurements of sensible and latent heat fluxes were made with the eddy covariance technique by Dyer (1961), Dyer and Pruitt (1962), and Dyer and Maher (1965) with an improved experimental system called the 'Evapotron'. Technological improvements continued with Dyer *et al.* (1967) reporting fluxes measured with the 'Fluxatron' system although losses due to poor instrument response were still significant.

Measured quantity	Instrument	Reference
wind speed	sonic anemometers	Kaimal (1978) Campbell and Unsworth (1979) Coppin and Taylor (1983)
	hot-wire anemometers	Bottemanne (1976)
	hot-film anemometers	Shaw *et al.* (1973)
water vapour density	Lyman-alpha, infra-red absorption hygrometers	Hyson and Hicks (1975) Ohtaki and Matsui (1982)
air temperature	fast response thermocouples and sonic thermometers	Dyer and Maher (1965) Dyer *et al.* (1967) Kaimal and Businger (1963)
CO_2 concentration	infra-red gas analysers	Ohtaki and Matsui (1982) Denmead and Bradley (1989)

Table 1.3.1 Examples of a few 'landmark' papers reporting major developments in instrumentation for eddy covariance.

The technique has become much more practical with the development of accurate, fast response sensors such as the examples given in Table 1.3.1. Studies of mass, energy and momentum exchange using the eddy covariance technique have been reported over a wide range of vegetation canopies (Table 1.3.2).

Vegetation/surface type	Reference
coniferous forest	Denmead and Bradley (1985) and (1989)
tropical rain forest	Fan *et al.* (1990)
Mediterranean *macchia* scrub	Valentini *et al.* (1991)
deciduous forest	Hollinger *et al.* (1993)
above a deciduous forest floor	Baldocchi *et al.* (1986) Verma *et al.* (1986) Baldocchi and Meyers (1991)
prairie grassland	Kim and Verma (1990)
field crops	Anderson *et al.* (1984) Suyker and Verma (1993)
rice paddy	Ohtaki (1980) Ohtaki and Oikawa (1991)

Table 1.3.2 Examples of eddy covariance experiments reported in the literature in recent years.

1.4 TECHNIQUES FOR EXAMINING TURBULENT EXCHANGE PROCESSES

Efforts to better understand the processes of turbulent transport above and within plant canopies have been made by many researchers over the years in conjunction with the studies of mass and energy exchanges discussed above. Comprehensive reviews by Raupach and Thom (1981), Raupach (1988) and Raupach *et al.* (1989) summarise our knowledge of canopy aerodynamics and the way in which turbulence transfers scalar quantities such as temperature, water vapour and CO_2 between the vegetation and the canopy.

Several useful analysis techniques have been applied to the problem of understanding turbulent transport in recent years which are employed in this thesis.

1.4.1 Spectral Analysis

Spectral analysis is the decomposition of time series data into the frequency domain. The frequency representation of turbulent fluid parcels in the air indicates the size and duration of the motions and allows us to identify dominant processes in the flow more easily. Departures from recognised forms in velocity spectra in the sublayers of the surface layer are a powerful tool in the study of momentum transport and the interaction of the turbulent flow with the vegetation.

Spectral analysis has been recognised for many years as a useful means of examining turbulent wind flow. Early studies in plant canopies, such as the work of

Allen (1968) in a Japanese larch plantation, were hampered by poor instrument response and signal processing. With the advent of faster response anemometry (Table 1.3.1) the use of spectral analysis increased.

A notable study of measurements made with sonic anemometers in 1968 in Kansas over wheat stubble provided empirical descriptions of velocity, temperature and humidity power and co-spectra in a wide range of thermal stabilities and which are still very much in use (Kaimal *et al.*, 1972; Wyngaard and Coté, 1972). Many spectral analyses have been carried out above and within a variety of plant canopies in field crops (Shaw *et al.*, 1974; Finnigan, 1979*a*; Wilson *et al.*, 1982; Ohtaki, 1984), in deciduous forest (Anderson *et al.*, 1986; Baldocchi and Meyers, 1988*b*; Amiro, 1990*b*), in a widely spaced Almond orchard (Baldocchi and Hutchison, 1988), in coniferous forest (Amiro and Davis, 1988; Bergström and Högström, 1989; Amiro, 1990*b*), and in wind tunnel canopies (Seginer *et al.*, 1976; Raupach *et al.*, 1986).

The calculation of co-spectral densities for measured fluxes is essential for the correction of fluxes for frequency-limited losses (Moore, 1986). Many researchers have used the unstable sensible heat co-spectral model of Kaimal *et al.* (1972) to represent CO_2 co-spectral response above plant canopies (Anderson *et al.*, 1986; Leuning and King, 1992; Suyker and Verma, 1993; Hollinger *et al.*, 1993). Although there are no comparisons in the literature between this model and actual CO_2 co-spectral responses above coniferous forest.

1.4.2 Velocity Cross-Correlation Analysis

The cross-correlation of velocities at different vertical heights through a canopy in time is a simple yet effective method of examining the turbulent flow. From the sign and magnitude of the resulting time lags much information can be gathered about the vertical structure of the turbulent transport and thus the exchange processes.

The first comprehensive use of velocity cross-correlation analysis was reported by Finnigan (1979*b*) from an experiment in a wheat canopy using hot-wire anemometers at different heights through the canopy. This work identified the dominant role of large energetic gusts in the transfer of momentum to the plants, which originate above the canopy. This direct method of comparing velocity flows at different levels in canopies has since been used in many canopy types. Crowther and Hutchings (1985) reported a cross-correlation analysis of velocity above a coniferous forest using propeller anemometers and Baldocchi and Meyers (1988*b*) carried out a comprehensive velocity cross-correlation analysis through a deciduous forest canopy with sonic anemometers. Work reported by Raupach *et al.* (1989) in a model wheat canopy in a wind tunnel, and in a Eucalyptus forest, used both spatial correlations in

three dimensions (the wind tunnel study) and profile space-time cross-correlations (both studies). From the three dimensional spatial cross-correlations Raupach *et al.* (1989) identified a form for the large energetic incursions observed above canopies, as 'double-roller' eddies (similar results having been found in smooth wall boundary layer work such as Antonia *et al.*, 1988). From the space-time cross-correlations Raupach *et al.* (1989) reported zero vertical velocity lags at all levels in a profile, with respect to measurements above the canopies, in both the wind tunnel and the forest.

In recent years, further velocity cross-correlation studies have been published in Australian bush (Chen, 1990) and in deciduous forest (Shaw and Zhang, 1992). Space-time streamwise velocity cross-correlations with negative lags in the trunkspace of a deciduous forest were reported by Shaw and Zhang (1992), who concluded that the turbulence in the sub-crown of the deciduous forest was driven by pressure perturbations rather than directly by penetrating gusts from above.

1.4.3 Quadrant Analysis

The technique of 'quadrant analysis' arose from smooth and rough wall laboratory boundary layer experiments (Lu and Willmarth, 1973; Raupach, 1981). The technique enables some information about the structure of turbulent transport to be deduced from conditionally sampled turbulence measurements at a single point. It involves conditionally averaging time series data according to the signs of the streamwise and vertical velocity fluctuations, u' and w', and the size of the instantaneous momentum flux, $u'w'$, in relation to the period mean (see section 2.1.6). The technique identifies events which are extreme in comparison to the mean flow and allows us to associate these momentum events with the transport of scalars.

Quadrant analysis was first used in a field experiment in a wheat canopy by Finnigan (1979*b*) and later by Shaw *et al.* (1983) in a corn canopy. These analyses showed that most of the momentum transfer in a canopy occurs during short, intermittent gusts or sweeps. Further studies have since been conducted in deciduous forests (Baldocchi and Meyers, 1988*a*; Moritz, 1989), in a widely spaced Almond orchard (Baldocchi and Hutchison, 1987), in model canopies in wind tunnels (Raupach *et al.*, 1986), above coniferous forest (Bergström and Högström, 1989) and above Australian bush (Chen, 1990). Above the coniferous forest canopy of Bergström and Högström (1989) more than 50 % of the momentum transport into the canopy was accounted for by events with instantaneous momentum fluxes about 4 - 5 times the mean period flux, which occurred only 7 - 11 % of the time. Similar intermittent and energetic structures were observed in the other canopy types.

1.5 RESEARCH AIMS

The aim of this research was to investigate the turbulent exchange of mass, energy and momentum in a northern hemisphere coniferous forest, with special attention to the exchange of carbon dioxide. The eddy covariance technique was considered to be the best method for examining these exchanges. The use of the technique for the reliable measurement of CO_2 fluxes above and within a dense coniferous forest will be evaluated.

The research also aimed at examining the turbulent transfer processes in the forest with reference to turbulence statistics and with the techniques of spectral analysis, velocity space-time cross-correlations and quadrant analysis. It was hoped that this would enable better interpretation of mass flux measurements and to aid the planning, implementation and interpretation of future eddy covariance experiments.

1.6 THESIS LAYOUT

The thesis is laid out in 8 chapters and a number of appendices containing additional detail and practical guidance for some of the topics covered. Each chapter is briefly described below:

Chapter 1 has been an introductory chapter giving background to the subject of study including some of the basic concepts of turbulent exchange between the atmosphere and plant canopies. The aims and presentation of the thesis are also discussed.

Chapter 2 presents theoretical considerations of analyses used in the thesis. The transfer function corrections applied to calculated eddy fluxes in the thesis are presented with examples and discussion of their application.

Chapter 3 describes the experimental and analytical methods employed for the presentation of the results in this thesis. Intercomparison experiments of sensors are described (for sonic anemometers and infra-red gas analysers measuring CO_2). A brief discussion of computer programs used to analyse data is included with reference to flow diagrams and program listings in appendices.

Chapter 4 presents results of CO_2 and energy exchanges in the forest system. The corrections applied to the CO_2 eddy covariance fluxes are discussed. Energy and radiation relationships are presented. Diurnal cycles of CO_2, radiation and energy fluxes are presented at several levels in the forest. An analysis of the response of the CO_2 flux across the forest system boundary to environmental variables is presented.

Chapter 5 presents the calculated turbulence statistics including Eularian integral time and length scales of the turbulence calculated from u and w autocorrelations at three heights above and within the forest. A space-time cross-correlation analysis is

presented for the three Cartesian velocity components at two heights within the forest canopy with respect to measurements above the canopy.

Chapter 6 contains a spectral analysis of the three Cartesian velocity components and the scalar quantities temperature, CO_2 and H_2O. Both power and co-spectra are presented at three heights above and within the forest.

Chapter 7 contains a quadrant analysis in a momentum framework at three heights through the forest. Also presented are the associated scalar flux fractions of sensible heat and CO_2 in the momentum quadrants and holes.

Chapter 8 completes the thesis by summarising the findings, discussing their implications and suggesting some areas for future work.

Appendix A.1 discusses the design, manufacture and performance of fifth order Butterworth low-pass electrical filters as used in field experiments.

Appendix A.2 discusses the procedures for co-ordinate rotation of three dimensional wind data. The mathematical development of the rotations, examples of their implementation in Turbo Pascal and their effect on measured momentum and CO_2 fluxes above the forest are included.

CHAPTER 2.
THEORETICAL CONSIDERATIONS

2.1 STATISTICAL METHODS

2.1.1 Introduction

Turbulent processes in the surface boundary layer of the atmosphere are complex three dimensional phenomena and are most easily quantified by stochastic methods. By describing the statistical properties of velocity and scalars in a fixed volume in space and time, we can begin to describe the physical processes occurring in a fluid as it flows through the volume. Such an approach is also referred to as 'Eularian'. By separating a flow into its mean and fluctuating parts, the turbulent and non-turbulent components can be examined separately. This separation is carried out by Reynold's averaging, as discussed in section 1.2.2, and it forms the basis for all of the analyses presented in this thesis.

A statistical approach to the analysis of turbulent flow is applicable when the flow is stationary (i.e. characteristic statistics of the flow do not change with time), or quasi-stationary (when the flow statistics change on a time scale much greater than the sampling time). The mean components of turbulent flow in the surface layer generally change with the passage of weather systems, whereas we are calculating statistics, typically, over half an hour.

2.1.2 Taylor's Hypothesis

The relationship between measurements of atmospheric turbulence made at one point in space over time, and measurements made simultaneously at many points are identical only under the specific conditions outlined below. Taylor (1938) suggested that under these certain conditions turbulence could be considered 'frozen' as it advected past a sensor above a uniform surface. Thus, large scale motions would be apparently advected past a sensor by the mean wind speed. This simplification is extremely useful in relating time series measurements to spatial structures such as eddies; the simplification breaks down when the eddies are changing in a shorter time than it takes them to be advected on the mean wind past the sensor.

Taylor's Hypothesis states that turbulence advecting past a sensor can be considered to be frozen for any variable ξ when:

$$\frac{d\xi}{dt} = \frac{\partial \xi}{\partial t} + U_j \frac{\partial \xi}{\partial x_j} = 0. \qquad (2.1.1)$$

Alternatively, the hypothesis can be stated in terms of wave number, κ, and frequency, f, as:

$$\kappa = f/\overline{U}, \qquad (2.1.2)$$

where $\kappa = 2\pi/\lambda$ and $f = 2\pi/T_P$, where λ is the wavelength and T_P is the time period of an eddy and $\overline{U}$ is the mean horizontal wind speed. Thus, we can directly relate the spatial and temporal dimensions or scales of eddies by $\overline{U}$.

Taylor's hypothesis breaks down in conditions of high turbulence intensity when large structures are vertically sheared. Also, inhomogeneous terrain results in spatial variations which are not represented in single point time series and the hypothesis is no longer valid. Similarly, the hypothesis is not valid within plant canopies where turbulent wakes from form drag are being created as the flow moves through the plants, although equation 2.1.2 is often used to obtain length and time scale estimates from frequency spectra within canopies, (Kaimal and Finnigan, 1993).

2.1.3 Reynold's Averaging

As already described in section 1.2.2 velocities and scalar concentrations can be split into mean and fluctuating parts as shown by equation 1.2.9. For a series of N velocity measurements, U_j we have:

$$U_j = \overline{U}_j + U_j', \qquad (2.1.3)$$

where an overbar denotes an average as :

$$\overline{U}_j = \frac{1}{N}\sum_{j=0}^{N-1} U_j, \qquad (2.1.4)$$

and a prime denotes the deviation from the mean. This averaging scheme can apply to temporal or spatial series. When considering three dimensional flow, the three velocity components, u, v and w can all be averaged in this way in both time and space. The mean velocities of the three components, $\overline{u}$, $\overline{v}$ and $\overline{w}$ are the most basic descriptors of the flow. The fluctuating components, u', v' and w' allow us to analyse the turbulent component of the flow and to calculate characteristic turbulence statistics.

It is often convenient to rotate the Cartesian co-ordinates so that u points in the direction of the mean horizontal flow and is referred to as streamwise flow. Thus, for a discrete sampling period, $\overline{v} = 0$ and the v component is referred to as ~~longitudinal~~ transverse flow, (see Appendix A.2).

2.1.4 Variance, Standard Deviation And Turbulence Intensity

The variance of a series is a measure of the distribution about the mean. For a series, U_j with N samples, the variance is given by σ_j^2, where

$$\sigma_j^2 = \frac{1}{N-1}\sum_{j=0}^{N}\left(U_j - \overline{U_j}\right)^2. \qquad (2.1.5)$$

Using equation 2.1.3 and assuming $1/N \cong 1/(N+1)$ as N is generally large, we have:

$$\sigma_j^2 = \frac{1}{N}\sum_{j=0}^{N}\left(U_j'\right)^2 = \overline{\left(U_j'\right)^2}. \qquad (2.1.6)$$

The standard deviation of the series, σ_j is defined as:

$$\sigma_j = \left(\sigma_j^2\right)^{1/2} = \left(\overline{\left(U_j'\right)^2}\right)^{1/2}. \qquad (2.1.7)$$

This quantity has the same dimensions as the original variable and is thus a useful measure of the magnitude of the spread of the variable about the series mean.

For a velocity in a turbulent flow we can define a turbulence intensity, I_j as:

$$I_j = \frac{\sigma_j}{\overline{U}}, \qquad (2.1.8)$$

where $\overline{U}$ is the mean velocity in the streamwise direction of the flow. This is a non-dimensional measure of the intensity of the turbulent velocity fluctuations.

2.1.5 Covariance, Skewness and Kurtosis

The covariance between two series a_i and b_i is defined as:

$$covar = \frac{1}{N}\sum_{j=0}^{N}\left(a_j - \overline{a_j}\right).\left(b_j - \overline{b_j}\right). \qquad (2.1.9)$$

From equation 2.1.3 we see that this is simply the sum of the product of the fluctuations of a_j and b_j:

$$covar = \frac{1}{N}\sum_{j=0}^{N} a_j'.b_j' = \overline{\left(a_j'.b_j'\right)}. \qquad (2.1.10)$$

When $a_j = b_j$ the covariance is equal to the variance of the single series, σ_a^2 or σ_b^2.

The covariance between two different series is a measure of the degree of agreement or similarity between the series. When the covariance is normalised by the

product of the standard deviations of the two series, the result is the linear correlation coefficient between the two.

The covariance between streamwise and vertical velocity fluctuations, $\overline{u'w'}$ is termed the Reynolds Stress or shear stress, and is a measure of the momentum flux at the point of measurement. Similarly, for a scalar with density fluctuations, ρ_c' the covariance with w', $\overline{w'\rho_c'}$, is a measure of the flux of that scalar concentration past the measurement point. As we saw from equations 1.1.9 and 1.1.10 these terms arise explicitly from the Reynolds averaging performed on the governing equations of turbulent flow.

In a perfect Gaussian turbulent flow the fluctuations of the velocity U_i, U_i' are symmetrically distributed about the mean $\overline{U}$. In a flow which has large excursions from the mean value which are biased in their occurrence, the distribution of the velocity fluctuations is said to be skewed. For instance, if there are more positive values of U_i' than negative ones then the distribution is positively skewed and if negative fluctuations dominate then it is negatively skewed. In a Gaussian distribution, skewness is zero. These three cases are shown schematically in Figure 2.1.1*a*. Skewness is represented statistically by Sk_i where:

$$Sk_i = \frac{\overline{\left(U_i'^3\right)}}{\sigma_i^3}. \qquad (2.1.11)$$

Values of skewness for u and w velocities approach zero well above plant canopies, (Raupach *et al.*, 1986; Shaw and Seginer, 1987; Amiro, 1990*a*). Within canopies, streamwise velocity is generally positively skewed with $Sk_u \sim 1$ in the densest part of the canopy, whereas vertical velocity is generally negatively skewed with $Sk_w \sim -1$, (Raupach, 1988). With the aid of conditional sampling analysis, section 2.1.6, positive Sk_u values can be attributed to faster moving air above the canopy occasionally 'sweeping' into the canopy with no equally strong upward motions. Similarly, the negative Sk_w values can be attributed to the dominance of the downward motions.

Turbulent flow can be further described by its kurtosis, which is an indication of the 'peakedness' or probability density distribution of the fluctuations. A Gaussian distribution has a kurtosis of three where more sharply peaked distributions have values > 3 and less sharply peaked distributions have kurtosis values < 3. Three such distributions are shown schematically in Figure 2.1.1*b*. Kurtosis, K_i, is given by:

$$K_i = \frac{\overline{\left(U_i'^4\right)}}{\sigma_i^4}. \qquad (2.1.12)$$

Experimental data shows that kurtosis of u and w velocities, K_u and K_w approach the Gaussian value well above a canopy, (Raupach *et al.*, 1986; Amiro, 1990*a*). Within a canopy maximum kurtosis values ~ 6 to 8 are observed where extreme events are occurring intermittently with respect to the Gaussian distribution, (Raupach *et al.*, 1986; Baldocchi and Meyers, 1988*a*; Amiro, 1990*a*).

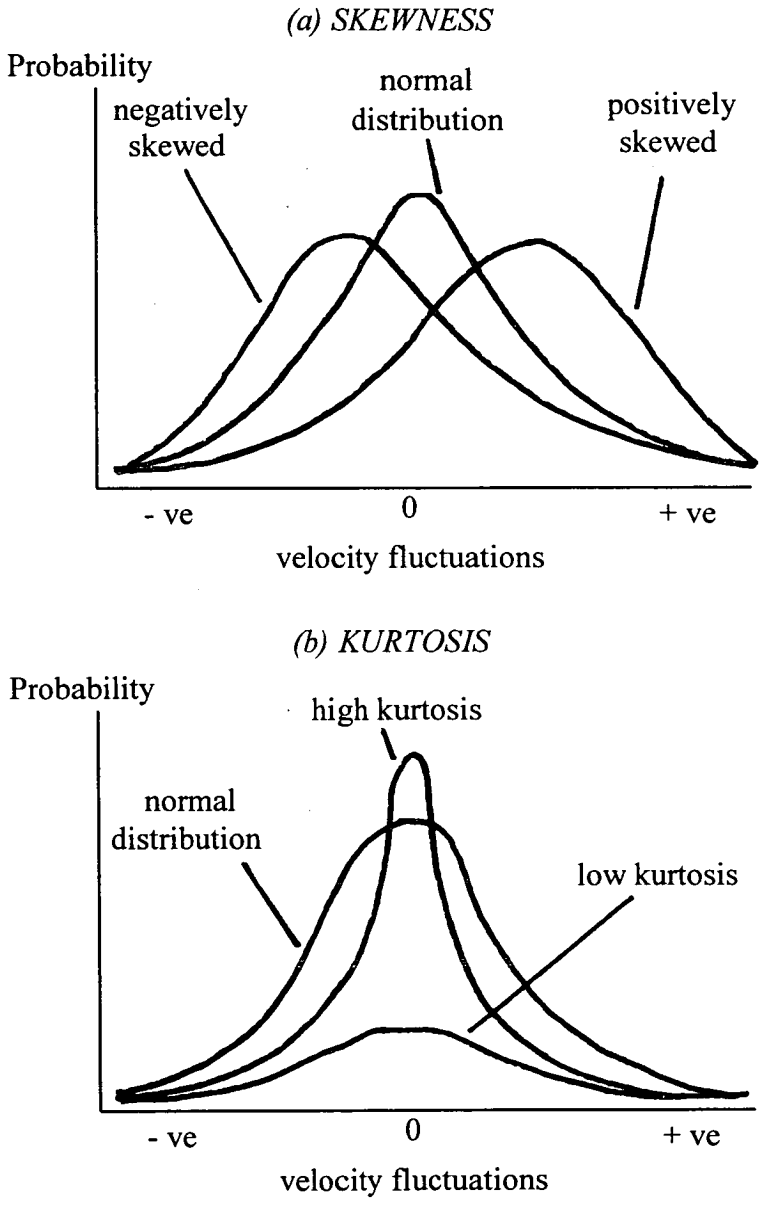

Fig. 2.1.1 Schematic diagram of skewness and kurtosis for velocity fluctuations in relation to a normal distribution.

Where (*a*) shows skewness and (*b*) shows kurtosis. A normal distribution has zero skewness and kurtosis of three.

2.1.6 Quadrant Analysis

Quadrant analysis of instantaneous momentum fluctuations (Lu and Willmarth, 1973) separates the values of horizontal and vertical velocity fluctuations into four classes or quadrants according to their orientation to the surface. (For velocity fluctuations we adopt the usual convention that downward fluctuations and fluxes are negative). The four quadrants, Q, are assigned as follows, (Lu and Willmarth, 1973; Finnigan, 1979*b*; Raupach *et al.*, 1986):

$Q_1 : u' > 0$ and $w' > 0$

$Q_2 : u' < 0$ and $w' > 0$

$Q_3 : u' < 0$ and $w' < 0$

$Q_4 : u' > 0$ and $w' < 0$

These quadrants represent certain physical processes in the turbulent flow. Negative instantaneous fluctuations represent air moving more slowly relative to the mean flow and positive fluctuations indicate air moving faster than the mean flow. Quadrants (1) and (3) clearly represent positive or upward instantaneous momentum fluxes $u'w'$ and quadrants (2) and (4) negative or downward fluxes. Quadrants (1) and (3) are often termed 'outward' and 'inward' interactions, respectively, and represent dissipation processes, i.e. turbulent wakes from form drag on tree elements and eddy interactions. Quadrants (2) and (4) are given the names 'ejections' and 'gusts' ,respectively (also 'bursts' and 'sweeps'). These quadrants represent processes which transport momentum to the surface, either by transporting faster moving air towards the surface (i.e. gusts in Q_4) or by transporting slower moving air away from it (i.e. ejections in Q_2). We can also seek to partition the momentum events within each quadrant by assigning a 'hole' in the quadrant, (Lu and Willmarth, 1973; Finnigan, 1979*b*; Raupach *et al.*, 1986). This hole is bounded by a maximum value of momentum flux $u'w'$ in the u' and w' plane, i.e. by the hyperbolic curve :

$$u'w' = \text{constant}. \qquad (2.1.13)$$

This constant boundary value, or hole size, is generally a multiple of the overall mean momentum flux thus, we can now define the size of the 'hyperbolic hole' in terms of this multiple, H. The curve delimiting the hole now becomes:

$$u'w' = H\left|\overline{u'w'}\right|. \qquad (2.1.14)$$

Such a curve is shown schematically in Figure 2.1.2.

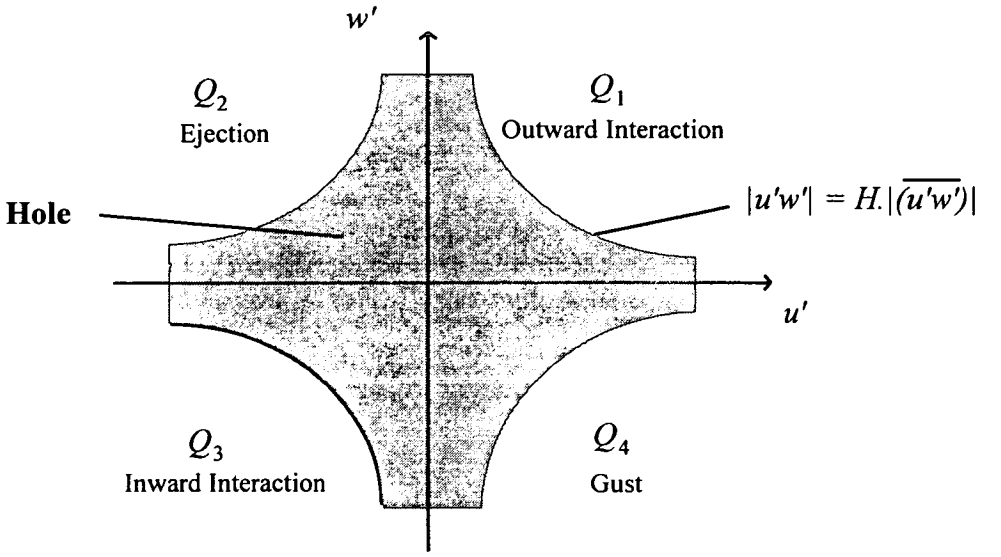

Fig. 2.1.2. Schematic drawing of quadrants and hyperbolic hole in a $u'w'$ plane.

Thus we can build up a picture of the relative intensities of momentum transport within each quadrant, in terms of fractional contributions to the overall mean momentum flux $\left(\overline{u'w'}\right)$. We construct a 'stress fraction', $S_{Q.H}$ which for a given quadrant Q and hole size H, contains the fractional contribution of events lying outside the hole H. An indicator function $I_{Q.H}(t)$ is used to represent the binning mathematically; it has a value of 1 when $w'(t)$ and $u'(t)$ lie in Q with a value of $u'w'$ inside the hole H and zero otherwise. Thus, the stress fraction $S_{Q.H}$ is given by :

$$S_{Q.H} = \frac{1}{T_P\left(\overline{u'w'}\right)} \int_0^{T_P} u'(t)\,w'(t)\,I_{Q.H}(t).\mathrm{d}t \qquad (2.1.15)$$

Where T_P is the period over which the mean is calculated and t is time. We can also define a 'time fraction', $T_{Q.H}$, which cumulates the indicator function $I_{Q.H}(t)$ and gives a measure of the distribution of individual events in the various quadrants Q with hole sizes H :

$$T_{Q.H} = \frac{1}{T_P} \int_0^{T_P} I_{Q.H}(t).\mathrm{d}t \qquad (2.1.16)$$

Clearly with a discrete time series these equations must reduce to summation approximations of the integrals :

$$S_{Q.H} = \frac{1}{T_P\left(\overline{u'w'}\right)} \sum_{t=0}^{T_P} u'(t)w'(t)I_{Q.H}(t) \qquad (2.1.17)$$

$$T_{Q.H} = \frac{1}{T_P} \sum_{t=0}^{T_P} I_{Q.H}(t) \qquad (2.1.18)$$

In our data, the time interval between time series points was 0.055 s (corresponding to a sample rate of 18.2 Hz). From spectral analysis of the time series, (Chapter 6), we see that we are sampling sufficiently quickly to detect all events and that the summation introduces negligible errors.

We can also extend the quadrant partitioning to scalar fluxes by building up a 'scalar flux fraction' at the same time as the momentum stress fraction. For a scalar ρ_c the values of u' and w' would determine the quadrant Q and the hole size H and the scalar flux fraction $R_{Q.H}$ would be accumulated as :

$$R_{Q.H} = \frac{1}{T_P\left(\overline{w'\rho_c'}\right)} \sum_{t=0}^{T_P} w'\rho_c' . I_{Q.H}(t) \qquad (2.1.19)$$

Rather than building up stress or flux fractions over a full range of hole sizes, fractions corresponding to 'normal' and 'extreme' events alone can be presented. A value of $H = 4$ is often used to represent the transition between 'normal' and 'extreme' events. Thus, an event which has an instantaneous value of $u'w'$ which is four times the mean value is considered to be an extreme event. This value has generally been chosen such that extreme events are seen to contribute ~ 50 % of the total mean momentum flux, (Raupach *et al.*, 1986; Bergström and Högström, 1989; Moritz, 1989).

2.1.7 Autocorrelation and Cross-Correlation Functions

The autocorrelation of a velocity time series gives a measure of the periodicity, persistence or 'memory' of velocity fluctuations in the time domain, (Kaimal and Finnigan, 1993). If we consider two functions $g(t)$ and $h(t)$ which each represent real, continuous time series and which form Fourier transform pairs with functions $G(n)$ and $H(n)$ where t is time and n is natural frequency, then the Fourier transform pairs are, (Press *et al.*, 1989):

$$g(t) = \int_{-\infty}^{\infty} G(n) e^{-2\pi i n t} \, dn \quad \text{and} \quad G(n) = \int_{-\infty}^{\infty} g(t) e^{2\pi i n t} \, dt \qquad (2.1.20)$$

$$h(t) = \int_{-\infty}^{\infty} H(n) e^{-2\pi i n t} \, dn \quad \text{and} \quad H(n) = \int_{-\infty}^{\infty} h(t) e^{2\pi i n t} \, dt \qquad (2.1.21)$$

Fourier transform pairs will in future be denoted as:

$$g(t) \Leftrightarrow G(n)$$

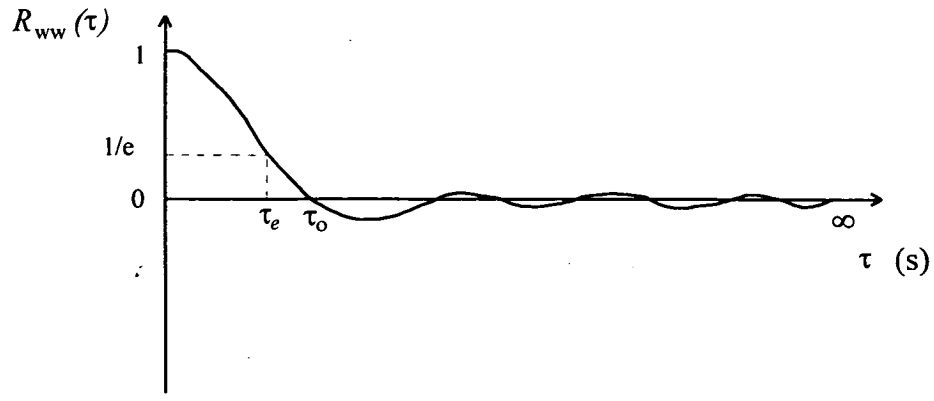

Fig. 2.1.3. Schematic diagram of a *w* velocity autocorrelation with lag τ.

The cross-correlation of the two functions $g(t)$ and $h(t)$ is $R_{gh}(\tau)$, where τ is the lag between the two functions. $R_{gh}(\tau)$ can be written:

$$R_{gh}(\tau) = \frac{1}{\sigma_g \sigma_h} \int_{-\infty}^{\infty} g(t+\tau)h(t)\,d\tau \qquad (2.1.22)$$

This correlation is a function of the lag, τ and lies in the time domain and is thus a member of the Fourier transform pair, (Press *et al.*, 1989)*:

$$R_{gh}(\tau) \Leftrightarrow G(n)H^*(n) \qquad (2.1.23)$$

where $H^*(n)$ is the complex conjugate of the function $H(n)$.

If the functions $g(t)$ and $h(t)$ are identical, then the cross-correlation function $R_{gh}(\tau)$ becomes the autocorrelation function, $R_{gg}(\tau)$:

$$R_{gg}(\tau) \Leftrightarrow G(n)G^*(n) \qquad (2.1.24)$$

where

$$G(n)^* G(n) = |G(n)|^2 \qquad (2.1.25)$$

In practice, autocorrelations and cross-correlations can be obtained from discrete time series using a Fast Fourier Transform (FFT) routine. If we consider discrete series, length N, of vertical velocity, w_k and streamwise velocity, u_k, where k = 0 to (N-1) which form the Fourier Transform pairs:

$$w_k \Leftrightarrow W_k \text{ and } u_k \Leftrightarrow U_k \qquad (2.1.26)$$

Then the cross-correlation between w_k and u_k is obtained by the procedure:

1. FFT both series to obtain the Fourier transforms W_k and U_k.
2. Form the product of W_k and the complex conjugate of U_k, $W_k.U_k^*$.

*Equation (2.1.23) applies explicitly for real functions $g(t)$ and $h(t)$. More generally the relationship would be: $R_{gh}(\tau) \Leftrightarrow G(n)H(-n)$

3. Perform an inverse FFT on the series $W_k.U_k^*$ to obtain the cross-correlation series, $R_{wu}(\tau)$.

2.1.8 Eularian Length And Time Scales

Turbulent flow regimes are often characterised by time and length scales which represent the dominant scale motions. The concept of a turbulent eddy is of an entity with sufficient coherence to simultaneously influence two spatially separated points in the flow. Time and length scales seek to quantify the realm of influence of these dominant eddies. The time scale can be regarded as the persistence time of the velocity of a fluid parcel, and the length scale is related to the time scale by a characteristic flow velocity, (Kaimal and Finnigan, 1993). The autocorrelation function for a turbulent velocity has a form similar to that shown in Figure 2.1.3.

Several time scales can be defined from the autocorrelation function. Lag times related to the autocorrelation function are often used as characteristic time scales. The time of the first zero crossing, τ_0, and the lag when $R_{ww}(\tau) = 1/e$, τ_e, Figure 2.1.3, are used in this way. However, integral time scales are generally preferred as they take account of the strength of the persistence of the various turbulent motions contributing to the autocorrelation. Integral time scales, T_w and T_u, can be defined for streamwise and vertical velocities as, (Raupach, 1988):

$$T_w = \int_0^\infty R_{ww}(\tau)d\tau \qquad (2.1.27)$$

$$T_u = \int_0^\infty R_{uu}(\tau)d\tau \qquad (2.1.28)$$

Clearly to estimate T_w a discrete $R_{ww}(\tau)$ series is required, extending to large lags which can be numerically integrated to approximate the continuous integral from $\tau = 0$ to ∞ In practice, the numerical integrations are often performed for the range $\tau = 0$ to τ_0, as it is assumed there will be little underestimation of the integral time scale if negative lobes in the autocorrelation function are small for large lags.

On the assumption that Taylor's hypothesis is valid, we can calculate Eularian length scales for u and w, L_u and L_w, from the appropriate time scales. Again several forms are used in the literature; Wilson *et al.* (1981), Raupach *et al.* (1986), and Raupach (1988) used the form:

$$L_u = \overline{U}.T_u \qquad (2.1.29)$$

$$L_w = \overline{U}.T_w \qquad (2.1.30)$$

The form used by Amiro and Davis (1988), Baldocchi and Meyers (1988*b*) and Amiro (1990a) uses T_w only:

$$L_u = \overline{U}.T_w \tag{2.1.31}$$

$$L_w = \sigma_w.T_w \tag{2.1.32}$$

The form in equations 2.1.29 and 2.1.30 is that used in this thesis.

2.1.9 Power Spectra And Co-Spectra

The Fourier transform of a time series maps the temporal information contained in the series into a frequency domain. It is most useful to examine the frequency domain series in terms of signal power or amplitude. The power spectrum gives the fractional variance contribution of each frequency component.

Consider a discrete time series g_k, of k = 0 to (N - 1) points, with a mean value, $\bar{g}$ which forms a Fourier transform pair with $G(n)$. For each component in the frequency series, we define a discrete spectral intensity (or energy), $P_g(n)$ which is given by:

$$P_g(n) = G(n).G^*(n) = |G(n)|^2 \tag{2.1.33}$$

Where the series of $P_g(n)$ is the power spectrum. The variance of velocity fluctuations has the same units as turbulent energy per unit mass and thus power spectra of velocity fluctuations are often called discrete energy spectra.

It can be shown that the sum of the discrete spectral intensities is (Press *et al.*, 1988):

$$\sum_{n=1}^{N-1} |G(n)|^2 = \frac{1}{N} \sum_{k=0}^{N-1} (g_k - \bar{g})^2 = \sigma_g^2 \tag{2.1.34}$$

Thus we can see that the power spectral intensities for each frequency component are directly proportional to the variance, σ_g^2, of the original time series.

This power spectral density series is often represented for a continuous function over all frequencies by a spectral density function, $S_g(n)$ where:

$$\int_{-\infty}^{\infty} S_g(n)\,dn = \sigma_g^2 \tag{2.1.35}$$

Velocity power spectra in the surface layer have three subranges; to the left of the spectral peak is the energy containing subrange, and to the right of the peak are the inertial and dissipation subranges. A schematic velocity power spectrum is shown in Figure 2.1.4.

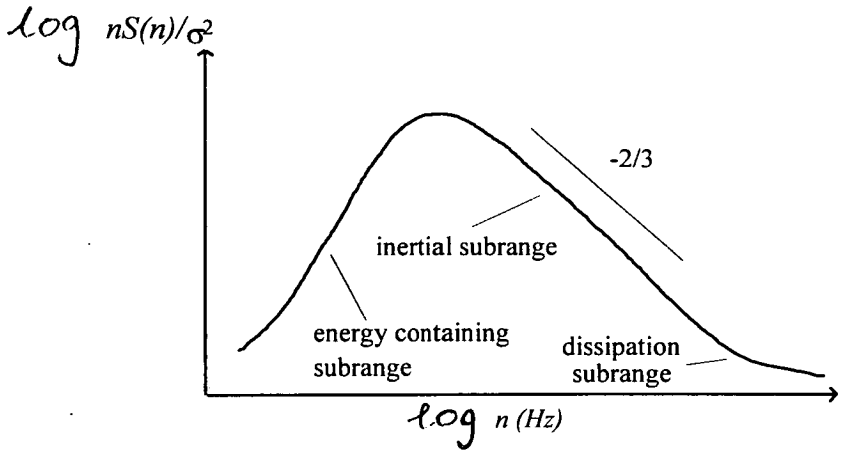

Fig 2.1.4 Schematic diagram of a velocity power spectrum, where the power spectral density $S(n)$ is multiplied by natural frequency, n, and normalised by the series variance, σ^2.

Similarity theory predicts that velocity power spectral density in the inertial subrange is ~~proportional to~~ dependent on wavenumber κ , (Panofsky and Dutton, 1984; Stull, 1988), as:

$$S(\kappa) \propto \kappa^{-5/3} \qquad (2.1.36)$$

Assuming Taylor's hypothesis that natural frequency and wavenumber can be related by $\kappa = 2\pi n/\overline{U}$ then $S(n)$ is proportional to $n^{-5/3}$. Power spectra are often presented in log-log form with power spectral density multiplied by n so that the inertial subrange slope is -2/3.

To enable comparisons between power spectra from differing canopy types or flow regimes, the power and frequency axes are frequently normalised and plotted as dimensionless quantities. The power spectral densities, $S(n)$, are divided by the series variance and the frequency axis is scaled either by a combination of wind speed and canopy parameters (i.e. $n(h - d)/\overline{U}$, where d is the zero plane displacement) or by a time scale (i.e. $n.T_{Ui}$, where T_{Ui} is an Eularian time scale from section 2.1.8).

Where the power spectrum of a series gives the fractional variance contribution of each frequency, a co-spectrum between two time series gives the fractional contribution to covariance of each frequency component. Again consider two discrete time series g_k and h_k with Fourier transforms $G(n)$ and $H(n)$, where $G(n)$ and $H(n)$ can be represented in real and imaginary parts (i.e. $G(n) = G_r(n) + iG_i(n)$). The spectral intensity between g_k and h_k is, from equation 2.1.33:

$$G(n).H^*(n) = G_r(n)H_r(n) + iG_r(n)H_i(n) - iG_i(n)H_r(n) - i^2G_i(n)H_i(n) \qquad (2.1.37)$$
$$G(n).H^*(n) = C_{gh}(n) - iQ_{gh}(n)$$

where $C_{gh}(n)$ is the co-spectrum or cross spectrum and $Q_{gh}(n)$ is the quadrature spectrum:

$$C_{gh}(n) = G_r(n)H_r(n) + G_i(n)H_i(n)$$
$$Q_{gh}(n) = G_i(n)H_r(n) - G_r(n)H_i(n) \qquad (2.1.38)$$

where the sum over all frequency components of $C_{gh}(n)$ is the covariance of the original series:

$$\sum_n C_{gh}(n) = \overline{(g'_k.h'_k)} \qquad (2.1.39)$$

As with power spectra, co-spectra are often presented in the form $nC(n)$ versus n. Co-spectra are also often normalised with $nC(n)$ being divided by the covariance between the series and n normalised as for power spectra. Co-spectra are plotted either in log-log form or in linear-log form when both positive and negative covariances are represented at different frequencies. Similarity arguments can be applied to co-spectral response in the inertial subrange (Wyngaard and Cote, 1972). For co-spectra between u and w and between w and potential temperature, θ in the surface layer:

$$C_{uw}(n) \propto \kappa^{-7/3} \quad \text{and} \quad C_{w\theta}(n) \propto \kappa^{-7/3} \qquad (2.1.40)$$

Thus for plots of $nC(n)$ against n the inertial subrange slope is -4/3. These relationships have been observed experimentally for co-spectra of uw and $w\theta$, (Kaimal *et al.* ,1972; Wyngaard and Cote, 1972) and also for other scalars such as CO_2 and H_2O, (Anderson *et al.*, 1986).

2.2 EDDY COVARIANCE THEORY

2.2.1 Introduction

The concept of 'eddies' is helpful in visualising turbulent transport in the atmosphere. The conceptual eddy is a rotating fluid parcel which has a time scale over which its fluid elements are coherent and a corresponding length scale or wavelength. From the continuity equation, equation 1.2.10, the mean vertical flux of dry air is zero. However the fluctuating vertical component w' is a 'carrier' for other quantities which are also fluctuating. These entities could for example be u, temperature, CO_2 or H_2O. For any vertical transport to take place, these entities must also be fluctuating and the degree and sign of the correlation of their fluctuations with w fluctuations determines the magnitude and direction of the flux. As we have seen in section 1.2.2 the vertical flux of a scalar quantity with density in air ρ_c, at a point in a flow above an extensive homogeneous surface in quasi-stationary conditions, is given by $\langle \overline{w'\rho_c'} \rangle$. In practice, the spatial averaging in this expression is assumed to come from the spatial sampling of the instrumentations and the time average is taken over 30 minutes. For fluxes of momentum, $\langle \overline{u'w'} \rangle$ and sensible heat, $\langle \overline{w'T'} \rangle$, the calculation of this eddy flux is relatively simple; however, for mass scalar quantities such as CO_2 and H_2O the situation is not so straightforward.

2.2.2 Eddy Covariance Measurement of Mass Scalars

The following analysis was originally described by Webb, Pearman and Leuning (1980) (hereafter referred to as WPL), and is applicable to the measurement of any mass scalar gas.

Changes of sensible and latent heat in a sampling volume cause changes in the scalars' density or concentration in that volume, thus, observed fluctuations of the scalar concentration need to be corrected.

Following WPL, we let E be the vertical flux of water vapour; F_c be the vertical flux of a scalar gas C; ρ be the total density of air; ρ_a be the density of dry air; ρ_v be the density of water vapour in the air; ρ_c be the density of C. The total density of the air is:

$$\rho = \rho_a + \rho_v + \rho_c \qquad (2.2.1)$$

But as the relative density of C in the air is much smaller than that of dry air and water vapour, we can assume:

$$\rho \cong \rho_a + \rho_v \qquad (2.2.2)$$

The ambient atmospheric pressure p is assumed to be constant with height over the measurement range, so we will consider actual, rather than potential, temperatures. The partial pressures of the constituents are given as:

$$p_a = \frac{\Re \rho_a T}{m_a}, \quad p_v = \frac{\Re \rho_v T}{m_v}, \quad p_c = \frac{\Re \rho_c T}{m_c} \tag{2.2.3}$$

Where m_a, m_v and m_c are the molecular masses of the constituents, $\Re$ is the universal gas constant and T is the absolute temperature. By Dalton's law of partial pressures, again assuming that $\rho_c << \rho_a + \rho_v$ we get:

$$\frac{\rho_a}{m_a} + \frac{\rho_v}{m_v} = \frac{p}{\Re T} \tag{2.2.4}$$

Now by expanding $T^{-1} = (\overline{T} + T')^{-1}$ in powers of $T'/\overline{T}$ we can obtain expressions for the *l.h.s.* of equation 2.2.4, for its mean, $\frac{\overline{\rho}_a}{m_a} + \frac{\overline{\rho}_v}{m_v}$, and for the departure from its mean, $\frac{\rho'_a}{m_a} + \frac{\rho'_v}{m_v}$. Thus, we can obtain an expression for ρ'_a, after neglecting higher order terms of $T'/\overline{T}$, which can be multiplied by w' and averaged to give:

$$\overline{w'\rho'_a} = -\mu \overline{w'\rho'_v} - \frac{\overline{\rho}_a}{\overline{T}}(1 + \mu\sigma)\overline{w'T'} \tag{2.2.5}$$

Where $\mu = m_a/m_v$ and $\sigma = \overline{\rho}_v/\overline{\rho}_a$. From the principle of conservation of mass we have the restraint that the mean vertical flow of dry air is zero:

$$\overline{w\rho_a} = 0 \tag{2.2.6}$$

Which can be written as $\overline{w}\,\overline{\rho}_a + \overline{w'\rho'_a} = 0$ and thus:

$$\overline{w} = -\frac{\overline{w'\rho'_a}}{\overline{\rho}_a} \tag{2.2.7}$$

So combining equations 2.2.5 and 2.2.7 we get:

$$\overline{w} = \frac{\mu}{\overline{\rho}_a}\overline{w'\rho'_v} + \frac{(1 + \mu\sigma)}{\overline{T}}\overline{w'T'} \tag{2.2.8}$$

Now the flux of the scalar C is given by:

$$F_c = \overline{w\rho_c} = \overline{w'\rho'_c} + \overline{w}\,\overline{\rho}_c \tag{2.2.9}$$

Generally, the second term of equation 2.2.9 $\overline{w}\,\overline{\rho}_c$, is zero as $\overline{w}$ is assumed to equal zero but we can see from equation 2.2.8 that the presence of sensible and latent heat fluxes can result in a non-zero value of $\overline{w}$. Thus, where fluctuations of density of c C

and of water vapour are measured, the true fluxes F_c and E are obtained by substituting equation 2.2.8 into equation 2.2.9:

$$F_c = \overline{w'\rho'_c} + \mu\left(\frac{\bar{\rho}_c}{\bar{\rho}_a}\right)\overline{w'\rho'_v} + (1+\mu\sigma)\left(\frac{\bar{\rho}_c}{\bar{T}}\right)\overline{w'T'} \qquad (2.2.10)$$

$$E = (1+\mu\sigma)\left\{\overline{w'\rho'_v} + \left(\frac{\bar{\rho}_v}{\bar{T}}\right)\overline{w'T'}\right\} \qquad (2.2.11)$$

These equations are made up of terms which are all directly measurable.

An experiment carried out by Leuning *et al.* (1982) measured an apparent CO_2 flux above an arid vegetation-free surface where there would be an expected zero CO_2 flux. After correction with the above equations the CO_2 flux was indeed shown to be negligible from the surface.

Further development of these equations for infra-red gas analysers (IRGAs) with open and closed optical paths and with a cross-sensitivity between CO_2 and water vapour responses is given in section 3.2.4, and also in Leuning and Moncrieff (1990) and Leuning and King (1992).

2.3 TRANSFER FUNCTION CORRECTIONS

2.3.1 Introduction

No instrument has a perfect response to the quantity that it is designed to measure. The loss of measured signal of an instrument, in the context of measurements of the atmosphere, is often dependent on frequency response of a system falling short of the frequency of change of the measured quantity. Other losses may arise from our methods of digitising and processing the data, these losses are also dependent on frequency, i.e. sampling frequency and time constants of filters. If we are able to obtain, either theoretically or by experiment, the dependence of the signal losses on frequency, then we can reconstruct the signal by comparing these frequency relationships, or transfer functions, with the spectrum of the signal.

While making eddy covariance measurements of scalar gas constituents which have a low density in air, it is particularly important to quantify errors arising from our methodology and instrumentation. The ability of the transfer functions to correct the CO_2 fluxes is demonstrated in section 6.3.2.

The approach here follows that of Moore (1986), where theoretically derived transfer functions are applied to our system. A more comprehensive review of these frequency response corrections for an eddy covariance system can be found in Moore (1986).

If we consider a vertical eddy flux F_c of a quantity which has a specific density ρ_c, then from Moore (1986) the correction of the flux ΔF_c is:

$$\frac{\Delta F_c}{F_c} = 1 - \frac{\int_0^\infty T_{w\rho_c}(n) C_{w\rho_c}(n) \mathrm{d}n}{\int_0^\infty C_{w\rho_c}(n) \mathrm{d}n} \qquad (2.3.1)$$

Where $T_{w\rho_c}(n)$ is the convolution of all transfer functions applicable to the measurement and $C_{w\rho_c}(n)$ is a typical co-spectrum for the flux F_c. The total transfer function $T_{w\rho_c}(n)$ is made up of many individual functions which will be discussed in detail below in sections 2.3.2 to 2.3.9, with typical examples. Included, are the transfer functions for: electronic low-pass filters, digital recursive filters, instrument dynamic frequency response, mismatching of the frequency responses of eddy covariance instruments, averaging losses over the open path IRGA sampling volume, averaging losses over the sonic anemometer transducer paths, losses due to the separation of correlated sensors, frequency attenuation in closed path IRGA sampling

tubes. Examples of typical total transfer functions, $T_{w\rho_c}(n)$, for the different instrumental arrays used in the field experiments are given in section 2.3.10.

The choice of co-spectral response functions $C_{w\rho_c}(n)$ is discussed and examples of frequently used models are given in section 2.3.11.

2.3.2 Electronic Low Pass Filters

To remove the effects of aliasing in the time series all instrument voltage signals were low-pass filtered with a fifth order Butterworth electronic filter, (Appendix A.1). Our data was sampled at a rate of 18.2 Hz, and thus had a Nyquist critical frequency of ~ 9 Hz. The 3dB cut-off frequency, where the filter gain falls from unity to $1/\sqrt{2}$, was 7.4 Hz and the gain function was found experimentally to be well represented by (Appendix A1):

$$T_B(n) = \left[1 + \left(\frac{n}{7.4}\right)^{12}\right]^{-\frac{1}{2}} \qquad (2.3.2)$$

This gain function is specific to the electronic filters used in our experimental work. $T_B(n)$ is plotted against a typical range of natural frequencies, n, in Figure 2.3.1.

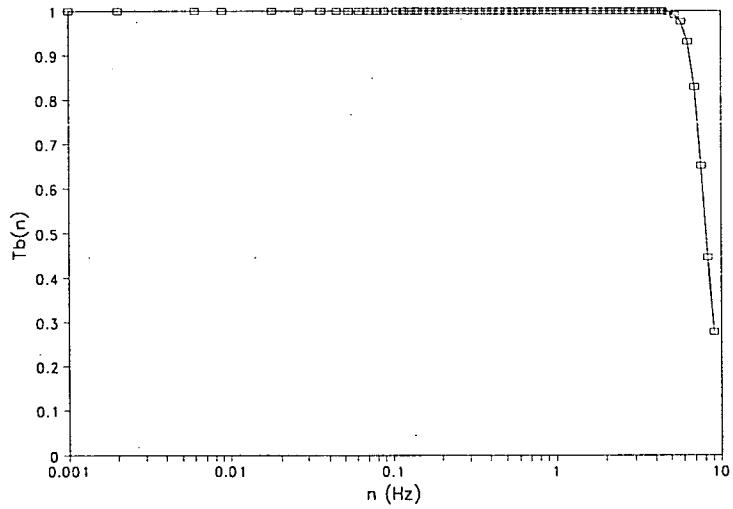

Fig. 2.3.1. 5 pole Butterworth electronic low-pass filter transfer function $T_B(n)$ from equation 2.3.2.

2.3.3 Digital Recursive Filter

To remove any unwanted sensor drift or trends present in sampling periods it is necessary to employ a software filter when calculating velocity or scalar

fluctuations, (Lloyd *et al.*, 1984; Shuttleworth, 1988). The use of an arithmetic mean removal filter is extremely expensive in computer processing time and consequently a 'running mean' or digital recursive filter is the preferred method. However, in removing these low frequency trends a certain amount of true flux signal is also removed.

The algorithms are based on analogue high pass electronic filters, (Dyer *et al.*, 1967). The real time running mean is computed as:

$$\bar{c}_i = \eta \bar{c}_{i-1} + (1-\eta)c_i \qquad (2.3.3)$$

Where $\bar{c}_i$ and $\bar{c}_{i-1}$ are the new and the previous running mean values, c_i is the current instantaneous value. The constant η is given by:

$$\eta = e^{-\Delta t/\Gamma} \qquad (2.3.4)$$

Where Γ is the time constant of the filter and Δt is the time interval between samples. The digital filter has a response function, $H_d(n)$ given by, (Moore, 1986):

$$H_d = \frac{\eta\left(1-e^{-2\pi jn/n_s}\right)}{\left(1-\eta e^{-2\pi jn/n_s}\right)} \qquad (2.3.5)$$

Where n_s is the sample frequency. However, for frequencies smaller than the Nyquist critical frequency, the gain function is given to a very good approximation by, (Moore, 1986):

$$T_r(n) = \frac{2\pi n\tau_r}{\sqrt{1+(2\pi n\tau_r)^2/\eta}} \qquad (2.3.6)$$

Where the effective time constant is given by $\tau_r = \eta\left(n_s(1-\eta)\right)^{-1}$. If the time constant is large compared to the sampling period then $\eta \rightarrow 1$ and equation 2.3.6 represents the gain of a first order high-pass filter. In our case, a value of $\Gamma = 200$ s was used, giving $\eta = 0.99973$, $\tau_r = 199.97$ where the sample period was 0.05 s. The function $T_r(n)$ is shown for these values in Figure 2.3.2.

2.3.4 Dynamic Frequency Response

The Dynamic frequency response of a sensor can be adequately described by a first order gain function of the form, (Moore, 1986):

$$T_d(n) = \frac{1}{\sqrt{1+(2\pi nt_r)^2}} \qquad (2.3.7)$$

Where t_r is the response time of the instrument.

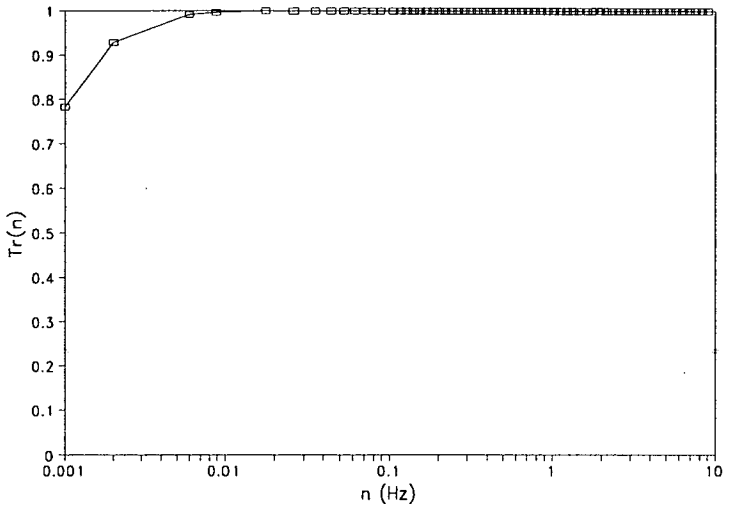

Fig. 2.3.2. Transfer function for digital recursive filter as given by equation 2.3.6, where Γ = 200 s and the sample rate is 18.2 Hz.

The function is plotted in Figure 2.3.3 for two time responses typical of instruments used here.

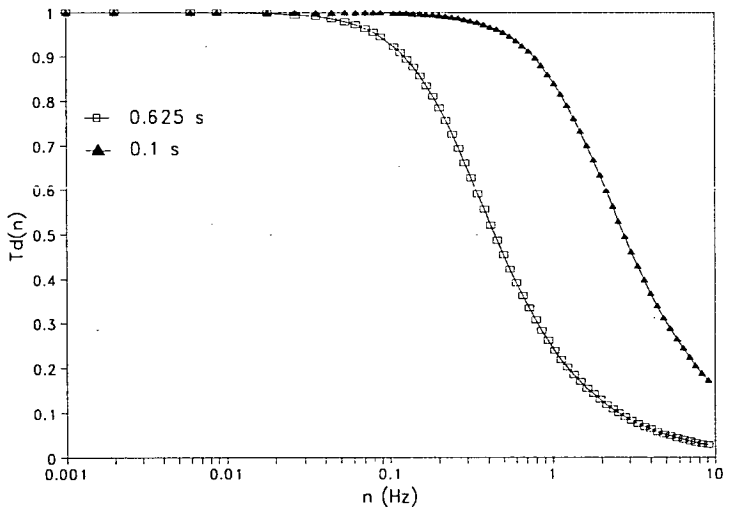

Fig 2.3.3. Transfer function for dynamic frequency response of sensors with response times, t_r of 0.625s and 0.1 s.

2.3.5 Sensor Mismatching

If the signals from two instruments with very different response characteristics are to be correlated, as in the eddy covariance method, then there will be a flux loss due to the frequency response mismatching. A phase shift is introduced between the

time series sampled from the two sensors which is larger with larger frequency mismatching. The transfer function for mismatching can be expressed as, (Zeller *et al.*, 1989):

$$T_m(n) = \cos(\varphi_1 - \varphi_2) \tag{2.3.8}$$

Where φ_1 and φ_2 are the phase shifts for sensors 1 and 2. For our sensors we can express the phase shifts as:

$$\begin{aligned} \varphi_1 &= \tan^{-1}(2\pi n t_{r_1}) \\ \varphi_2 &= \tan^{-1}(2\pi n t_{r_2}) \end{aligned} \tag{2.3.9}$$

Where t_{r_1} and t_{r_2} are the response times of the sensors. Thus, by means of the trigonometric identity for $\cos(\varphi_1 - \varphi_2)$ we obtain the transfer function, (Zeller *et al.*, 1989):

$$T_m(n) = \frac{1 + (2\pi n)^2 t_{r_1} t_{r_2}}{\sqrt{\left(1 + (2\pi n t_{r_1})^2\right)\left(1 + (2\pi n t_{r_2})^2\right)}} \tag{2.3.10}$$

The function $T_m(n)$ is plotted in Figure 2.3.4 for typical values of t_{r_1} and t_{r_2}.

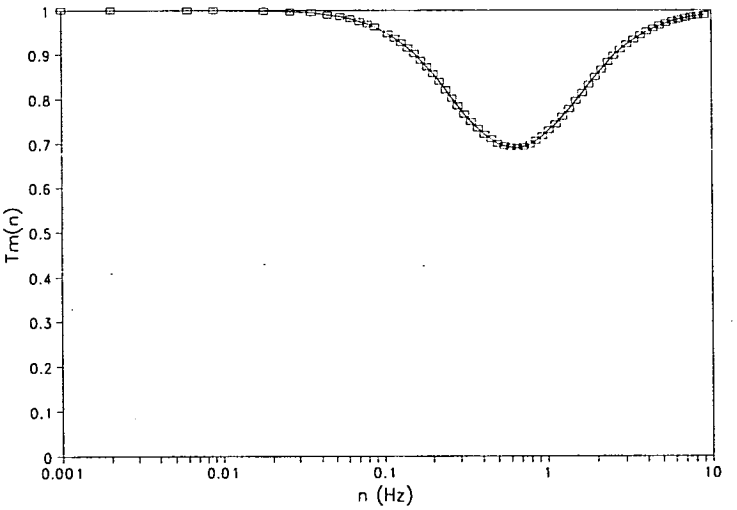

Fig. 2.3.4. Transfer function for the frequency response mismatching of two sensors with time responses, t_{r_1} and t_{r_2} equal to 0.1 and 0.625 s.

2.3.6 Scalar Path Averaging

IRGAs measuring CO_2, H_2O or any other atmospheric scalar gas which have their optical path open to the atmosphere are averaging the gas concentration over the

volume of the optical path. This is termed sensor 'path' or 'line'-averaging. The transfer function derived by Silverman (1968) for spatial averaging of turbulent fluctuations of normalised frequency f_p, ($f_p = np_l/\overline{U}$), for an instrument with an open path length p_l, where the path is at an angle θ to the wind vector is:

$$T_p(f_p,\theta) = \frac{0.142}{f_p \sin\theta} \int_{-\infty}^{\infty} \left[1 + \left(\frac{x/\pi f_p - \cos\theta}{\sin\theta} \right)^2 \right]^{-4/3} \frac{\sin^2 x}{x^2} dx \qquad (2.3.11)$$

If we assume that the averaging path is always perpendicular to the wind direction then θ = π/2 and equation 2.3.11 takes the form given by Gurvich (1962). A simplified form of this equation which has an accuracy of better than 5% for values of f_p up to about 10 is given by Moore (1986):

$$T_p(f_p,\pi/2) = \frac{1}{2\pi f_p} \left(3 + e^{-2\pi f_p} - \frac{4\left(1 - e^{-2\pi f_p}\right)}{2\pi f_p} \right) \qquad (2.3.12)$$

This equation applies to cases where $\theta < 30^o$ and for averaging volumes which, when considered as a cylinder, have a diameter less than about $0.2p_l$, (Moore, 1986).

The sensor path averaging transfer function is plotted in Figure 2.3.5 for sensors used in this work, against n with a value having been assumed for the mean wind speed, $\overline{U}$.

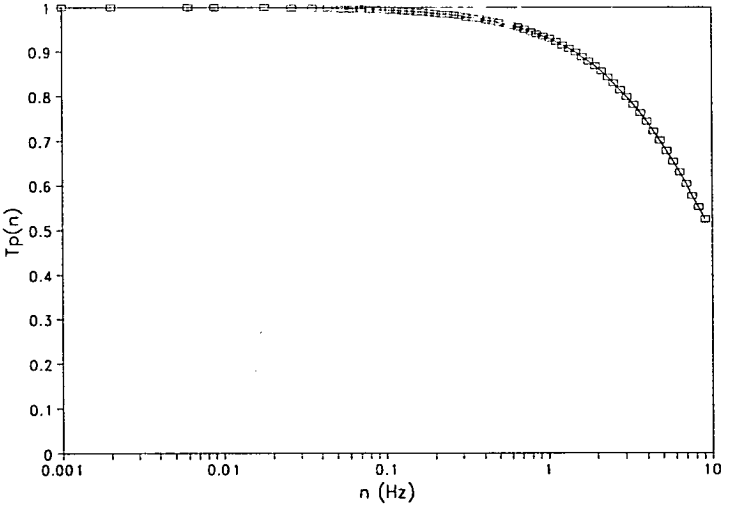

Fig. 2.3.5. Transfer function $T_p(n)$ from equation 2.3.12 for a sensor with path length p_l of 0.2m and a mean wind speed $\overline{U}$ of 3 m s^{-1}.

2.3.7 Sonic Anemometer Path Averaging

The measurement of velocity from a sonic anemometer also suffers from path averaging. Kaimal *et al.* (1968) and Horst (1973) derived a spectral transfer function for a wind component from a sonic anemometer, U_i as:

$$T_i(k_1, p) = \frac{\int_{-\infty}^{\infty}\int \frac{\sin^2(\mathbf{k}.\mathbf{p}/2)}{(\mathbf{k}.\mathbf{p}/2)^2}\Phi_{ii}(\mathbf{k})\,dk_2\,dk_3}{\int_{-\infty}^{\infty}\int \Phi_{ii}(\mathbf{k})\,dk_2\,dk_3} \qquad (2.3.13)$$

Where $\mathbf{k}$ is the wavenumber vector with components k_1, k_2 and k_3, $\mathbf{p}$ is the path vector, p_l is the path length and Φ_{ii} is the spectral density tensor. As our flux calculations involve only w, we can reduce this transfer function to its vertical component T_3 or T_w and take this as the relevant function for our sonic anemometer. An approximation to T_w is given by Moore (1986) which is accurate to ~ 2%:

$$T_w(f_p) = \frac{2}{\pi f_p}\left(1 + \frac{e^{-2\pi f_p}}{2} - \frac{3\left(1 - e^{-2\pi f_p}\right)}{4\pi f_p}\right) \qquad (2.3.14)$$

where $f_p = np_l/\overline{U} = k_l p_l/2$.

The transfer function in equation 2.3.14 is shown in Figure 2.3.6 for instruments used by us, against n with a typical value of mean wind speed, $\overline{U}$.

The applicability of this function depends on the sonic anemometer head

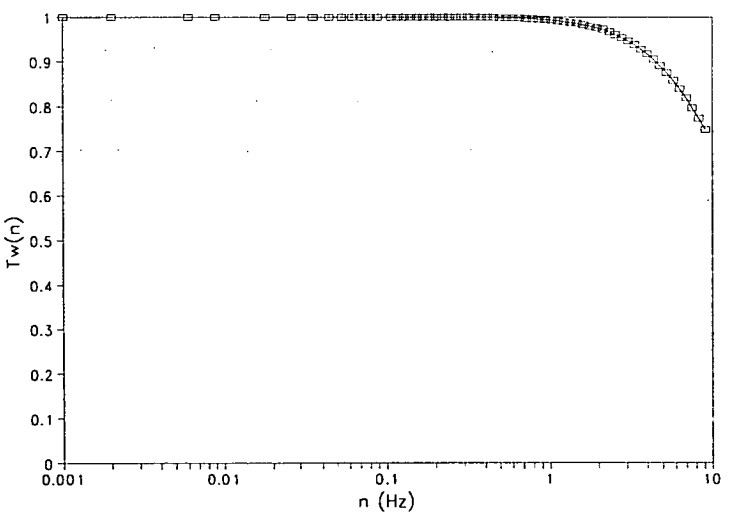

Fig. 2.3.6. Transfer function for vertical velocity path averaging for a sonic anemometer with a path length, p_l, of 0.15 m and an assumed mean wind speed, $\overline{U}$ of 3 m s^{-1}.

configuration. All of the sonic anemometers used in the work presented in this thesis have pyramidal head configurations, such that the response of all three pairs of sonic transducers contribute to the calculated vertical velocity. The vertical velocity signal is made up of three separate measurements over three path lengths p_l. In the absence of a more appropriate transfer function for our sonic head configuration, the above function is the best approximation. Horst (1973) and Zeller *et al.* (1989) found that the effect of path separation in the vertical direction was negligible, with Zeller *et al.* (1989) concluding the same for horizontal velocity measurements.

2.3.8 Sensor Separation Losses

As turbulent eddies are of a finite size we must consider the underestimation of flux due to lateral sensor separation. We will consider two instruments separated by a distance s, where the line between them is perpendicular to the wind flow, and s is small (i.e. ~ 10% of (z - d)). This is representative of the deployment of our instruments in the field. If we assume that the small separation only effects measured turbulent fluctuations in the co-spectral inertial subrange, then we can employ the co-spectral transfer function of Irwin (1979):

$$T_s(f_s) = \frac{2^{1/6}}{\Gamma(5/6)}(2\pi f_s)^{5/6} K_{5/6}(2\pi f_s) \qquad (2.3.15)$$

Where $f_s = ns/\overline{U}$ and $K_{5/6}$ is a modified Bessel function of the second kind. This function has been approximated by Moore (1986), to a good approximation as:

$$T_s(f_s) = \exp\left(-9.9 f_s^{1.5}\right) \qquad (2.3.16)$$

This function is shown in Figure 2.3.7 for instruments used by us, plotted against n with a typical value of mean wind speed, $\overline{U}$.

It is apparent that only normalised frequencies $f_s > 0.01$ are attenuated by this function. (In terms of natural frequencies, only frequencies $n > 0.01\overline{U}/s$ are attenuated). For the above model of sensor separation loss to be valid, these frequencies must lie in the inertial subrange of the measured co-spectra.

2.3.9 Frequency Attenuation in Sample Tubes

When air is transported to a closed optical path IRGA by means of a tube and a pump, high frequency fluctuations in the sampled air are attenuated. The damping of the fluctuations occurs as a result of differences in streamwise velocities across the cross section of the tube due to the resistance to motion of the tube walls and of radial

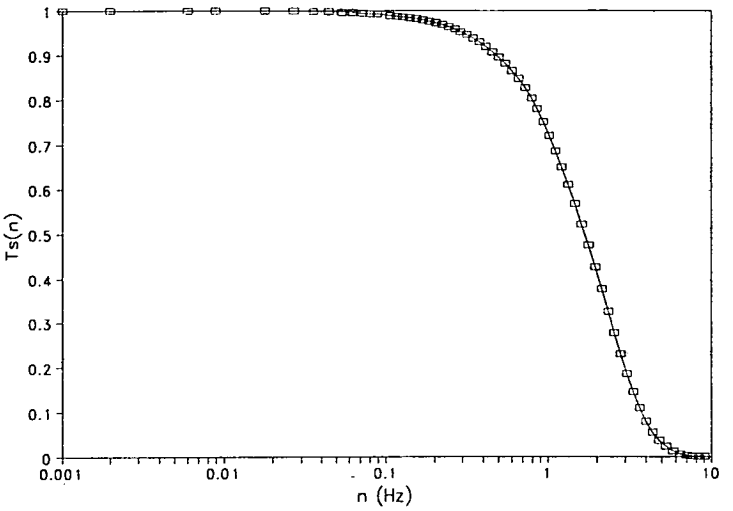

Fig. 2.3.7. Transfer function for sensor separation where the separation, s is taken as 0.3 m and an assumed mean wind speed, $\overline{U}$ of 3 m s^{-1}.

diffusion. Much work over the years has gone into calculating the flux loss from such an experimental arrangement: initially, for laminar flow in the tube (Taylor, 1953, 1954; Philip, 1963a, 1963b, 1963c; Leuning and Moncrieff, 1990); and considering both laminar and turbulent flow (Lenschow and Raupach, 1991; Massman, 1991; Leuning and King, 1992; Suyker and Verma, 1993).

Taylor (1953) postulated that for laminar flow, the one dimensional diffusion equation to describe the change in mean concentration, $\bar{C}$, was:

$$\frac{\partial C}{\partial t} = D_V \frac{\partial^2 C}{\partial x^2}, \qquad (2.3.17)$$

where x is distance along the tube relative to a co-ordinate system moving in the direction of the discharge velocity U, and D_V is a virtual diffusion coefficient incorporating differential advection and cross-stream diffusion effects. A solution for this equation in terms of wavenumber κ, assuming a periodic solution for C in the tube is (Lenschow and Raupach, 1991):

$$C(x,t) = C_0 \exp(i\kappa x - \alpha_1 T), \qquad (2.3.18)$$

where $k = \frac{2\pi n}{U}$, α_1 is an attenuation coefficient and C_0 is the amplitude of the harmonically varying concentration at the tube entrance. Applying equation 2.3.17 for the partial derivative of C, to equation 2.3.18 then $\alpha_1 = D_V k^2$.

Thus, we can define the transfer function describing variance changes in the concentration between the tube inlet and outlet as (Lenschow and Raupach, 1991):

$$T_t = \left(\frac{C_{out}}{C_{in}}\right)^2, \tag{2.3.19}$$

where C_{in} and C_{out} are the concentrations at the inlet and outlet respectively and can be identified as, (Lenschow and Raupach, 1991):

$$\begin{aligned} C_{in} &\equiv C(x,0) = C_0 \exp(i\kappa x), \\ C_{out} &\equiv C(x,t_t) = C_0 \exp\left(i\kappa x - D_v \kappa^2 X/U\right), \end{aligned} \tag{2.3.20}$$

where the time taken for a fluid parcel to travel through the tube is $t_t = X/U$, and X is the tube length.

Taylor (1953) showed that for laminar flow:

$$D_v \cong \frac{r^2 U^2}{48 D_c}, \tag{2.3.21}$$

where r is the tube radius and D_c is the molecular diffusion coefficient for CO_2 in air. Thus, the transfer function applicable to correct concentration attenuation of CO_2 in a sample tube with laminar flow is:

$$T_t(n) = \exp\left(-\pi^2 r^2 n^2 X/6 D_c U\right). \tag{2.3.22}$$

In practice, the time for the sample to travel down the tube, t_t, is a more useful parameter than X, as it can be calculated from correlations between scalars sampled down the tube and those sampled *in situ,* i.e. temperature. Thus, equation 2.3.22 can be expressed:

$$T_t(n) = \exp\left(-\pi^2 r^2 n^2 t_t/6 D_c\right). \tag{2.3.23}$$

A similar expression for this transfer coefficient was obtained by Philip (1963c) by a more detailed analysis. A factor of two which is missing in the exponent of equation 4.2 of Philip (1963c), accounts for the slight difference to the expression presented here, (Lenschow and Raupach, 1991; Leuning and King, 1992).

Whenever the air was sampled via a tube during our experiments, the sampling flows were always laminar, with $Re \cong 1190$ and, thus, the appropriate transfer function used in this thesis is given by equation 2.3.23. This transfer function is shown in Figure 2.3.8 for a typical sampling tube as used in the field experiments.

The flow in the tube is said to be turbulent when the Reynolds number, Re is $\geq$ 2300, where:

$$Re = \frac{2rU}{\nu}, \tag{2.3.24}$$

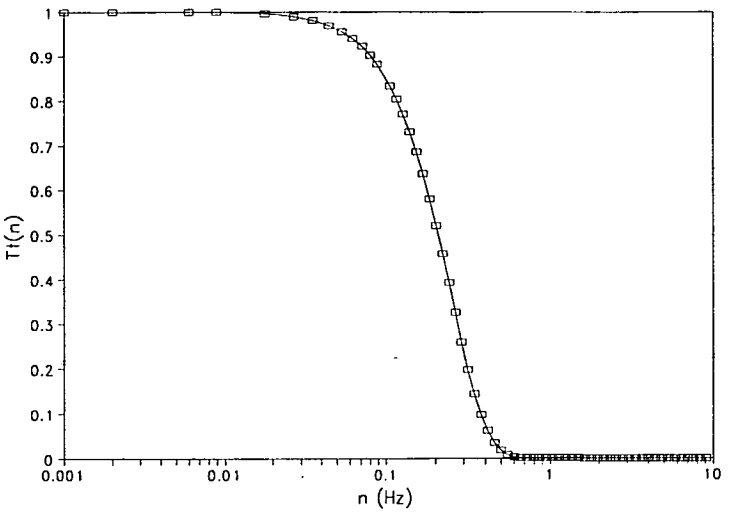

Fig. 2.3.8. Transfer function for tube attenuation for laminar flow. t_t is 18 s, the r is 2.75 mm and D_c is taken as 14×10^{-6} m^2 s^{-1}.

where ν is the kinematic viscosity of the sampled fluid. For turbulent flows in the range $Re_c < Re < 10^5$, where $Re_c \cong 2300$, Taylor (1954) obtained an expression for D as:

$$D = 10.1 r u_t^*, \tag{2.3.25}$$

where u_t^* is the friction velocity at the tube wall. Lenschow and Raupach (1991) used equation 2.3.25 and the empirical Blasius resistance formula, (Eckert and Drake, 1959) such that:

$$\frac{u_t^*}{U} = 0.2 Re^{-1/8}, \tag{2.3.26}$$

to obtain the transfer function for the attenuation of a turbulent sample tube flow as:

$$T_t(n) = \exp\left(-160(Re) r n^2 X / U^2\right). \tag{2.3.27}$$

Comparisons of the signal losses in systems when they have turbulent or laminar flows indicate that under certain circumstances the losses are significantly reduced in the turbulent flow system, (Lenschow and Raupach, 1991; Suyker and Verma, 1993). Situations where tube lengths are relatively long are not improved as markedly as short tube lengths (i.e. ~ 3 m). The extremely high flow rates required for turbulent flow to occur in even relatively small bore tubing is a practical difficulty, especially with very long tubes such as those employed at our site. The transfer functions given here, for both laminar and turbulent flow, would appear to accurately reconstruct scalar fluxes in most conditions and only in very extreme cases would it seem to be essential to ensure turbulent flow in sample tubes.

2.3.10 Total Transfer Functions

The total transfer function for a particular flux measurement, say flux F of a quantity with specific density ρ, as in section 2.3.1, is $T_{w\rho_c}(n)$. This function is a convolution of all the applicable transfer functions associated with the measurement of vertical velocity w and the scalar density ρ. As the flux of the scalar is a covariance between w and ρ, then transfer functions applying to measurement of just one of these quantities appears in the total transfer function to the power of 1/2. As an example of typical total transfer functions used in the analysis of data presented in this thesis, we will consider the measurement of CO_2 flux with two different experimental arrangements:

(*i*) An open optical path IRGA with $p_l = 0.2$ m, with a response time to change in CO_2 concentration of 0.1 s, and a three component sonic anemometer with $p_l = 0.15$ m and a response time to wind speed changes of 0.02 s.

(*ii*) A closed optical path IRGA, with a response time of 0.625 s, sampled down a tube with radius 2.75 mm, with a travel time $t_t = 18$ s and a Reynolds number of 1190, and the same anemometer as in (*i*).

For situation (i) The total transfer function for the measurement of CO_2 is:

$$T_{w\rho}(n) = T_B(n)T_r(n)T_{d(IRGA)}^{1/2}(n)T_{d(sonic)}^{1/2}(n)T_m(n)T_p^{1/2}(n)T_w^{1/2}(n)T_s(n) \qquad (2.3.28)$$

and for situation (ii):

$$T_{w\rho}(n) = T_B(n)T_r(n)T_{d(IRGA)}^{1/2}(n)T_{d(sonic)}^{1/2}(n)T_m(n)T_w^{1/2}(n)T_s(n)T_t^{1/2}(n) \qquad (2.3.29)$$

These functions are shown graphically in Figure 2.3.9.

2.3.11 Co-spectral models

The most widely used co-spectral models are those from Kaimal *et al.* (1972). These models are empirical functions derived from spectral data gathered over wheat stubble in the Kansas boundary layer experiment. Moore (1986) normalised these models so that their numerical integrals equalled unity over an unspecified frequency range. These normalised models have been widely used in the literature for $C_{w\rho_c}(n)$ in equation (2.3.1), (Leuning and Moncrieff, 1990; Leuning and King, (1992); Suyker and Verma, 1993). There are occasions where these models are not appropriate for use in equation 2.3.1, section 4.2.1, and empirical functions must be derived for individual data sets in a way similar to that followed by Kaimal *et al.* (1972) in their original paper.

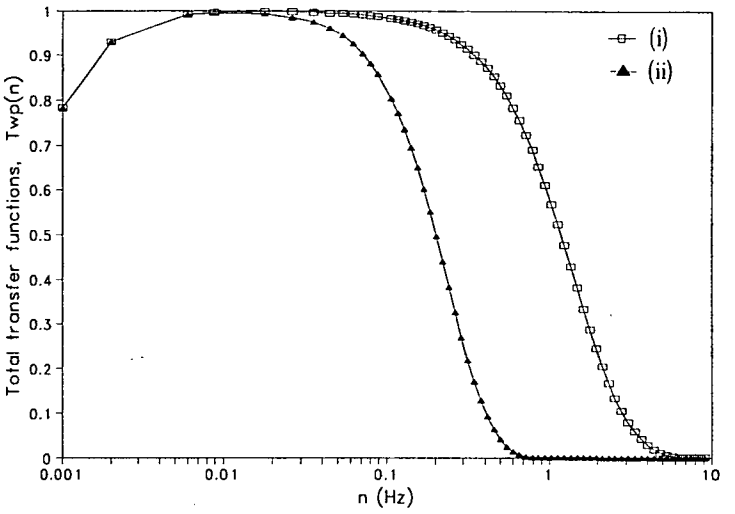

Fig. 2.3.9. Total transfer functions, $T_{w\rho_c}(n)$ for the two examples (*i*) and (*ii*).

The co-spectral model functions for stable conditions, (i.e. $(z-d)/L>0$ where L is the Monin-Obukhov length and (z - d) is the height above the zero plane), all take the form, (Moore, 1986):

$$nC_{w\alpha}(n)=\frac{f_k}{A_{w\alpha}+B_{w\alpha}f^{2.1}} \qquad (2.3.30)$$

Where f_k is the normalised frequency, $f_k=n(z-d)/\overline{U}$, α is a subscript denoting either $\overline{T}$ for temperature or u for streamwise velocity, thus, the equation applies to $C_{wT}(n)$ and $C_{uw}(n)$. The terms $A_{w\alpha}$ and $B_{w\alpha}$ are related to the peak co-spectral frequency. The terms for A_{wT}, A_{uw}, $B_{w\alpha}$, (where B_{wT} = B_{uw}), as given by Moore (1986) include a typographical error in the paper in the term for $B_{w\alpha}$, (C. J. Moore, personal communication). Returning to Kaimal *et al.* (1972), their equation (33) is:

$$\frac{nC_{wT}(n)}{\overline{w'T'}}=\frac{0.88(f_k/f_0)}{1+1.5(f_k/f_0)^{2.1}} \qquad (2.3.31)$$

Where $\overline{w'T'}$ is the covariance between vertical velocity and temperature in the measured band width, and f_0 is given by Kaimal *et al.* (1972), equation (35b) for sensible heat flux as:

$$(f_0)_{wT}=0.23\left[H\left((z-d)/L\right)\right]^{0.75} \qquad (2.3.32)$$

and from Kaimal *et al.* (1972), equation (14), in the range $0 \le (z\text{-}d)/L \le 2$, $H\left((z-d)/L\right)$ is:

$$H\left((z-d)/L\right)=1+6.4\left((z-d)/L\right) \qquad (2.3.33)$$

So rewriting equation (2.3.31) in the Moore (1986) form, i.e. equation (2.3.30), where we include a constant c_k representing the normalisation factor, we obtain:

$$nC_{wT}(n)=\frac{f_k}{\left(\frac{c_k}{0.88}\right)f_0+1.5\left(\frac{c_k}{0.88}\right)\left(\frac{f_0}{f_0^{2.1}}\right)f_k^{2.1}} \qquad (2.3.34)$$

Thus, we see that:

$$A_{wT}=\left(\frac{c_k}{0.88}\right)f_0 \quad \text{and} \quad B_{wT}=\left(\frac{1.5c_k}{0.88}\right)\frac{f_0}{f_0^{2.1}} \qquad (2.3.35)$$

By substitution of equations 2.3.32 and 2.3.33 into 2.3.35, we get an expression for A_{wT} as:

$$A_{wT}=0.261c_k\left[1+6.4\left((z-d)/L\right)\right]^{0.75} \qquad (2.3.36)$$

The equation for A_{wT} given by Moore (1986), equation (21b) is:

$$A_{wT}=0.284\left[1+6.4\left(\frac{z-d}{L}\right)\right]^{0.75} \qquad (2.3.37)$$

By inspection of equation (2.3.37) we deduce that the normalisation factor c_k is equal to 1.087. Thus, by manipulation of equations 2.3.35 and 2.3.36 we get an expression for B_{wT} as:

$$B_{wT}=2.34A_{wT}^{-1.1} \qquad (2.3.38)$$

As $B_{wT} = B_{uw}$, equation (2.3.38) replaces the expression for $B_{w\alpha}$ in equation (21*b*) of Moore (1986) which was in error with the exponent being -1.1 rather than +1.

Thus, the models for sensible heat flux for stable conditions can now be represented by equations 2.3.30, 2.3.37 and 2.3.38. The functions for sensible heat co-spectra are shown in Figure 2.3.10 for three stable values of $(z - d)/L$ with values of $(z - d) = 5.4$ m and $\overline{U} = 3$ m s^{-1}.

The co-spectral model functions for unstable conditions, (i.e. $(z-d)/L<0$), all take the form, (Moore, 1986):

$$nC_{w\alpha}(n)=\frac{a_{w\alpha}f_k}{\left[1+b_{w\alpha}f_k\right]^{c_{w\alpha}}} \qquad (2.3.39)$$

where again α denotes either a temperature or u co-spectra with w. The co-spectral functions are again normalised such that the numerical integral of the function is

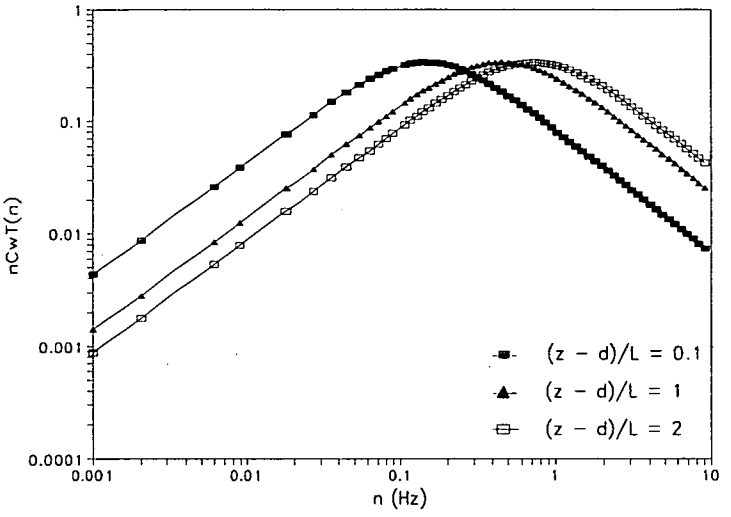

Fig. 2.3.10. Empirical functions for sensible heat co-spectra in stable conditions, from equations 2.3.30, 2.3.37 and (2.3.38) for $(z - d) = 5.4$ m and $\overline{U} = 3$ m s^{-1}.

unity. The functions for sensible heat and Reynolds stress co-spectra are, (Moore, 1986):

$$nC_{wT}(n) = \frac{12.92 f_k}{\left[1+26.7 f_k\right]^{1.375}} \qquad f_k < 0.54$$
$$nC_{wT}(n) = \frac{4.378 f_k}{\left[1+3.8 f_k\right]^{2.4}} \qquad f_k \geq 0.54 \qquad (2.3.40)$$

$$nC_{uw}(n) = \frac{20.78 f_k}{\left[1+31 f_k\right]^{1.575}} \qquad f_k < 0.24$$
$$nC_{uw}(n) = \frac{12.66 f_k}{\left[1+9.6 f_k\right]^{2.4}} \qquad f_k \geq 0.24 \qquad (2.3.41)$$

The model function for sensible heat co-spectra in unstable conditions from equation (2.3.40) is shown in Figure 2.3.11 for the same wind speed and measurement height as for the stable co-spectra.

If we wish to apply the transfer function corrections to a scalar other than sensible heat, then we must assume that the sensible heat co-spectral function approximates the scalar co-spectral response. This has been a common approach in the literature (Moore, 1986; Zeller *et al.*, 1989; Leuning and Moncrieff, 1990; Leuning and King, 1992; Suyker and Verma, 1993), and would seem to be not

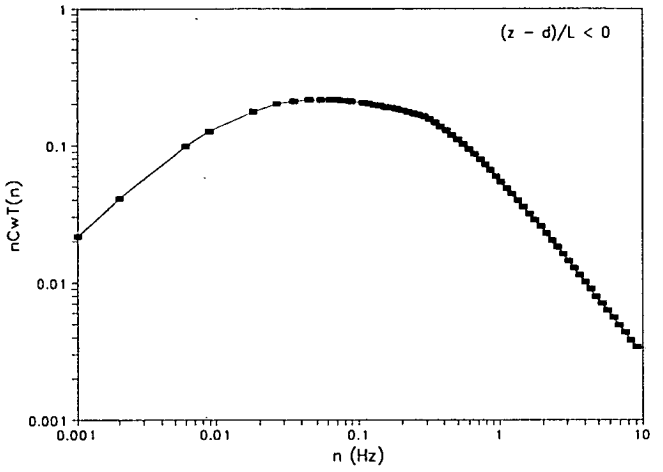

Fig. 2.3.11. Empirical functions for sensible heat co-spectra in unstable conditions, from equations 2.3.40 for $(z - d)$ = 5.4 m and $\overline{U}$ = 3 m s^{-1}.

unreasonable in most cases, as the co-spectra of sensible heat, latent heat and CO_2 flux are similar, (Ohtaki, 1985; Anderson *et al.*, 1986). However, it is good policy to compare the appropriate stability form of the above sensible heat models with the actual co-spectra of the quantity under consideration. The empirical functions derived by Kaimal *et al.* (1972) were obtained over a smooth surface (wheat stubble) and differences in power and co-spectral response may be evident over surfaces with substantively different roughness characteristics. If differences are apparent, then functions which can be numerically integrated, must be derived from the spectral data by curve fitting the appropriate stability form, (i.e. equations 2.3.30 and 2.3.39). This procedure has been carried out for our above canopy CO_2 data in section 4.2.1.

2.4 CONVENTIONS

2.4.1 Time Convention

All times throughout this thesis are British Summer Times (BST). To convert to Greenwich Mean Time one hour must be subtracted from BST values.

2.4.2 Flux Direction Convention

Throughout this thesis the common meteorological convention will be adopted regarding the signs of mass, energy and radiation fluxes as follows: mass and heat fluxes directed away from the earth's surface are positive; and radiation fluxes

EU BIBL. UNIV. EDINBURGH

directed towards the earth's surface are positive. This convention is summarised in Figure 2.4.1.

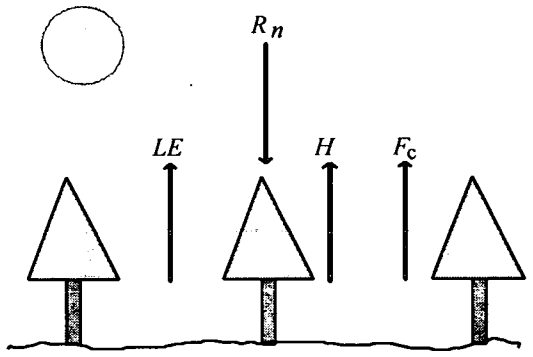

Fig. 2.4.1 Positive fluxes of mass (F_c), heat (LE and H) and radiation (R_n) are shown with arrows indicating their direction with respect to the earth's surface. (Where F_c is CO_2 flux).

CHAPTER 3.
MEASUREMENT AND ANALYSIS METHODS

3.1. INTRODUCTION

All the data analysed and presented in this thesis were collected in two field campaigns during two successive summers at the same site in South West Scotland. The methodologies employed both in the field experiments and in the data analysis are set out in the following sections. The software used for the data analysis is discussed generally, with references to Appendices.

3.2 FIELD MEASUREMENTS

3.2.1 Field Site

Measurements were made at Rivox forest, Dumfriesshire, SW Scotland, (55° 19.5' N, 3° 53' W). Measurements reported here were made in June to August of 1990 and 1991. The forest is a Sitka spruce plantation, planted at 3584 stems/ha in 1962 and, to date, unthinned. The median tree height was 15 ± 3 m and LAI was estimated at 10.2, (Milne and Browne, 1990; Gardiner, 1993). The zero plane displacement, d, was estimated as $0.84h$ which was the figure derived from 66 mean hourly wind speed profiles by Jarvis (1993) for a Sitka spruce plantation of similar planting density and tree height. Tree rows were separated by 2m and trees were planted 1.5m apart along the rows. Between the rows were drainage channels ~ 0.1 - 0.2 m deep. The tree canopy crowns were touching with complete closure. The live crown base was at ~ $0.6h$ with dead branch trunkspace extending to ~ $0.15h$ and a clear trunkspace with no understorey beneath.

The site has a gentle slope of ~ 6° running perpendicular to the prevailing wind direction with over 1 km of fetch in all directions. The most level approach is to the South West which is also the prevailing wind direction. Data from all other wind directions was rejected. Data was also rejected from periods with rain or 'wet' fog or mist.

Instruments were mounted on scaffolding booms at two heights, $1.2h$ and $0.7h$, on a 'walk-up' tower ('Hi-Way scaffolding', Martin-Thomas Ltd, Andover, UK), with the instruments being placed higher in 1991 to maintain the heights above the zero-plane. The instruments at $1.2h$ were placed ~ 2 m above the tower structure to reduce distortion effects (Dyer, 1981; Wyngaard, 1982; Dyer, 1982). Further instruments were placed ~ 3 m in the general upwind direction from the tower at an instrument mid-point height of $0.1h$ on a scaffolding pole sunk into the forest floor.

The instruments at $0.1h$ were so placed to minimise flow distortion effects from the tower and to site them away from areas disturbed by its erection.

AC power at the site was provided by a generator and DC power from batteries trickle-charged by a small wind generator.

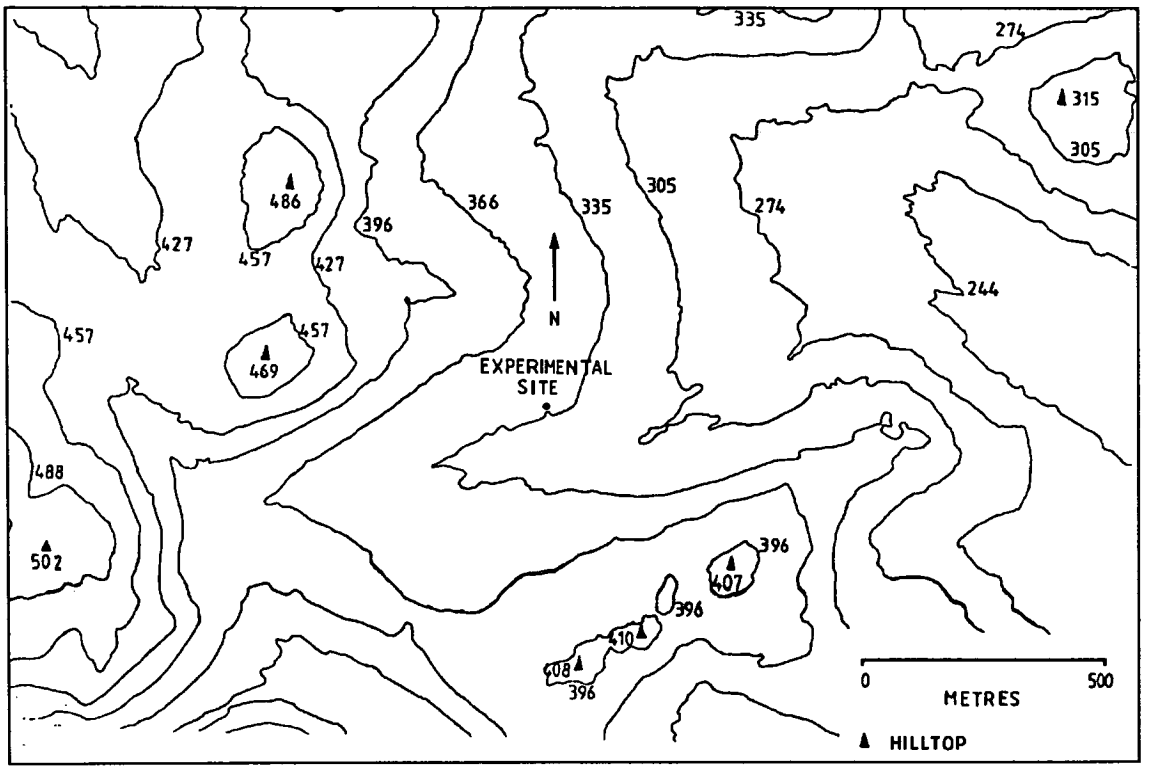

Fig. 3.2.1 Topography of the experimental site at Rivox forest, Dumfrieshire (Ordnance Survey Map Reference NT 020 042). Spot heights are in metres. (Reproduced from Crowther and Hutchings, 1985).

3.2.2 Data Acquisition

To produce a statistical description of a measured quantity, ideally we should employ an ensemble average, i.e. averaging over many data sets collected in identical conditions. In practice, our averages are Reynolds averages over time, section 2.1.3. To relate these two averaging methods, we make the ergodic hypothesis whereby we assume that the different averaging methods are equivalent as long as the measured quantity is statistically stationary over the period of measurement. If we consider a time series $\alpha(t)$ then it will be stationary if variances and covariances associated with the series approach stable values as the averaging or sampling period T_P is increased. This expectation implies that an integral time scale, τ_α, exists for the series. Thus, to

help us estimate appropriate sampling times we can define the variance of the measured time mean, $\overline{\alpha}$, about the ensemble mean as $\sigma^2_{\overline{\alpha}}$, and also the ensemble variance of $\alpha(t)$ as σ^2_α. Thus, for $\sigma^2_{\overline{\alpha}}$ we have (Lumley and Panofsky, 1964; Kaimal and Finnigan, 1993):

$$\sigma^2_{\overline{\alpha}} \propto \frac{2\sigma^2_\alpha \tau_\alpha}{T_P}. \qquad (3.2.1)$$

Thus, when $T_P >> \tau_\alpha$ then $\sigma^2_{\overline{\alpha}}$ is negligible. If we define an acceptable level of error ε:

$$\varepsilon = \frac{\sigma^2_{\overline{\alpha}}}{\overline{\alpha}}, \qquad (3.2.2)$$

then:

$$T_P \propto \frac{2\sigma^2_\alpha \tau_\alpha}{\overline{\alpha}^2 \varepsilon^2}. \qquad (3.2.3)$$

We can now apply the ergodic assumption that the ensemble variance, σ^2_α, is equivalent to the time average variance, which is a more readily available parameter. Thus, for a typical vertical velocity series we might expect $\sigma_w \sim 1$ m s^{-1}, $\tau_\alpha \sim 3$ s, $\overline{U} \sim 3$ m s^{-1}. If we specify the acceptable error, ε, as 2 %, i.e. $\varepsilon \sim 0.02$, then we get from equation 3.2.3 that $T_P \sim 1667$ s. Thus, in this case a sampling or averaging time of around 30 minutes would be appropriate.

The next choice we must make is the rate at which we sample. If we let the sampling interval be Δt, where $\Delta t > \tau_\alpha$, then in a similar way to equation 3.2.1 we can express the variance of the mean about the ensemble mean, $\sigma^2_{\overline{\alpha}}$, as:

$$\sigma^2_{\overline{\alpha}} = \frac{\sigma^2_\alpha}{N}, \qquad (3.2.4)$$

where N is the number of samples collected in the sampling period i.e. $N = T_P/\Delta t$. To estimate a level of error in $\overline{\alpha}$ due to the finite sample rate we can again take typical values for w, i.e. for $\sigma_w = 1$ m s^{-1} we require $N = 100$ to ensure $\sigma_{\overline{\alpha}} \leq 0.1$ m s^{-1}.

In practice, we need to consider what frequency components the measured quantity contains. In the case of measurements of wind velocity above a relatively smooth surface we might expect there to be contributions to the overall signal at frequencies up to ~ 10 Hz, i.e. to a cut-off frequency we shall call n_c. In most cases for the measurement of turbulent statistics, we should sample at least up to this frequency. Thus for $n_c \sim 10$ Hz, a sampling interval $\Delta t = 0.1$ s and $T_P \sim 1800$ s, then we require $N \sim 18{,}000$ samples.

If we wish to examine our sampled time series in the frequency domain with spectral analysis, we must be aware of the phenomena of 'aliasing'. To resolve a wave

in a signal we must have a minimum of two measurements or data points per wavelength or period. With only one data point per cycle, we cannot determine the wavelength correctly as many waves can contain the same signal at the same time. With this restriction in mind, we can define the sampling interval in terms of n_0, the Nyquist frequency which is half the sample frequency, as, (Stull, 1988; Kaimal and Finnigan, 1993):

$$\Delta t = \frac{1}{2n_0}. \qquad (3.2.5)$$

Information at frequencies above n_0 is folded back around n_0 and added to the spectral powers at lower frequencies , this is aliasing or spectral folding.

If $n_0 = n_c$ then we are said to be sampling at the critical frequency as we are sampling at the lowest possible frequency that will resolve all frequency components in the time series, i.e. attains the minimum two samples per cycle of the highest frequency. It is thought to be good practice to sample at a frequency such that $n_0 > n_c$ to minimise the effect of aliasing on the resulting spectra, (for instance if noise is present above n_c it may be folded back into lower frequency components).

Aliasing can be eliminated by sampling at a frequency such that $n_0 > n_c$ and to low-pass filter the voltage signals from the instruments with electronic filters which have a frequency cut off lower than n_0. For our data acquisition system, a sample rate of 18.2 Hz was chosen, i.e. Δt = 0.055 s and n_0 = 9.1 Hz, and voltage signals were low-pass filtered with electronic filters with a 3 dB* cut-off frequency of 7.4 Hz (Appendix A.1). The filter response function is shown in Figure 2.3.1.

After the data has been sampled and digitised by an analogue to digital converter, (A/D board) the raw voltage signals can then be stored on a computer hard disk or on magnetic tape for processing.

3.2.2.1 Acquisition procedures

Signal outputs from the instruments were sampled with an A/D board and stored on the hard disk of a portable personal computer. In the course of the field experiments two A/D boards were used: in 1990 a PCL-714 A/D board with 14 bit resolution over ± 5 volts, (Advantech Co. Ltd, Taiwan); in 1990 and 1991, both the PCL-714 card and a Strawberry Tree A/D board with 12 bit resolution over ± 5 volts, (Strawberry Tree Inc., Sunnyvale, California). The voltage resolutions of the PCL-714 and the Strawberry Tree A/D boards are thus 0.61 and 2.4 mV respectively. Both of

*The 3 dB cut-off frequency is that where the gain of the filter falls to $1/\sqrt{2}$ of the value at low frequencies (i.e. unity).

these A/D boards were used in conjunction with a Compaq personal computer with a 386 processor and a 120 Mb hard disk, (Compaq Computer Corporation, USA). The sample rates for both A/D boards was set to 18.2 Hz. Data files contained 30 minutes of sampled signal voltages and were saved, with each sample saved as a two byte 'word' to conserve disk space ('word' is an ordinal type defined in Borland Turbo Pascal). The data files were backed up to magnetic tape at the end of each data collection run, using a tape streamer.

All signal voltages were electronically low-pass filtered before being sampled and digitised. The low pass filters used were fifth order Butterworth filters with a cut off frequency of 7.4 Hz, (Appendix A.1). The data acquisition was controlled by software written by my colleagues J.B. Moncrieff and J.M. Massheder over a number of years.

3.2.3 Sonic Anemometers

In the field experiments, we employed sonic anemometers to measure mean wind speed and turbulent velocity fluctuations. Sonic anemometry became a viable method of wind speed measurement in the 1970s, and has many advantages over other methods of wind speed measurement because of its fast response, lack of cosine errors and much lower resolvable wind speed compared to propeller or cup anemometers. In the early stages of the technological development, single component anemometers were used, measuring only in the vertical Cartesian axis, but increasingly anemometer configurations measuring in all three Cartesian orientations have been employed. These so called 'three component' or '3-d' sonic anemometers have either an orthogonal or a pyramidal arrangement of the three pairs of sensors and have the advantage that co-ordinate rotation of the components into the streamline flow can be performed, significantly reducing errors in the measured fluxes to surfaces, (McMillen, 1986). Also it is clearly of interest when studying turbulent flow to measure all flow components.

Two models of three component sonic anemometers were used simultaneously in the field experiments reported here: a Solent A1002R, (with both the symmetric and asymmetric head configuration), (Solent, Lymington, UK), and a Kaijo Denki WA-200, (Kaijo Denki Co. Ltd., Tokyo). A CA27 one dimensional sonic anemometer, (Campbell Scientific Inc., Logan, Utah, USA) was used for comparison experiments.

The Solent anemometers also output a virtual temperature from the transit time of the ultra-sonic pulses, (Kaimal and Businger, 1963; Schotanus *et al.*, 1983; Kaimal and Gaynor, 1991). Following Kaimal and Businger (1963) the relationship between

the speed of sound and absolute air temperature is:

$$c_s^2 = 403 T_{air}(1 + 0.32 e/p), \qquad (3.2.6)$$

where c_s is the speed of sound in air, T_{air} is absolute air temperature, e is the vapour pressure of water in air and p is the absolute pressure of the atmosphere. We can define a sonic temperature T_s from (3.2.6) as, (Kaimal and Gaynor, 1991):

$$T_s \approx \frac{c_s^2}{403} = T_{air}(1 + 0.32 e/p). \qquad (3.2.7)$$

This sonic temperature is very close to the virtual or potential temperature, θ_v, which to a very good approximation, (Stull, 1988), is:

$$\theta_v \approx T_{air}(1 + 0.38 e/p) \qquad (3.2.8)$$

For typical diurnal values of water vapour pressure and absolute air temperature of 1 - 1.6 kPa and of 285 - 295 K, and assume p = 100 kPa then the corresponding range of values of θ_v and T_s, from equations 3.2.8 and 3.2.7, are (286.1 - 296.8 K) and (285.9 - 296.5 K) respectively. Thus we can see that the values of θ_v and T_s vary very little in the typical range of values encountered in the field. More importantly, Kaimal and Gaynor (1991) showed that even when errors in the absolute and virtual temperatures where largest, i.e. when p is small and e is large, the fluctuations of temperature from both sources are still very similar. The difference in temperature fluctuations is small enough to neglect when calculating fluxes of sensible heat.

The output from the sonic anemometer is in the form of transit times between a pair of sonic transducers, (in units of average number of transits per 24 MHz block), t_1 and t_2 being the times for the pulse to travel in opposite directions. Thus, by considering the sound ray vectors between the transducers, the sonic temperature is given by, (Appendix A of Kaimal and Gaynor, 1991):

$$T_s = \frac{1}{403}\left[\left(\frac{d^2}{4}\right)\left(\frac{1}{t_1} + \frac{1}{t_2}\right)^2 + \overline{U}^2\right]. \qquad (3.2.9)$$

Here d is the path length between the ultrasonic transducers and $\overline{U}$ is the magnitude of the horizontal wind vector. For horizontal wind vector magnitudes between 1 and 5 m s^{-1} this term is of the order of 0.0025 to 0.062 m s^{-1} and can be safely neglected in most instances.

The Solent A1002R sonic anemometer outputs an average transit time, t_{avg}, for the pulse travelling back and forward between the pairs of transducers. We can thus say that:

$$t_{avg} = \left(\frac{t_1 + t_2}{2} \right). \qquad (3.2.10)$$

As the outward and return transit times are likely to be very similar, then to a good approximation:

$$t_{avg} \approx t_1 \approx t_2. \qquad (3.2.11)$$

Thus equation 3.2.4 becomes:

$$T_S \approx \left(\frac{d^2}{1612} \right) \left(\frac{2}{t_{avg}} \right)^2 = \frac{d^2}{403 t_{avg}^2}. \qquad (3.2.12)$$

Thus, in equation 3.2.12 we are arriving back at our definition for $T_S \approx c_s^2/403$ K in equation 3.2.7.

The value of t_{avg} is an average over 8 complete forward and back transducer firings every 48 ms for all three Cartesian directions and, thus, should make equation 3.2.7 a very good approximation to equation 3.2.4 and, hence, to virtual temperature as discussed above.

3.2.3.1 Sonic Anemometer Inter-Comparisons

To calibrate a 3-d sonic anemometer requires a large and homogeneous wind tunnel. In the absence of such a facility we can only verify the zero wind speed response and compare the response of two or more instruments under identical conditions.

The Solent anemometers have floating earth electronics and fixed analogue output voltage ranges, i.e. zero wind speed always corresponds to the same voltage. The Kaijo Denki anemometer has an adjustable zero wind speed response. This response was checked in the field by placing a rigid box or bag over the sonic sensor heads to simulate zero wind speed conditions. This test was conducted for all the sonic anemometers used in the field and all of them responded satisfactorily, requiring no adjustment.

The Solent anemometers were newly manufactured instruments, and before field use were individually calibrated in a large wind tunnel at Southampton University by the manufacturers. In addition to a calibration for wind speed response they were calibrated for the degree of error introduced by strut interference at different angles of incidence. Up to 5° from a strut the correction factor is ~ 8 %, 15 - 50° away from the support arm, the correction is less than 3 % and up to 60° away it is less than 2 %. The resulting corrected calibration was installed in software in the anemometer units and was used throughout the experiments. The wind tunnel

calibration of the anemometers carried out by the manufacturer shows errors in mean wind speeds of less than 1 % from 0 - 360° from the North strut.

The Kaijo Denki anemometer was an older instrument and also relied on a manufacturer's calibration but had no corrections for strut interference. As we were selective in choosing data from a particular band of south westerly wind directions, section 3.2.1, the instrument was always operated above the canopy and oriented to have an unobstructed flow in the direction of the wind.

An inter-comparison experiment was carried out between two Solent anemometers, (serial numbers 09 and 20), a 1-d CA27 anemometer and the Kaijo Denki anemometer on days J199 to J201, 1990. In all, 78 half hour means are presented from 10:30 on J199 to 02:30 on J201. This was the longest set of anemometer intercomparison data gathered with dry weather and winds from the favoured south west direction; other intercomparison data sets showed more variability which we attribute to less favourable weather conditions (namely, unstable wind directions and rain).

The instruments were placed at 1.2*h* on a boom perpendicular to the prevailing wind direction as shown schematically in Figure 3.2.2. The anemometers were placed with their sensing volume centres 0.9 m apart to avoid 'cross-talk' of ultra-sonic pulses between anemometers and to avoid obstructing other eddy covariance instruments sited close to the centrally placed Kaijo Denki. The 1-d CA27 anemometer was levelled with respect to gravity and the 3-d anemometers underwent a co-ordinate rotation in software, forcing the streamwise component to zero and minimising the transverse stress covariance $\overline{v'w'}$, (McMillen, 1986). Co-ordinate rotation of 3-d sonic anemometers is further discussed in Appendix A.2.

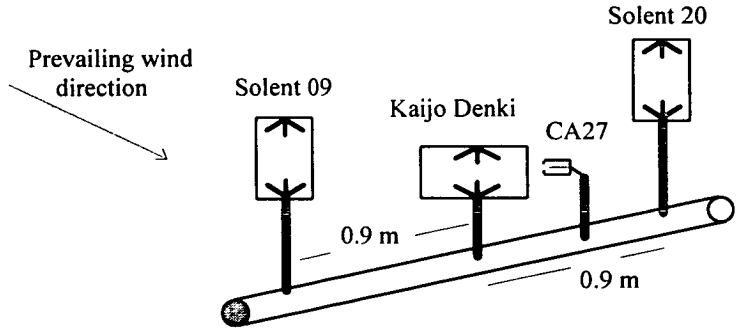

Fig. 3.2.2 Schematic diagram of sonic anemometer inter-comparison instrument array carried out at 1.2*h* above Rivox on J199, 1990. (Not to scale).

The vertical velocity variances, σ_w^2, for the two Solents are plotted against σ_w^2

from the Kaijo Denki in Figure 3.2.4. Similarly inter-comparisons are shown for: horizontal wind speed, $\overline{U}$, in Figure 3.2.3; total horizontal variance, σ^2_{horiz}, in Figure 3.2.5; Reynolds Stress, in Figure 3.2.6; and sensible heat flux, in Figure 3.2.7. Total horizontal variance, σ^2_{horiz}, is given by:

$$\sigma^2_{horiz} = \left(\left(\sigma^2_u\right)^2 + \left(\sigma^2_v\right)^2\right)^{1/2}.$$

Linear regression statistics are given in Table 3.2.1.

The plot of sensible heat fluxes shows a comparison of the covariance between each anemometer *w* fluctuations and the fast response thermocouple of the CA27T anemometer. This plot merely shows the effect on a typical eddy flux calculation of the variations observed in the vertical velocity fluctuations of the various instruments.

	Slope	Standard Error	Constant	Standard Error	R^2
Solent 09 $\overline{U}$	0.952	0.003	-0.03	0.03	0.9994
Solent 20 $\overline{U}$	1.025	0.007	-0.05	0.08	0.9964
Solent 09 σ^2_w	0.976	0.005	-0.02	0.01	0.9981
Solent 20 σ^2_w	0.979	0.006	0.00	0.02	0.9969
CA27 (1-d) σ^2_w	1.150	0.007	-0.03	0.02	0.9972
Solent 09 σ^2_{horiz}	0.951	0.02	-1.08	0.16	0.9851
Solent 20 σ^2_{horiz}	0.947	0.02	-0.57	0.20	0.9766
Solent 09 $\overline{u'w'}$	0.919	0.02	0.07	0.03	0.9774
Solent 20 $\overline{u'w'}$	0.845	0.02	0.06	0.03	0.9776
Solent 09 $\overline{w'T'}$	0.936	0.009	1.53	7.89	0.9946
Solent 20 $\overline{u'w'}$	1.010	0.011	5.38	9.50	0.9932
CA27 $\overline{w'T'}$	0.948	0.015	0.814	12.69	0.9864

Table 3.2.1 Linear regression values for Solent 09, Solent 20 and a CA27 versus the Kaijo Denki anemometer for $\overline{U}$, σ^2_w, σ^2_{horiz}, $\left(\overline{u'w'}\right)$ and sensible heat flux as plotted in Figures 3.2.3, 3.2.4, 3.2.5, 3.2.6 and 3.2.7. Data comprises 78 half hour means from J199, 10:30 to J201, 02:30.

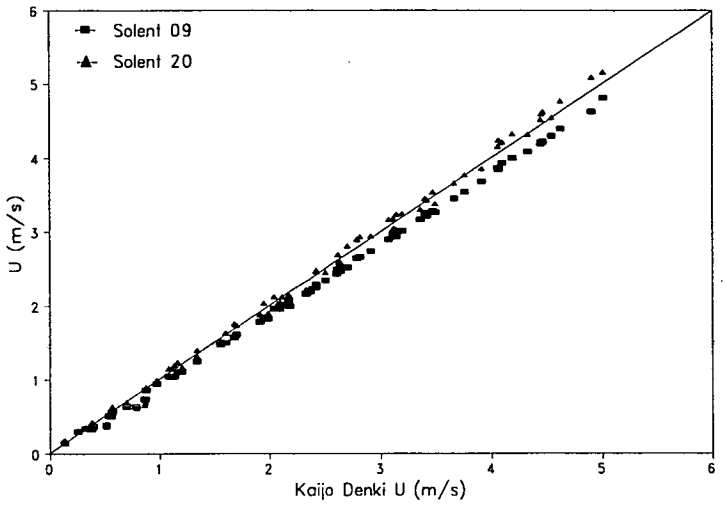

Fig. 3.2.3 Inter-comparison of two Solent 3-d sonic anemometers against a Kaijo Denki 3-d sonic anemometer for mean horizontal wind speed, $\overline{U}$, response. Data comprises 78 half hour means from J199, 10:30 to J201, 02:30.

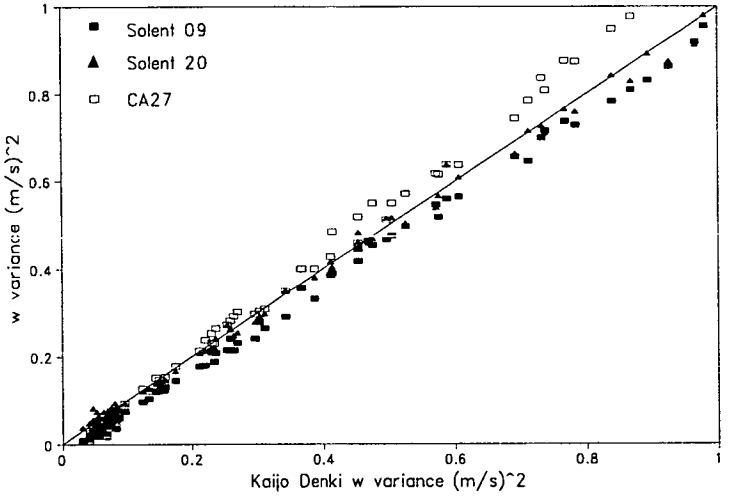

Fig. 3.2.4 Inter-comparison of two Solent 3-d sonic anemometers and a CA27 1-d anemometer against a Kaijo Denki 3-d sonic anemometer for vertical velocity variance, σ_w^2. Data comprises 78 half hour means from J199, 10:30 to J201, 02:30.

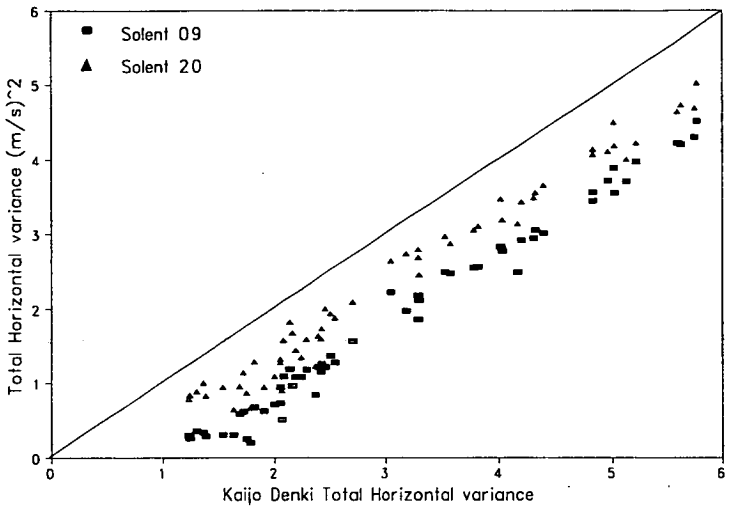

Fig. 3.2.5 Inter-comparison of two Solent 3-d sonic anemometers against a Kaijo Denki 3-d sonic anemometer for total horizontal velocity variance σ^2_{horiz}. Data comprises 78 half hour means from J199, 10:30 to J201, 02:30.

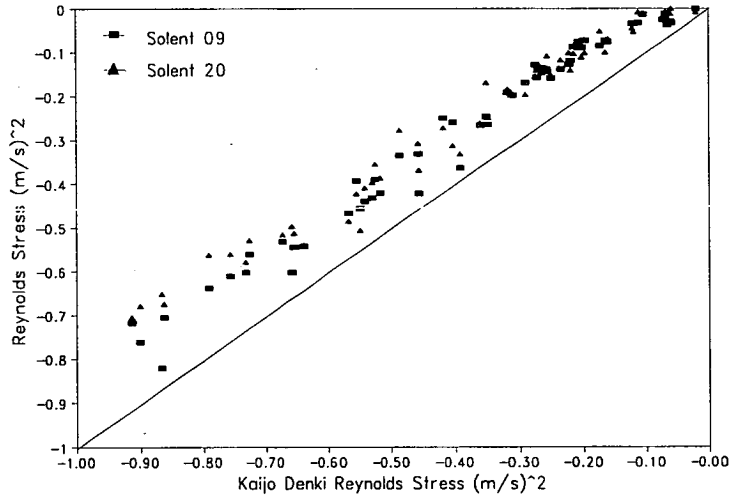

Fig. 3.2.6 Inter-comparison of two Solent 3-d sonic anemometers against a Kaijo Denki 3-d sonic anemometer for Reynolds Stress, $\left(\overline{u'w'}\right)$. Data comprises 78 half hour means from J199, 10:30 to J201, 02:30.

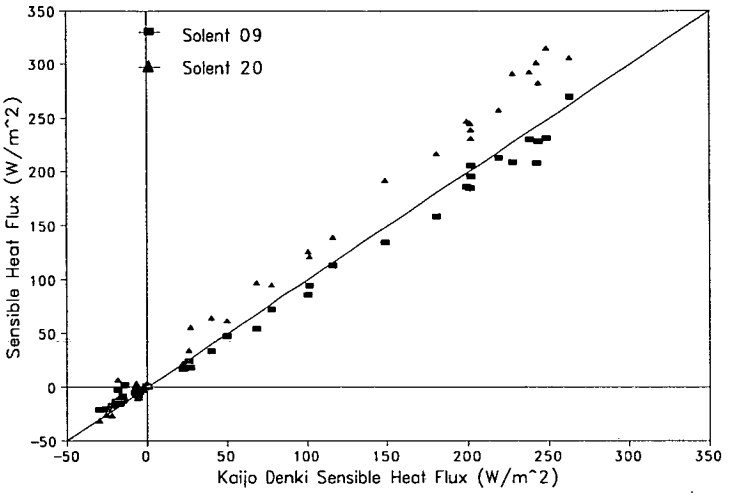

Fig. 3.2.7 Inter-comparison of two Solent 3-d sonic anemometers and a CA27 1-d anemometer against a Kaijo Denki 3-d sonic anemometer for sensible heat flux for a common temperature signal. Data comprises 78 half hour means from J199, 10:30 to J201, 02:30.

The agreement between vertical velocity variances shown in Figure 3.2.4, and mean for horizontal wind speeds in Figure 3.2.3, for the anemometers is remarkably good. The 3-d anemometers show a greater difference in response to the total horizontal variance, or Reynold's stress, Figures 3.2.5 and 3.2.6. The Solent anemometers are apparently underestimating the magnitudes of these quantities. It is difficult to attribute this behaviour to calibration errors in the two instruments as the mean horizontal wind speeds, $\overline{U}$, agreed well. The Solent and the Kaijo Denki anemometers have physically different sensor heads as the Solent anemometer is smaller in structure with thinner, less obstructive struts. Software built into the Solent anemometer corrects the output data for strut interference, but these corrections are not made in the Kaijo Denki instrument. It is thus possible that more spurious turbulent horizontal variance is observed with the Kaijo Denki instrument whereas, in the Solent instruments, such over-estimations of variance are minimised by the software corrections. We could equally well conclude that the Solent instruments are 'correcting' for turbulent wake effects which are not there and, thus, underestimating the true signal as given by the Kaijo Denki! It would be more satisfactory to carry out such inter-comparison experiments in the controlled environment of a large wind tunnel.

Following the error analysis of Dyer *et al.* (1982) we can estimate the errors we might expect to find in variance and covariance measurements at each instrument.

Dyer *et al.* (1982) give the 'probable error' in a variance measurement as ε_v, where:

$$\varepsilon_v = 2\sqrt{\frac{\tau}{T_P}}, \qquad (3.2.13)$$

where τ is the relevant time scale for the measurement and T_P is the sampling period in seconds. Thus in our case we might expect an error in the w variance of ~ 5 % if we take T_w as the vertical velocity time scale, section 2.1.8, where T_w is ~ 1 s from Table 5.3.1. Similarly, the error in a covariance ε_{ab} can be described, (Wyngaard, 1973; Dyer *et al.*, 1982), as:

$$\varepsilon_{ab} = \sqrt{\frac{2\tau}{t_r}\left(1 + r_{ab}^{-2}\right)}, \qquad (3.2.14)$$

where r_{ab} is the cross-correlation between a and b at a single point. This can be obtained from the relationship, (Stull, 1988):

$$r_{ab} = \frac{\overline{a'b'}}{\sigma_a \sigma_b}. \qquad (3.2.15)$$

Thus ε_{uw} might be expected to range from ~ 11 % to 30 % and ε_{wT} between ~ 16 to 21 % for our measurements. These statistical considerations do not, however, address the problems with the comparisons of horizontal variance and Reynolds stress values already discussed.

3.2.4 Infra-Red Gas Analysers

A variety of infra-red gas analysers was used in the field experiments reported in this thesis to measure both CO_2 and water vapour fluctuations in the atmosphere. All the IRGA's used were of the non-dispersive type i.e. the transmission of broad-band, unselected infra-red radiation is measured, (Jarvis and Sandford, 1985). By placing optical filters in the beam path the measurement can be made selective for a particular gas. The possibility does however exist that other gases in the optical path of the analyser will also absorb infra-red radiation in the selected bands i.e. there is a cross-sensitivity between the two gases. The absorption bands for CO_2 lie at wavelengths: 2.69; 2.77; 4.26 and 14.99 μm; with the 4.26 μm band being by far the strongest and thus the band most commonly used for CO_2 measurement, (Jarvis and Sandford, 1985). A 2.59 μm absorption band is the one generally favoured for water vapour measurement. The absorption of infra-red by water vapour overlaps that by CO_2 at 2.7 μm which leads to a cross-sensitivity between the two.

The IRGAs employed in our experiments fall into two categories: closed optical path and open optical path, the optical path being the volume through which

gas passes where the infra-red beam is absorbed. If this pathway is enclosed within the analyser, then it is said to be a closed path and, if it is outside the analyser and open to the free atmosphere, then it is said to be an open path. An important consequence of these different instrument configurations is that the equations outlined in section 2.2.2 for calculating mass fluxes, incorporating the analysis of Webb, Pearman and Leuning (1980), can be adapted for each case. We can also include in the equations the effect of cross-sensitivity of CO_2 measurements to water vapour density, (Leuning and Moncrieff, 1990). The measurement of CO_2 is our prime interest, so we will concentrate on an analyser measuring CO_2 in the presence of water vapour. Following Leuning and Moncrieff (1990) we can write the electrical signal, V, from the analyser as:

$$V - V_o = \alpha\rho_c + \beta\rho_v, \tag{3.2.16}$$

where V_0 is a reference voltage obtained under standard conditions, ρ_c and ρ_v are the densities of CO_2 and water vapour, as before, and α and β are the analyser sensitivities to CO_2 and water vapour respectively. We assume that α is independent of ρ_v and, similarly, β is independent of ρ_c. If we firstly consider the case of an open path analyser, we can rearrange equation 3.2.16 and, solving for fluctuating quantities obtain:

$$\rho_c' = V'/\alpha - \beta\rho_v'/\alpha. \tag{3.2.17}$$

From section 2.2.2 equation 2.2.10 for the flux of a mass scalar with density in air ρ_c, in this case CO_2, was:

$$F_c = \overline{w'\rho'_c} + \mu\left(\frac{\bar{\rho}_c}{\bar{\rho}_a}\right)\overline{w'\rho'_v} + (1+\mu\sigma)\left(\frac{\bar{\rho}_c}{\bar{T}}\right)\overline{w'T'}. \tag{2.2.10}$$

Now combining equations 3.2.17 and 2.2.10 we get:

$$F_c = \frac{\overline{w'V'}}{\alpha} + \left(\frac{\mu\bar{\rho}_c}{\bar{\rho}_a} - \frac{\beta}{\alpha}\right)\overline{w'\rho_v'} + (1+\mu\sigma)\frac{\overline{w'T'}}{\bar{T}}\widetilde{\rho_c} \tag{3.2.18}$$

This equation can also be expressed in the form of heat and water vapour fluxes:

$$F_c = \frac{\overline{w'V'}}{\alpha} + \left(\frac{\mu\bar{\rho}_c}{\bar{\rho}_a} - \frac{\beta}{\alpha}\right)\frac{E}{(1+\mu\sigma)} + \frac{\bar{\rho}_c}{\bar{\rho}}\left(1 + \frac{\beta\bar{\rho}_v}{\alpha\bar{\rho}_c}\right)\frac{H}{c_p\bar{T}}, \tag{3.2.19}$$

where $\bar{\rho}$ and c_p are the mean density and specific heat capacity of moist air respectively, H is sensible heat flux and E is the water vapour flux where:

$$\begin{aligned} H &= c_p\bar{\rho}\overline{w'T'}, \\ E &= (1+\mu\sigma)\left[\overline{w'\rho_v'} + (\bar{\rho}_v/\bar{T})\overline{w'T'}\right]. \end{aligned} \tag{3.3.20}$$

For the case of a closed path analyser, we must consider the effect on the air sample of being ducted into the analyser, which results in the fluctuating components coming to a common temperature and pressure inside the IRGA. Again following Leuning and Moncrieff (1990), the CO_2 density in the sample can be related to that measured in the IRGA by:

$$\rho_c = \left(\frac{pT_i}{p_i T}\right)\rho_{ci}, \tag{3.2.21}$$

where the suffix i denotes conditions inside the IRGA. The fluctuations in the analyser can now be given as: assuming, to a good approximation, $\bar{T}-T' \sim \bar{T}$, ie $T' \ll \bar{T}$

$$\rho_c' = \left(\frac{pT_i}{p_i \bar{T}}\right)\left[\rho_{ci}' - \left(\frac{\bar{\rho}_{ci}}{\bar{T}}\right)T'\right]. \tag{3.2.22}$$

Thus by multiplying equation 3.2.22 by w' and Reynolds averaging we can obtain an eddy covariance $\overline{w'\rho_c'}$. By combining equations 2.2.10, 3.2.21 and 3.2.22, we can obtain:

$$F_c = \left(\frac{pT_i}{p_i \bar{T}}\right)\overline{w'\rho_{ci}'} + \left(\frac{\mu\bar{\rho}_c}{\bar{\rho}_a}\right)\left[\overline{w'\rho_v'} + \left(\frac{\bar{\rho}_v}{\bar{T}}\right)\overline{w'T'}\right] \tag{3.2.23}$$

As can be seen the major term in $w'T'$ has been removed from equation 2.2.10 due to the air sample being brought to a common temperature in the analyser. If we include the effect of cross-sensitivity to water vapour as:

$$\overline{w'\rho_{ci}'} = \overline{w'V'}/\alpha - (\beta/\alpha)\overline{w'\rho_{vi}'}. \tag{3.2.24}$$

We can now obtain an expression for $\overline{w'\rho_{vi}'}$ in a similar way to that for $\overline{w'\rho_{ci}'}$ from equation 3.2.22 and combine these with equation 3.2.23 to obtain:

$$F_c = \left(\frac{pT_i}{p_i \bar{T}}\right)\left(\frac{\overline{w'V'}}{\alpha}\right) + \left(\frac{\mu\bar{\rho}_c}{\bar{\rho}_a} - \frac{\beta}{\alpha}\right)\left[\overline{w'\rho_v'} + \left(\frac{\bar{\rho}_v}{\bar{T}}\right)\overline{w'T'}\right]. \tag{3.2.25}$$

Again in terms of fluxes we have:

$$F_c = \left(\frac{pT_i}{p_i \bar{T}}\right)\left(\frac{\overline{w'V'}}{\alpha}\right) + \left(\frac{\mu\bar{\rho}_c}{\bar{\rho}_a} - \frac{\beta}{\alpha}\right)\frac{E}{(1+\mu\sigma)}, \tag{3.2.26}$$

where E is given by:

$$E = \left(\frac{pT_i}{p_i \bar{T}}\right)(1+\mu\sigma)\overline{w'\rho_{vi}'}. \tag{3.2.27}$$

By comparing the final flux equations 3.2.19 and 3.2.26 for the open and closed path cases we see that the correction terms in E are identical for both cases but

the closed path analyser has no terms in H as the fluctuations in the air sample are brought to a common temperature. The value of the ratio β/α is indicative of the degree of cross-sensitivity of the CO_2 measurement to water vapour and this ratio must be determined experimentally for each type of IRGA.

3.2.4.1 Open Path IRGA

The open path IRGA used in the field work, was the Advanced Systems E009, (Advanced Systems Inc., Okayama City , Japan): one old model E009, and two of the newer E009a models over the two field campaigns. The instrument is based on the prototype sensor described by Ohtaki and Matsui (1982). It has a 0.2 m open optical path and is generally employed in the field with this path vertical. It has a sampling rate of 33 Hz and thus has a nominal response time of ~ 0.03 s. The instrument was designed for use in eddy covariance systems and measures both CO_2 and H_2O fluctuations simultaneously. The Advanced System sensors suffer from a drift in the gain, or sensitivity, and zero offset of the analyser to both CO_2 and H_2O. This has been attributed to the processing electronics by the manufacturers and care must be taken to keep the instruments on scale. These trends are removed from the data with a running mean digital recursive filter during processing, section 2.3.3. The drift in gain could not be attributed to any environmental parameters during our field work and was also present under controlled laboratory conditions. This behaviour has also been noted by Moncrieff *et al.* (1992) during an inter-comparison experiment of open path CO_2 analysers in the FIFE field campaign in Kansas in 1989.

3.2.4.2 Closed Path IRGAs

Three closed path IRGAs were used in the field at different times: a laboratory ADC 225 (III), (The Analytical Development Company Ltd., Hoddesdon, UK); a prototype WA468 (I), (The Analytical Development Company Ltd., Hoddesdon, UK); and a Li6252, (Li-Cor Inc., Lincoln, Nebraska, USA). All the instruments measured CO_2 and the ADC WA468 (I) also measured water vapour. The respective response times of the analysers, as quoted by the manufacturers, are given in Table 3.2.2.

The ADC 225 (III) and Li6252 could be operated in either differential mode or absolute mode. Both were operated in differential mode in the field with either a standard span gas or CO_2 and H_2O chemically scrubbed air passing through the reference cell. The ADC WA468 (I) is always operated with an intermittently scrubbed reference.

Air was ported to the closed path analysers in the field by means of 5.5 mm

IRGA	90% minimum Response Time
ADC 225 (III)	3 s
ADC WA468 (I)	0.1 s
Li-Cor Li6252	0.44 s

Table 3.2.2 Response times to 90 % step concentration change for three closed path analysers, quoted by the manufacturers.

inside diameter tubing made of material with low CO_2 absorptivity, (Dekabon 1300 Tubing, J.P. Deane and Co. Ltd, Glasgow). In addition to the length of Dekabon tubing there was also ~ 3 m of 7 mm inside diameter copper tubing added just before the connection to the IRGA. This short length of tubing ensured that all the temperature fluctuations in the sampled air were removed before entering the analyser, (Leuning and Moncrieff, 1990), although a stable internal IRGA temperature would probably have been sufficient to remove temperature fluctuations at the flow rates used. The tube lengths varied from ~ 57 m, for the ADC 225 (III) and the Li6252 which were housed in a hut a short distance away from the tower, to ~ 5 m for the ADC WA468 (I) which was placed at the top of the tower close to the sonic anemometer mounting boom. Flow rates through the closed path analysers differed for each instrument, with flow rates of ~ 3 l min^{-1} for the ADC 225 (III), 4.5 l min^{-1} for the Li6252 and 6 l min^{-1} for the ADC WA468 (I).

3.2.4.3 IRGA Calibrations and Cross-Sensitivity

IRGAs need to be calibrated for both zero offset and sensitivity to the measured gas density. Frequency of calibration is partly dictated by the characteristics of the individual instrument and partly by the changes in environmental factors such as temperature, pressure, humidity and ambient gas concentration. The most common form of calibration involves introducing gases of known density into the analyser. This was the best calibration method for the analysers employed during this work, as the same system could be used on all the different analyser configurations. The lack of an accurate portable manometer in the field prevented the choice of pressure variation methods of calibration.

The aim of the calibration is to interpret the voltage output of an analyser in

terms of the gas density in its measurement cell, in units appropriate to the application. IRGAs measure the partial pressure of CO_2 in air, i.e. ρ_c in kg m^{-3}, or the partial pressure in Pa, (Jarvis and Sandford, 1985). Scale gases which are passed through an analyser for calibration purposes are generally defined in mole or volume fractions (i.e. generally in μmol mol^{-1} or ppm). If the volume fraction of a gas is c then the partial density, ρ is given by, (Jarvis and Sandford, 1985):

$$\rho = c\rho_{stp}\left(\frac{pT_{stp}}{p_{stp}T}\right) = 5.239\times10^{-3}\left(\frac{cp}{T}\right), \qquad (3.2.28)$$

where subscript *stp* denotes values of standard temperature and pressure, and T is absolute temperature.

Calibrations should thus be carried out in terms of partial densities of the gas as these will be unaffected by changes in temperature and pressure during measurement. If the analyser is to be calibrated and operated at different pressures then this must be taken into account in the sensitivity or gain values that are obtained from calibration. In closed path analysers the calibration and measurements should either be carried out at the same flow rate through the cells or an adjustment made in the calibration factors for the pressure change. The open path instrument is calibrated with a sealed hood over the measurement volume. During calibration, gas is pumped through this chamber and the pressure increases slightly with respect to ambient. This must be taken into account in the calibration factors used when the instrument is open to the atmosphere.

For the closed path instruments operating in differential mode, where a comparison of gas density is being made between a sample and a reference cell, it is important to maintain the same temperature and pressure in both the cells. In most closed path analysers the interior temperature is uniform and the size of the cells are the same. Thus an identical flow rate through both sample and reference cell will generally satisfy this condition. It is important, however, to monitor pressure in gas lines and in the measurement cells, as large pressures can build up in gas circuits if, for instance, lines become obstructed. Flow meters were used to monitor the flow in the tubes during calibrations and normal use, both in the field and in the laboratory. For a small pressure difference between the sample and reference cells of 50 Pa, say from the presence of 5 mm H_2O, with an ambient pressure of 101.33 kPa and CO_2 concentration of 340 ppm, the result is an apparent concentration difference of 0.2 ppm.

Obtaining a range of standard gases for calibration is a major difficulty in calibrating gas analysers. Commercially available standard gases are generally supplied with an accuracy of ± 5 % on the volume fraction. As a gas cylinder empties,

the volume fraction can change if the gas is insufficiently mixed and it is a good policy to gently heat the bottom of large gas bottles to ensure good mixing when calibrating. Aside from gas bottles, volume mixing systems can often give better accuracy and reproducibility. Such a system can be based on Wosthoff mixing pumps (H. Wosthoff OHG, Bochum, Germany) or, alternatively, rely on mass flow meters, (Jarvis and Sandford, 1985).

Three bottles of standard CO_2 in dry air were purchased from B.O.C., (British Oxygen Company, Special Gases, Crewe, UK) with a volume fraction certified to within ± 5 %. These were calibrated at regular intervals against a mixing system, employing three Wosthoff pumps, which was treated as an absolute standard. Before field experiments, the bottles were calibrated against the mixing system and the bottles alone were used for field calibrations.

The Li6252 was used in differential mode with a chemically scrubbed zero concentration reference according to manufacturers recommendations, and thus a zero concentration air stream was used to set the zero offset. The span was set with the highest concentration scale gas and the calibration checked with the two remaining gases. The E009 open path analysers and the WA468 (I) were calibrated as absolute analysers with the three standard gases and a sensitivity calculated from the resulting regression. The ADC 225 (III) analyser was calibrated using the 'tube-length' method, (Jarvis and Sandford, 1985), where the sample cell can be split into short and long sections with known lengths. This instrument was used in differential mode throughout the experiment, with one of the scale gases as reference. The differential zero was set by passing this reference gas through the reference cell, the short sample tube, and the long sample tube. The span was set by passing the reference gas through the reference and long sample tube and then passing CO_2 free air through the short sample tube. In all the analysers, a linear response in the range of measurement and calibration was assumed, i.e. typically 300 - 500 ppm. The Li6252 has an option of a linearised voltage output in addition to a curvilinear sensor voltage output; the linear output was the one that was sampled.

Calibration for water vapour was carried out in a similar way with air of known water vapour density being passed through the analysers to set their zero response, span, and to calculate their sensitivities. Standard saturated air can be obtained from a water bath system were air is saturated by being bubbled through water and then passed through a thermostatically controlled water bath at various temperatures. From the dew point of water in air the water vapour density in the air stream can be calculated. Our calibrations were carried out with a simple water bath system as shown in Figure 3.2.8 for the E009 open path analyser with its calibration

hood. (The water bath contained a solution of water and Ethylene Glycol so that lower temperatures could be maintained).

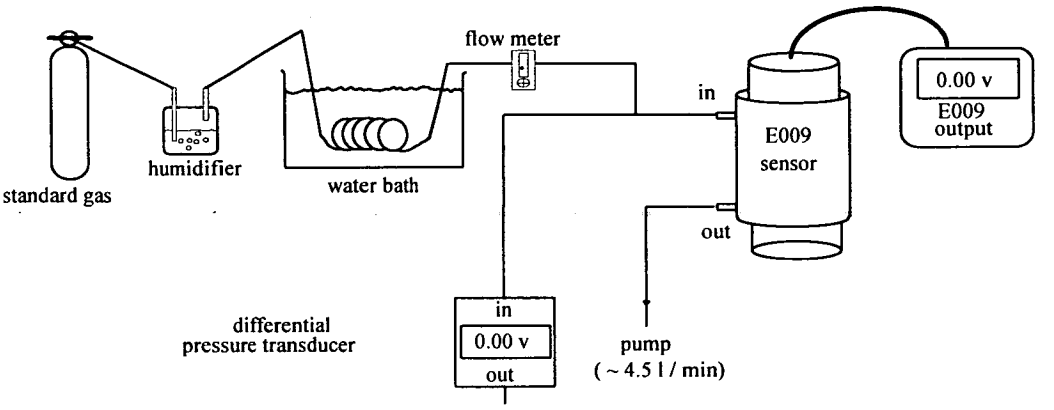

Fig. 3.2.8 Schematic diagram of E009 water vapour response calibration system.

Calibrations for water vapour response of the E009 and the WA468 (I) analysers were carried out in the laboratory prior to and immediately after field experiments. To verify that the laboratory calibrations were applicable to field conditions, the E009 sensors were calibrated once in the field with an EG&G model 440 dew point hygrometer, (EG&G, Newton, Massachusetts, USA), which had been calibrated in the laboratory with the water bath system. Saturated air was mixed with air from the atmosphere and passed through the dew point hygrometer and the analysers to test their responses to water vapour. The calibrations were found not to have changed significantly either between laboratory experiments or with the field test at the test gain settings used by the manufacturers (for the newer model E009 the field calibration was 0.88 ± 0.16 V $(g\ kg^{-1})^{-1}$, and the laboratory calibration was 1.0 ± 0.03 V $(g\ kg^{-1})^{-1}$, similarly, for the old model E009 in the field the calibration was 0.66 ± 0.05 V $(g\ kg^{-1})^{-1}$ and the laboratory calibration was 0.61 ± 0.06 V $(g\ kg^{-1})^{-1}$, where all errors are standard errors).

Experiments in the laboratory were carried out to quantify the cross-sensitivity of CO_2 density to the presence of water vapour for the E009 and Li6252 analysers. The experimental system shown schematically in Figure 3.2.8 was used for this experiment. Following the procedure of Leuning and Moncrieff (1990) one CO_2 standard scale gas was sampled alternately 'dry' and 'wet', i.e. directly into the analyser or through the water bath system. The apparent increase in CO_2 density due to the presence of different absolute water vapour densities from this experiment is shown in Figure 3.2.9.

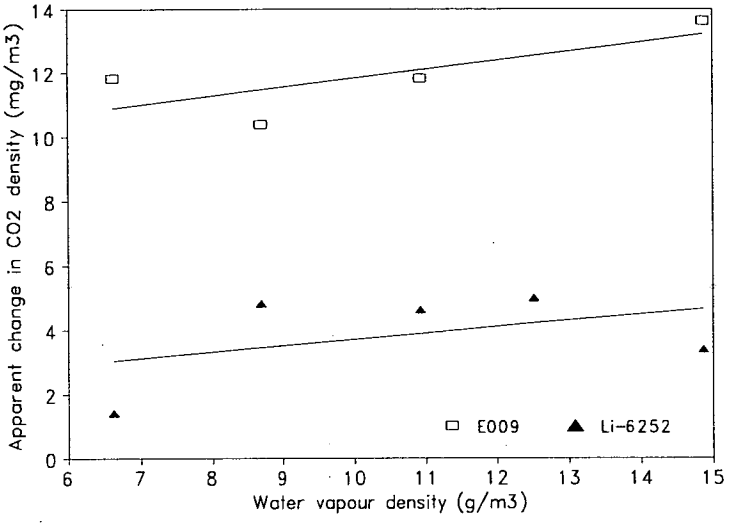

Fig. 3.2.9 Apparent change in CO_2 concentration in the E009 and Li6252 IRGAs in the presence of different water vapour densities. Solid lines are linear regressions.

Leuning and Moncrieff (1990) carried out this experiment for the WA468 (I) analyser used in the experiments presented in this thesis. The ADC 225 (III) was unavailable for inclusion in the experiment. The values of α, β, and β/α for three analysers are shown in Table 3.2.3

IRGA	α V $(kg(CO_2)\ m^{-3})^{-1}$	β $V(kg(H_2O)\ m^{-3})^{-1}$	β/α
E009	27.9×10^{-3}	7.8×10^{-6}	2.8×10^{-4}
Li6252	18.7×10^{-3}	4.0×10^{-6}	2.1×10^{-4}
WA468 (I)	5.8×10^{-3} *	1.6×10^{-6} *	2.7×10^{-3} *

Table 3.2.3 CO_2 sensitivity, α, CO_2 voltage cross-sensitivity to water vapour, β and the ratio β/α for three IRGA's, (*from Leuning and Moncrieff, 1990).

As no value of β/α for the ADC 225 (III) was obtained by experiment, the β/α value for the ADC WA468 (I) analyser was assumed for this analyser as an estimate of a possibly large cross-sensitivity.

The relative effect of the cross-sensitivity, water vapour and sensible heat fluxes on the overall CO_2 flux is best illustrated by an example. If we consider the flux equations 3.2.19 and 3.2.26 from WPL (section 2.2.2), with the additions for the

effect of cross-sensitivity for the specific analysers, we can split the terms up as follows:

For the open path analysers the flux equation is:

$$F_c = \frac{\overline{w'V'}}{\alpha} + \left(\frac{\mu\bar{\rho}_c}{\bar{\rho}_a} - \frac{\beta}{\alpha}\right)\frac{E}{(1+\mu\sigma)} + \frac{\bar{\rho}_c}{\bar{\rho}}\left(1 + \frac{\beta\bar{\rho}_v}{\alpha\bar{\rho}_c}\right)\frac{H}{c_p\overline{T}}, \qquad (3.2.19)$$

$$F_c = F_{raw} + \Delta F_E + \Delta F_H, \qquad (3.2.29)$$

where E and H is given by equation 3.2.20.

For the closed path analysers the flux equation is:

$$F_c = \left(\frac{pT_i}{p_i\overline{T}}\right)\left(\frac{\overline{w'V'}}{\alpha}\right) + \left(\frac{\mu\bar{\rho}_c}{\bar{\rho}_a} - \frac{\beta}{\alpha}\right)\frac{E}{(1+\mu\sigma)}, \qquad (3.2.26)$$

$$F_c = F_{raw} + \Delta F_E, \qquad (3.2.30)$$

where E and H is given by equation 3.2.27.

If we consider a typical field situation with an ambient CO_2 concentration of 340 ppm, a relative humidity of 80 %, (thus $\bar{\rho}_c/\bar{\rho}_a \approx 5.2 \times 10^{-4}$ and $\sigma \sim 8.3 \times 10^{-3}$), a mean air temperature of 20 °C, latent heat of vaporisation $\lambda_q = 2.442 \times 10^6$ J kg^{-1}, a latent heat flux of 200 W m^{-2} and a sensible heat flux of 300 W m^{-2}. For the closed path analysers the internal pressure differential is typically no greater than ~ 125 Pa and internal temperature is no greater than ~ 300 K with atmospheric pressure ~ 100 kPa. The partial fluxes in equations 3.2.29 and 3.2.30 are given for these conditions in Table 3.2.4 for three analysers.

As can be seen from Table 3.2.4 the size of the largest addition to the overall

IRGA	β/α	F_{RAW} mg(CO_2) m^{-2} s^{-1}	ΔF_E mg(CO_2) m^{-2} s^{-1}	ΔF_H mg(CO_2) m^{-2} s^{-1}
E009	2.8×10^{-4}	$\left(\overline{w'V'}/\alpha\right)$	0.045	0.52
Li6252	2.1×10^{-4}	$1.02 \times \left(\overline{w'V'}/\alpha\right)$	0.0051	—
WA468 (I)	2.7×10^{-3} *	$1.02 \times \left(\overline{w'V'}/\alpha\right)$	-0.15	—

Table 3.2.4 Relative contributions to total CO_2 flux for the terms in equations 3.2.19 and 3.2.26 for three IRGAs for the outlined conditions, (*from Leuning and Moncrieff, 1990).

'raw' flux is from the sensible heat term in the open path analyser case. The values of the term ΔF_E for the two closed path analysers shows, the effect of the cross-sensitivity. If we consider, however, that the total flux, F might typically be ~ 1 mg(CO_2) m^{-2} s^{-1} then the size of ΔF_E even for the WA468 (I) IRGA is small. Leuning and Moncrieff (1990) produced isopleths for IRGAs with different β/α values over a wide range of latent and sensible heat values which more clearly illustrates the effect of analyser cross-sensitivity on overall CO_2 flux, (see Figure 2 of Leuning and Moncrieff, 1990).

3.2.4.4 IRGA CO_2 Inter-Comparison

An inter-comparison of three of the IRGAs was carried out on J195, 1990 at 1.2*h* above Rivox forest. Mean fluxes from fourteen half hour periods were calculated from 11:00 on J195. Three instruments were compared: an E009; the ADC WA468 (I); and the ADC 225 (III). The WA468 (I) was sampled through a 5 m tube, made up of 2 m of 5.5 mm inside diameter Decabon tubing and 3 m of 7 mm inside diameter copper tubing, with a flow rate of ~ 6 l min^{-1}. The ADC 225 (III) was sampled through about 57 m of tube, made up of 5.5 mm inside diameter Decabon tubing with 3 m of 7 mm inside diameter copper tubing at the analyser inlet, with a flow rate of ~ 3 l min^{-1}. The resulting lags, calculated with respect to the *in situ* measurements for the WA468 (I) and the ADC 225 (III) respectively were 54 and 539 samples of 18.2 Hz data, i.e. 3.0 and 29.6 s. The three IRGAs were placed at 1.2*h* adjacent to a sonic anemometer, as shown in Figure 3.2.10. All CO_2 flux calculations take account of

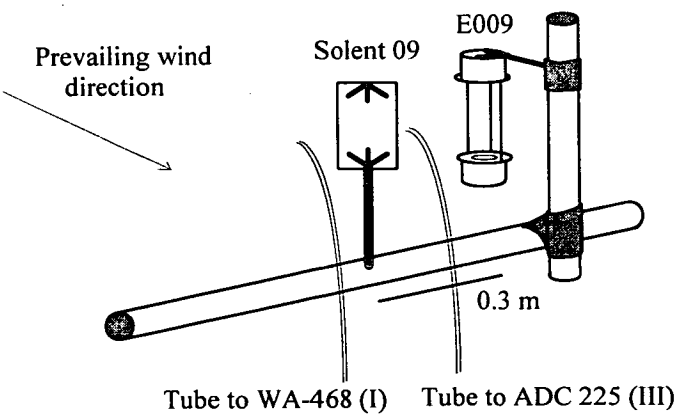

Fig. 3.2.10 Schematic diagram showing the position of the open path IRGA and the closed path IRGA sampling tubes during the inter-comparison experiment at 1.2*h* above Rivox on J195, 1990.

WPL effects, cross-sensitivity corrections and the appropriate transfer function corrections, namely: sensor separation; low-pass filtering; digital recursive filtering; sonic anemometer and IRGA path averaging, (E009); dynamic frequency response of sonic anemometers and IRGAs; sensor mismatching; sample tube smearing in closed path IRGAs, (ADC 225 (III) and WA468 (I)).

The results of the inter-comparison are shown in Figures 3.2.11 and 3.2.12. The analysers were calibrated for CO_2 response in the middle of the measurement period, hence there is a gap in the data. Results from linear regressions of the closed path analyser responses with respect to the open path analyser response are given in Table 3.2.5.

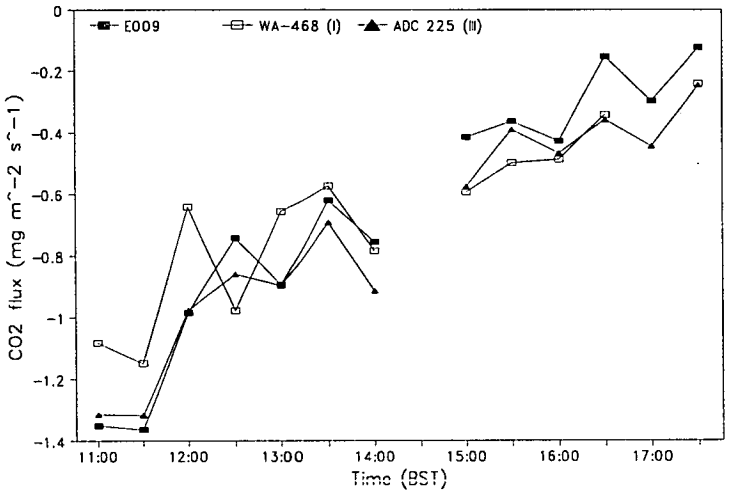

Fig. 3.2.11 Time variation of CO_2 fluxes calculated for two closed path IRGAs (WA468 (I) and the ADC 225 (III)) and the open path E009 IRGA at 1.2*h* above Rivox forest on J195, 1990. Time is BST.

We can see that the E009 and ADC 225 (III) analysers agree well throughout the day, whereas the relationship with the WA468 (I) analyser is somewhat more scattered. From the slope of the linear regressions, the typical underestimation of CO_2 flux with respect to the E009 IRGA is: for the WA468 (I) ~ 39 %; and for the ADC 225 (III) ~ 15 % . In a more extensive inter-comparison experiment carried out during the FIFE experiment in Kansas 1989, Moncrieff *et al.* (1992) found that fluxes between two E009 sensors agreed to within 15 % with other designs of open path analysers.

The WA468 (I) IRGA was only employed in the field on this day, with the other two analysers being employed on all other days in 1990.

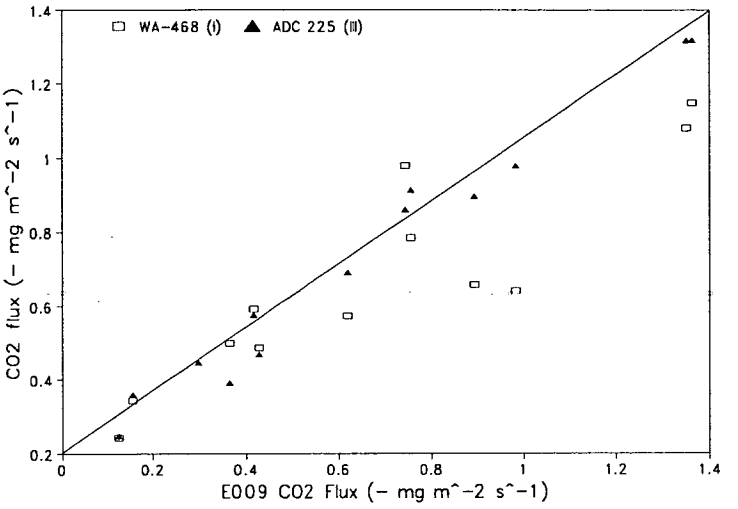

Fig. 3.2.12 Inter-comparison between CO_2 fluxes calculated for two closed path IRGAs: WA468 (I); and the ADC 225 (III); with the open path E009, as in Figure 3.2.11. The solid line is the 1:1 line.

	Slope	Standard Error	Constant	Standard Error	R^2
WA468 (I)	0.61	0.09	0.13	0.25	0.809
ADC 225 (III)	0.85	0.04	0.17	0.06	0.976

Table 3.2.5 Linear regression statistics for CO_2 flux inter-comparison at $1.2h$ above Rivox forest, J195, 1990.

For a measurement period in 1991, a comparison of an E009 was carried out alongside the Li6252 with an identical arrangement to the experiment described above. The inter-comparison between the Li6252 and the E009 analysers for CO_2 flux on day J191, 1991 is shown in Figure 3.2.13.

Once again typical errors suggested by the linear regression statistics between CO_2 flux measurements are ~ 19 %. Considering the magnitudes of the WPL correction factors applied to the three sets of data, section 4.2, this agreement is encouraging, and sets a reasonable limit on the accuracy of the measured CO_2 fluxes.

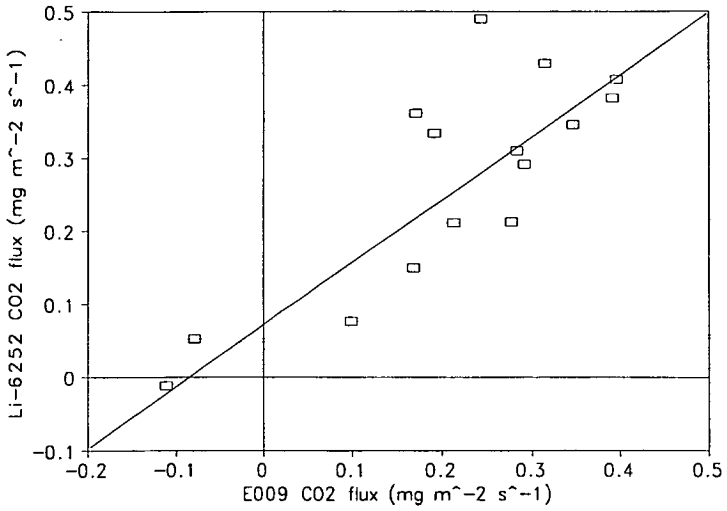

Fig. 3.2.13 Inter-comparison between CO_2 fluxes calculated for the closed path Li6252 with the open path E009, with all corrections applied. The solid line is the 1:1 line.

	Slope	Standard Error	Constant	Standard Error	R^2
Li6252	0.81	0.16	0.10	0.09	0.66

Table 3.2.6 Linear regression statistics for CO_2 flux inter-comparison between Li6252 and E009 IRGAs at 1.2*h* above Rivox forest, J191, 1991.

3.2.5 Meteorological Measurements

A set of meteorological instruments were placed on small booms at the top of the walk-up tower, in a position unlikely to disturb the eddy covariance instruments placed on other booms. A net radiometer was mounted on the end of a 3 m boom. Two soil heat flux plates were placed ~ 2.0 ± 0.5 cm below the surface of the needle litter on the forest floor. One of the plates was placed in the bottom of a shallow drainage channel and the other on the ridge where the trees were planted (section 3.2.1). The measurements made and the instruments used are summarised in Table 3.2.5.

MEASUREMENT	INSTRUMENT	MODEL and SUPPLIER
Horizontal wind speed	Cup anemometer	A100R, Vector Instruments, Clwyd, UK
Horizontal wind direction	Wind vane	W200P, Vector Instruments
Solar Radiation, S	Pyranometer	Li-200sz, Li-Cor, Lincoln, Nebraska, USA
Net Radiation, R_n	Single dome net radiometer	Siemen Ersking, Frederikssund, Denmark
Photosynthetically Active radiation, I_P.	Quantum sensor	Li-190sz, Li-Cor, Lincoln, Nebraska, USA
Wet and Dry Bulb Temperature (at 1.2h and on the forest floor)	Ventilated pyschrometers	Micro-met. lab., I.E.R.M., Edinburgh University, EH9 3JU*
Soil Heat Flux, G	Soil heat flux plates	HFT-1, (Radiation and Energy Balance Systems), supplied by Campbell Scientific Inc., Logan, Utah, USA
Air Temperature	Thermistor (shielded)	SKH103, (MP-100, Rotronic), Campbell Scientific Inc., Logan, Utah, USA
Relative Humidity	Capacitance humidity probe (shielded)	

Table 3.2.5 Measurements made and instrument types used in field weather station.

The weather station instruments were logged continuously with either CR21X or CR10 micro-loggers with an AM-416 multiplexer, (Campbell Scientific Inc.,

* Dry bulb temperature was measured by a platinum resistance thermometer , and the difference between wet and dry bulb temperatures by two differential thermocouples. Air was drawn over the sensors by a small fan to fully aspirate them.

Logan, Utah, USA). The net radiometer was only operated in conjunction with the eddy covariance instruments. A large proportion of the measurements made with the net radiometer were of no value due to a suspected error in the logging software, resulting in only a few days of reliable net radiation data, (e.g.: J199, 1990; J205, 1990; and J207, 1991). A smaller amount of data was also lost from the psychrometer for a similar reason.

The cup anemometer was calibrated in the departmental wind tunnel. The platinum resistance thermometer and thermocouples in the psychrometer were calibrated in a water bath. The pyranometer and I_P sensor and temperature and humidity probe were all new instruments and the manufacturers calibrations were used. The wind vane response was checked for voltage response at different angles and was found to be accurate to within one or two degrees. The net radiation sensor was sent for re-calibration to the manufacturer in 1985 and, as no standard of net radiation was available for comparison, this calibration factor was used unverified. The soil heat flux plates were calibrated by my colleague D.J. McCafferty for a related study in a sand box following the procedure of Biscoe *et al.* (1977).

3.2.6 Data Set Durations and Instruments Deployed

Details of the experimental runs from which data are to be presented in this thesis are given in Table 3.2.3. At the three heights the presence of 3-d sonic anemometers ("*uvw*"), fast response temperature sensors ("*Temp.*") and infra red gas analysers measuring CO_2 or CO_2 and H_2O ("*IRGA*") are indicated by codes denoting the various instruments. Data runs will be referred to by the Julian day and year of measurement throughout i.e. 2nd February would be J33.

3.2.7 Data Contamination and Cleaning

Subsequent to the 1991 field campaign, the PCL-714 A/D board was found to intermittently record spurious voltage values rather than the actual analogue voltage signals. On some occasions the spurious values were either 0 V, ± 2.5 V or ± 5.0 V, while at other times other intermediate voltage values were recorded as well. The recording of the 0, ± 2.5 or ± 5.0 V values with high precision indicated a problem in the digital electronics of the board. In data sets where the corrupt points were either 0, ± 2.5 or ± 5.0 V, cleaning routines were written which searched for these precise values. When the values occurred more than three standard deviations away from the mean they were replaced by the mean of the preceding and the following points. These files were almost entirely recovered; however, the power spectra of

instrumental signals suffering this corruption show white noise up-turn in the high frequency region, (Chapter 6). For files which had the worst contamination, no such cleaning could be carried out. This data was discarded for spectral analysis purposes but it was found that it could be filtered with a software low-pass filter and could be used for eddy flux calculation. As the co-spectra of unaffected data show, sections 6.2.2 and 6.3.2, there is negligible eddy flux component above the canopy at frequencies greater than 1 Hz. Thus corrupted files were low-pass filtered with a software filtering program with a cut-off frequency of 1 Hz before being used for flux calculation with the EDDYQ program. Fortunately this applied to a very small body of data affecting only J195, 1990.

Julian Day	Hours of Data	1.2*h* (ABOVE CANOPY)			0.7*h* (CROWN)		0.1*h* (FOREST FLOOR)		
		uvw	*Temp.*	*IRGA*	*uvw*	*Temp.*	*uvw*	*Temp.*	*IRGA*
1990									
J195	7	KD	CA27	AS#0 ADCF ADCS					
J199-J201	48	KD	CA27	ADCS					
J205-206	43	KD	CA27				S20	S20T	ADCS
1991									
191	8.5	KD	CA27	AS#1 L6252					
198	7.5	KD	CA27	AS#1 L6252			S12	S12T	AS#2
207	8.5	KD		AS#1 L6252	S34	S34T	S12	S12T	AS#2
213	4	KD	CA27	AS#1	S34	S34T	S12	S12T	

Instrument codes :

KD : Kaijo Denki WA-200 3-d sonic anemometer.
S12 & S34: Solent A1002R 3-d sonic anemometers, serial numbers 12 & 14, where S12T and S34T denote sonic temperature measurements.
CA27 : Campbell Scientific CA27T fast response thin wire thermocouple.
AS#0 : Advanced Systems E009 open path IRGA (CO_2 and H_2O), (old model).
AS#1 & AS#2 Advanced Systems E009a open path IRGA (CO_2 and H_2O), (new model).
ADCF : Prototype WA468 (I) ADC closed path IRGA (CO_2 and H_2O).
ADCS : ADC 225 Mk. III laboratory IRGA (CO_2 only).
L6252 : Licor Li6252 closed path IRGA (CO_2 only).

Table 3.2.3 Details of data run durations and instrument arrays.

A portion from one 30 minute file from J195, 1990 is shown in Figure 3.2.14 for the ADC 225 Mk. III CO_2 response. The file contains the worst type of corruption found from the A/D board, and filtering was the only option in this case. The 1 Hz low-pass filtered voltage signal is shown in Figure 3.2.15; eddy fluxes were subsequently calculated from this data set.

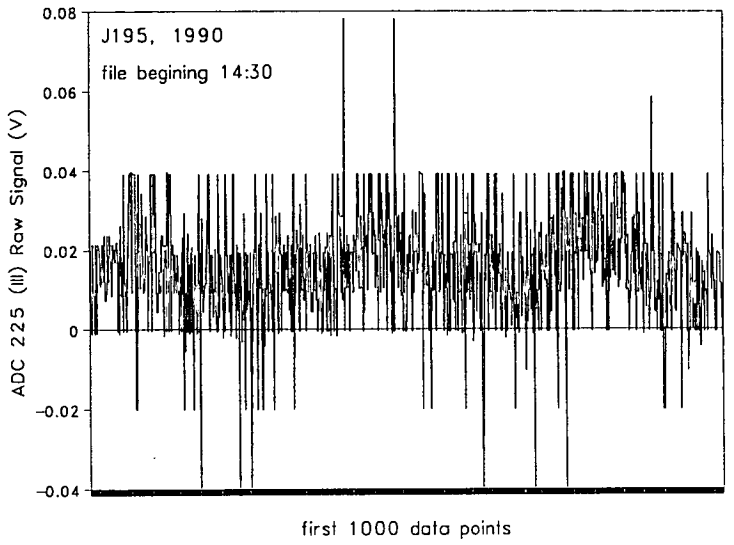

Fig. 3.2.14 Raw CO_2 voltage signal of the ADC 225 Mk. III from J195, 1990. The first 1000 points of the 30 minute file, beginning 14:30, are shown.

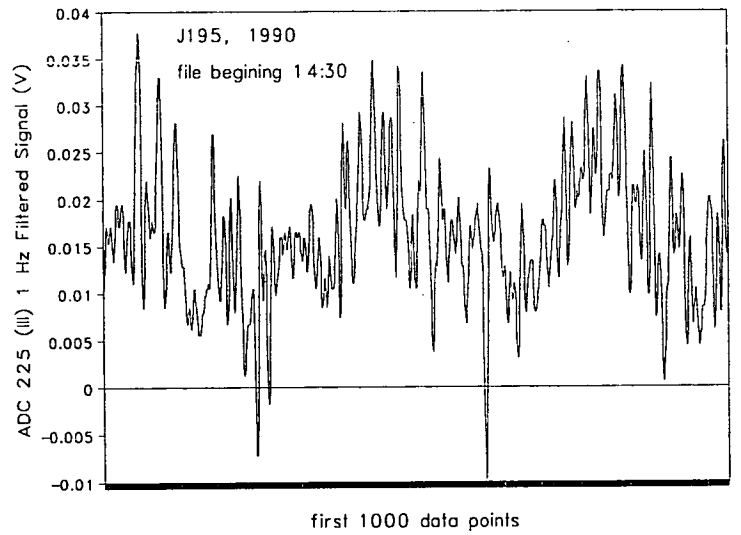

Fig. 3.2.15 CO_2 voltage signal of the ADC 225 Mk. III from J195, 1990 after 1 Hz low-pass filtering. The first 1000 points of the 30 minute file, beginning 14:30, are shown.

Figure 3.2.16 shows the effect of the filtering on the ADC 225 Mk. III CO_2 flux (uncorrected for WPL effects and for transfer functions adjustments). A linear regression between the raw data and the filtered data results in a relationship with slope 0.922 (s.e. 0.05) and constant 0.01 (s.e. 0.05) with an R^2 of 0.975. This demonstrates the relative insensitivity of the eddy covariance technique to noisy instrumentation, and fluxes can still be calculated accurately as long as vertical velocity fluctuations are not correlated with the noise signal.

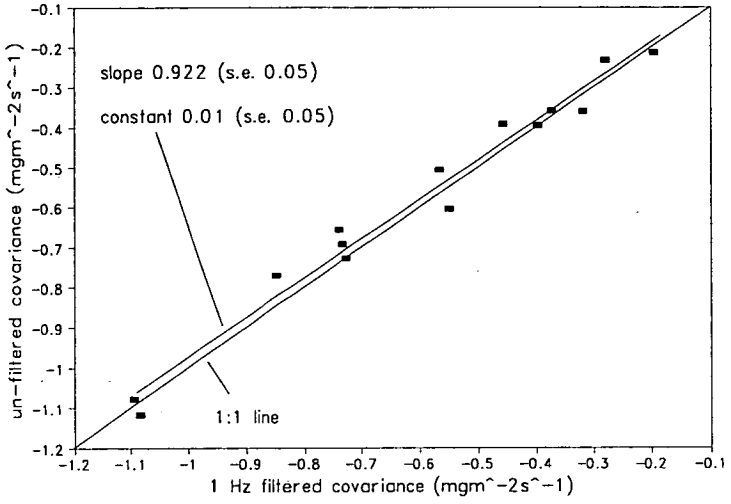

Fig. 3.2.16 Comparison of uncorrected CO_2 covariance from the ADC 225 Mk. III on J195, 1990, for file beginning 11:30, for unfiltered and 1 Hz low-pass filtered case.

3.3 DATA ANALYSIS

All data analysis was carried out in the laboratory after the field experiments. Several computer programs have been developed by myself and my colleagues J.B Moncrieff and J.M. Massheder, over several years. The concepts and algorithms employed in the analysis routines will be described by means of flow diagrams and examples. ~~Some of the programs and units discussed here are listed in Appendix A.3~~.

3.3.1 Eddy Fluxes and Turbulence Statistics

3.3.1.1 Program Structure

All eddy covariance data were analysed with a program with the generic name EDDYQ which was written in Turbo Pascal, on an IBM compatible PC. The program

reads in the data from the original data files, calibrates it, removes trends with a digital recursive filter, as described in section 2.3.3, calculates running means which are used to calculate fluctuations from each data point, and builds up the statistics from these fluctuations which are, finally, written to a data file for future analysis.

The structure of the Turbo Pascal program EDDYQ1_1.PAS is shown schematically in Figure 3.3.1. (The listing of the program is not included in this thesis). Calls to procedures outside the main body of the program in Turbo Pascal Unit files, (hereafter referred to as TPU files), are indicated in the flow diagram. ~~These TPUs can also be found in Appendix A.2.~~

The program was designed to perform two tasks: to produce eddy fluxes from raw data files with all calibrations and co-ordinate rotations applied; and secondly to carry out Quadrant analysis on the same data files. Each task will be described in turn. At each stage of development, the eddy flux output of the program was tested against an earlier version which incorporated the same algorithms and had itself been tested against an independent flux calculation program during the FIFE experiment in Kansas, 1989, (J.B. Moncrieff, personal communication).

The first loop of the program calculates the eddy fluxes and the second loop, which is optional, deals with the quadrant analysis. In the first loop, data is input and calibrated and then the fluctuating component of each measurement is calculated by use of a running mean or digital recursive filter, section 2.3.3. These fluctuations are summed and covariances are accumulated until the end of a data file is reached; they are then averaged to give a 30 minute eddy flux. These covariances are formed into a tensor or matrix of the form:

$$\begin{pmatrix} \overline{u'u'} & \overline{u'v'} & \overline{u'w'} & \overline{u'T'} & \overline{u'\rho'_{CO_2}} & \overline{u'\rho'_{H_2O}} & \overline{u'\rho'_{misc1}} & \overline{u'\rho'_{misc2}} \\ \overline{v'u'} & \overline{v'v'} & \overline{v'w'} & \overline{v'T'} & \overline{v'\rho'_{CO_2}} & \overline{v'\rho'_{H_2O}} & \overline{v'\rho'_{misc1}} & \overline{v'\rho'_{misc2}} \\ \overline{w'u'} & \overline{w'v'} & \overline{w'w'} & \overline{w'T'} & \overline{w'\rho'_{CO_2}} & \overline{w'\rho'_{H_2O}} & \overline{w'\rho'_{misc1}} & \overline{w'\rho'_{misc2}} \end{pmatrix} \quad (3.3.1)$$

Thus the Reynolds stress covariance is given by the matrix elements [1, 3] and [3, 1] and the CO_2 flux is given by [3, 5]. This matrix is passed into the co-ordinate rotation sub-routines, (Appendix A.2), and a matrix of rotated elements in the same format as equation 3.3.1 is returned to the program and output as the final eddy fluxes.

If quadrant analysis is to be carried out on a file, the above procedure is repeated only with each fluctuation individually rotated using the rotation angles from the flux calculation loop. These rotated fluctuations are sorted into quadrants and probability bins, as indicated in section 3.3.2, and stress fractions and probability

densities are built up for the 30 minute file. At the end of a file, the stress fractions and probabilities are averaged, normalised and then output.

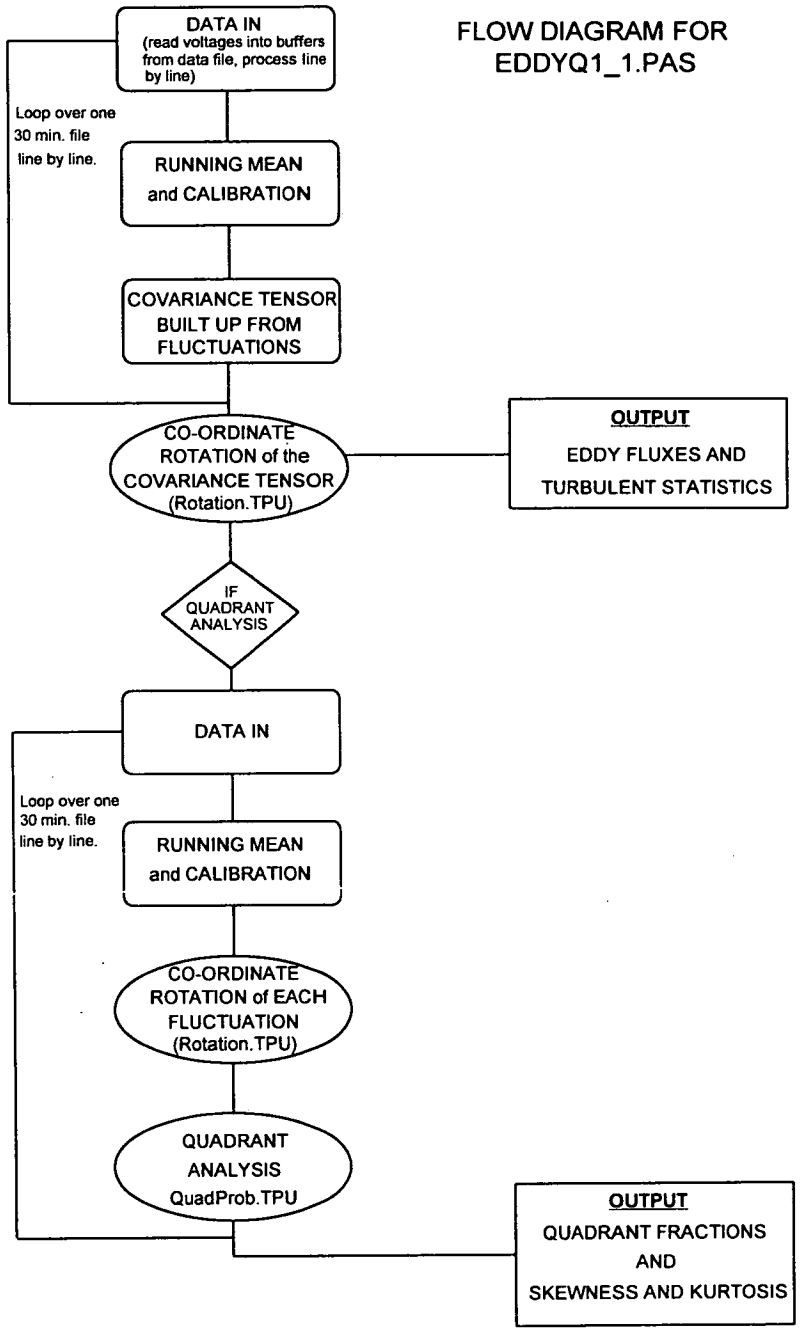

Fig. 3.3.1 Flow diagram for EDDYQ1_1.PAS, where oval boxes denote calls to TPUs.

3.3.1.2 Digital Recursive Filter Time Constant

A time constant of 200 s was chosen for the digital recursive filter, as the limit for significant contributions to variances and covariances is ~ 1/200 Hz from spectral analysis, Chapter 6. Other researchers have chosen time constants ranging between 100 and 1000 s depending on their instruments, logging capabilities and site terrain. McMillen (1986) found that Reynold's stress values calculated with time constants between 160 and 640 s were very similar and thus that the flux calculations were relatively insensitive to the value of the time constant. The change in values of velocity variances and various covariances with differing time constants are shown in Figures 3.3.2 and 3.3.3. All variances and covariances are shown normalised by their value with a 200 s time constant. The covariances are seen to be relatively insensitive to the value of the time constant with losses of only about 1 % between 200 - 1000 s filter calculations, Figure 3.3.3. Similarly, for w variance in the range 200 - 1000 s, losses are less than 0.5 %. However, the horizontal velocity variances have a peak response around ~ 450 s, probably due to the larger scale motions in the horizontal flow compared with the vertical flow, and show a loss of ~ 3 % at the 200 s value. It is important to remember, however, that these losses will be corrected for by the application of the transfer function for a digital recursive filter, as discussed in section 2.3.

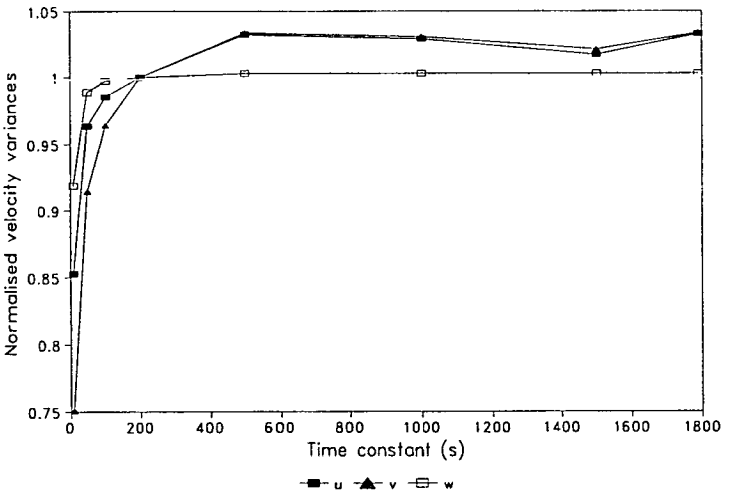

Fig. 3.3.2 Normalised u, v and w velocity variances at $1.2h$ above Rivox forest for several digital recursive filter time constants. Variances are normalised by the value when the time constant is 200 s.

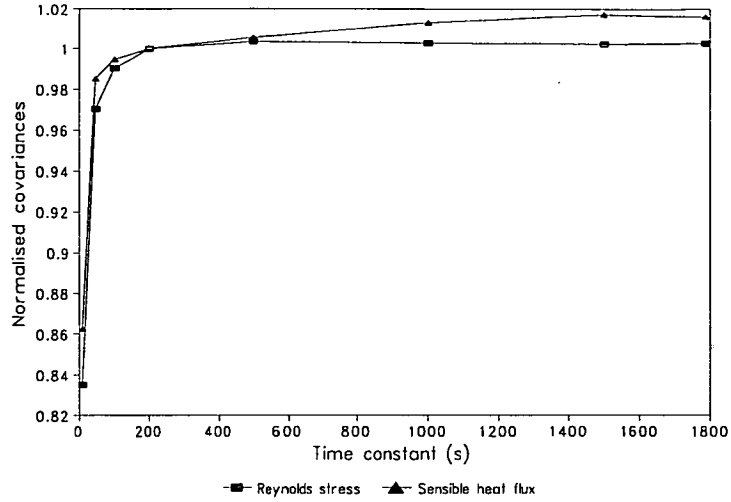

Fig. 3.3.3 Normalised Reynolds stress and sensible heat flux at 1.2*h* above Rivox forest for several digital recursive filter time constants. Covariances are normalised by the value when the time constant is 200 s.

3.3.1.3 Closed Path IRGA Delay

When processing data from closed path IRGAs a delay is introduced into the IRGA signal, relative to the *w* signal, (or other *in situ* measurements), as a result of sampling the air down a tube. The delay can be calculated either by an arithmetic correlation algorithm or a spectral FFT correlation routine (section 2.1.4). Both approaches were used and agreed well, generally giving distinct correlations between the IRGA CO_2 signal and an independent *in situ* signal (i.e. open path CO_2, temperature or *w*). A typical cross-correlation between a closed and open path CO_2 sensor above the forest is shown in Figure 3.3.4.

The largest delays occurred for the IRGAs housed in the hut where the tube length was about 57 m. For example, the Li6252 with a flow rate of 4.5 l min^{-1} typically had a peak correlation occurring at 327 samples, Figure 3.3.4, which at a sample rate of 18.2 Hz represents a delay of 18.0 s. This lag value might have been expected to change slightly with atmospheric stability, however all our data was collected in near neutral conditions and the lag values varied very little during our experimental runs.

3.3.1.4 Co-ordinate Rotation of Velocity Components

The co-ordinate rotation procedure is outlined in Appendix A.2 and is required to correct for any streamline distortions at the site and for calculation of the true vertical fluxes from the surface, (McMillen, 1986; Baldochhi *et al.*, 1988). Above the forest

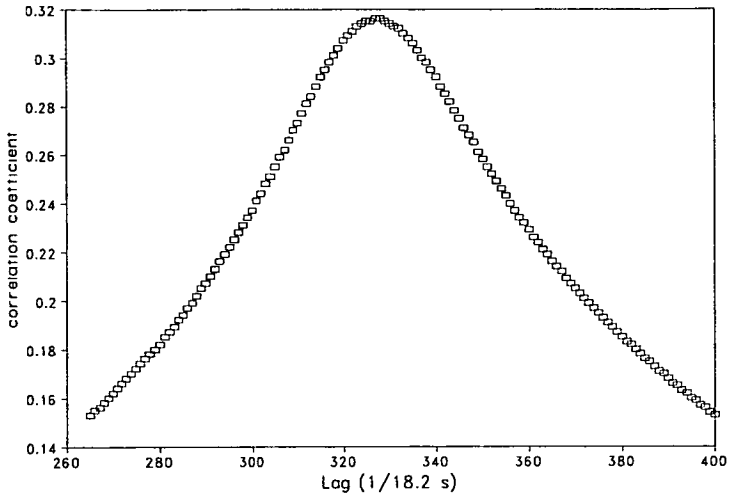

Fig. 3.3.4 Cross-correlation between the CO_2 signals of the closed path Li6252 and the open path E009 (#2) IRGAs on J207, 1991 at 1.2*h* above Rivox forest.

three rotations were performed: the first rotation being about the *z* axis, aligning the *u* velocity with the mean horizontal wind direction (i.e. forcing *v* to zero); the second rotation being about the *v* axis and aligning *u* into the mean wind vector such that $\overline{w} = 0$; and the third rotation being about the *u* axis and iteratively minimising the tangential momentum stress $\overline{v'w'}$. Above the canopy, the Reynold's stress decreases as each of these rotations is performed, i.e. the momentum flux to the surface is maximised as is expected if the rotation scheme is valid. At a flat, uniform airfield site McMillen (1986) observed Reynolds stress values change sign from positive to negative under application of the co-ordinate rotations described. The effect of the three rotations on Reynolds stress at our site on day J208 is shown in Figure 3.3.5, with the Reynolds stress becoming more negative with the last two rotations. This is a strong indication that the rotations are necessary and are working properly.

3.3.2 Quadrant Analysis

The quadrant analysis was carried out with the EDDYQ program earlier, as discussed. Flux fractions for momentum, sensible heat and CO_2 can be constructed for the four quadrants for a range of hole size bins or merely for a 'normal' and 'extreme' case as discussed in section 2.1.3. (From section 2.1.3 hole size, *H*, is given by the instantaneous momentum covariance divided by the period mean momentum flux, i.e. $H = \left| u'w' / \overline{u'w'} \right|$). Thus, if we consider momentum flux above the forest canopy, we

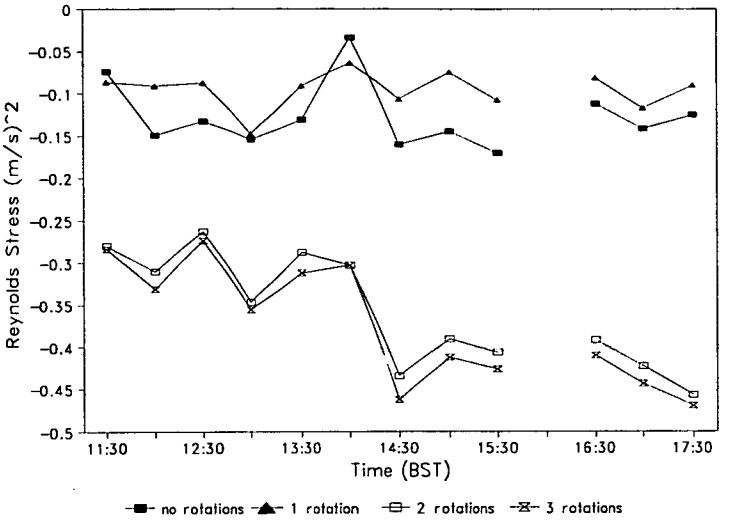

Fig. 3.3.5 Reynolds stress values with no rotations, one, two and three rotations for a Kaijo Denki 3-d sonic anemometer at 1.2*h* above Rivox forest for J208, 1991.

can postulate that an 'extreme' event is one that has an instantaneous Reynolds stress greater than or equal to four times the mean value for the half hour period (section 2.1.6). In the EDDYQ program, individual lines of velocity fluctuations are sorted for each quadrant Q, into an arbitrary number (26) of bins representing different hole sizes (Table 3.3.1). Time fractions are calculated by summing the number of occurrences in each bin and then normalising them by the total number of lines in each analysed file. The momentum fraction is calculated for each bin by summing the instantaneous covariances and than normalising the sum by the mean total flux over the file.

The scalar covariances of temperature and CO_2 with w, associated with each line of velocity data are also sorted into scalar flux fractions in a manner similar to the momentum covariances. Instead of sorting the scalar flux fractions into 26 bins of hole sizes, they are simply sorted into normal ($H < 4$) and extreme ($H \geq 4$) classes.

3.3.3 FFT Spectral and Correlation Analyses

The spectral, autocorrelation and cross-correlation analyses were all carried out with a program made available to me by B.A. Gardiner, (Forestry Commission, Northern Research Station, Roslin, UK). This program performs a fast Fourier transform on a time series block with a maximum size of 2048 data points. The

program written to use this unit is called FFT_ANAL.PAS and a flow diagram indicating the structure of the program is shown in Figure 3.3.6.

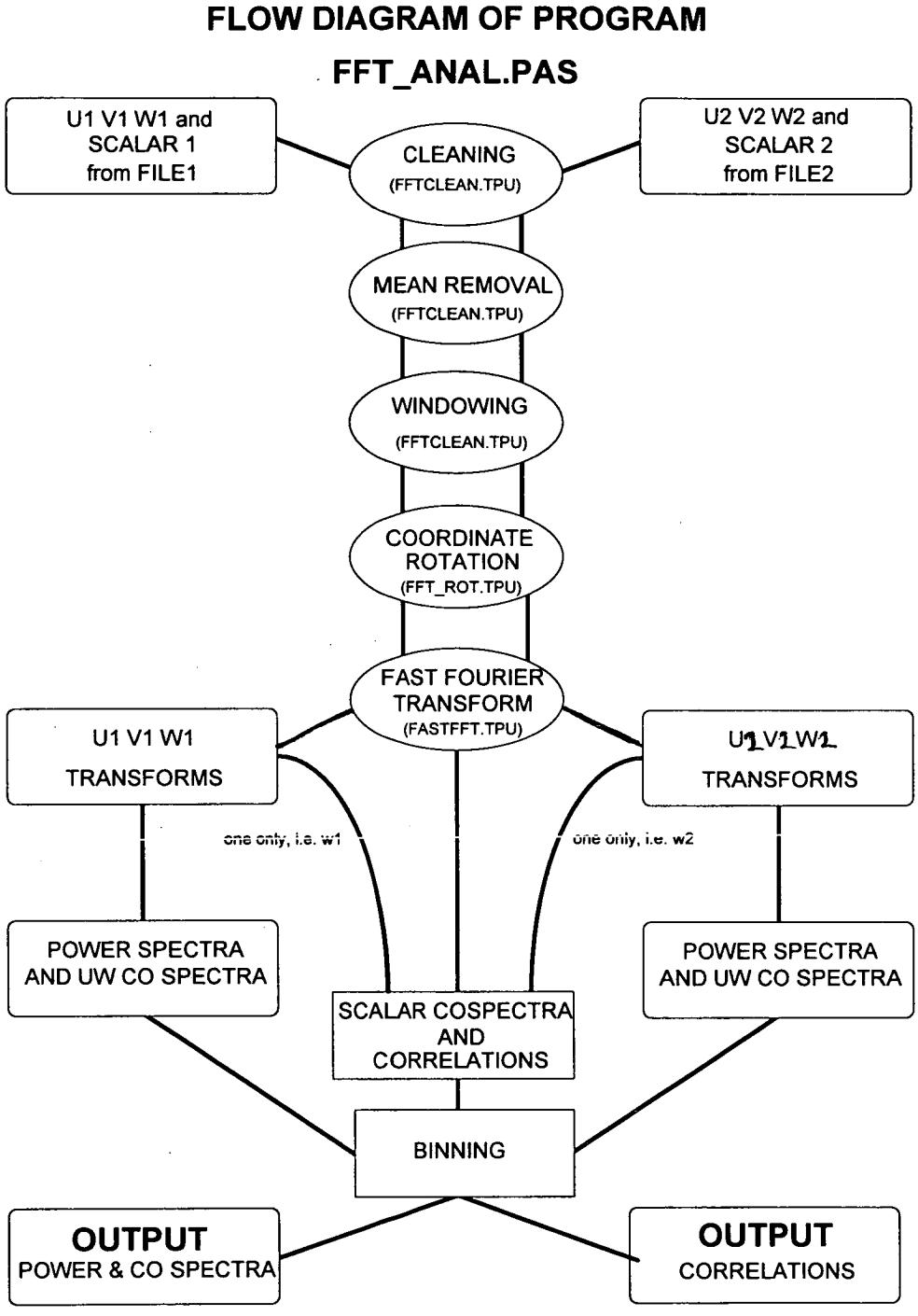

Fig. 3.3.6 Flow diagram for program FFT_ANAL.PAS.

BINS	RANGE
bin 1	$H \geq 0$
bin 2	$H \geq 1$
bin 3	$H \geq 2$
bin 4	$H \geq 3$
bin 5	$H \geq 4$
•	
•	
bin 25	$H \geq 24$
bin 26	$H \geq 25$

Table 3.3.1 Definition of bins for momentum covariance. Bin 1 contains all events, bin 5 contains all extreme events and all normal events are clearly given by subtracting bin 5 from bin 1.

The main limitation on the program is the data point block size of 2048 (2^{11}). Which arises from the limit in Borland Turbo Pascal on the size of any declared structured type which is violated by the next possible block size of 4096, (2^{12}). This block size limitation could cause problems where atmospheric spectral components extended into very low frequencies or when the sampling rate is higher than the 18.2 Hz rate employed here. Problems may also arise in cross-correlation analyses where only events occurring within the 2048 point block are cross-correlated. (At a sample rate of 18.2 Hz, 2048 data points correspond to 112.5 s). This problem could be overcome by altering the program either to operate on lines of data rather than blocks (allowing any length of FFT block) or, possibly, by including block overlapping, whereby the data is analysed block by block with the blocks moving through the file half a block at a time.

The program can obtain two data sets from two separate data files which are associated with particular sonic anemometers. Thus each data set has u, v and w values and an associated scalar channel, e.g. CO_2 or temperature. Each of the two data sets are operated on by four procedures before being Fast Fourier Transformed. The 'cleaning' operation in the flow diagram refers to a procedure which searches data files for corrupted data, (0, ± 2.5 and ± 5 V values only, as discussed in section 3.2.6). The 'mean removal' procedure acts on each channel in each block and simply subtracts the channel's block mean from each point, such that the mean of the resulting series

equals zero. This procedure removes any trends in the series with time. Spectral 'windowing' is carried out on all data series that are to be transformed. The purpose of the windowing is to reduce spectral leakage away from distinct spectral peaks in the data (Press *et al.*, 1989). As our spectral responses are relatively smooth, the effect is minimal but it is generally good practice in any spectral analysis. The window function takes the form of a series identical in size to the time series. The windowing is carried out by simply multiplying each time series point by the corresponding window series point. Several window functions are commonly used, the choice of function depending on circumstance. Three such window functions for a series of N points where $j = 1$ to N are given by, (Press *et al.*, 1989):

$$w_j = 1 - \left| \frac{j - 0.5(N-1)}{0.5(N+1)} \right| \equiv \text{'Parzen window'} \qquad (3.3.2)$$

$$w_j = 1 - \left(\frac{j - 0.5(N-1)}{0.5(N+1)} \right)^2 \equiv \text{'Welch window'} \qquad (3.3.3)$$

$$w_j = 0.5\left[1 - \cos\left(\frac{2\pi j}{N-1} \right) \right] \equiv \text{'Hanning window'} \qquad (3.3.4)$$

Where a '*square*' window is often defined as $w_j = 1$, i.e. the equivalent of no window at all. These four windows are shown graphically in Figure 3.3.7.

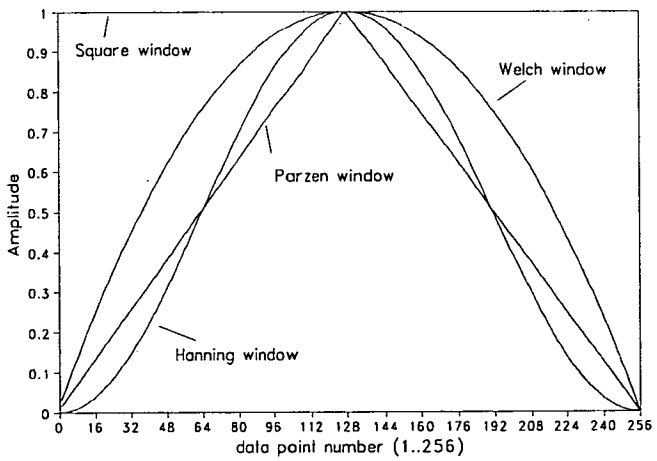

Fig. 3.3.7 Four types of commonly used window functions with amplitudes w_j, for a series with $j = 1$ to 256 points, (after Press *et al.*, 1989).

The window used in all our spectral analyses was the Parzen window, but in fact no discernible differences arose from tests using any of the equations 3.3.2 to 3.3.4 and only very small differences resulted from using a square window.

The effect of the window on the series power spectral density must be corrected by normalising the densities by the sum of the squared amplitudes, W_{ss} where:

$$W_{ss} = N \sum_{j=0}^{N} w_j^2 \qquad (3.3.5)$$

The next step in the program is for the *uvw* data blocks from the sonic anemometer to be co-ordinate rotated. The number of rotations is either none, one, or two, and they are performed line by line through the data blocks. In practice, no rotations were performed on below canopy data and two rotations were performed on above canopy data. The limit on processing memory in the program did not allow the full three co-ordinate rotations to be carried out as the third rotation includes an iteration minimising $\overline{v'w'}$. However, as can be seen from Figure 3.3.5 the final rotation has little effect on the magnitude of the calculated momentum flux and, with respect to power or co-spectra the shape and form are unchanged.

After the velocity components and the scalar components have been Fourier transformed, the power spectral densities, co-spectral densities, and correlation coefficients are built up. All co-spectra are formed from one data set, i.e. the scalar fluxes will be covariances between *w*1 and *scalar*1 and *w*2 and *scalar*2. The correlations are formed across the data sets, with both a velocity and a scalar cross-correlation being output. If *file*1 and *file*2 are the same, then the cross-correlations become autocorrelations.

All final output series are logarithmically binned to smooth the log plots of the spectra or correlations. The frequencies, n_j, represented in the spectral output extend over the range:

$$n_j = n_s\left(\frac{j}{2m}\right) \quad \text{where } j = 1 \text{ to } (m-1) \qquad (3.3.6)$$

Where n_s is the sample rate in Hz, $2m$ is the number of points in the FFT block (i.e. 2048). Thus in our case: n_s = 18.2 Hz, $2m$ = 2048 and thus n_j = 8.887 × 10^{-3} to 9.091 Hz in steps of 8.887 × 10^{-3} Hz.

The very lowest frequency components are not averaged over logarithmic intervals as a few data points may span several decades. The frequencies n_j up to $j = \text{trunc}(0.01m)$, where *trunc* returns an integer, are chosen not to be binned, i.e. for

the above case j = 1 to 10, thus frequencies, n_j = 8.887 × 10^{-3} to 0.098 Hz in steps of 8.887 × 10^{-3} Hz, are left unbinned.

An example of the logarithmic binning is shown in Figure 3.3.8 for a u velocity power spectrum plotted as the normalised spectral density, $nS(n)/\sigma_u^2$, against n for the unbinned and binned cases.

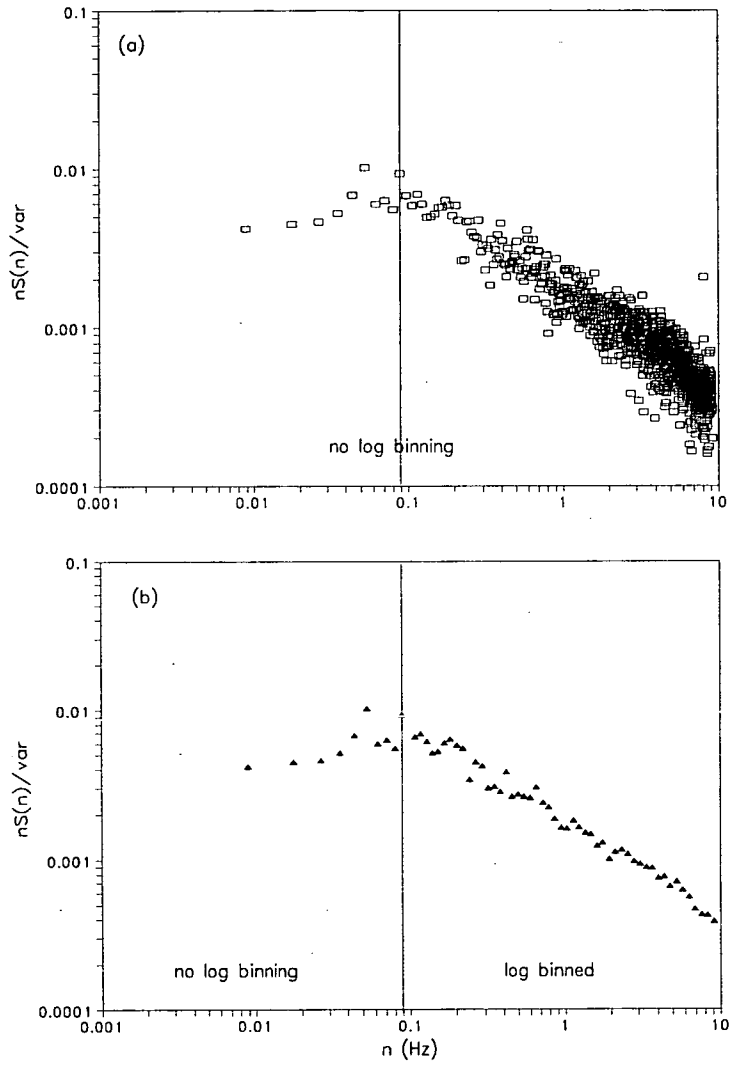

Fig. 3.3.8 Normalised power spectral density for u velocity at 1.2h above Rivox forest on J191, 1991, where *var* is the u variance. The spectral densities are unbinned in (a) and the high frequency spectral densities are binned in (b).

The program is designed to loop through a data file performing as many 2048 point FFTs as possible, averaging the spectral densities and correlation coefficients,

logarithmically binning the results and then outputting them. All spectral and correlation outputs presented in this thesis are averages of the outputs of several 30 minute files which have been produced in this way. Typically ~ 8 files were averaged together, with each one of these files already being an average of fifteen FFT segments. Consequently, each spectral or correlation plot typically contains information from ~ 120 separate Fast Fourier Transforms.

3.3.4 Numerical Integration of Co-spectral Functions

The transfer function corrections discussed in section 2.3 were summarised in equation 2.3.1, viz.:

$$\frac{\Delta F_c}{F_c} = 1 - \frac{\int_0^\infty T_{w\rho_c}(n) C_{w\rho_c}(n) \mathrm{d}n}{\int_0^\infty C_{w\rho_c}(n) \mathrm{d}n} \qquad (2.3.1)$$

Where $T_{w\rho_c}(n)$ is the convolution of all transfer functions applicable to the measurement and $C_{w\rho_c}(n)$ is a typical co-spectral response for the flux F_c. The form of the total transfer function, $T_{w\rho_c}(n)$, was discussed in detail for two systems in section 2.3.10 and the co-spectral function in section 2.3.11. In practical terms, an exact, analytical integration of the terms in equation 2.3.1 is not feasible and thus we must turn to a numerical integration method. The method of numerical integration of relatively smooth functions with no singularities in the function or endpoints recommended by Press *et al.* (1989), is the Romberg method. A program called was constructed around the routines supplied from Press *et al.* (1989), with all the relevant transfer functions and co-spectral models included as functions. The fractional error limit for the numerical integration was set at 1×10^{-6} in the program; when this level of accuracy is achieved, the function evaluations cease. All functions and integrations are carried out in the natural frequency domain rather than normalised frequency. The Kaimal *et al.* (1972) functions are formulated in terms of natural frequency f, where $f = n(z-d)/\overline{U}$ so ranges of values of (z - d) and $\overline{U}$ are used to produce integrations for the desired field conditions. Integration limits were chosen as $n = 10^{-4}.\overline{U}/(z-d)$ to $10.\overline{U}/(z-d)$ which, from the co-spectral data, adequately covers the significant frequencies observed in the field.

The output from this program was verified by integrating numerically functions which could be integrated analytically over discrete limits. For instance, if

we take the function from Kaimal *et al.* (1972) for the covariance ($\overline{w'T'}$) in unstable conditions, i.e. equation 2.3.39:

$$nC_{w\alpha}(n) = \frac{a_{w\alpha} f_k}{[1+b_{w\alpha} f_k]^{c_{w\alpha}}}, \qquad (2.3.39)$$

where $f_k = n(z-d)/\overline{U}$. If we consider the case where $a_{w\alpha}(z-d/\overline{U})$ and $b_{w\alpha}(z-d/\overline{U})$ equal 1 and $c_{w\alpha} = 2$ the function $C_{w\alpha}(n)$ is given by:

$$C_{w\alpha}(n) = \frac{1}{(1+n)^2} \qquad (3.3.7)$$

Thus if we assume $\overline{U}$ = 3 m s^{-1} and (z - d) = 5 m, then the limits of integration from above will be n_1 = 0.6 × 10^{-4} Hz and n_2 = 6 Hz. The analytical solution of the integration is:

$$\int_{n_1}^{n_2} C_{w\alpha}(n)\,dn = \int_{n_1}^{n_2} \frac{dn}{(1+n)^2} = \left[-\left(\frac{1}{1+n}\right)\right]_{n_1=0.6\times10^{-4}}^{n_2=6} \qquad (3.3.8)$$

$$= 0.8570828 \text{ W m}^{-2}$$

Numerically integrating the function with the program yields the result:

$$\int_{n_1}^{n_2} C_{w\alpha}(n)\,dn = 0.8570830 \text{ W m}^{-2} \qquad (3.3.9)$$

As can be seen the analytical and numerical results are effectively identical.

CHAPTER 4.
CARBON DIOXIDE AND ENERGY EXCHANGES IN THE FOREST SYSTEM

4.1 INTRODUCTION

Our aim in making flux measurements is to understand the forest atmosphere interaction and, specifically, to understand how environmental variables control the exchange of heat, mass and momentum. Carbon exchanges between the atmosphere and northern hemisphere coniferous forests are currently of particular interest as there is a shortage of studies reported in the literature (Jarvis, 1993). Measured CO_2 fluxes require supporting measurements of water vapour fluxes (latent heat flux) and sensible heat fluxes so that they can be correctly adjusted for WPL density effects (Webb *et al.* (1980).

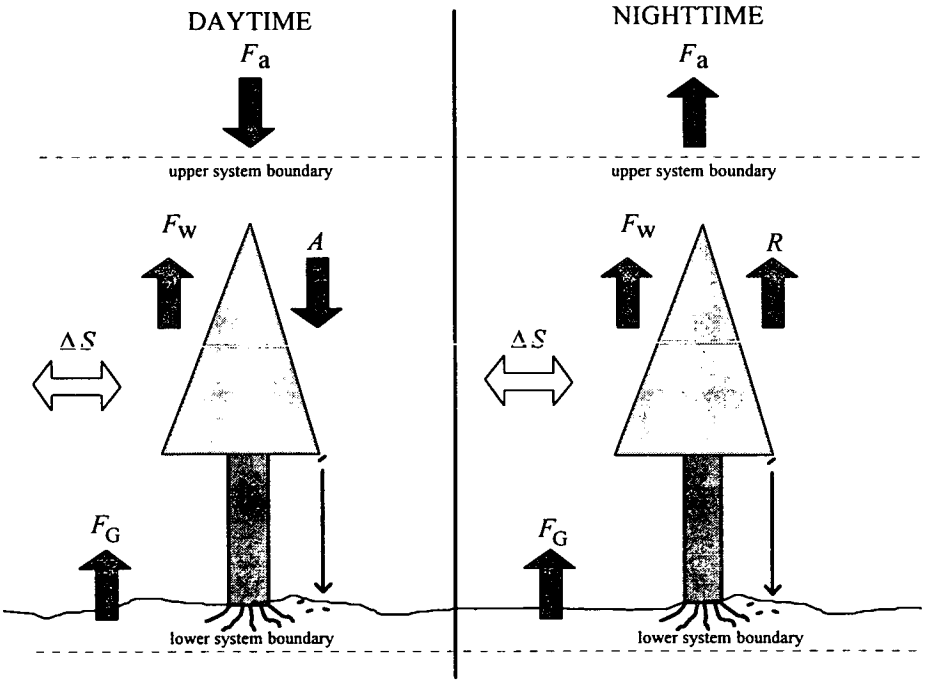

Fig. 4.1.1 Diagram showing the main CO_2 fluxes in a simple forest system. Where F_a is the net CO_2 flux across the upper boundary; F_W is the respiratory flux from the wood; F_G is the respiratory flux from the soil and the roots; A and R are the net assimilation and respiratory exchanges of the leaves; and ΔS is the change in storage of CO_2 in air within the system. (After Jarvis, 1987).

Fluxes of CO_2 measured by eddy covariance above the forest represent net exchange of CO_2 between the forest ecosystem and the atmosphere. Such stand scale measurements are of great interest to those who are attempting to model forest stand contributions to local or global CO_2 exchanges. This exchange includes the assimilation and respiration of the trees, the respiration of soil micro-organisms, root respiration, changes in CO_2 storage in the air with time, respiration from animals dwelling in the forest ecosystem etc. The major flux terms in a simple forest system are shown schematically in Figure 4.1.1 for a forest with no under-storey.

Respired CO_2 from soil organisms and roots is a net source of recycled CO_2 to the trees in the daytime (directly from the roots, and via breakdown of leaf litter by soil organisms), and both processes result in a loss from the stand at night (Jarvis, 1993). By day, these inputs reduce the uptake, F_a, of the stand across the upper system boundary. If we assume a combined assimilation/respiration response from the trees, we can define a net sink into the trees, or net assimilation by the canopy as $F_{A/R}$, where - $F_{A/R}$ represents assimilation, A, and + $F_{A/R}$ respiration, R. From Figure 4.1.1 we can see that in the short term this assimilation/respiration flux is related to the net flux across the system boundary, F_a, the wood, soil respiration and storage terms, F_G and F_W and the change in storage in the air within the system, ΔS, as:

$$F_{A/R} = F_a - (F_W + F_G) \pm \Delta S. \qquad (4.1.1)$$

(Where the meteorological convention for F_a and F_G is preserved such that downward fluxes are negative).

The degree of cycling of CO_2 within the system between respiration and assimilation processes is not clearly understood. A better understanding of these processes would, for instance, give us an insight into the relationship between timber production and atmospheric CO_2 removal. It is also presently of great interest to obtain accurate carbon budgets for forests in the present environment, so that we can model the response of the forests to increased atmospheric CO_2 levels in the future (Jarvis, 1993).

The data periods analysed and presented here were chosen because they included several days of continuous measurements, when the weather was fine and the wind direction was favourable. In addition to reporting the mass and radiation fluxes for the data periods in section 4.3 and 4.4, details of corrections to the calculated fluxes are also discussed in section 4.2. This section includes discussion of transfer function corrections, WPL corrections and possible errors in the flux estimates arising from changes in storage of CO_2, sensible and latent heat in the canopy. The response of the calculated CO_2 flux above the canopy to photosynthetically active photon flux (I_P), air temperature (T_{air}) and vapour pressure deficit (D) is discussed in section 4.5.

4.2 FLUX CORRECTION SCHEMES

As described earlier, the 'raw' scalar flux values, obtained from the analysis software EDDYQ (section 3.3.1), were corrected in a spreadsheet program for the WPL density effects, including corrections for CO_2 signal cross-sensitivity to water vapour (sections 2.2.2 and 3.2.4), and for frequency losses with appropriate transfer function corrections (section 2.3). Calculated fluxes from the CO_2 intercomparison experiment, section 3.2.4, are shown to illustrate the typical effect of these corrections

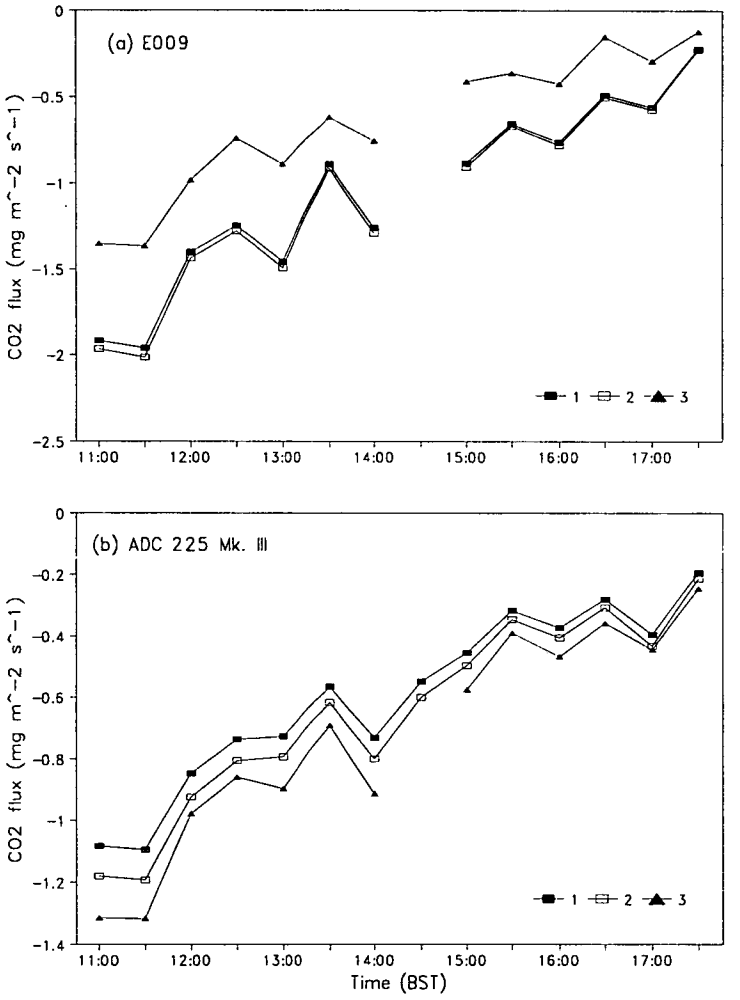

Fig 4.2.1 Effect of applying corrections to simultaneously measured raw CO_2 fluxes (J195, 1990), from (*a*) open path (E009) and (*b*) closed path (ADC 225 Mk. III) IRGAs. Where (1) is raw CO_2 flux, (2) is with transfer function corrections and (3) is with both transfer function and WPL corrections. Fluxes are half hour means at 1.2*h* on J195, 1990.

on CO_2 fluxes from open and closed path analysers in Figure 4.2.1.

WPL corrections are much larger for the open path analyser as a result of *in situ* temperature fluctuations, i.e. a sensible heat flux in the measuring volume, as discussed in section 3.2.4. On average, the WPL correction to the CO_2 flux, as a percentage of the transfer function corrected flux, was 43 % for the open path analyser and 17 % for the closed path analyser during this intercomparison experiment (J195, 1990). The effect of the WPL corrections was to reduce the apparent CO_2 flux from the open path analyser and to increase the apparent flux from the closed path analyser. The WPL corrections were smaller for the closed path instrument as temperature fluctuations in the air stream were removed in the copper sampling tube and in the constant temperature analyser. However, frequency attenuation in the sample tube results in a larger transfer function correction for the closed path instrument. (The fully corrected fluxes from the two analysers are compared in Figure 3.2.11, section 3.2.4).

4.2.1 Transfer Function Corrections

Transfer function corrections were applied to all above canopy scalar flux data but not to any forest floor flux data. The inability to represent properly scalar co-spectral response in the sub-canopy, and thus to apply transfer function corrections, is discussed in section 6.3.3.

Above the canopy, at $1.2h$, the scalar co-spectra of sensible heat, latent heat and CO_2 were compared to the Kaimal *et al.* (1972) sensible heat co-spectra for unstable conditions, equation 2.3.40. Typical co-spectra are shown in Figure 4.2.2, with the Kaimal *et al.* (1972) sensible heat co-spectra arbitrarily normalised for comparison with the data, (CO_2 co-spectra for the open path sensor only is shown).

The fit to the CO_2 spectral response, shown in Figure 4.2.2, was obtained by fitting the Kaimal *et al.* (1972) function (equation 2.3.39) to CO_2 co-spectral densities from the E009 IRGA at frequencies up to ~ 1 Hz. Three equations in different frequency ranges of the form of equation 2.3.39 gave the best fit to the calculated co-spectral densities. The parameters for the equations are given in Table 4.2.1.

The three scalar co-spectra for H, LE and CO_2 correspond well, up to about $f \sim 2$, ($n \sim 1$ Hz). The rapid roll-off of the scalar co-spectra in the high frequency region is a result of the signal losses predicted by the transfer functions in section 2.3. The ability of the transfer functions to recreate the correct spectral shape is discussed in section 6.3.2.

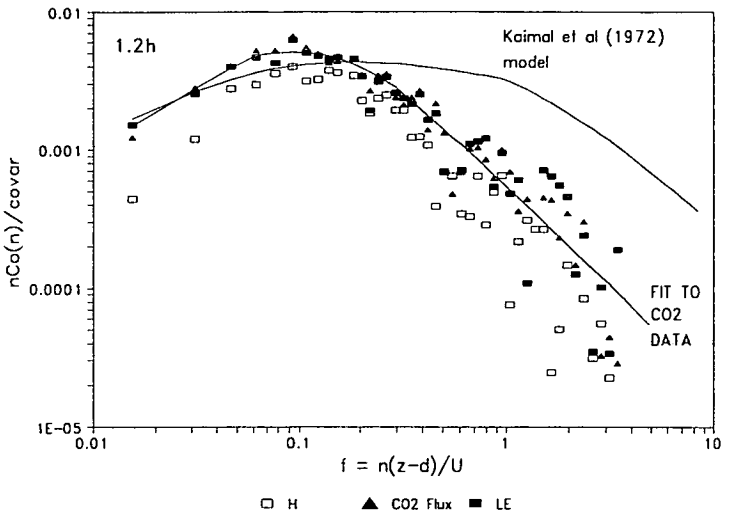

Fig. 4.2.2 Normalised co-spectral densities, $nC_{wx}(n)/\overline{w'\alpha'}$, where α denotes temperature, CO_2 (open path IRGA), or H_2O (open path IRGA), plotted against normalised frequency, $n(z-d)/\overline{U}$, at height $1.2h$. Solid lines are the Kaimal *et al.* (1972) H model co-spectra, and a fit to the CO_2 co-spectral data. [$(z - d) \sim 5.4$ m and $\overline{U} = 3.1$ m s^{-1}].

Normalised Frequency Range $f = n(z-d)/\bar{U}$	a_{wpc}	b_{wpc}	c_{wpc}
0.0144 - 0.0719	0.1117	4.0371	1.3192
0.0719 - 0.2724	0.1873	3.8317	4.0339
0.2724 - 14.68	3.4740	34.5618	2.4826

Table 4.2.1 The fitted parameters for the CO_2 co-spectral data, J207, 1991 at $1.2h$.

Extending the fitted function to the higher frequencies, along the expected -4/3 slope, we see that the responses of the function and of the Kaimal *et al.* (1972) model are somewhat different. The effect of using the Kaimal *et al.* (1972) function in equation 2.3.1 to calculate the appropriate transfer function corrections for the site, compared to using our own co-spectral functions in the numerical integrations, is to overestimate the corrections substantially.

The two situations outlined in section 2.3.10, were:

(*i*) An open optical path IRGA (i.e. E009) with p_l = 0.2 m, with a response time for a change in CO_2 concentration of 0.1 s, and a Solent three component sonic anemometer with p_l = 0.15 m and a response time for changes in wind speed of 0.02 s.

(*ii*) A closed optical path IRGA (i.e. LI-6252), with a response time of 0.625 s, sampled down a tube with radius 2.75 mm, with a travel time t_t = 18 s and a Reynolds number of 1190, and the same anemometer as in (*i*).

The total transfer functions for these situations (see Figure 2.3.9), were integrated, as in equation 2.3.1, for a range of $\overline{U}$ and (z - d) values. Both the Kaimal *et al.* (1972) sensible heat co-spectral model and our own fitted CO_2 co-spectral model were used to approximate CO_2 co-spectral response, $C_{w\rho}(n)$. The different representations of $C_{w\rho}(n)$ gave quite different flux correction factors over the ranges of $\overline{U}$ and (z - d) (see Figure 4.2.3). It is evidently important to represent $C_{w\rho}(n)$ correctly for a particular site with a realistic function if transfer function corrections are not to be over estimated. For a site with (z - d) ~ 5 m and $\overline{U}$ ~ 4 m s^{-1}, the calculated corrections to CO_2 flux using the Kaimal *et al.* (1972) model and the fitted model are: for the open path case (*i*), 6.3 % and 1.4 %, respectively; and for the closed path case (*ii*), 34.5 % and 14.0 %, respectively (Figure 4.2.3).

Transfer function corrections were not applied to fluxes measured at the forest floor as the calculated scalar co-spectral densities were not sufficiently distinct to verify the validity of a suitable function or indeed to fit such a function, (see section 6.3.2).

4.2.2 WPL Correction Schemes

Fully corrected CO_2 and H_2O fluxes were obtained by applying WPL corrections to the transfer-function-corrected fluxes using equations 3.2.19 and 3.2.26. Forest floor fluxes from J205, 1990, could not be corrected fully as no simultaneous water vapour measurements were available. An estimate of the correction was calculated for a constant latent heat flux of 50 W m^{-2}, since this value was not atypical of fluxes at the forest floor on other days. Similarly on J199, 1990 there were no simultaneous *LE* fluxes above the canopy, and values of *LE* were estimated as (R_n - G - H). On J207, 1991 there were no sensible heat flux measurements above the canopy so the closed path LI-6252 CO_2 data is presented rather than the open path E009 data which could not be properly WPL corrected.

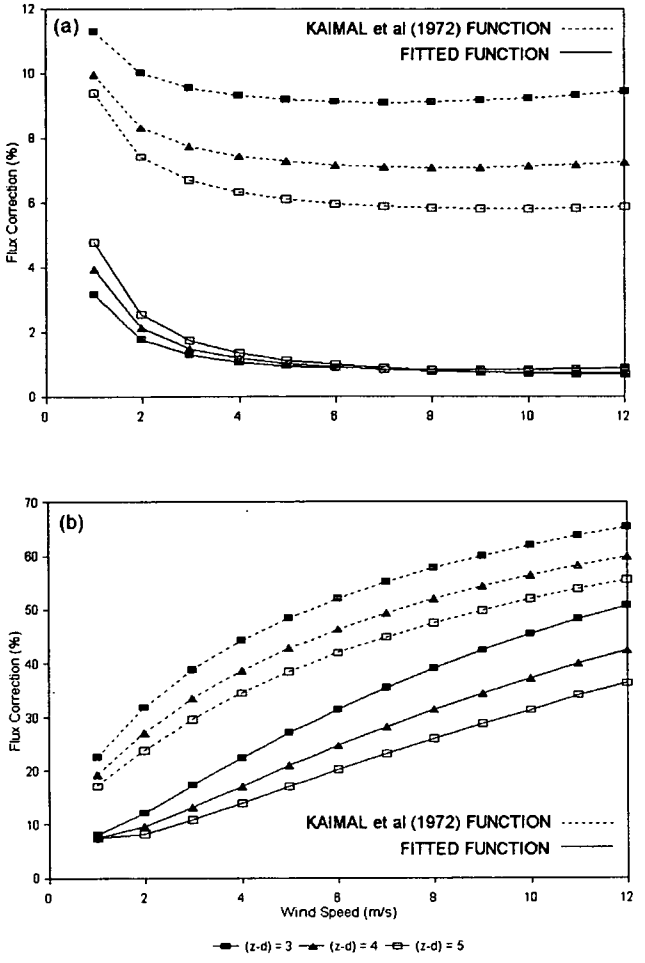

Fig. 4.2.3 Transfer function CO_2 flux corrections ($\Delta F_c / F_c$) as percentages for (*a*) case (*i*) and (*b*) case(*ii*). With $\Delta F_c / F_c$ calculated using both the Kaimal *et al.* (1972) *H* model for unstable conditions, equation 2.3.40, and a fitted model, equation 2.3.39 and Table 4.2.1, to represent CO_2 co-spectral response.

4.2.3 Scalar Storage Considerations

4.2.3.1 Air Volume Storage of CO_2

The change of concentration of CO_2 in the canopy air volume with time represents a possible change in storage of CO_2 in the forest system shown in Figure 4.1.1. Fluxes of CO_2 available for assimilation by the trees cross the system boundaries (F_a or F_G) or are respired into the system (F_W or *R)* and are stored in the canopy air spaces. Estimation of the assimilation rate of the system, $F_{A/R}$, from equation 4.1.1 on a short time scale depend on the change of storage over that short time. In examining the relationship of F_a, which is the quantity that we measured,

with environmental variables, we may treat the whole system, as a big leaf and the effects of the recycling of respired CO_2 in the system and changes in storage become unimportant.

Much of the storage in a forest system is a result of a build up of CO_2 concentrations at night in the sub-canopy when it is decoupled by a temperature inversion from the atmosphere above. In conifer forest, the trunkspace air volume is usually well coupled to the atmosphere and the penetration of gusts into the lower parts of the canopy transport respired CO_2 from the system, (Denmead and Bradley, 1985).

No measurements of CO_2 concentration profiles were made during the experiments at our site. However, profile data from an experiment in a Sitka spruce plantation in the Forest of Mearns in North East Scotland ~~in 1979~~ (Jarvis *et al.*, 1976) showed a minimum CO_2 concentration in the canopy crown ~ 3 ppm less than that at $1.2h$ and a concentration at $0.1h$ ~ 2 ppm larger than at $1.2h$. Similar CO_2 concentration profiles were reported in a *Pinus ponderosa* forest (Denmead and Bradley, 1985) with tree height ~ 16 m and a very sparse understorey, indicating maximum to minimum CO_2 concentration differences of less than 2 ppm day to day. The minimum concentration was in the densest part of the canopy and maximum concentrations occurred close to the forest floor.

The small size of the canopy air volume and small CO_2 concentration changes through the canopy makes CO_2 storage considerations relatively unimportant in coniferous forests such as Rivox.

4.2.3.2 Air and Biomass Storage of Sensible and Latent Heat

Throughout a diurnal cycle, changes in the air temperature and vapour pressure of the air volume of the forest, and in the water content of the trees, lead to energy storage in the form of sensible and latent heat. The energy budget of the forest over a full diurnal cycle, neglecting energy consumed in photosynthesis, is given by:

$$R_n = H + LE + G. \qquad (4.2.2)$$

However, at any instant, or for a time period over which averaged measured fluxes of R_n, H and LE are obtained (e.g. 30 minutes), we must include a term which accounts for the flux of energy to storage, i.e.:

$$R_n = H + LE + G + S_T. \qquad (4.2.3)$$

Where S_T represents a flux of heat into storage, either in the air, S_{air}, or the biomass, S_{bm}, and can be written as:

$$S_T = S_{air} + S_{bm}. \qquad (4.2.4)$$

Following Stewart and Thom (1973), the energy flux to storage into a column of air of unit cross-section, S_{air}, between the ground and the measurement height, neglecting advection, is given by:

$$S_{air} = S_{H_a} + S_{LE_a}, \qquad (4.2.5)$$

where S_{H_a} and S_{LE_a} are the fluxes into storage of sensible and latent heat respectively. S_{H_a} can be written as:

$$S_{H_a} = \rho c_p z \overline{\Delta T} \qquad (4.2.6)$$

Where ρ is the density of dry air, c_p is the specific heat capacity of air, z is the measurement height and $\overline{\Delta T}$ is the average change in air temperature with time in units of (K s^{-1}). Ideally, $\overline{\Delta T}$ should be averaged over height through the canopy, however, as no profile measurements of temperature were available, $\overline{\Delta T}$ was taken as the average change at the measurement height. Similarly, S_{LE_a} can be calculated as:

$$S_{LE_a} = \rho \lambda_q z \overline{\Delta q}, \qquad (4.2.7)$$

where λ_q is the latent heat of vaporisation and $\overline{\Delta q}$ is the change in specific humidity of the air with time in units of (g kg^{-1} s^{-1}). Again $\overline{\Delta q}$ was taken as the average change at z rather than an average through the canopy.

With respect to heat storage the forest system biomass can be estimated as an thermally equivalent depth of water in kg m^{-2}. From core samples taken from 30 year old Sitka spruce trees at the Forest of Mearns in North East Scotland in 1979, the average volume fractions of water, air and wood of the sapwood and hardwood were estimated, Table 4.2.2, (Ross Edwards, Horticulture and Food Research Institute of New Zealand Ltd., personal communication).

To obtain an estimate of the water content in the tree stems it was assumed for simplicity that the radius of the tree was equally divided into sapwood and heartwood. If we assume that the trees have a conical trunk and approximate diameter of 0.17m and height 15 m then the approximate mass of water in one tree is ~ 63 kg. As the planting density is 3584 stems/hectare, the mass of water per unit area is ~ 23 kg m^{-2}. (The calculation proves to be relatively insensitive to the arbitrary assumption of the ratio of heartwood to sapwood radius; taking the heartwood as a third of the radius gives a final water content of ~ 25 kg m^{-2}). Assuming that the volume of air in the trees is much less than the air volume between trees, and that the water content of the branches and needles is much smaller than that of the trunk wood, then the biomass heat storage can be expressed in terms of the heat storage of the water in the trunk. Thus, similarly to equation 4.2.6 we can express the heat storage of the biomass as:

$$S_{bm} = \rho_q c_q \overline{\Delta T} \qquad (4.2.8)$$

	WATER	AIR	WOOD
SAPWOOD	0.66	0.13	0.22
HEARTWOOD	0.26	0.52	0.22

TABLE 4.2.2 Estimates of volume fractions of Sitka spruce core samples, (Ross Edwards, Horticulture and Food Research Institute of New Zealand Ltd., personal communication).

Where ρ_q is the mass of water per unit area of forest, (i.e. ~ 23 kg m^{-2} from above), c_q is the heat capacity of water.

For day J199, 1990, with clear sunny skies, the storage terms were calculated and are shown in Figure 4.2.4. The total storage term is shown in Figure 4.2.5 in comparison to net radiation and sensible and latent heat fluxes at 1.2*h*. The largest fluxes into storage occurred in early morning and in late evening Figure 4.2.5, i.e. at sunrise and sunset. Maximum changes in storage over the 48 hour period were on the order of ~ ± 70 W m^{-2}, however, the average storage was -0.3 ± 31 W m^{-2}, (where the error is ± one standard deviation). To close the energy balance of the forest successfully on a half hourly basis, it would be necessary to include the changes in storage of latent and sensible heat. However, over several diurnal cycles the total storage of latent and sensible heat is effectively zero as expected.

The changes in the averaged quantities $\overline{\Delta T}$ and $\overline{\Delta q}$ at the measurement heights may also reflect regional changes in the temperature and water vapour density and may not be a result of the storage properties of the forest system. To accurately calculate short term storage fluxes of sensible and latent heat profiles of temperature and water vapour density are required. As with CO_2 storage fluxes, the heat storage fluxes are relatively unimportant at a site such as Rivox.

4.3 ENERGY BALANCE

Energy balance closure from our measurements at Rivox forest was not verified. The quantities R_n, G, H and LE, required to close the energy budget equation, equation 4.2.3, were never successfully measured simultaneously. This was partly because of the loss of net radiation data as a result of a fault in a logger program, section 3.2.5. Neither the CA27 1-d anemometer, (which housed the fast response thermocouple) nor the E009 IRGAs were water proof and to avoid serious

damage they could not be operated on days when rain was likely. The absence of the fast response thermocouple or the E009 IRGA resulted in loss of sensible or latent heat data, respectively.

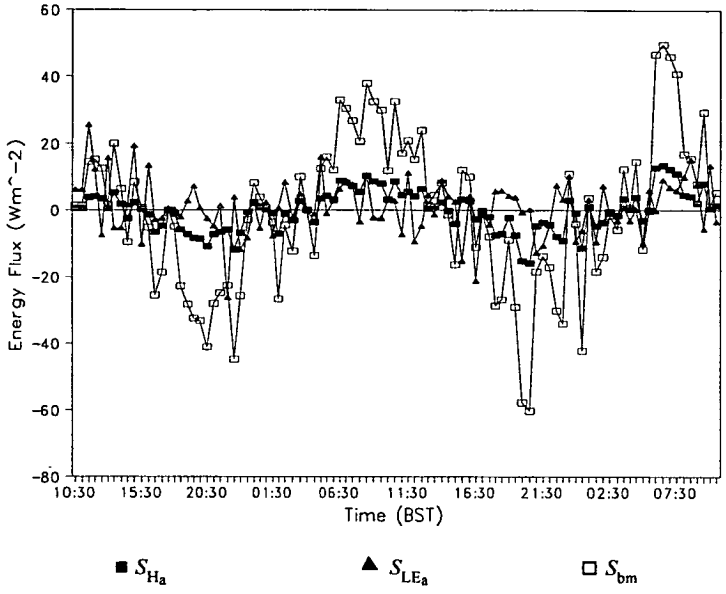

Fig. 4.2.4 Estimates of sensible and latent heat storage fluxes in the air and biomass for Rivox forest, J199, 1990.

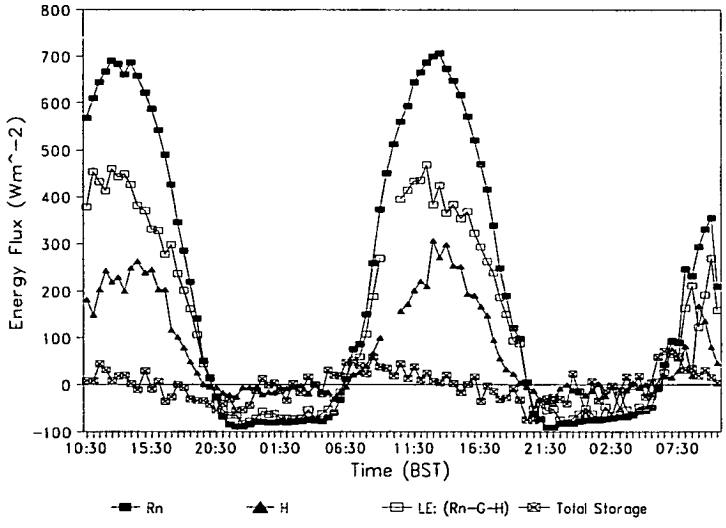

Fig. 4.2.5 Comparison of total above ground storage term (S_T) with net radiation, sensible heat and estimated latent heat fluxes, (R_n - G - H), for Rivox on J199, 1990.

4.4 DIURNAL TRENDS

Two data sets were collected in 1990 on days J199 and J205 which spanned full diurnal cycles, (48 and 43 hours respectively, Table 3.2.3). The weather on both days was sunny, with clear skies and light winds, ($\overline{U}$ ~ 2 - 5 m s^{-1}). Both these data sets were without *LE* flux data for reasons discussed in section 4.3. Full details of the instruments deployed are given in Table 3.2.3. Net radiation measurements were uncorrupted for both these data sets by the software error discussed in section 3.2.5.

The variation of PAR, I_P, with solar radiation, *S*, was found to have an apparent hysterisis loop Figure 4.4.1*a* and 4.4.2*b*. Morning and afternoon I_P values differed by up to ~ 180 μmol m^{-2} s^{-1} for identical values of solar irradiance, i.e. up to

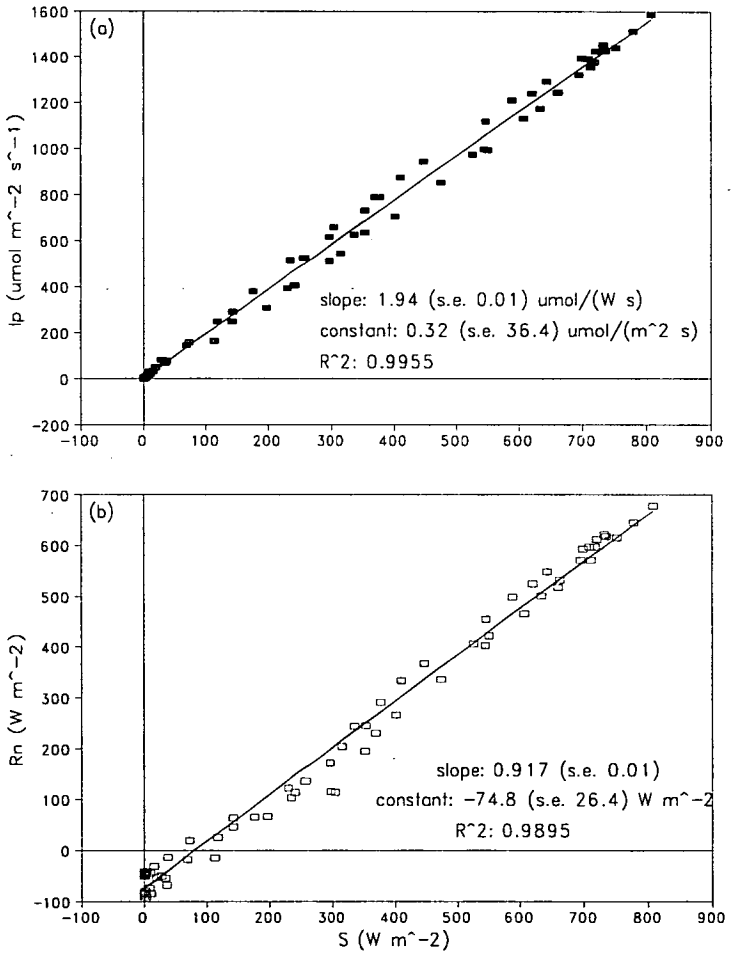

Fig 4.4.1 Linear regressions of: (*a*) I_P and *S*; and (*b*) R_n and *S*; for J205, 1990. Linear regression slopes and constants are given with standard errors. In (*a*), generally points above the line are from mornings and those below from afternoons.

~ 25 % of the signal, but this effect was not present in the data collected in 1991 with a different pyranometer and the same quantum sensor. However, the regression results between S and I_P are similar for the periods in both years. It seems likely that the sensors in 1990 were incorrectly levelled on the days presented below.

The relationship between I_P and S for the two data sets was found, by linear regression to be: 1 W m^{-2} = 1.94 μmol m^{-2} s^{-1} for J205; and 1 W m^{-2} = 2.01 μmol m^{-2} s^{-1} for J199, Figures 4.4.1*a* and 4.4.2*a*. These values agree well with a value of 1 W m^{-2} = 2.06 μmol m^{-2} s^{-1} from 300 hours of summer month data collected at the Forest of Mearns in North East Scotland in 1979, Jarvis (1993). Similarly, the relationship between R_n and S was found to be: 1 W m^{-2} R_n = 0.917 W m^{-2} S for J205; and 1 W m^{-2} R_n = 0.951 W m^{-2} S for J199, (Figures 4.4.1*b* and 4.4.2*b*). These relationships are

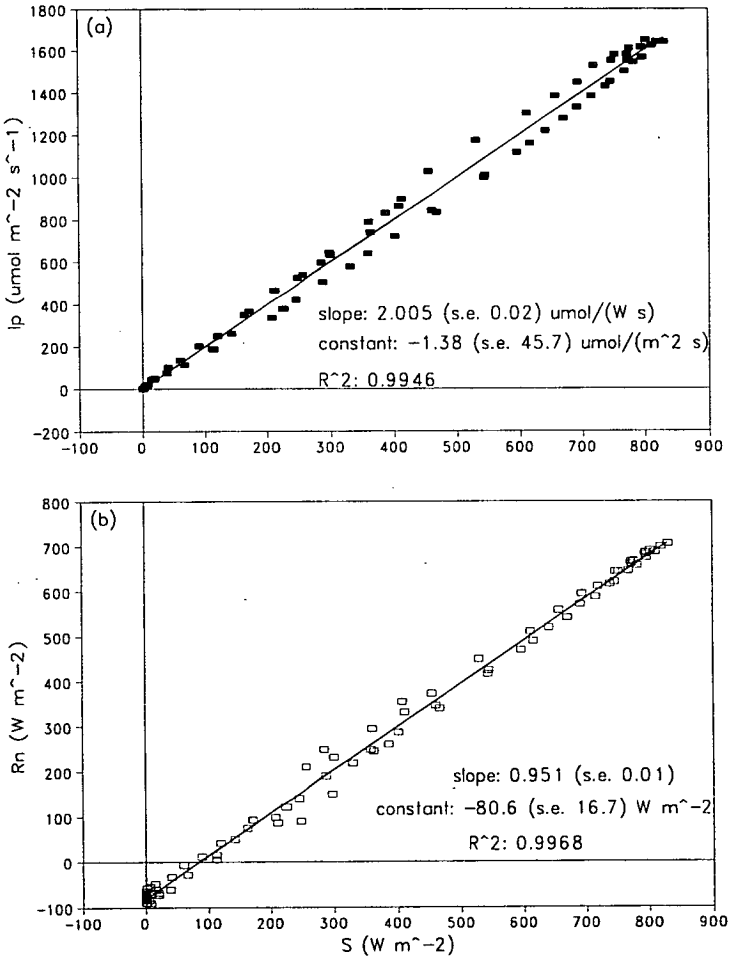

Fig 4.4.2 Linear regressions of: (*a*) I_P and S; and (*b*) R_n and S; for J199, 1990. Linear regression slopes and constants are given with standard errors. In (*a*), generally points above the line are from mornings and those below from afternoons.

higher than expected for a Sitka spruce forest. In a review of the literature, Jarvis *et al.* (1976) reported that 1 W m^{-2} R_n = 0.86 and 0.87 W m^{-2} S for sunny conditions and 1 W m^{-2} R_n = 0.76 W m^{-2} S for overcast conditions.

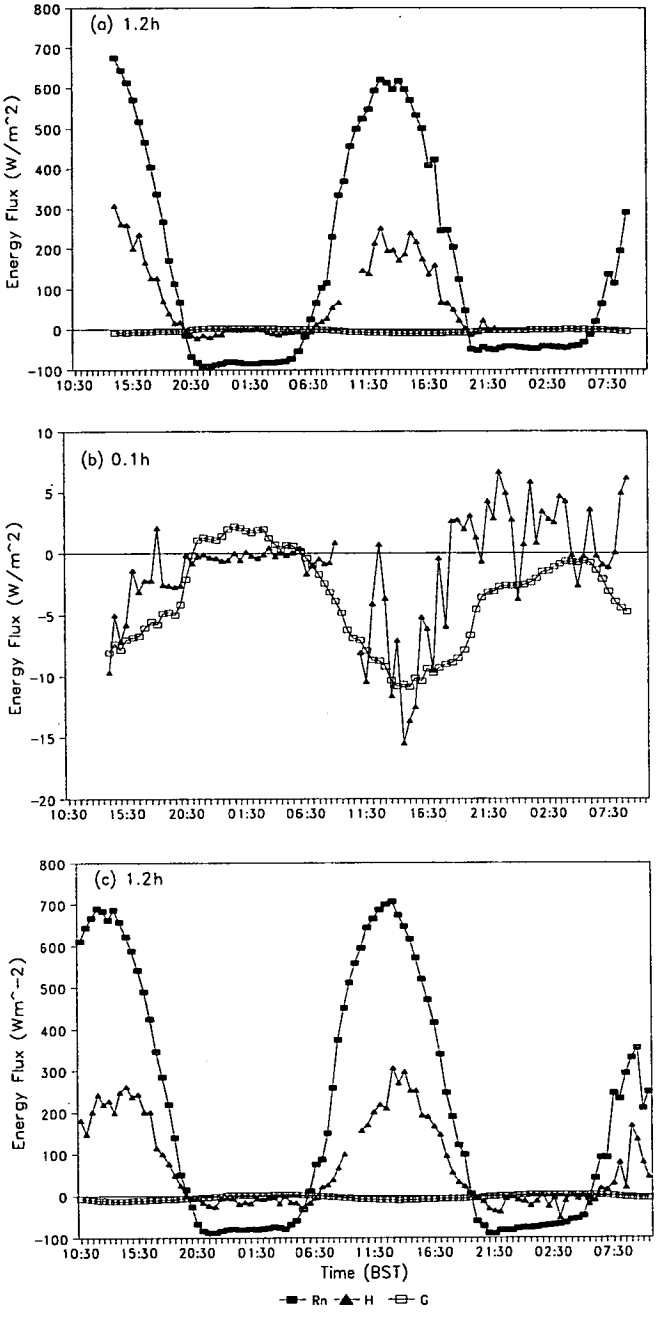

Fig. 4.4.3 Diurnal energy fluxes of R_n, H and G for two data sets in 1990: (*a*) J205 at 1.2*h*; (*b*) J205 at 0.1*h*; and (*c*) J199 at 1.2*h*.

It seems likely that the net radiometer calibration factor was not correct as it was not verified prior to the field experiment but was derived by the manufacturers some five years previously. The net radiation measurements presented here must necessarily be treated with some caution. Assuming that the correct relationship is 1 W m^{-2} R_n = 0.86 W m^{-2} S then our measurement of net radiation is over-estimated by ~ 10 %. Where net radiation values are used to estimate either H or LE fluxes from the energy budget equation 4.2.2, this uncertainty in R_n is a possible source of error.

Peak net radiation values of ~ 700 (± 10 %) W m^{-2} were observed around 13:00 while night time values lay between -50 and -100 (± 10 %) W m^{-2}, (Figures 4.4.3*a* and 4.4.3*c*). Corresponding peak values of sensible heat flux were found to be ~ 300 W m^{-2} around 13:00 with night time values of ~ -10 W m^{-2}. Figure 4.4.3*b* shows that at 0.1*h* the sensible heat flux had a much less distinct diurnal trend. At 0.1*h* above the forest floor around 13:00 sensible heat flux was directed towards the forest floor with measured soil heat flux of similar proportion, i.e. ~ -10 W m^{-2}, Figure 4.4.3*b*. The diurnal cycles of I_P, S and R_n were very similar for both these clear sunny days as shown in Figure 4.4.4.

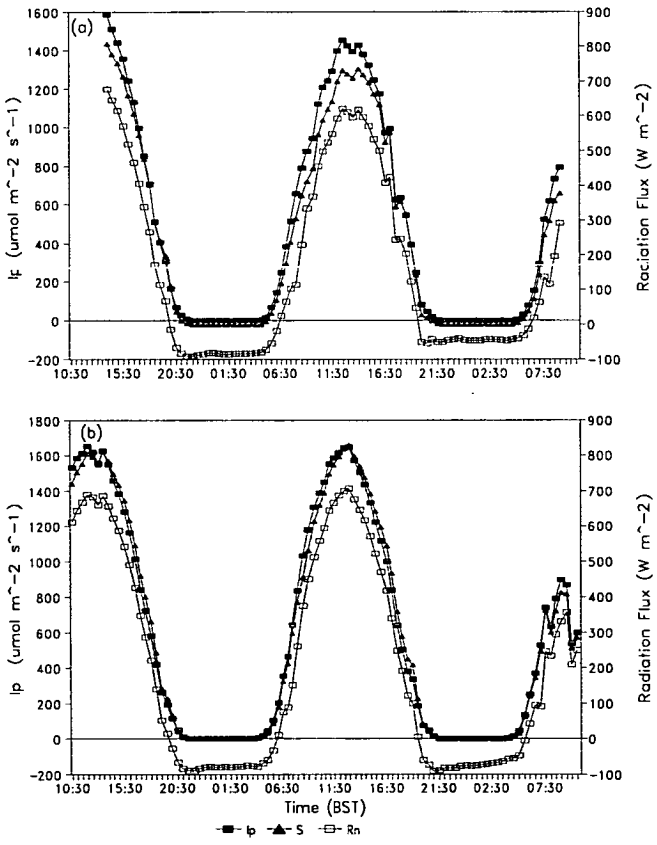

Fig. 4.4.4 Diurnal fluxes of I_P, S and R_n for two data sets in 1990: (*a*) J205 and (*b*) J199.

Air temperature, T_{air}, and vapour pressure deficit, D, corresponded closely throughout the two measurement periods (Figure 4.4.5). On day J205, T_{air} and D at $1.2h$ were higher than at the forest floor by ~ 12 % and 25 % respectively.

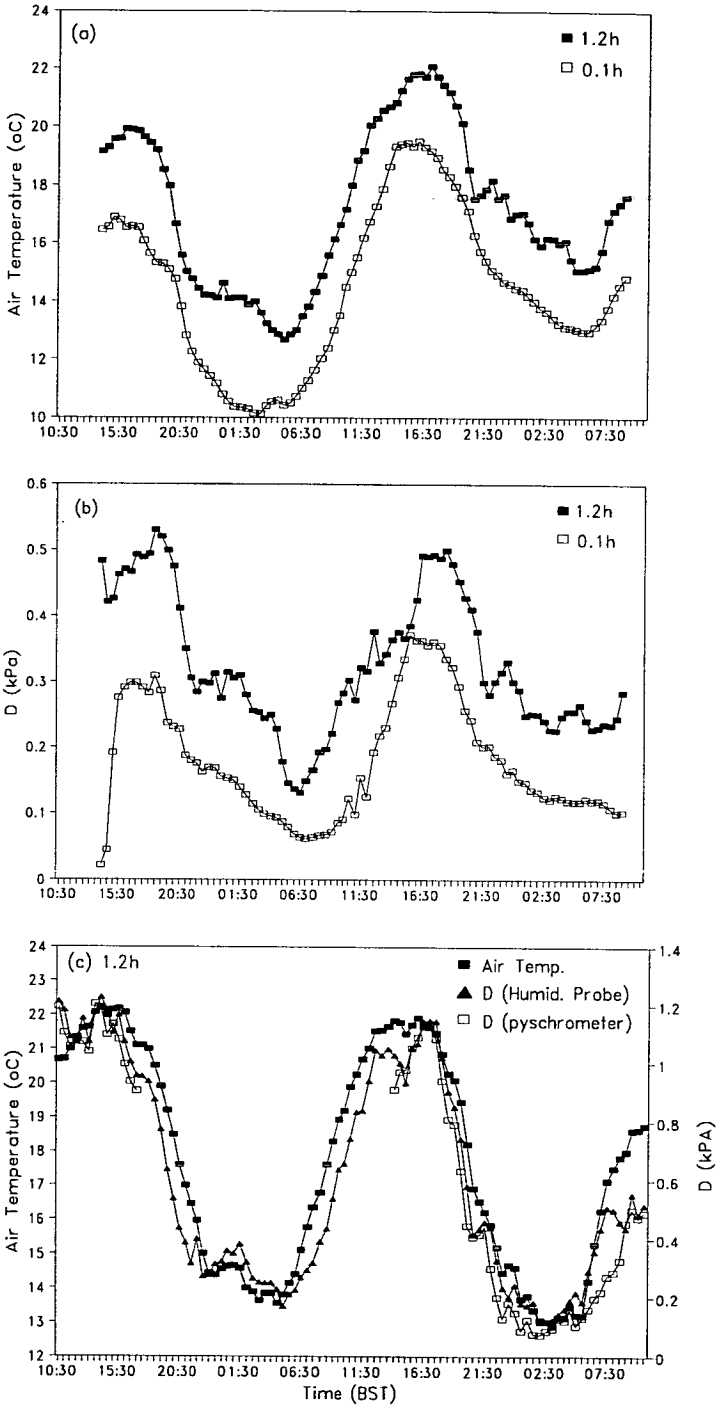

Fig. 4.4.5 Diurnal variation of air temperature, T_{air}, and saturation vapour deficit, D, for two data sets in 1990: (*a*) J205 T_{air} at $1.2h$ and $0.1h$; (*b*) J205 D at $1.2h$ and $0.1h$; and (*c*) J199 T_{air} and D at $1.2h$, with D from both humidity probe and psychrometer shown.

The CO_2 flux measured at $0.1h$ on J205 exhibits a large amount of scatter and little diurnal pattern, Figure 4.4.6*a*. The net fluxes were generally directed away from the forest floor with peak values of the uncorrected flux of ~ 0.1 mg m^{-2} s^{-1}. The average net CO_2 flux across the $0.1h$ plane for the data set was ~ 0.06 mg m^{-2} s^{-1} for the uncorrected fluxes and ~ 0.03 mg m^{-2} s^{-1} for the estimated correct fluxes. From the estimate of the size of the WPL corrections shown in Figure 4.4.6*a*, the uncertainty in the WPL uncorrected fluxes is on average ~ 50 %. More importantly, the lack of a reliable co-spectral response from measurements of CO_2 efflux at $0.1h$

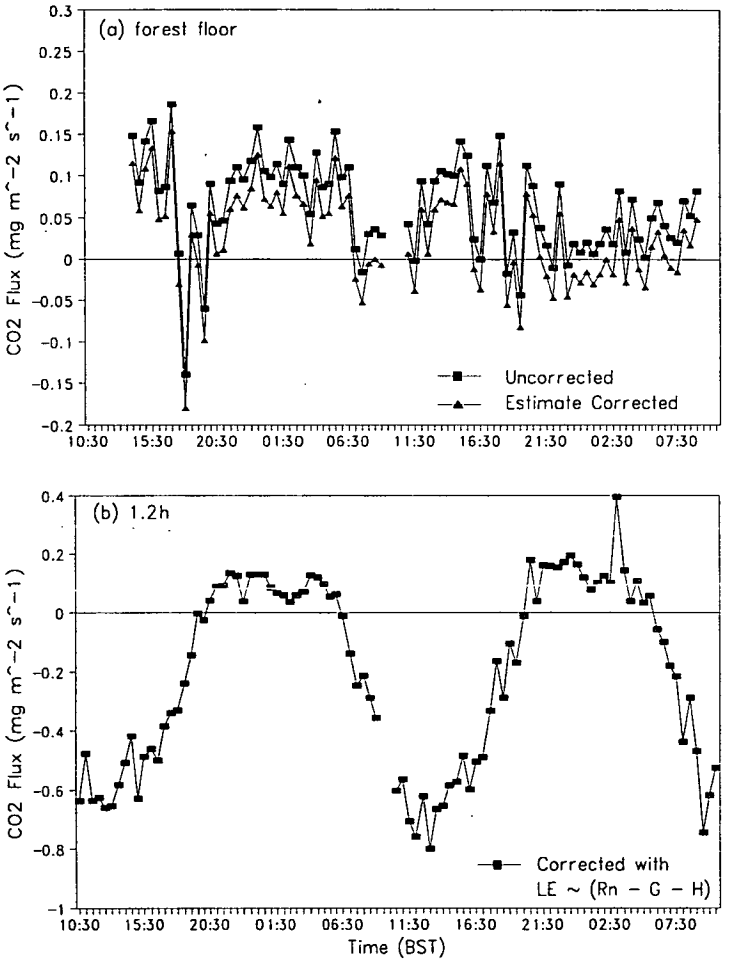

Fig. 4.4.6 Diurnal variation of CO_2 flux at $0.1h$ and $1.2h$ from two separate data sets in 1990: (*a*) J205 at $0.1h$; and (*b*) J199 at $1.2h$. The fluxes at $0.1h$ in (*a*) are shown both uncorrected for WPL effects and WPL corrected using a constant *LE* flux of 50 W m^{-2}. The $1.2h$ data is WPL corrected using an estimate of *LE* as $(R_n - G - H)$.

does not allow us to apply transfer function corrections to the measured fluxes as discussed in section 6.3.2. The transfer functions for sensor separation, scalar and sonic anemometer path averaging as presented in section 2.3, apply only when Taylor's hypothesis is valid. With the low wind speeds found in the trunkspace, the corrections as a result of sensor separation and path averaging might be expected to be large but we have no means of applying them. At best, we can only take these fluxes as an estimate of the likely CO_2 efflux, F_G, from the forest floor under the prevailing conditions of J205. Ideally, experiments using eddy covariance to measure forest floor fluxes should be carried out in conjunction with surface chamber measurements.

The diurnal pattern of the net CO_2 flux at $1.2h$ is extremely similar to the environmental variables already presented. Peak values of F_a occurred around 13:00, with values of about -0.8 mg m^{-2} s^{-1}. On a slightly cooler day, J195, 1990, with very small vapour pressure deficit, the peak CO_2 flux was about -1.4 mg m^{-2} s^{-1} at 11:30 when T_{air} was ~ 18 °C and D ~ 0.15 kPa (Figure 3.2.11). These values of CO_2 influx agree well with the CO_2 influxes for similar temperatures and vapour pressure reported in the literature for coniferous forests, (Price and Black, 1990; Jarvis, 1993)

It is important to note that the data presented here for scalar and energy fluxes are heavily biased towards good weather in the summer months and cannot ~~not~~ be used to give the net CO_2 uptake of the forest system over a full year. At this site, with an annual rainfall of ~ 1800 mm, warm, sunny, and dry days are the exception rather than the rule even in the summer months. Thus, to estimate accurately CO_2 budgets for this forest, measurements must be made throughout the year and in all weather conditions, including wet weather. The limitations of our making eddy covariance measurements in rainy or wet weather at Rivox were practical ones, i.e. droplets formed on the sonic anemometer transducer heads blocking the signal, open path analysers were not weather proof, sampling down tubes to a closed path IRGA could have led to water being sucked into the analyser, etc. It will be a major challenge to solve these problems and measure annual CO_2 budgets.

4.5 RESPONSE OF CO_2 FLUX TO ENVIRONMENTAL VARIABLES

The assimilation and respiration rates of all the components in the forest system are controlled by a number of environmental variables: solar irradiance, vapour pressure deficit, air temperature, nitrogen and other nutrient supply, soil temperature, static pressure fluctuations, etc. As a result, we cannot differentiate between counteractive processes in the forest system as a whole. For instance, if air temperature rises and F_a drops proportionally, we may not conclude that air temperature directly controls assimilation rate, as the increase in temperature may result in higher soil efflux of CO_2 which is, consequently, assimilated by the trees.

For the purposes of examining the relationship between CO_2 influx to the system and the above environmental variables, we will reverse the sign convention such that CO_2 flux into the system, F_a, is positive rather than negative.

The overall limit to annual tree growth is available solar irradiance (Jarvis, 1987). The response of CO_2 influx, F_a, to available photosynthetically active radiation can be approximated by a rectangular hyperbola as shown in Figures 4.5.1*a* and 4.5.3*a*, whereas the relationships between air temperature and vapour pressure deficit with I_P were in the form of hysterisis loops, during the course of the day, (Figures 4.5.1*b* and 4.5.1*c*). To examine the relationships between CO_2 flux and T_{air} and D we can make use of the hysterisis relationships between these variables to I_P. By sorting data into different parts of the diurnal cycle we can attempt to associate levels of CO_2 flux with T_{air}, D and I_P simultaneously as in Figure 4.5.1*a*. If a strong relationship existed between F_a and either T_{air} or D, then we might expect to be able to differentiate between morning and afternoon values of CO_2 flux with identical I_P.

The data, however, are scattered on both sides of the fitted rectangular hyperbola in Figure 4.5.1*a* and show little distinction between morning and afternoon at identical I_P values. The level of uncertainty in the values of F_a may be large enough to mask a response to T_{air} or D; however, it may be that I_P is the major variable controlling F_a for this data set. Classifying values of the CO_2 flux explicitly by D values also shows no discernible relationship between F_a and D (Figure 4.5.2). The CO_2 assimilation rate of a Sitka spruce forest was demonstrated to be dependant on both radiation input (S) and vapour pressure deficit, D, by Jarvis (1993), where 145 hours of net assimilation data was plotted against S in five classes of vapour pressure deficit in the range 0 - 2.0 kPa. Each class of D showed a distinct curvilinear response. The comparatively small amount of data presented here (48 hours) and the smaller range of vapour pressure deficits (0 - 1.3 kPa) may explain the lack of a similar result.

The data from J207, 1991, were gathered on an overcast day, whereas J199, 1990 was clear and sunny. The two rectangular hyperbolic fits of CO_2 flux to I_P in Figures 4.5.1 and 4.5.3 also give an indication of the quantum efficiency of the forest system on the two days.

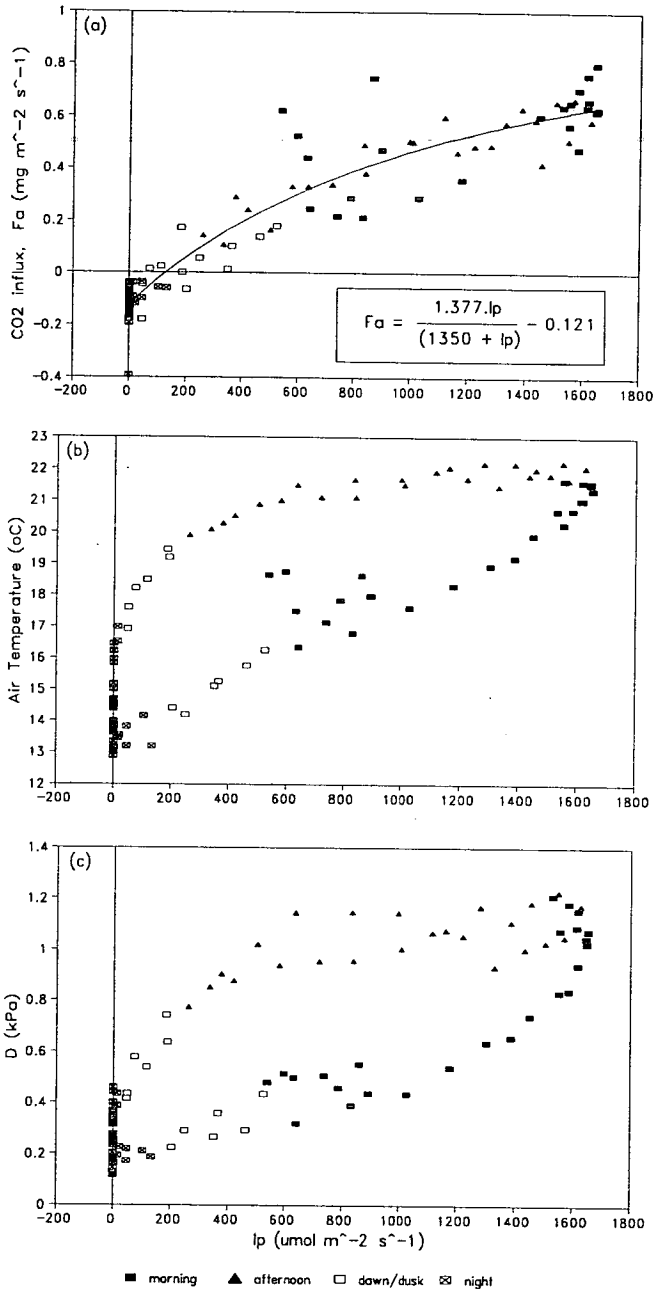

Fig. 4.5.1 Response of three variables: (*a*) CO_2 flux; (*b*) air temperature; and (*c*) saturation vapour pressure; to changes in I_P for the data set J199, 1990, at 1.2*h*. Data are sorted by time: morning is 07:30 - 13:00; afternoon is 13:30 - 19:00; dawn and dusk are 06:00 - 07:00 and 19:30 - 20:30, respectively; and night is 21:00 - 05:30.

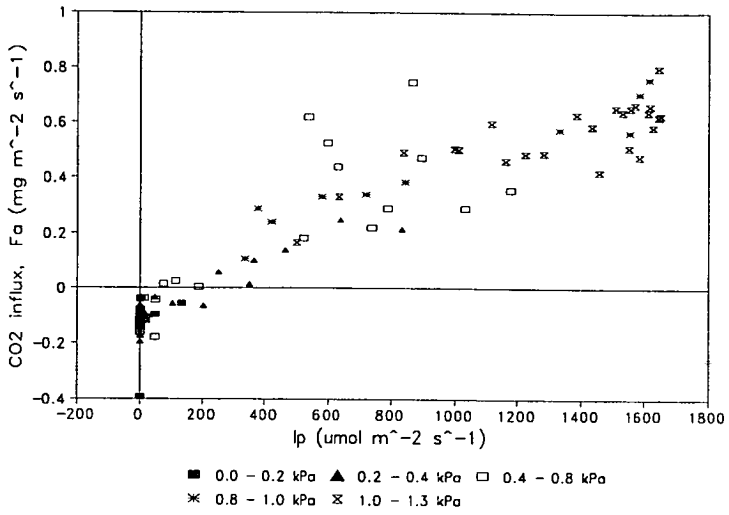

Fig. 4.5.2 Response of CO_2 flux to changes in I_P for the data set J199, 1991, at 1.2*h*. The data are plotted in terms of classes of D as shown.

The general form of the equation for a rectangular hyperbola is:

$$F_a = \left(\frac{a I_P}{a/b + I_P} \right) + c, \qquad (4.5.1)$$

where a, b and c are constants. By differentiating equation 4.5.1 it can be shown that the initial slope of the curve at zero I_P is given by b, i.e. when the CO_2 flux is entirely dark respiration c. Furthermore the value of F_a where the curve approaches the asymptote is given by $(a + c)$, i.e. the saturation value of F_a. The initial slope b, in units of moles of CO_2 fixed per *incident* photon*, is often referred to as the apparent quantum efficiency of a system for photosynthesis. The reciprocal of this slope is the apparent quantum requirement, i.e. the number of quanta required to fix one mole of CO_2. This concept is more commonly used at the scale of individual leaves of a plant rather than at a stand or canopy scale. In the context of an entire forest system rather than a leaf, the apparent quantum requirement indicates the irradiance levels required above the forest for the forest to begin have a net gain of CO_2 from the atmosphere above. From the fitted rectangular hyperbolic equations for J199 and J207 shown in Figures 4.5.1*a* and 4.5.3*a*, the stand apparent quantum efficiencies are ~ 0.023 and 0.043 mol CO_2 fixed per incident photon, respectively, or alternatively apparent quantum requirements of 43 and 23 incident photons per mol CO_2 fixed.

* Where one mg(CO_2) ≡ 22.7 μmol(CO_2)

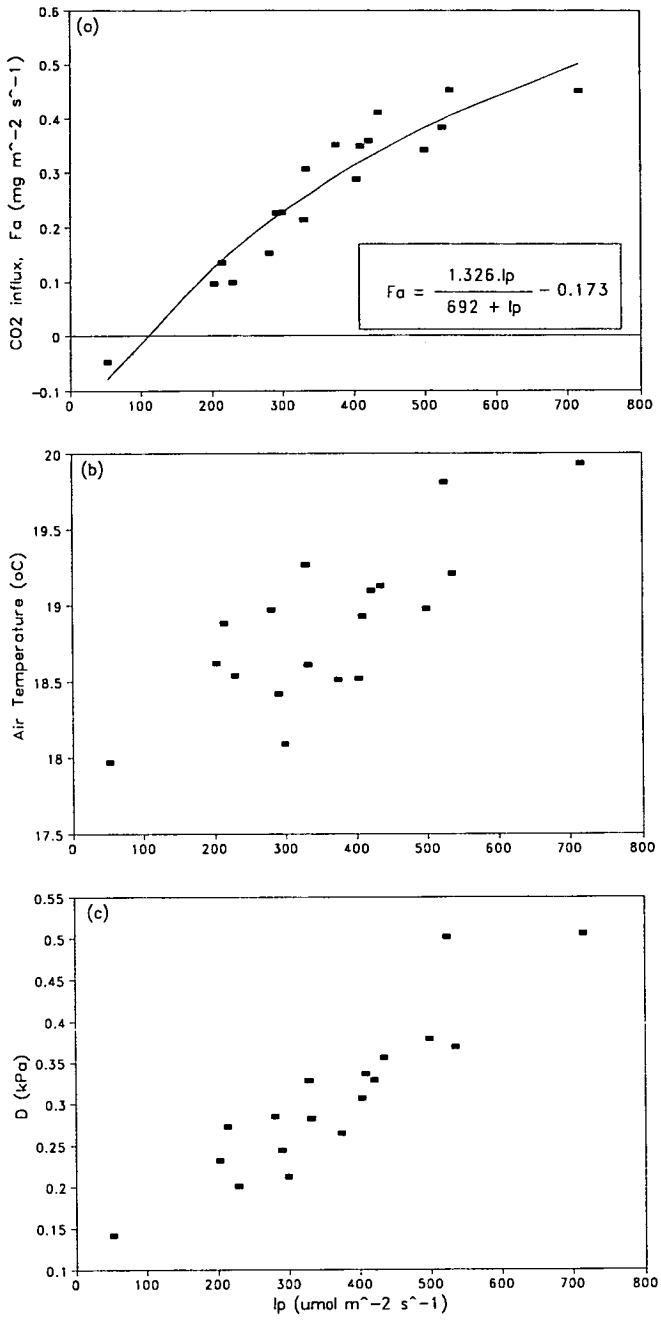

Fig. 4.5.3 Response of three variables: (*a*) CO_2 flux; (*b*) air temperature; and (*c*) saturation vapour pressure; to I_P for the data set J207, 1991, at 1.2*h*. The data set runs from 11:30 - 20:00 (BST).

From CO_2 porometer measurements of shoots on Sitka spruce trees in Scotland in similar temperatures, the apparent quantum requirement was found, from fitted models of CO_2 assimilation with I_P, to be ~ 27 photons (molecule CO_2 fixed)$^{-1}$ (Griffiths, 1983; Jarvis, 1987). Current-year-needles from Sitka spruce trees grown in

a greenhouse, and those detached from forest tress, were reported to have quantum requirements of 17 and 13 photons per mol CO_2 fixed (Jarvis *et al.*, 1976; Ludlow and Jarvis, 1971). Quantum requirement of an entire forest system would be expected to be larger than that for single shoots because of the presence of large respiratory fluxes of CO_2 within the canopy. From the 48 hour data period on J199 - J201 the value of 43 photons per mol CO_2 fixed predicted by the fitted rectangular hyperbola is indeed higher than that reported for individual shoots and needles. The value predicted for the shorter overcast data period from J207, 1991, of 23 photons (molecule CO_2 fixed)$^{-1}$ appears to be close to that for the assimilation of individual shoots and needles. This difference may be a result of the higher proportion of diffuse to direct beam radiation on the overcast day. It has been shown from simple models of CO_2 flux response to different fractions of diffuse and beam radiation that diffuse radiation is used more efficiently used by plants (Jarvis *et al*, 1985). Diffusion radiation also penetrates a canopy more deeply than direct beam radiation which will increase the apparent quantum efficiency (Ross, 1975).

Values of I_P predicted by the curves when $F_a = 0$ indicate the photon flux densities required to change the flux direction into the forest system or the 'compensation point'. For J199, 1990 and J207, 1991 the compensation points were 130 and 104 μmol m^{-2} s^{-1}, respectively, this compares to a compensation point of 50 μmol m^{-2} s^{-1} reported by Griffiths (1983) for individual shoots. Values of F_a from the curves when $I_P = 0$, i.e. the dark respiration fluxes c, were 0.12 and 0.17 mg m^{-2} s^{-1} on J199 and J207, respectively, this compares to values of 0.04 mg m^{-2} s^{-1} for shoots (Griffiths, 1983), 0.045 and 0.031 mg m^{-2} s^{-1} for current year needles from greenhouses and forest trees, respectively (Ludlow and Jarvis, 1971). The predicted asymptotic values of influx F_a, $(a + c)$ are 1.3 and 1.2 mg m^{-2} s^{-1} for J199 and J207, respectively, which compares to values of 1.48 and 1.74 mg m^{-2} s^{-1} reported by Ludlow and Jarvis (1971) for current year needles from greenhouses and forest trees, respectively. As we can see from these comparisons the uptake of CO_2 by the forest system in response to photon flux density is different to that of individual leaves as a result of the action of the forest floor, the woody branches and trunks and the canopy architecture. The forest system has a greater dark respiration flux, a higher compensation point and a lower asymptotic saturation influx than the individual leaves.

4.6 SUMMARY AND CONCLUSIONS

(i) WPL density effect corrections to CO_2 fluxes were found to be larger for the open path E009 IRGA than for the closed path ADC 225 Mk. III IRGA, (43 % for the E009 compared to 17 % for the ADC 225 Mk. III).

(ii) The Kaimal *et al.* (1972) model for sensible heat co-spectra did not provide a good approximation of the CO_2 co-spectral response at Rivox. A model was obtained by fitting an equation of the form of the Kaimal *et al.* (1972) model for sensible heat to the data. Using both of these models to apply transfer function corrections to CO_2 fluxes from an open path E009 IRGA and a closed path ADC 225 Mk. III IRGA, the sizes of the corrections were found to be significantly different. Using the Kaimal *et al.* (1972) model, the correction for the E009 open path IRGA was 6.3 % while using our fitted model it was 1.4 %. Similarly, for ADC III closed path analyser the Kaimal *et al.* (1972) model gave a correction of 34.5 % while our model gave a correction of 14.0 %. It is evidently important to represent the co-spectral response of a variable correctly for a particular site with a realistic function, if transfer function flux corrections are to be accurately estimated.

(iii) Changes in storage of sensible and latent heat in the canopy air spaces and biomass were estimated over a 48 hour warm, sunny, and dry period. The maximum changes in storage for half hour periods were $\pm$ 70 W m^{-2}; however, the average change in storage over the entire 48 hour period was -0.3 $\pm$ 31 W m^{-2}, (where the error is $\pm$ one standard deviation).

(iv) Closure of the energy balance was not verified at Rivox for the measurement periods due to the lack of simultaneous measurements of R_n, H, LE and G.

(v) Regressions between solar radiation, S, and photosynthetically active photon flux, I_P, indicated that 1 W m^{-2} S = 1.98 μmol m^{-2} s^{-1} I_P on average between the two data sets. This value agrees well with reported data from a similar forest. Also regressions between R_n and S indicated that, on average, 1 W m^{-2} R_n = 0.934 W m^{-2} S. This value is considerably higher than reported in the literature and probably indicates an over estimation of ~ 10 % in the net radiation fluxes presented here.

(vi) At $0.1h$ in the forest trunkspace, CO_2 fluxes showed much scatter and little diurnal pattern. The uncorrected fluxes had an average value over 48 hours of data of 0.06 mg m^{-2} s^{-1}. Estimates of the WPL correction of these fluxes, using a constant value of LE = 50 W m^{-2}, were ~ 50 % of the raw values. Transfer function corrections also could not be applied to the fluxes at $0.1h$ as some of the functions are not applicable in regions where Taylor's hypothesis is invalid and, furthermore, as no reliable co-spectral response functions could be obtained. Consequently, the partially

WPL corrected CO_2 fluxes at $0.1h$ can only be considered as rough estimates of the true flux.

(vii) At $1.2h$ the CO_2 flux showed the expected diurnal cycle, with maximum fluxes into the canopy of ~ -0.8 mg m^{-2} s^{-1} occurring around mid-day and indicating a net system assimilation, and fluxes out of the canopy at night of ~ 0.15 mg m^{-2} s^{-1} indicating net system respiration. The data presented were from a warm, sunny, and dry period which is not typical of the site and thus the CO_2 fluxes reported here are not representative of the forest over a longer period.

(viii) The major controlling variable on net CO_2 flux into the forest system was found to be I_P. No evidence of strong secondary relationships with air temperature, T_{air}, or vapour pressure deficit, D, was found.

(ix) The relationship between influx of CO_2 to the canopy and incident I_P, was reasonably represented by a rectangular hyperbola. Curves of this form were fitted to data from a sunny day and an overcast day. These curves indicated that the forest system quantum requirements were 43 and 23 photons (molecule CO_2 fixed)$^{-1}$ for sunny and overcast days, respectively. The curves also predicted values of dark respiration flux of 0.12 and 0.17 mg m^{-2} s^{-1}, asymptotic net influxes of 1.3 and 1.2 mg m^{-2} s^{-1} and compensation points of 130 and 104 μmol m^{-2} s^{-1}, for sunny and overcast periods, respectively.

CHAPTER 5.
TURBULENCE STATISTICS AND VELOCITY CORRELATION ANALYSIS

5.1 INTRODUCTION

In considering transport of mass or energy and momentum in the forest system, the degree of coupling of the airspace below the canopy with the atmosphere above the forest is crucial. The penetration of gusts into a forest canopy has been shown to be the dominant process in the transport of momentum, mass and energy between the atmosphere and the forest (Denmead and Bradley, 1985; Raupach, 1988; Raupach *et al.*, 1989; Bergström and Högström, 1989). Deviations from Gaussian flow in the lower canopy obtained from statistics of skewness and kurtosis, are indications of the presence of these events. Velocity autocorrelations through the canopy yield typical time and length scales for the turbulence and are a further indication of the penetration of large events.

The degree of coupling can also be investigated directly by means of cross-correlation of velocity fluctuations above and within the canopy. In a forest where momentum events above the trees have little effect on sub-canopy regions, we would expect the cross-correlation of velocities above and below to be very weak. We might expect velocity cross-correlations in such a system to result from pressure waves which move ahead of large gusts, rather than the penetrating gusts themselves (Allen, 1968; Shaw and Zhang, 1992), and thus for correlated events to occur nearly simultaneously throughout the canopy (Raupach *et al.*, 1989). Conversely in a canopy which is well coupled to the atmosphere at all levels, we might expect to see evidence of lagged cross-correlations from gusts penetrating to the lowest parts of the canopy (Baldocchi and Meyers, 1988*b*; Raupach *et al.*, 1989).

Turbulence velocity statistics, velocity auto- and cross-correlations were obtained at three measurement heights $1.2h$, $0.7h$ and $0.1h$ from simultaneous measurements on days J207 (13:30 - 17:00) and J213 (13:30 - 17:00), 1991. The mean wind speed at $1.2h$ on J207 was about half that on J213, (2.5 and 4.2 m s^{-1} respectively). On J213 the thermal stability index $(z - d)/L \sim -0.01$, indicating very slightly unstable or near neutral conditions. On day J207, no sensible heat flux data were gathered but stability was estimated to be slightly unstable or near neutral, as the sky was overcast with an average solar radiation flux over the data set of 250 W m^{-2}.

The skewness values for J207 and J213, 1991 were somewhat different to those reported in other studies in dense conifer forests, (Amiro and Davis, 1988; Amiro, 1990*a*; Gardiner, 1993) and in many other canopy types. It was found that

contamination from the PCL-714 A/D board was present, on a very small scale, in the data as discussed in section 3.2.6. The contamination was of the type that could be successfully removed, i.e. specific voltage values 0, ± 2.5 or ± 5 V; however, the higher order moment statistics were effected despite cleaning the data. In an uncleaned data file with one contaminated point out of 32,700, the kurtosis values could be > 1000, with the effect being much smaller after cleaning and more difficult to detect as kurtosis values returned to expected values around 3.

The skewness and kurtosis statistics were thus extremely useful for checking the quality of data files before analysis but cannot be relied on in themselves. Skewness and kurtosis statistics are presented for J213 only to illustrate the effect on a cleaned data set.

The 3m upwind displacement of the $0.1h$ anemometer, adds an uncertainty to our cross-correlation results as the anemometer array was not truly vertical. In the dense canopy only very energetic motions from above (with large length scales comparable to tree height) were likely to be able to penetrate to the lowest levels. Such length scales above a conifer canopy have been reported by Amiro (1990*a*) for a spruce canopy ($L_u \sim h$, $L_w \sim 0.07h$) and by Gardiner (1993) for Rivox ($L_u \sim h$). Since lateral displacement is small in relation to length scales of the gust events, we may assume that our imperfect array will give meaningful estimates for the $0.1h$ - $1.2h$ cross-correlations. The u and w auto-correlations and all cross-correlations between the $1.2h$ and $0.7h$ levels are unaffected by the placement of the $0.1h$ anemometer.

5.2 TURBULENCE STATISTICS

Mean normalised turbulent statistics are presented for the data sets J207 and J213, 1991, from three sonic anemometer measurements at heights $1.2h$, $0.7h$, and $0.1h$, Figure 5.2.1. The profiles generally conform to profiles of turbulence statistics reported in the literature for coniferous forests (Amiro and Davis, 1988; Amiro, 1990*a*; Gardiner 1993). Both mean wind speed profiles are strongly sheared below the canopy top, where the mean wind speed values are normalised by their value at $1.2h$, Figure 5.2.1*a*. The unnormalised wind speed magnitude at each height was greater on J213 than on J207.

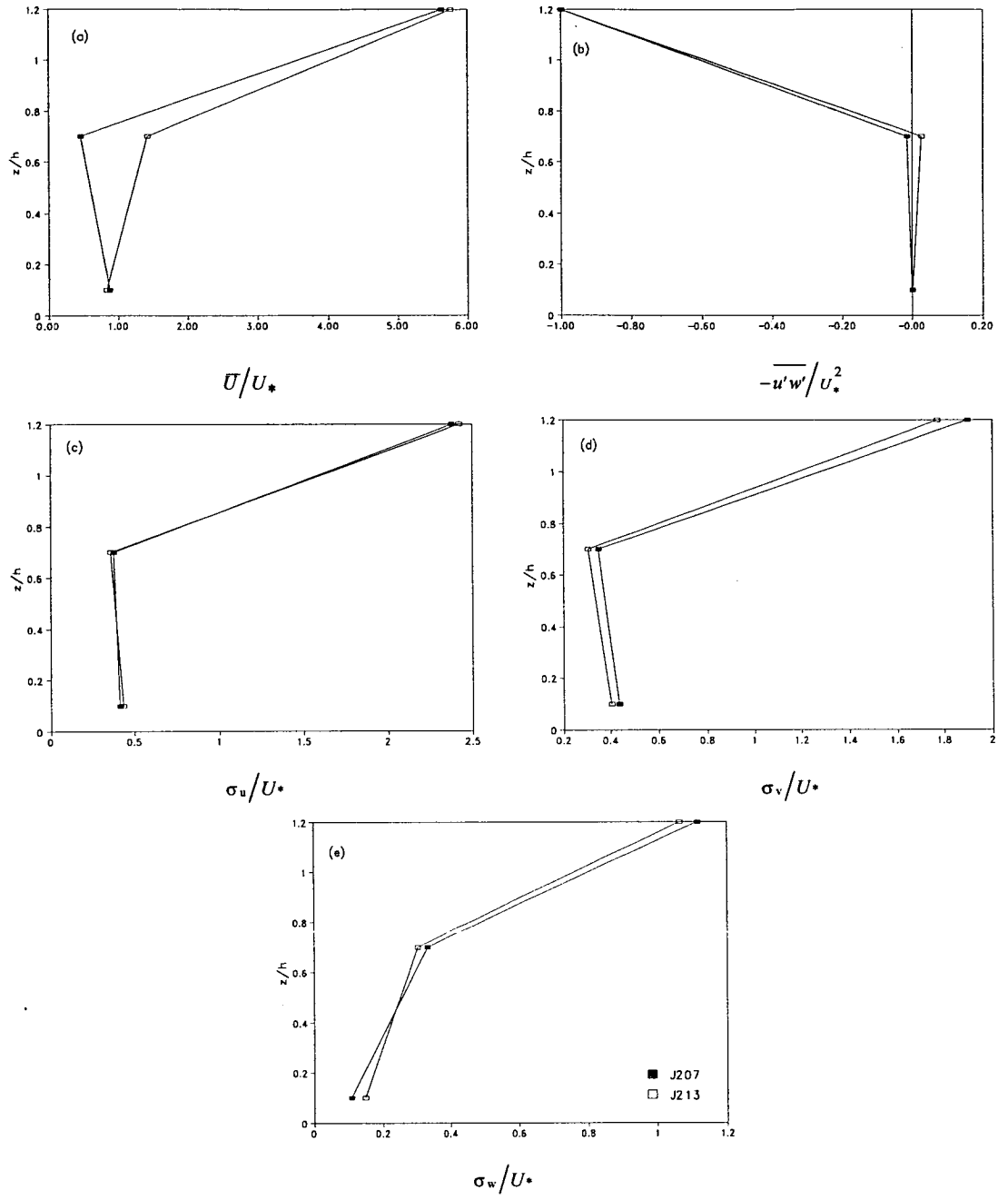

Fig. 5.2.1 Mean profiles of turbulence statistics for J207 and J213, 1991 where: (*a*) $\overline{U}/U_*$; (*b*) $-\overline{u'w'}/U_*^2$; (*c*) σ_u/U_*; (*d*) σ_v/U_*; and (*e*) σ_w/U_*; with normalised height, *z/h*, where U_* = 0.44 and 0.72 m s^{-1} for J207 and J213 respectively.

The trunkspace mean wind speed on J207 was greater than that in the canopy crown, whereas the opposite was true on J213. This phenomenon has previously been

reported in a spruce forest, Amiro (1990*a*), and pine forests, (Raupach, 1988; Kaimal and Finnigan, 1993).

Reynolds stress values in the canopy crown, at $0.7h$, were positive on J213 (Figure 5.2.1*b*). A similar result is apparent in the data of both Amiro (1990*a*), in a spruce forest, and Gardiner (1993) at Rivox. Upward momentum fluxes in the densest parts of the canopy may be evidence of the dispersive component of momentum flux (Amiro, 1990*a*), which is given explicitly by the space and volume averaging of the equations of motions (section 1.2). To measure correctly such a dispersive term, a larger spatial average would be required than one instrument at one point.

In the canopy crown, the tree elements were within 0.5 m of the anemometer transducers and many of the velocity fluctuations may have been extremely local in origin. To attempt to place many instruments in a small area to improve the spatial averaging might introduce problems with instrument obstruction and might also require creation of artificial gaps in the foliage. It is also a possibility that the instrument was sited too close to tree branches whose turbulent wakes might have resulted in spurious upward momentum fluxes. The important point to note from the Reynolds stress profiles is, however, that the attenuation of momentum by the canopy crown is extremely efficient. The momentum transported from above the canopy is almost entirely absorbed by the canopy crown, Figure (5.2.1*b*).

The profiles of u, v and w standard deviation, normalised by U_*, indicate that horizontal velocity standard deviations have a minimum in the canopy crown, whilst the vertical velocity standard deviation has a minimum in the trunkspace (Figures 5.2.1*c*, 5.2.1*d* and 5.2.1*e*). A similar result was reported for pine, aspen, and spruce canopies over this range of heights by Amiro (1990*a*).

Turbulence intensities can be defined as $I_i = \sigma_i/\overline{U}$, where i = 1, 2 and 3 correspond to I_u, I_v or I_w and $\overline{U}$ is the mean horizontal wind speed. On J207, the maximum turbulence intensity for u, v and w, occurred in the canopy crown (Figure 5.2.2), corresponding to the largest LAI in the canopy as reported elsewhere (Amiro, 1990*a*). In contrast, on J213, the maximum turbulence intensity for u and v occurred in the trunk space and for w in the crown (Figure 5.2.2). The turbulence intensities are also considerably smaller on J213 at $0.7h$ but very similar at $1.2h$ and $0.1h$, compared to J207. The difference in behaviour on the two days relates to the differences in the mean wind speed profile (Figure 5.2.1*a*), and is an indication of the different distribution of turbulent energy in the canopy on each day.

The mean skewness and kurtosis profiles are presented for J213 in Figure 5.2.3 after cleaning of the data for contamination. The cleaning of the data would seem to adversely effect the skewness statistics much more than the kurtosis values.

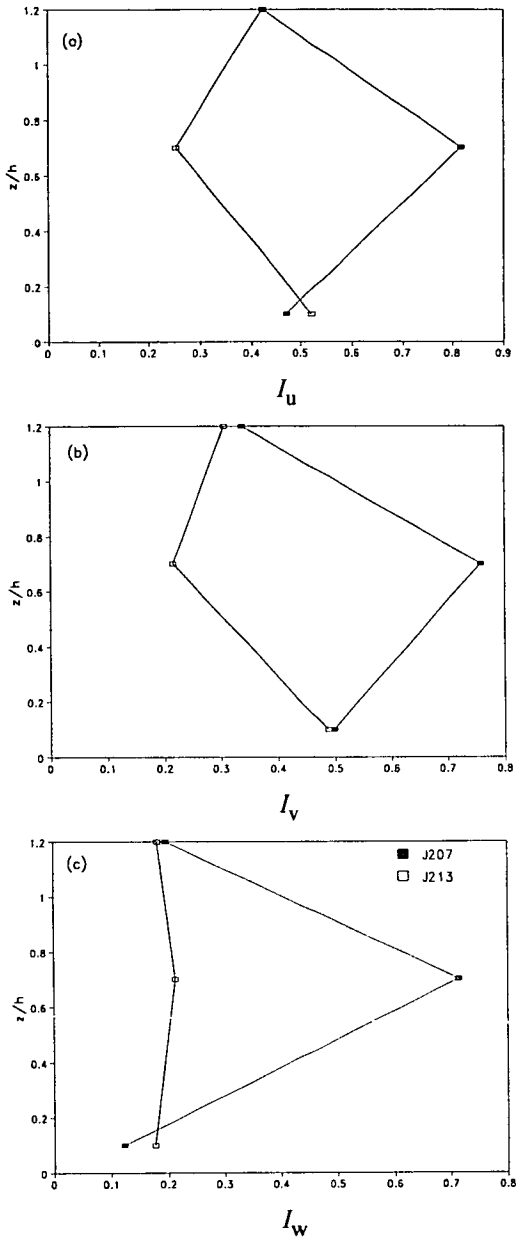

Fig. 5.2.2 Mean profiles of turbulence intensities for J207 and J213, 1991 where: (*a*) $I_u = \sigma_u/\overline{U}$; (*b*) $I_v = \sigma_v/\overline{U}$; and (*c*) $I_w = \sigma_w/\overline{U}$; with normalised height *z/h*.

The statistic of skewness indicates the distribution of velocity fluctuations about the zero value. In the case of *u*, a positive skewness, indicates a domination of air parcels or eddies with advection velocities larger than that of the mean flow (Kaimal and Finnigan, 1993). For *w* motions, turbulent events penetrating the canopy have negative *w* velocities compared to the mean flow. These motions are balanced by ejection events out of the canopy, but as incursions tend to dominate, Sk_w is negative.

Strongly positive Sk_u and strongly negative Sk_w values indicate that the turbulent flow above the canopy is dominated by intermittent downward moving gusts (Kaimal and Finnigan, 1993).

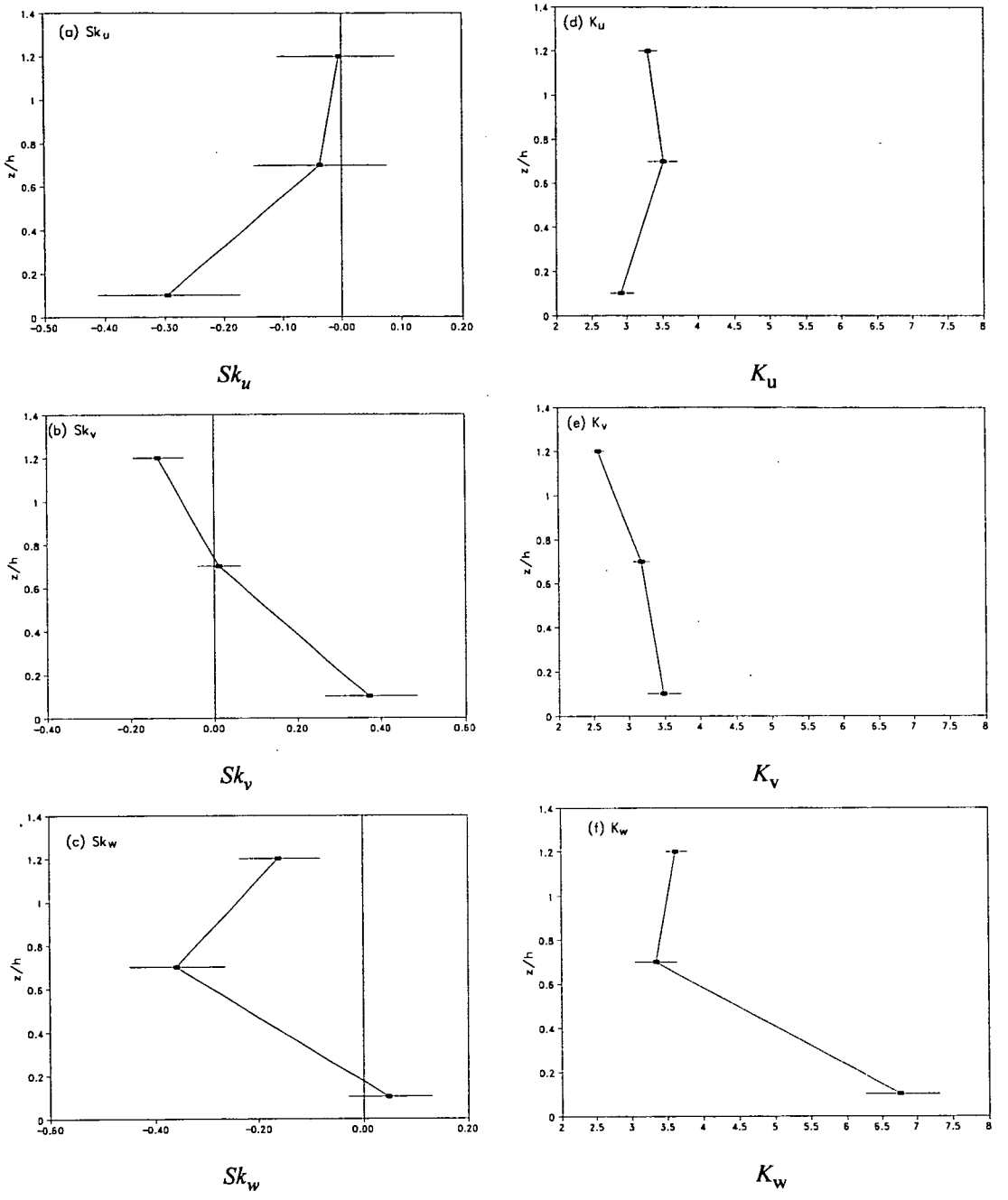

Fig. 5.2.3 *u*, *v* and *w* velocity skewness and kurtosis profiles for J213, 1991, where: (*a*) Sk_u; (*b*) Sk_v; (*c*) Sk_w; (*d*) K_u; (*e*) K_v and (*f*) is K_w. Error bars are ± 1 standard deviation.

Many comprehensive studies of the profiles of skewness through plant canopies have been published for various canopy types (Raupach *et al.*, 1986; Shaw and Seginer, 1987; Baldocchi and Hutchison, 1987; Baldocchi and Meyers, 1988*b*; Raupach, 1988 Amiro and Davis, 1988; Amiro, 1990*a*; Gardiner, 1993). The most relevant work is that of Amiro and Davis (1988) in a black spruce forest; Amiro (1990*a*) in jack pine and black spruce forests; and Gardiner (1993) at Rivox. All the studies report maximum values of Sk_u of ~ 1, and maximum negative values of Sk_w ~ -1 in the canopy crowns. The data presented in Figure 5.2.3*a*, 5.2.3*b* and 5.2.3*c* shows none of these characteristics except a negative Sk_w peak at ~ 0.7*h*. The lateral *v* velocity skewness, Sk_v, is expected to be around zero as canopy homogeneity should not lead to a net velocity cross-stream component. The Sk_v value at 0.1*h* is rather larger than might be expected, although this may be due to the slightly sloping terrain at the site (Figure 5.2.3*b*).

The kurtosis profiles at Rivox show a situation closer to that expected. The kurtosis fourth moment statistic gives a measure of the peakedness of the distribution of fluctuations, with a Gaussian distribution having a value of three. The kurtosis values of all three velocity components above the canopy are close to the Gaussian value as we would expect (Figures 5.2.3*d*, 5.2.3*e* and 5.2.3*f*). The profile of K_u shows a slight maximum in the canopy crown indicating more extreme events contributing to the *u* velocity fluctuations. For the *v* and *w* components, the maximum kurtosis is found at 0.1*h*, in the trunk space, with the K_w profile having a value of about 7. These results broadly agree with other studies in spruce forest although K_u and K_v often exhibit similar maxima in the canopy crown (Amiro, 1990*a*).

The unexpected behaviour of the skewness statistic is probably due to the corruption present in the raw data but why it seems to have a lesser effect on the kurtosis values is unclear. It would be expected that any data contamination would effect the kurtosis values more strongly than the skewness.

5.3 EULARIAN INTEGRAL TIME AND LENGTH SCALES

Integral Eularian time and length scales were derived for the *u* and *w* velocity components from their respective autocorrelations as described in section 2.1.8. The autocorrelation functions for *u* and *w* on days J207 and J213 are shown in Figures 5.3.1 and 5.3.2. The derived integral time and length scales are given in Tables 5.3.1 and 5.3.2 and shown in Figures 5.3.3 and 5.3.4.

The time scales at the different heights in the canopy, indicate the persistence or 'memory' of the flow at a point in space. By integrating over all the lags in the autocorrelation function, we can asses the strength of the memory of the dominant

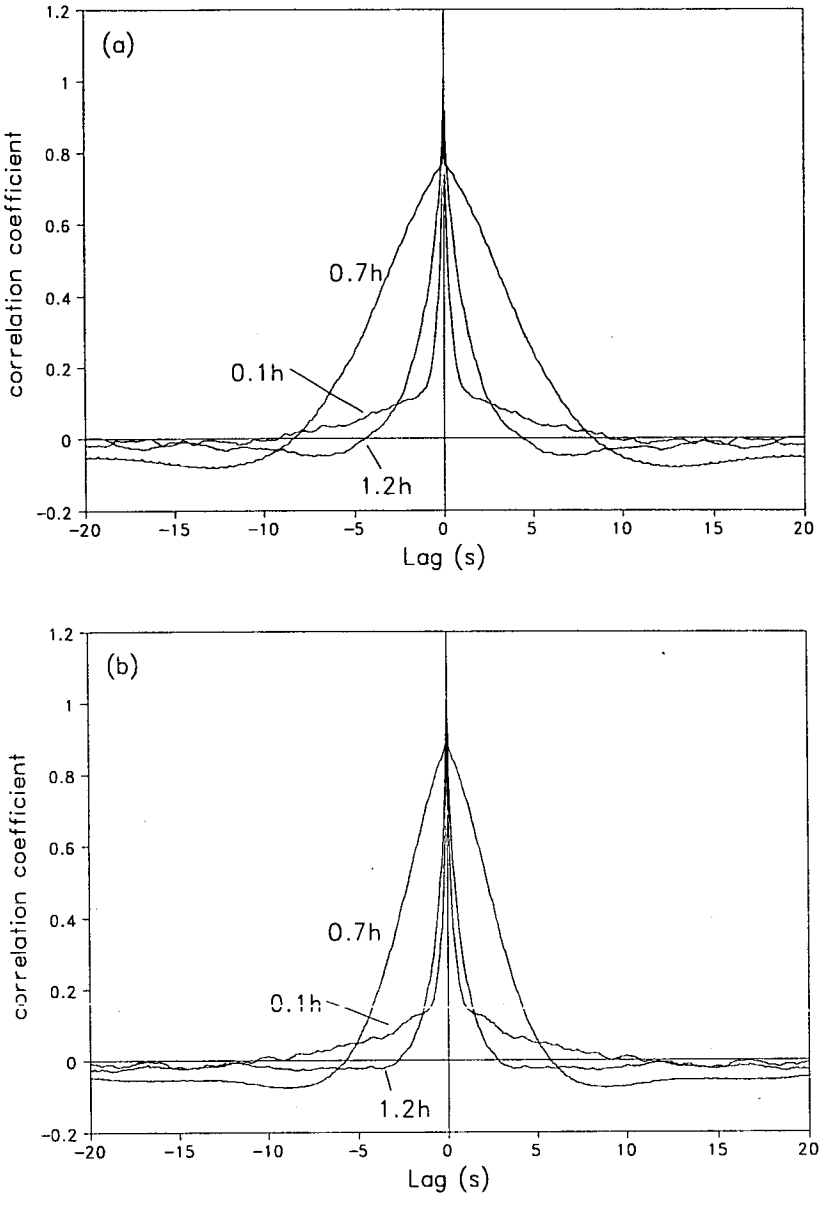

Fig. 5.3.1 Autocorrelations of w velocity for the three heights $1.2h$, $0.7h$ and $0.1h$ for days: (*a*) J207, 1991 and (*b*) J213, 1991.

portions of the flow. In the case of the w autocorrelation, the longest 'remembered' events occur in the trunkspace, where the first zero crossing occurred later than at $0.7h$. However, the autocorrelation function at $0.7h$ is considerably broader than that at $0.1h$ and so the integral time scale is greater in the canopy crown at $0.7h$.

The vertical velocity integral time scale, T_w, is seen in Figure 5.3.3*b* to be a maximum in the canopy crown, with the time scales at $1.2h$ and $0.1h$ again being similar. The streamwise velocity integral time scale, T_u, has a minimum in the canopy

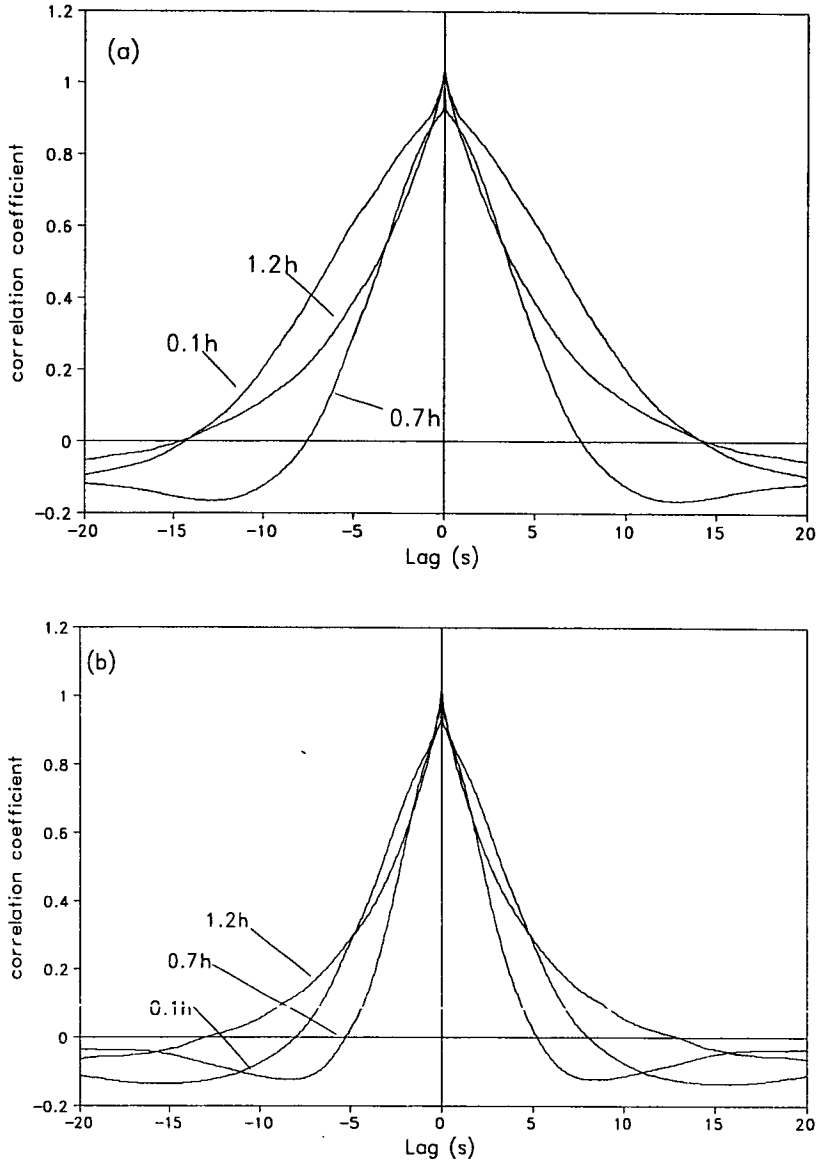

Fig. 5.3.2 Autocorrelations of u velocity for the three heights $1.2h$, $0.7h$ and $0.1h$ for days: (*a*) J207, 1991 and (*b*) J213, 1991.

crown, while the scales above the canopy and in the trunk space are of comparable duration, Figure 5.3.4*b*. The efficient attenuation of momentum in the canopy crown, as displayed in the Reynolds stress profiles is shown in Figure 5.2.1, and suggests that there would be a large amount of wake production in the crown as the predominantly horizontal flow interacts with the plant elements. This is confirmed by the time scales derived from the autocorrelations as the horizontal motions are broken up into turbulent wakes containing vertical velocity fluctuations.

The length scales for the two velocities are computed on the assumption that Taylor's Hypothesis is valid (section 2.1.8). As estimates of the size of dominant events, the length scales are useful, but it is likely that Taylor's Hypothesis is not valid within the canopy, despite the turbulence intensities being < +1 (Figures 5.2.3 and 5.2.4). Above the canopy, at $1.2h$ $L_w \sim 0.2h$ and $L_u \sim h$, and in the trunk space at $0.1h$ $L_w \sim 0.02h$ and $L_u \sim 0.15h$. These values compared well with other results in the literature (Raupach *et al.*, 1986; Raupach 1988, Raupach *et al.*, 1989; Amiro, 1990*a*; Gardiner, 1993). Previously reported results have $L_w \sim h/3$ and $L_u \sim h$ at the canopy top whereas our values are slightly smaller than these. The variation with height of the time and length scale profiles presented here are also in general agreement with those in the literature.

Relative Height, (h)	τ_0 (s)		T_w (s)		$L_w = \overline{U}T_w$ (h)	
	J207	J213	J207	J213	J207	J213
1.2	5.8	2.8	1.4	0.6	0.23	0.18
0.7	8.4	5.7	3.0	2.3	0.03	0.15
0.1	9.1	9.1	0.8	0.8	0.02	0.03

Table 5.3.1 Integral Eularian time and length scales, T_w and L_w, and the lag at first zero crossing, τ_0, derived from the w autocorrelation functions, Figure 5.3.1, for J207 and J213, 1991.

Relative Height, (h)	τ_0 (s)		T_u (s)		$L_u = \overline{U}T_u$ (h)	
	J207	J213	J207	J213	J207	J213
1.2	14.4	12.9	4.7	3.7	0.79	1.02
0.7	7.6	5.2	3.6	2.3	0.04	0.15
0.1	14.2	8.1	6.4	3.5	0.17	0.14

Table 5.3.2 Integral Eularian time and length scales, T_u and L_u, and the lag at first zero crossing, τ_0, derived from the u autocorrelation functions, Figure 5.3.2, for J207 and J213, 1991.

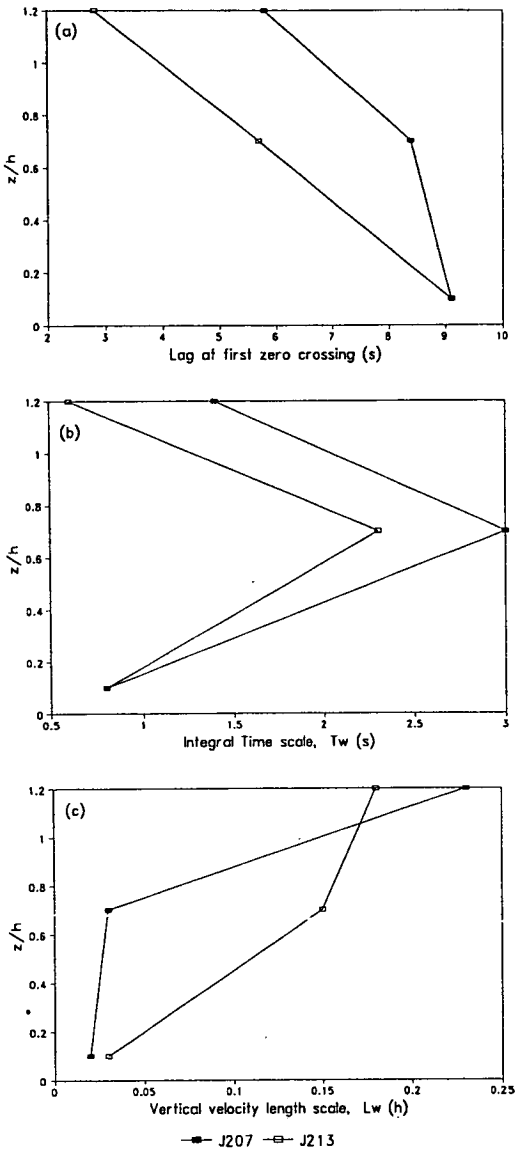

Fig. 5.3.3 Mean *w* Eularian length and time scales for J207 and J213, 1991, against normalised height *z/h*, calculated from the *w* autocorrelations in Figure 5.3.1. Where: (*a*) shows τ_0; (*b*) T_w and (*c*) L_w.

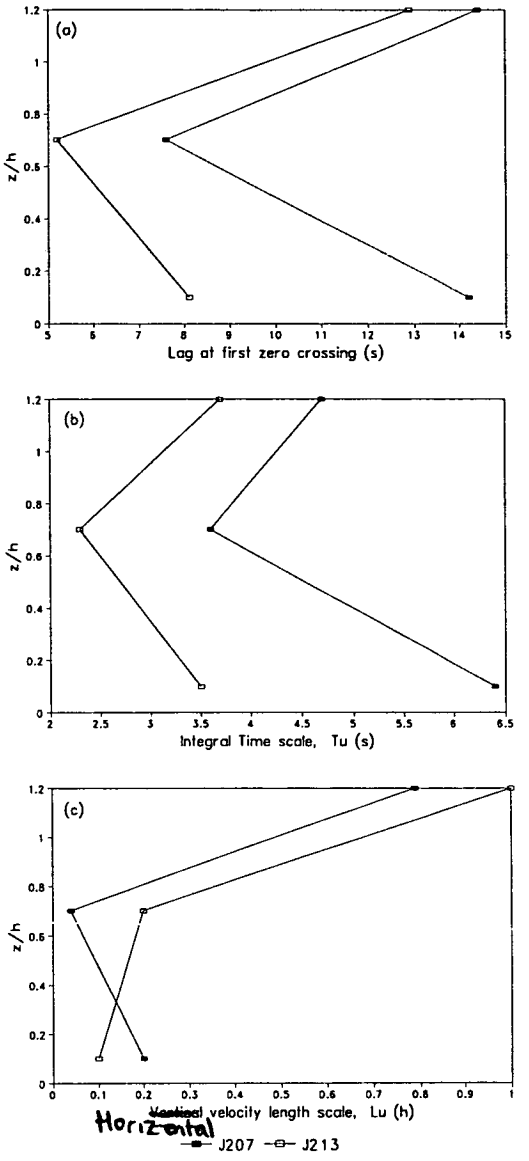

Fig. 5.3.4 Mean *u* Eularian length and time scales for J207 and J213, 1991, against normalised height *z/h*, calculated from the *u* autocorrelations in Figure 5.3.2. Where: (*a*) shows τ_0; (*b*) T_u and (*c*) L_u.

5.4 CROSS-CORRELATION ANALYSIS OF VELOCITY FLUCTUATIONS

The main limitation of the Fast Fourier Transform program used for the correlation analysis, was the maximum block size of 2048 data points as discussed in section 3.3.3. This block size corresponds to a time period of 112.5 seconds of data. If cross-correlations are performed on data with this block size, then any events overlapping the block edges will not be fully correlated. In practice, the lags of ± 60 s were adequate to represent the velocity cross-correlations between the three heights, when averaged over 15 blocks per 30 minute file.

The velocity cross-correlation results for u, v and w at $0.7h$ and $0.1h$, with $1.2h$ as reference, for J207 and J213, are presented in Figures 5.4.1 to 5.4.4 as ensemble averages over 17 and 8 data files, respectively. The lags are shown in seconds but can be converted into normalised lags by multiplying them by $\overline{U}/\Delta z$ where $\overline{U}$ is mean wind speed at the reference level and Δz is the height separation between the two sensors. For cross-correlations on J207, $\overline{U}/\Delta z$ = 0.33 and 0.15 s^{-1}, at $0.7h$ and $0.1h$, respectively, and similarly for J213, $\overline{U}/\Delta z$ = 0.56 and 0.25 s^{-1}, at $0.7h$ and $0.1h$ respectively.

At $0.7h$ on both days the u velocity cross-correlations at $0.7h$ were lagged with respect to those at $1.2h$ (see Figures 5.4.1*a* and 5.4.2*a*). Thus, momentum events occurring in the canopy crown first appeared above the canopy. The lag time for J207 was 6.0 s and for J213, 3.8 s, indicating the faster penetration of correlated events on the day with greater wind speed above the canopy. On J213, and to a lesser degree on J207, u cross-correlations exhibited a negative secondary peak occurring at negative lag, i.e. events occurring first within the canopy. There is evidence from observations of organised structures in other forests, (Gao *et al.*, 1989) and in Rivox forest, (Gardiner, 1993) that large gust events are both preceded and followed by a gentle updraft out of the forest, i.e. an ejection. These secondary negative correlations could thus be explained physically as correlations between a pre-gust ejection detected at $0.1h$ and the gust itself, detected at $1.2h$ at a later time. ~~Alternatively, it could equally well result from the detection of the gust at $0.1h$ and the later detection of a post-gust ejection at $1.2h$. The secondary peak probably results from a combination of these two processes.~~

The v velocity peak cross-correlations at $0.7h$ both have negative lags of less than 1 s, (-0.77 s and -0.93 s for J207 and J213 respectively) as shown in Figures 5.4.1*b* and 5.4.2*b*. This implies that there are lateral v velocity fluctuations occurring inside the canopy which are subsequently transported outwards and detected at the $1.2h$ instrument. These fluctuations would occur as gusts penetrate the canopy and

produce turbulent wakes due to the form drag of tree elements. It is postulated that these fluctuations are then transported upward by ejections where they are detected above the canopy (Baldocchi and Meyers, 1988*b*).

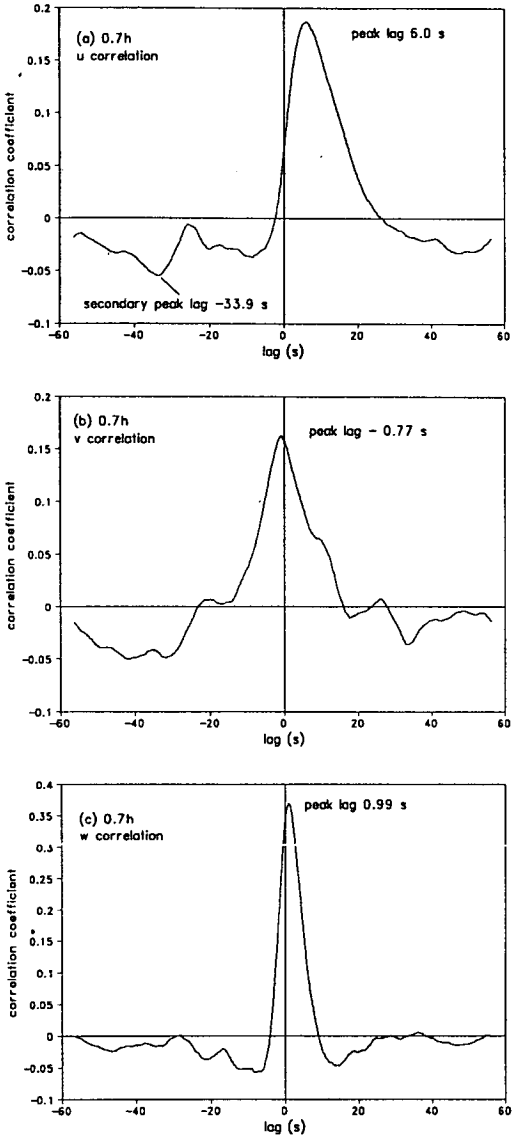

Fig. 5.4.1 Cross-correlations of: (*a*) *u*, (*b*) *v* and (*c*) *w* at 0.7*h* with respect to 1.2*h* for J207, 1991.

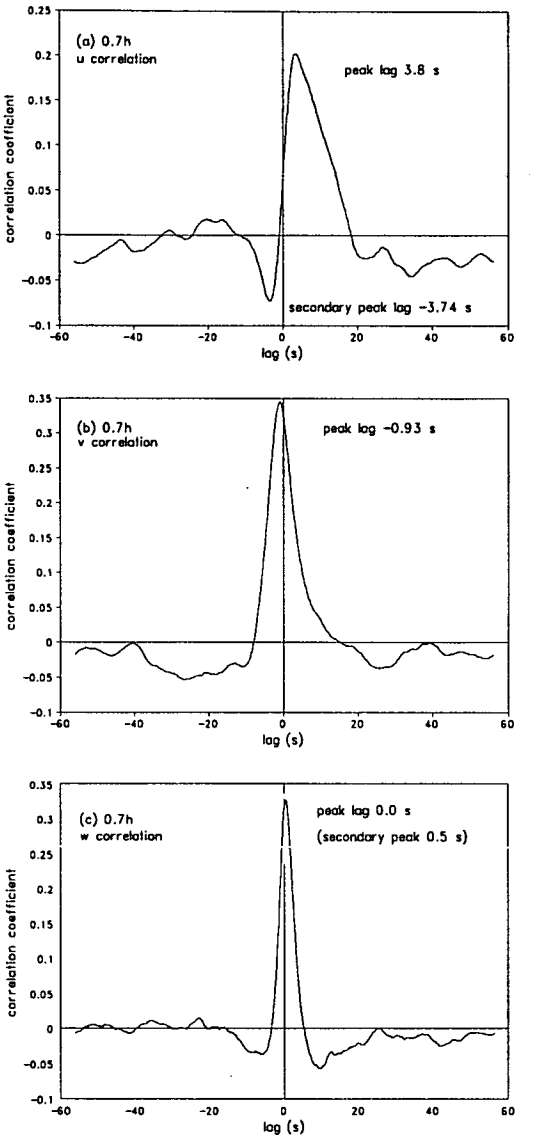

Fig 5.4.2 Cross-correlations of: (*a*) *u*, (*b*) *v* and (*c*) *w* at 0.7*h* with respect to 1.2*h* for J213, 1991.

The *w* peak cross-correlations at 0.7*h* for J207 and J213 with respect to 1.2*h* occurred at lags of 0.99 s and 0.0 s respectively, Figures 5.4.1*c* and 5.4.2*c*. The *w* cross-correlation on J213 had a secondary peak at 0.5 s which was very similar in size to the main peak. The positive peak lag on J207 and the positive secondary peak lag

on J213 indicate again that events are penetrating the canopy crown from above. The peak lag on J213 at 0.0 s indicates vertical velocity fluctuations occurring simultaneously at $0.7h$ and $1.2h$.

Zero lags in vertical velocity cross-correlations are difficult to visualise but can be explained in physical terms with reference to the prognostic equation for a turbulent gust, U_i', derived from the governing equation for the conservation of momentum, (Stull, 1988):

$$\frac{\partial U_i'}{\partial t} = -\overline{U}_j \frac{\partial U_i'}{\partial x_j} - U_j' \frac{\partial \overline{U}_i}{\partial x_j} - U_j' \frac{\partial U_i'}{\partial x_j} - \frac{1}{\overline{\rho}} \frac{\partial p'}{\partial x_j} + \nu \frac{\partial^2 U_i'}{\partial x_j^2} + \frac{\partial \left(\overline{U_i' U_j'} \right)}{\partial x_j} \qquad (5.4.1)$$

where the terms for buoyancy and the Coriolis force are omitted.

From examination of contributions to velocity fluctuations from high frequency spectral components, Allen (1968) postulated that at the lowest level in the canopy: "most of the variation in horizontal air flow is due to pressure waves associated with large scale eddies". The pressure perturbation term in equation 5.4.1, $1/\overline{\rho}.\partial p'/\partial x_j$, is the force due to the gradient of pressure fluctuations and it shows explicitly the link between pressure and velocity fluctuations. In physical terms, a large gust impinging on the canopy has an associated pressure front, which propagates through the canopy, creating in-phase velocity fluctuations of a similar scale to the pressure fluctuations, Holland (1989). Most importantly, the pressure front will propagate to the lowest levels in the canopy to create irrotational motions, whereas the gust itself is attenuated by the canopy into rotational velocity fluctuations in turbulent wakes. The propagation of the pressure wave through the canopy is essentially instantaneous and results in zero w velocity cross-correlation lags with height.

The strength of mean and turbulent winds in the canopy crown swamps the effect of pressure perturbations on the velocity fluctuations, where the positively lagged cross-correlations occur as a result of the passage of the gust through the instrument array. The primary zero lag peak in the J213 w velocity cross-correlation, which is a result of the pressure front, is superimposed on the positive lags from the passage of the gust, Figure 5.4.2*c*. The lack of zero lag in the J207 w cross-correlation at $0.7h$ may be attributed to the weaker wind speeds on that day, as is the case for the $0.1h$ cross-correlations.

Zero lags for w velocity fluctuations have been reported previously: in two deciduous forests (Baldocchi and Meyers, 1988*b*; Shaw and Zhang, 1992); in a mixed deciduous forest at Camp Borden, Ontario, (Gao *et al.*, 1989); in a Eucalyptus forest, (Raupach *et al.*, 1989); and in a model wheat crop in a wind tunnel, (Raupach *et al.*,

1989). Raupach *et al.* (1989) cite similar observations made in a wind tunnel study of smooth-wall boundary layers by Antonia *et al.* (1988).

In the trunk space at $0.1h$, the cross-correlation results on J213 are similar to those at $0.7h$ in the canopy crown (Figure 5.4.4). The u velocity again lags that above the canopy, this time with a slightly larger lag of 4.7 s. The negative secondary peak is now more pronounced and also at a slightly larger negative lag. The v velocity cross-correlation has a negative lag of less than one second with a well defined peak. These results are consistent with gust/ejection events penetrating deep into the canopy. The w velocity peak cross-correlation again occurs at zero lag, although now with a much reduced correlation coefficient than observed at $0.7h$. The w velocity fluctuations at the forest floor would thus appear to be a result of pressure gradient forces, whereas the horizontal velocity fluctuations are a direct result of large momentum structures penetrating through the canopy which swamp any contribution from pressure gradient forces. The trunk space on J213 was clearly well coupled to the atmosphere above the forest.

At $0.1h$ for J207 the velocity cross-correlations with respect to $1.2h$ are much weaker than those at $0.7h$ on the same day or at $0.1h$ on J213 (Figure 5.4.3). They also show little of the characteristics of the other cross-correlations, with no well defined peaks, and they indicate that the trunkspace on J207 is effectively decoupled from the atmosphere above the canopy. This is perhaps not entirely unexpected as the wind speed was less on this day, implying fewer, less energetic, gust events, with weaker associated pressure fronts.

In a mixed deciduous forest at Camp Borden, Ontario, Shaw and Zhang (1992) reported negative lags of streamwise velocities in the trunk space of the forest relative to the tree top measurements. The implication of their results was that the horizontal flow in the trunk space was leading that above the forest and was being driven by pressure gradient forces. In Rivox, our results show that when the trunk space is coupled to the atmosphere above, there is direct transfer of momentum from above the forest, with positive lags in the horizontal velocity cross-correlations. The velocity fluctuations induced by pressure fronts associated with large structures are only detectable in the vertical velocity component, as they also were in the Shaw and Zhang experiment. Clearly, the density of the canopy effects the degree of influence of these processes. In the dense canopy at Rivox, none of the ensemble averaged cross-correlations, or individual FFT block results, showed any leading streamwise flow in the sub-canopy.

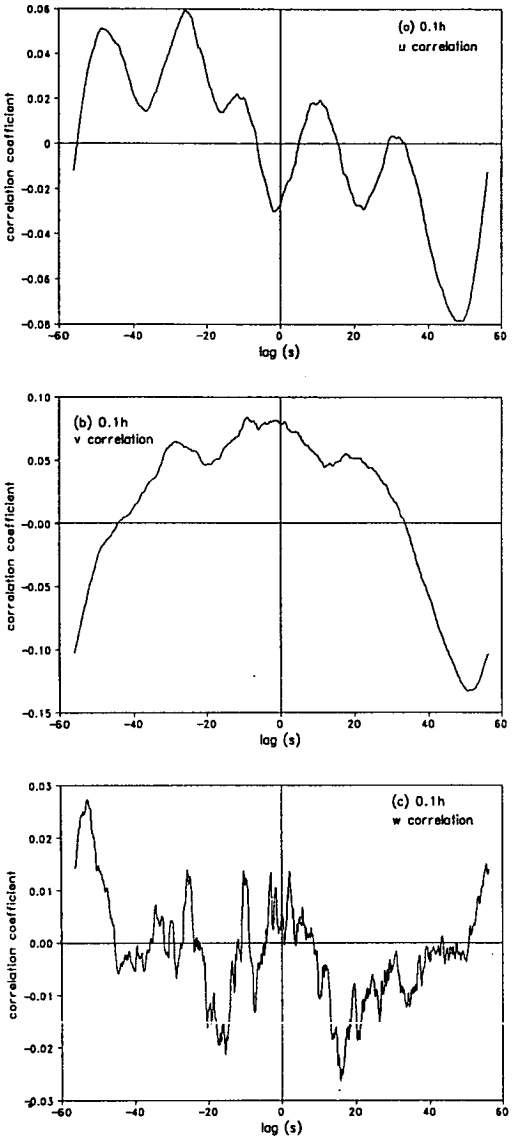

Fig 5.4.3 Cross-correlations of: (*a*) *u*, (*b*) *v* and (*c*) *w* at 0.1*h* with respect to 1.2*h* for J207, 1991.

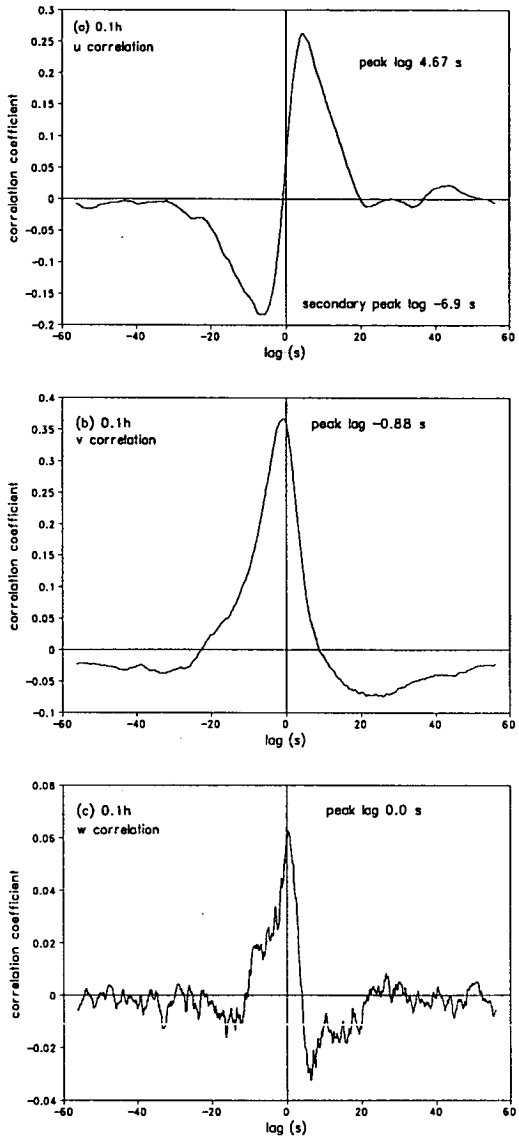

Fig 5.4.4 Cross-correlations of: (*a*) *u*, (*b*) *v* and (*c*) *w* at 0.1*h* with respect to 1.2*h* for J213, 1991.

5.5 SUMMARY AND CONCLUSIONS

(i) On the two days, J207 and J213, mean horizontal wind speed and Reynolds stress profiles were highly sheared in the canopy crown. The attenuation of momentum by the forest canopy was observed to be extremely efficient with the momentum flux at $0.7h$ being ~ 2 - 3% of that at $1.2h$.

(ii) The maximum turbulence intensities for u, v and w occurred in the canopy crown on J207, the day with lighter wind speeds. The maximum turbulence intensities for u and v on J213 occurred in the trunk space, and for w in the canopy crown.

(iii) The skewness values for all days and heights did not conform to the numerous normalised plant canopy profiles published elsewhere. The presence of corruption in the data files was thought to have adversely affected the higher order statistics. The kurtosis statistics appeared to represent reasonably the expected form for the canopy but, because of the corrupted data, neither skewness or kurtosis statistics were considered reliable.

(iv) Eularian integral time sales for u and w had their minimum and maximum values, respectively, in the canopy crown. The integral Eularian length scale, L_u, was of the order of tree height, h, above the canopy at $1.2h$, and ~ $0.15h$ in the trunk space at $0.1h$. Similarly L_w was of order ~ $0.2h$ above the canopy, and ~ $0.02h$ in the trunk space.

(v) The canopy crown at $0.7h$ was well coupled to the atmosphere above the forest on both days, with the dominant influence on velocity fluctuations being from the penetration of motions originating above the forest. Cross-correlation lags of 3.8 and 6.0 s were found for streamwise velocities between $1.2h$ and $0.7h$ on the two days. A zero lag peak was observed in the w cross-correlation on one of the days, probably indicating the influence on w velocity fluctuations of pressure fronts associated with large gust events.

(vi) On J213 the flow at $0.1h$ was found to be well coupled to that at $1.2h$, with positively lagged peak streamwise cross-correlations of 4.7 s. This same day also had a zero lagged w cross-correlation with respect to $1.2h$ indicating the influence on w velocity fluctuations of pressure fronts associated with large gust events.

Results from J207 showed no coupling between $0.1h$ and $1.2h$ which is perhaps attributable to the lower wind speeds than those occurring on J213.

CHAPTER 6.
SPECTRAL ANALYSIS

6.1 INTRODUCTION

Spectral analysis in and above plant communities can tell us much about the nature of the interaction between the canopy and the atmosphere. Dominant transport events give rise to spectral peaks, which allow us to estimate typical time and length scales through the canopy. The form of the u, v and w velocity power spectra at different levels in the canopy also gives an insight into the changes in the flow through the canopy. Deviations of peak spectral frequencies and inertial subrange slopes within plant canopies from those expected in the free atmosphere, are a result of physical processes such as drag forces exerted on the flow by vegetation, waving of plant elements, and shelter effects. These processes are extremely important in the context of scalar transport in the canopy, and spectral analysis can aid our understanding of them.

There have been many spectral analyses reported in the literature, employing sensors with a sufficiently fast response time, in a variety of real and artificial canopies. There are, however, relatively few studies in dense forests, with LAI $\geq$ 10, which have a dense closed canopy and open trunk space, (Amiro and Davis, 1988; Bergström and Högström, 1989; Amiro, 1990*b*; Gardiner, 1993).

There have been fewer studies reporting spectral analyses of scalar quantities (over a pine forest by Bergström and Högström (1989), over wheat stubble by Kaimal *et al.* (1972), over field crops by Ohtaki (1985), over deciduous forest by Anderson *et al.* (1986) and Baldocchi and Meyers (1991), and over three boreal forest types Amiro (1990*b*). The study by Amiro (1990*b*) is the most comprehensive, reporting velocity and temperature measurements above and within three forest canopies, black spruce, jack pine and Aspen. The work of Gardiner (1993) was conducted at Rivox in 1989 with an array of propeller anemometers, and reports on periods with higher wind speeds than presented here, (at 1.2h $\overline{U}$ ~ 6.5 m s^{-1}), and was restricted to velocity measurements.

Two sets of data were analysed, the first of these data sets is a combination of days J191, J198 and J207. Average wind speed at 1.2h was of 3.1 m s^{-1} for J191/ J198, and 2.5 m s^{-1} for J207. All spectra at 1.2h in this data set comes from a combination of files on days J191/ J198, all 0.7h and 0.1h spectra come from J207. The velocity power and co-spectra at 1.2h on days J207 and J191/ J198 were very similar, and consequently the J207, 1.2h velocity spectra are not shown. The second data set came from day J213 and had an average wind speed of 4.2 m s^{-1} at 1.2h.

Thermal stability was again very slightly unstable/near neutral for all days, where the average thermal stability index, $(z-d)/L$, was - 0.003 on J191, and - 0.01 on J198 and J213. Stability on J207 was estimated also to be unstable/near neutral as discussed in section 5.1.

Contamination of data files was present as discussed in section 3.2.6 and in Chapter 5. The contamination was present on specific A/D board input channels and can be identified in power spectral plots of $nS(n)$ plotted against n, by an upturn in the high frequencies with a log - log slope of +1, characteristic of noise spikes, (Kaimal and Finnigan, 1993).

All power and co-spectra presented are plotted in normalised form against the normalised frequency $n(h-d)/\overline{U}$ which allows comparison of spectra between very different canopy types and flow regimes (Kaimal and Finnigan, 1993). Power and co-spectral densities are normalised by the time series variance and covariance, respectively, so that the areas under the spectral density curves equal unity (section 2.1.9). Variance and covariance statistics were calculated from the time series prior to them being Fast Fourier transformed, i.e. after windowing and mean removal (section 3.3.3).

6.2 VELOCITY SPECTRA

6.2.1 Velocity Power Spectra

The u, v and w velocity power spectra at $1.2h$, for both data sets, exhibit the expected form above a canopy and are shown in Figures 6.2.1 and 6.2.2. As reported elsewhere, the peak frequencies for the horizontal and vertical components are different, with u and v power spectral peaks occurring at a lower frequency than the w peak (Tables 6.2.1 and 6.2.2). This indicates that above the canopy horizontal motions are of a larger scale than vertical motions, assuming they share a common advection velocity past the sensor (Kaimal and Finnigan, 1993).

The inertial sub-range log-log slopes in the $1.2h$ power spectra were estimated by linear regression on frequency ranges estimated to bound the inertial subrange, and are given in Tables 6.2.3 and 6.2.4. The values at $1.2h$ generally approach the expected value of -2/3, section 2.1.9, but in both data sets the w power spectra has a slope slightly less than this value. In the J213 data set, the determination of the end of the inertial sub-range is made more difficult due to the rapid attenuation of the signal, after about 6 Hz, by the electronic low-pass filters . The same filters were used during all

BCN: L 6538292 Owner:LOUGH Civl: U Tech: MON
Record Status: rec/rec
Original operator: IRENE 11-01-94 Update operator: IRENE 11-01-94
Proof Last : y 00-00-00 (last print) MARC Request : n
MARC to CURC : n Remove from CURC : n
Non-Circulating : n LSP Request : n

001 GeacU06852921
004 UUzae1e2698371
008 940111s1993 st L C eng
Date <940111>Natur <s>Date1 <1993>Date2 < >Cntry <st >Illus < >Intel < >Matde <L>Form < >
Gov < >Cont < >Fest < >Index <0>Tithd < >Lit¶m < >Biog < >Lang <eng>Per < >BL < .
049 UUzac
100 1Uza McCracken£hPeter J.£kPeter John
245 10£aTurbulent exchange of momentum and carbon dioxide of a sitka spruce plantation£dPeter J. McCracken
260 UU£c1993
502 UU£aThesis (Ph.D)--University of Edinburgh, 1993

No errors found

HOLDINGS INFORMATION

001 GeacU06852921
966 UU£c1£iSP.COL£mREF£sTheses Sect.1
966 2 UU£b30150011720718£c2£1DARWIN£mNORMAL£sTheses Section

Error Summary of record
Tag 966 Occ 01 Error no. 00044
Missing mandatory subfield b

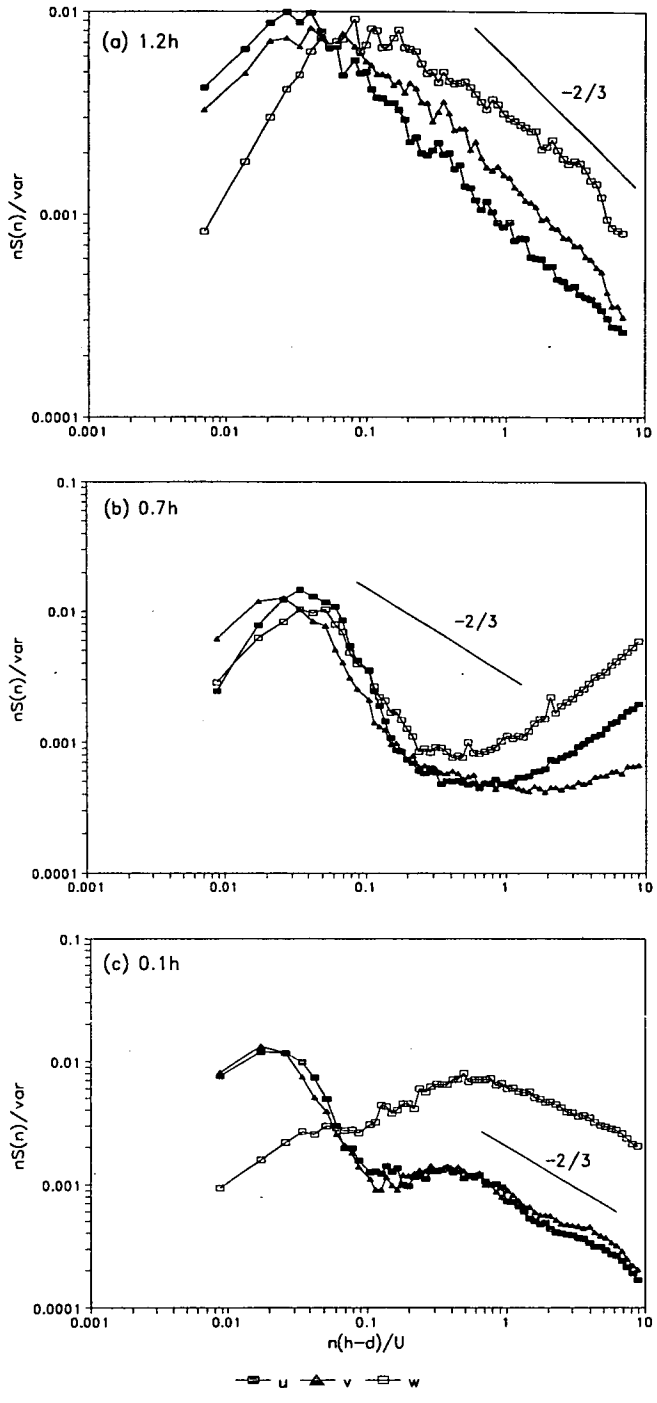

Fig 6.2.1 J207/ J191/ J198 normalised power spectral densities $nS_i(n)/\sigma_i^2$, where *i* denotes the *u*, *v* and *w* velocity components, plotted against normalised frequency, $n(h-d)/\overline{U}$, at heights: (*a*) 1.2*h*; (*b*) 0.7*h*; and (*c*) 0.1*h*. [$\overline{U}$ = 3.1 and 2.5 m s^{-1} for J191/ J198 and J207, respectively, and $(h - d) \sim 2.4$ m.]

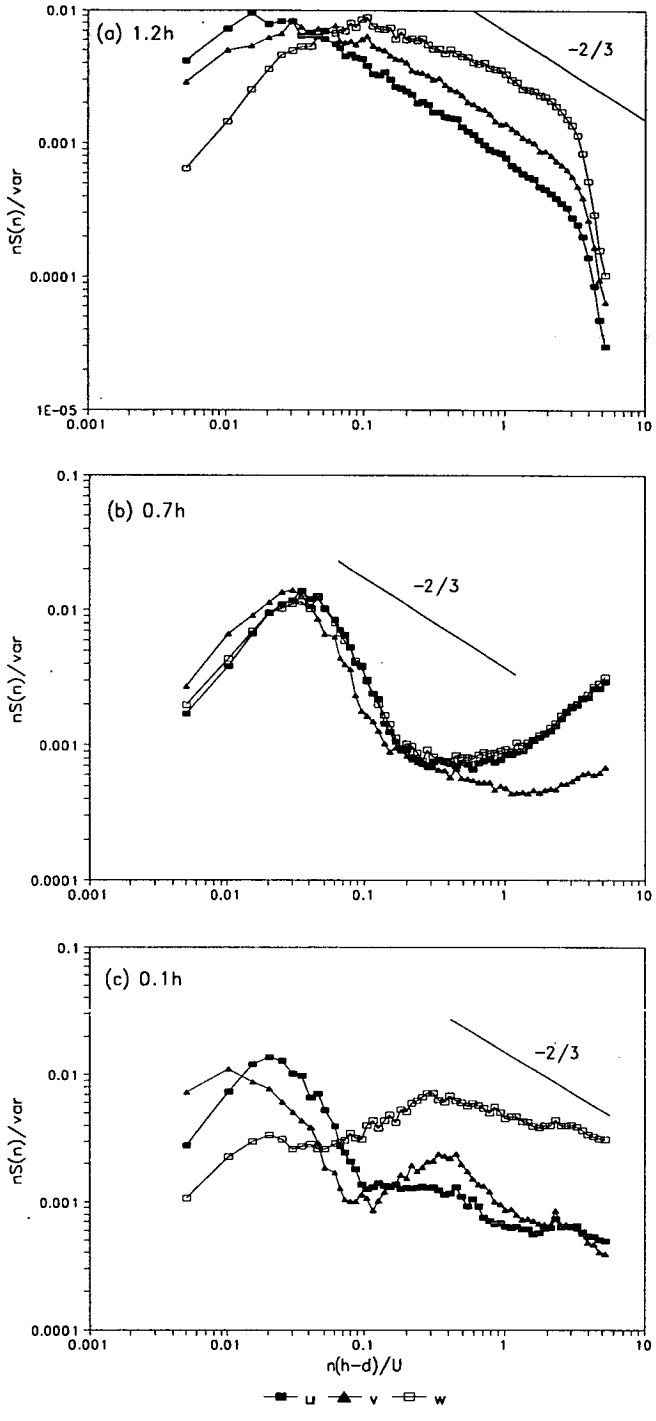

Fig 6.2.2 J213 normalised power spectral densities $nS_i(n)/\sigma_i^2$, where i denotes the u, v and w velocity components, plotted against normalised frequency, $n(h-d)/\overline{U}$, at heights: (*a*) 1.2h; (*b*) 0.7h; and (*c*) 0.1h. [$\overline{U}$ = 4.2 m s^{-1} and (h - d) ~ 2.4 m.]

z/h	velocity component	n_p (Hz)	$n_p(h-d)/\overline{U}$
1.2	u	0.03 – 0.06	0.02 – 0.05
1.2	v	0.02 – 0.09	0.02 – 0.07
1.2	w	0.09 – 0.25	0.07 – 0.2
0.7	u	0.02 – 0.05	0.02 – 0.04
0.7	v	0.01 – 0.03	0.01 – 0.02
0.7	w	0.03 – 0.06	0.02 – 0.05
0.1	u	0.01 – 0.03	0.01 – 0.03
0.1	v	0.01 – 0.03	0.01 – 0.03
0.1	w	0.3 – 0.8	0.4 – 0.5

Table 6.2.1 Peak frequencies of J207/ J198/ J191 u, v and w power spectra where: natural peak frequency is n_p; and normalised peak frequency is $n_p(h-d)/\overline{U}$.

z/h	velocity component	n_p (Hz)	$n_p(h-d)/\overline{U}$
1.2	u	0.02 – 0.07	0.01 – 0.04
1.2	v	0.05 – 0.1	0.03 – 0.06
1.2	w	0.1 – 0.4	0.09 – 0.2
0.7	u	0.03 – 0.09	0.02 – 0.05
0.7	v	0.03 – 0.09	0.02 – 0.05
0.7	w	0.03 – 0.09	0.02 – 0.05
0.1	u	0.03 – 0.09	0.02 – 0.05
0.1	v	0.01 – 0.02	0.008 – 0.01
0.1	w	0.35 – 0.7	0.2 – 0.4

Table 6.2.2 Peak frequencies of J213 u, v and w power spectra where: natural peak frequency is n_p; and normalised peak frequency is $n_p(h-d)/\overline{U}$.

measurements and the presence of such severe attenuation in the J213, 1.2h data set (Figure 6.2.2a) and not in others is puzzling.

In the canopy crown, at 0.7h, the spectra exhibit the high frequency noise associated with the data contamination discussed in section 6.1, which has a log - log slope of about +1, typical of white noise. Fortunately, the main signal lies in lower frequency ranges than the noise; the spectral peaks for u, v and w lie at similar frequencies to those at 1.2h, with the w peak frequency being shifted to slightly lower frequencies. The slope after the spectral peak, indicates a rapid roll-off of energy with

a slope much greater than the -2/3 exhibited above the canopy as shown in Figures 6.2.1*b* and 6.2.2*b*. Clearly, the large dominant eddies represented by the peak frequencies, are being dissipated much more quickly than in the free atmosphere. The interaction of the flow with plant elements by form drag has been postulated to provide this short-circuit of the normal energy cascade (Amiro and Davis, 1988; Baldocchi and Meyers, 1988*b*; Kaimal and Finnigan, 1993). Form drag of the tree parts on the flow produces wakes of higher frequency than the impinging turbulence, similarly waving of branches and leaves can cascade low frequency energies to higher frequencies (Amiro and Davis, 1988; Baldocchi and Meyers, 1988).

The form of the velocity power spectra of the horizontal and vertical components of the flow in the trunk space diverges (Figures 6.2.1*c* and 6.2.2*c*). The horizontal components still display a rapid roll-off after the spectral peak which lies at normalised frequencies of about 0.02 (Tables 6.2.1 and 6.2.2), up to an apparent secondary peak at normalised frequencies of about 0.3 - 0.4. The vertical velocity displays a diminished spectral peak at lower frequencies and has a peak at the peak frequency of the secondary peak in the horizontal velocity spectra. The inertial sub-range slopes after the secondary peaks approach the -2/3 slope of the of the free atmosphere (see Tables 6.2.3 and 6.2.4).

This secondary peak in trunk space velocity power spectra has been reported before in a variety of canopy types, (Baldocchi and Hutchison, 1988; Amiro and Davis, 1988; Baldocchi and Meyers, 1988*b*; Amiro, 1990*b*; Gardiner, 1993). It has

z/h	velocity component	frequency range of regression (Hz)	slope	standard error	R^2
1.2	*u*	0.18 – 1.03	-0.698	0.042	0.939
1.2	*v*	0.22 – 1.03	-0.654	0.047	0.923
1.2	*w*	0.22 – 0.6	-0.584	0.070	0.873
0.7	*u*	0.07 – 0.17	-2.090	0.100	0.984
0.7	*v*	0.07 – 0.17	-2.349	0.148	0.973
0.7	*w*	0.07 – 0.17	-1.590	0.103	0.972
0.1	*u*	0.5 – 2.13	-0.637	0.028	0.971
0.1	*v*	0.5 – 2.13	-0.804	0.048	0.949
0.1	*w*	1.95 – 5.78	-0.520	0.024	0.977

Table 6.2.3 Inertial subrange slope regressions of $\log(nS_i(n))$, where *i* is *u*, *v* or *w*, against $\log(n)$, as shown in Figure 6.2.1, for J207/ J191/ J198.

z/h	velocity component	frequency range of regression (Hz)	slope	standard error	R^2
1.2	u	0.15 – 2.8	-0.718	0.008	0.995
1.2	v	0.2 – 2.8	-0.647	0.009	0.994
1.2	w	0.2 – 2.8	-0.416	0.013	0.972
0.7	u	0.11 – 0.22	-1.936	0.068	0.992
0.7	v	0.11 – 0.22	-2.241	0.159	0.966
0.7	w	0.11 – 0.22	-1.900	0.074	0.990
0.1	u	—	—	—	—
0.1	v	—	—	—	—
0.1	w	—	—	—	—

Table 6.2.4 Inertial subrange slope regressions of $\log(nS_i(n))$, where i is u, v or w, against $\log(n)$, as shown in Figure 6.2.2, for J213.

often been attributed to the interaction of the turbulent flow with tree elements, i.e. wake or waving production, but it was noted by Amiro (1990*b*) that this secondary spectral peak usually occurs in the dead branch trunk space. He further states that in the trunk space there are few canopy elements which could be responsible for wake or waving production, and such turbulence would require to be transported from the canopy crown where these processes are more likely to occur.

It would appear that between the canopy crown and the trunk space a process, or processes, are taking place that diminish a mid-frequency portion of the u and v spectral densities and those of the w component in the low to mid-frequencies. The cross-correlation analysis of Chapter 5 identified that mainly horizontal gusts were able to penetrate the trunk space when the sub-canopy was well coupled to the atmosphere above the forest, whereas w fluctuations in the trunk space were much weaker and linked to pressure gradient forces associated with the gusts. The large low frequency peak in the u and v power spectra at $0.1h$, may represent gust/ejection structures penetrating to the trunk space. The w spectral densities at this frequency are much smaller, possibly reflecting that the w velocities are a result of pressure gradient forces associated with the gust.

The secondary peak could tentatively be attributed to the large scale horizontal motions in the trunkspace interacting with the tree trunks as low frequency horizontal energies would be fed into turbulent wakes with both horizontal and vertical components with higher frequency than originally. The secondary spectral peak

occurs in the trunk space at a frequency of about 0.5 Hz. At 0.1h the mean wind speed $\overline{U}$ was about 0.6 m s^{-1} on J213, thus this frequency indicates eddies with a duration of around 2 s and a length scale about 1 m. This distance is of the order of the tree spacing throughout the forest.

Amiro (1990*b*) suggested that the secondary spectral peak in forest trunk spaces were a result of u and v components continually feeding energy into the w component giving rise to the dip in the spectra at frequencies around the secondary spectral peak. No mechanism was postulated to explain this phenomenon. A further hypothesis was put forward by Gardiner (1993), namely that the dip in the power spectra is a result of extremely efficient absorption of energy at the tree resonant frequency. At the top of the canopy, and in the canopy crown, Gardiner (1993) postulated that there was sufficient energy to feed this absorption. The dip in the 0.1h power spectra presented here, however, would appear to be at a lower frequency than the tree resonant frequency indicated by Figure 16 of Gardiner (1993).

To obtain an estimate of the time and length scales of the dominant motions at the three levels, we can assume that Taylor's hypothesis is valid, and thus that the time scale of a dominant motion is simply the reciprocal of the peak frequency. These estimated time scales are shown in Table 6.2.5, with associated length scales using the definitions in section 2.1.8. These values are somewhat different to the Eularian time scales derived from the w and u autocorrelations in Chapter 5, Tables 5.3.1 and 5.3.2. This is not unexpected as the peak frequency indicates the scales of the dominant eddies, whereas the w autocorrelation Eularian integral time scales take account of all eddy motions.

The length scales of the dominant motions between the two data sets agree well for L_u and L_w at all levels except in the canopy crown. Above the canopy, the dominant motions have L_u values of the order of ~ 4 - 14h, while L_w values are of order ~ 1 - 3h. Within the canopy, Taylor's hypothesis is not valid and the estimated time and length scales are not reliable in magnitude. The low mean horizontal wind speed at 0.7h on J207, resulted in lower values of L_u and L_w than found on J213 at 0.7h. A similar effect was noted in the length scales derived in Chapter 5, and again indicates that large horizontal gusts did not penetrate to the 0.7h level on J207 as strongly as on J213.

height (h)	T_u (s)	T_w (s)	$L_u = \bar{U}T_u$ (h)	$L_w = \bar{U}T_w$ (h)
(J207/ J198/ J191)				
1.2	17 – 33	4 – 11	4 – 7	0.8 – 2.3
0.7	20 – 50	17 – 33	0.2 – 0.6	0.2 – 0.4
0.1	33 – 100	1 – 3	0.9 – 2.7	0.03 – 0.09
(J213)				
1.2	14 – 50	3 – 10	4 – 14	0.8 – 2.8
0.7	11 – 33	11 – 33	0.7 – 2.2	0.7 – 2.2
0.1	11 – 33	1 – 3	0.4 – 1.3	0.04 – 0.12

Table 6.2.5 Estimated time and length scales of the dominant horizontal and vertical motions for J207/ J191/ J198 and J213, estimated from $n_p(u)$ and $n_p(w)$, Tables 6.2.1 and 6.2.2. Taylor's hypothesis is assumed to be valid such that $T_i \sim (n_p(i))^{-1}$ s, where i is u or w.

6.2.1.1 Local Isotropy

Isotropy is defined thus by Panofsky and Dutton (1984): "A motion field in which statistics are invariant to rotation of the co-ordinate axis". Local, as opposed to general, isotropy refers to only the smallest scale motions, i.e. those with highest frequency. In the surface layer, eddies in the inertial subrange are said to be locally isotropic, i.e. the statistics of u, v and w components are identical in this frequency range. It is clear from the velocity power spectra in Figures 6.2.1 and 6.2.2 that this is not true within a forest canopy. The frequency ranges of the inertial subranges themselves are quite different between the components (see Tables 6.2.4 and 6.2.5).

A common test for local isotropy is that the ratios of the power spectral densities $S_v(n)/S_u(n)$ and $S_w(n)/S_u(n)$ are equal to 4/3, (Kaimal *et al.*, 1972, Panofsky and Dutton, 1984). This relationship is stability dependent, where the ratios approach 4/3 at higher normalised frequencies as the atmosphere becomes more stable (Kaimal *et al.*, 1972).

Plots of the ratios $S_v(n)/S_u(n)$ and $S_w(n)/S_u(n)$ for the two data sets are shown in Figures 6.2.3 and 6.2.4. None of the spectral ratios at any height approach the 4/3 value as in the free surface layer. (The ratios at 0.7h, at high frequencies are effected by the noise from contamination spikes). This result has been reported elsewhere by Shaw *et al.* (1974) in corn with $S_w(n)/S_u(n)$ = 0.94, Baldocchi and

Meyers (1988*b*) in a deciduous forest with $S_v(n)/S_u(n) \approx S_w(n)/S_u(n) \approx 1 \pm 0.25$, Amiro (1990*b*) in spruce, pine and aspen forests with $S_v(n)/S_u(n) \approx S_w(n)/S_u(n) \approx 1 \pm 0.15$ and Kaimal and Finnigan (1993) for Eucalyptus forest with $S_w(n)/S_u(n) = 1.7$.

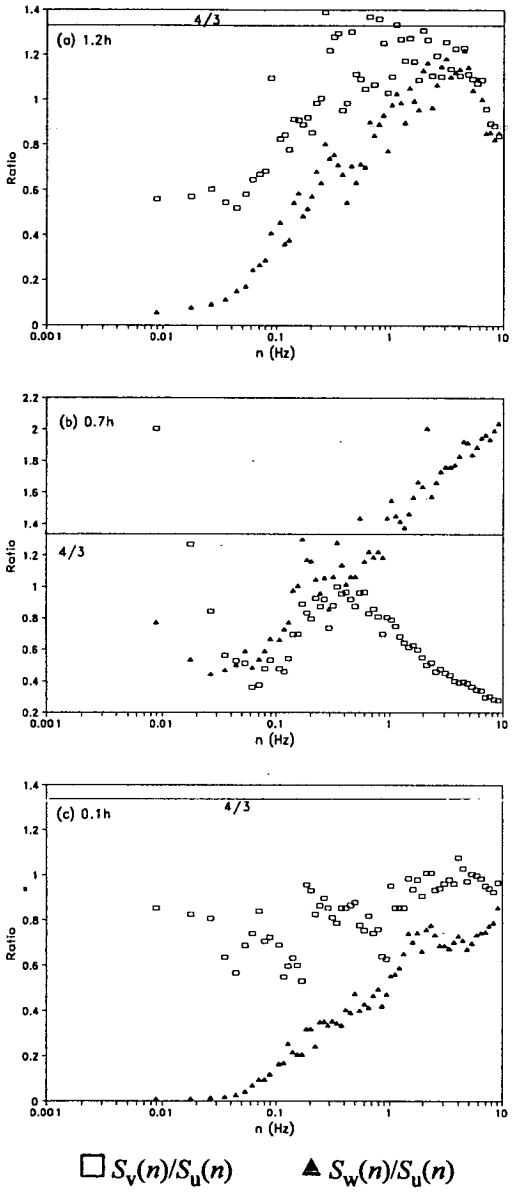

Fig 6.2.3 J207/ J191/ J198 ratios of velocity power spectral densities at heights: (*a*) 1.2*h*; (*b*) 0.7*h* and (*c*) 0.1*h*.

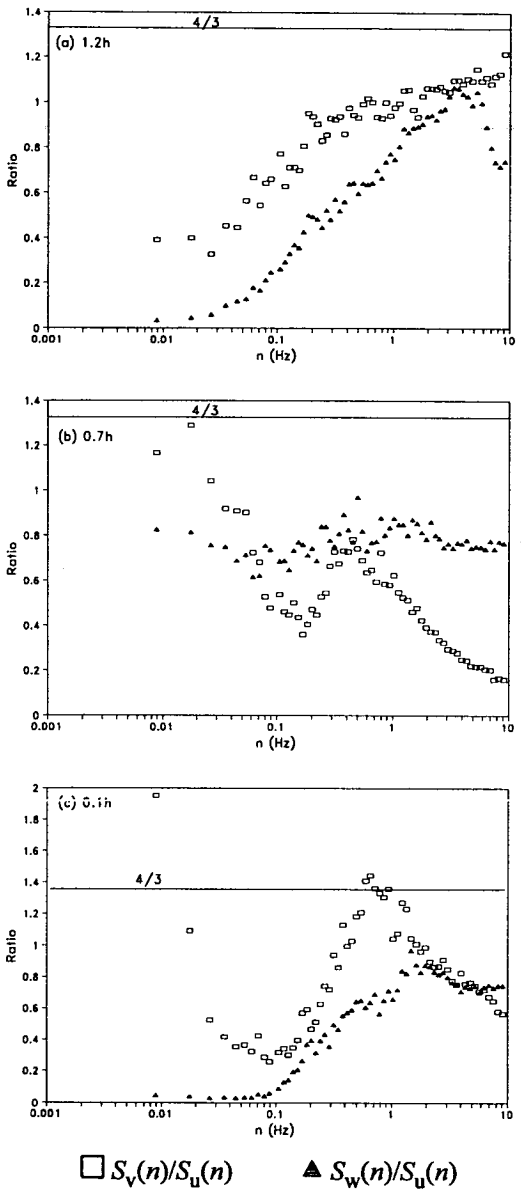

Fig 6.2.4 J213 ratios of velocity power spectral densities at heights: (*a*) 1.2*h*; (*b*) 0.7*h* and (*c*) 0.1*h*.

The interaction of the foliage with the air flow through wake and waving production clearly results in different turbulent characteristics in the three Cartesian components as we have already seen in the velocity power spectra.

6.2.2 Velocity Co-Spectra

The momentum co-spectra from the two data sets have similar characteristics, with a higher degree of scatter than in the power spectra (Figures 6.2.5 and 6.2.6). Momentum co-spectral peaks were similar throughout the canopy, more clearly on J213 than J207/ J191/ J198. The peak values for the J213 momentum co-spectra were ~ 0.05, 0.07 and 0.04 Hz at 1.2h, 0.7h and 0.1h, respectively (Figure 6.2.6). By assuming that Taylor's hypothesis is valid through the canopy and using the mean wind speeds at the three levels, these peak frequencies correspond to dominant length scales of ~ 5h at 1.2h and ~ h at 0.7h and 0.1h, (where on J213: $\overline{U}$ = 4.2, 1.0 and 0.6 m s^{-1} at 1.2h, 0.7h and 0.1h, respectively).

Both momentum co-spectra at 1.2h had inertial subranges with the expected -4/3 slope as shown in Figures 6.2.5*a* and 6.2.6*a*. There is rapid roll-off of co-spectral density in the crown compared to above the canopy and, again, in the trunk space compared to the crown. This result relates well to the profiles of Reynold's stress, Figure 5.2.1, and to a similar roll-off in the velocity power spectra, Figures 6.2.1 and 6.2.2. The up turn in the high frequencies at 0.7h on J213 is attributable to data contamination as the log - log slope is about +1, Figure 6.2.6.

Momentum co-spectra reported by Amiro (1990*b*), in black spruce, pine and Aspen forests did not show the rapid roll-off of co-spectral densities with height, shown most clearly in Figure 6.2.6, with the inertial sub-range slopes changing from about -4/3 above the canopy, to about -1 at 0.6h and 0.2h. The black spruce canopy was similar to that of Rivox, with LAI ~ 10, a density of 7450 trees ha^{-1} and height 10 m. The momentum absorption of the spruce was also similar to that observed at Rivox, (see Figure 5.2.1*b* and Figure 4 of Amiro, 1990*a*). Why the momentum attenuation is much more clearly observed in the Rivox co-spectra is puzzling. The momentum flux at a point in space is equal to the integral under the unnormalised momentum co-spectra (section 2.1.9). If there is a dramatic decline in the momentum flux through the canopy, we would expect a similar dramatic reduction in area beneath the momentum co-spectra, as is observed in the Rivox data.

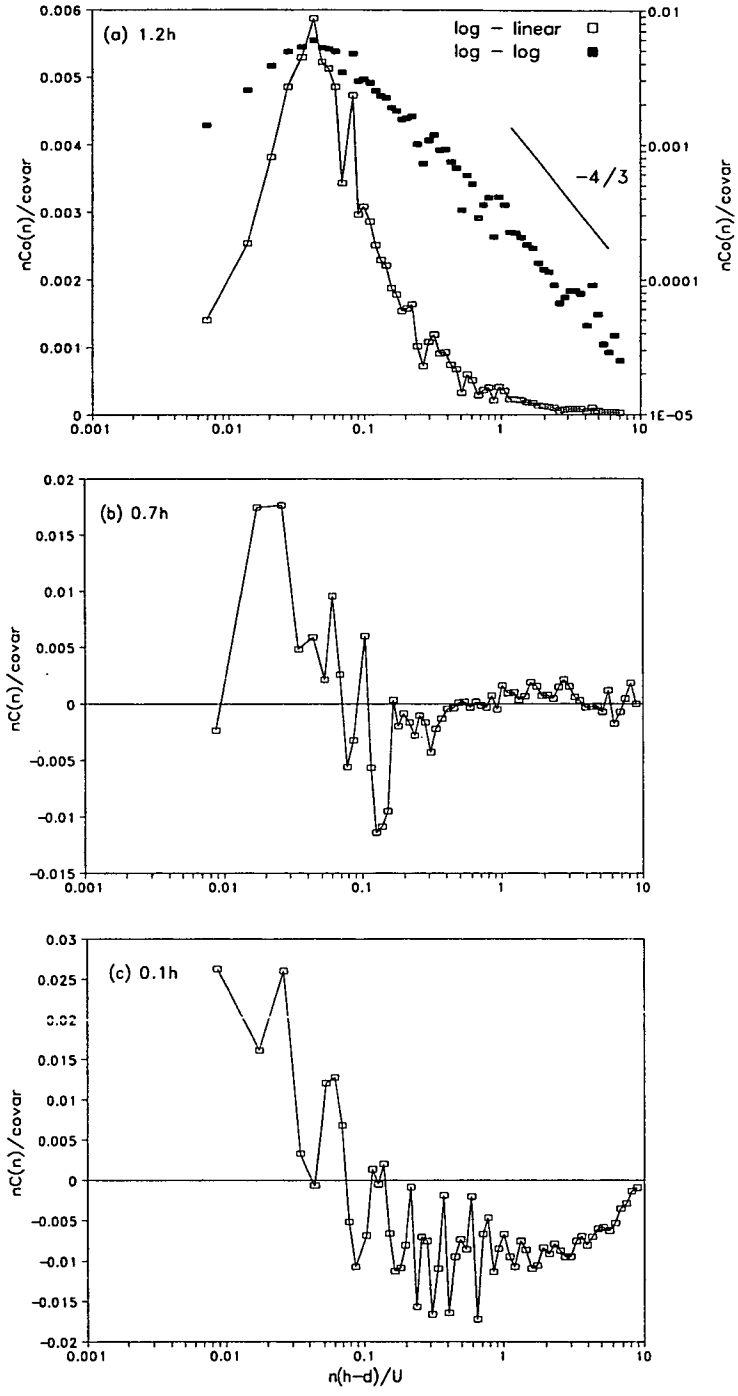

Fig 6.2.5 J207/ J191/ J198 normalised momentum co-spectral densities $nC_{uw}(n)/|\overline{u'w'}|$, plotted against normalised frequency, $n(h-d)/\overline{U}$ in linear-log and log-log form, at heights: (*a*) 1.2*h*; (*b*) 0.7*h*; and (*c*) 0.1*h*. [$\overline{U}$ = 3.1 and 2.5 m s^{-1} for J191/ J198 and J207, respectively, and (h - d) ~ 2.4 m.].

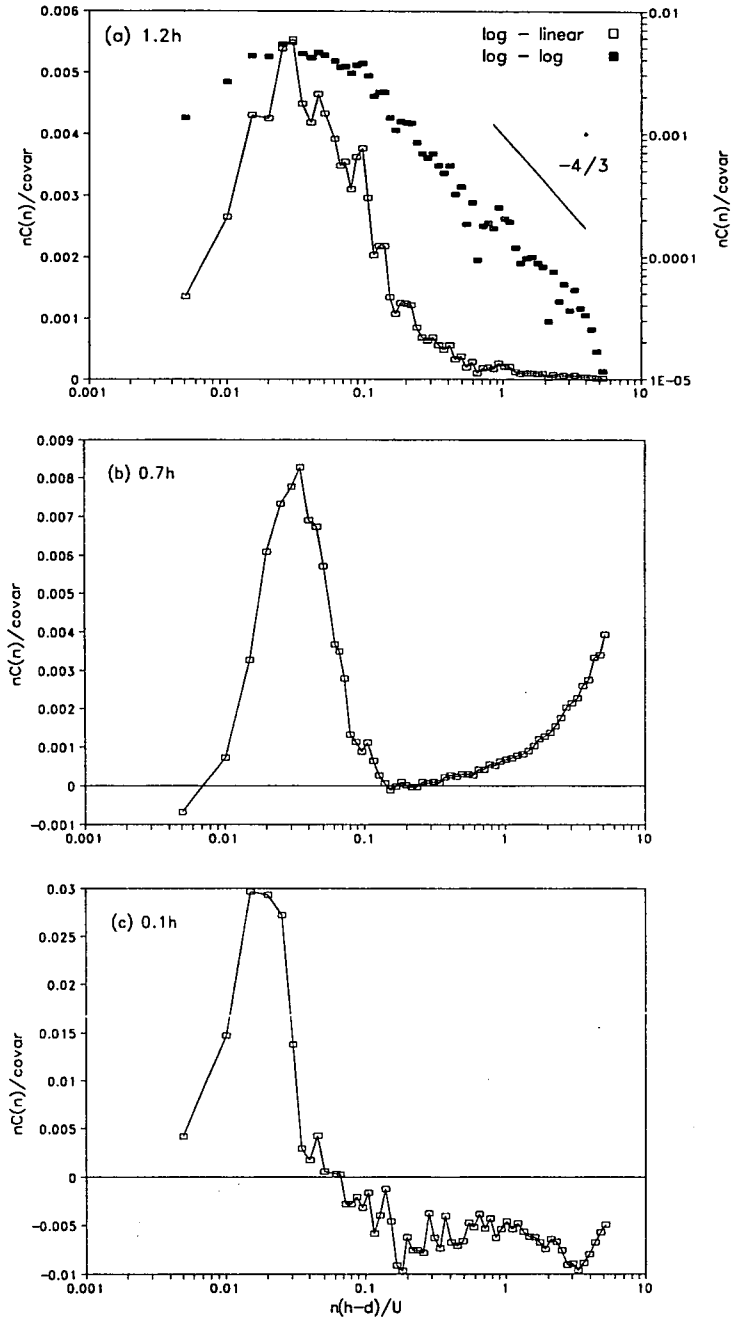

Fig 6.2.6 J213 normalised momentum co-spectral densities $nC_{uw}(n)/|\overline{u'w'}|$, plotted against normalised frequency, $n(h-d)/\overline{U}$ in linear-log and log-log form, at heights: (*a*) 1.2*h*; (*b*) 0.7*h*; and (*c*) 0.1*h*. [$\overline{U}$ = 4.2 m s^{-1} and (*h* - *d*) ~ 2.4 m.]

It is important to note that all the velocity co-spectra are uncorrected for losses with frequency as predicted by the transfer functions in section 2.3. At 1.2*h* the expected attenuation would be very small as sensor separation is zero and the other transfer functions are negligible. This is indeed observed in Figures 6.2.5*a* and 6.2.6*a*, which have straight slopes of ~ -4/3 up to the highest frequencies. Below the canopy the expected losses, although larger, are still small, with r.m.s. cut off frequencies well above the apparent onset of attenuation in Figures 6.2.5*b* and 6.2.5*c* and 6.2.6*b* and 6.2.6*c*. The lack of a definitive unattenuated momentum co-spectrum in the canopy crown or trunk space would not allow us to apply a total transfer function properly in any case. The assumption that momentum co-spectra have a very similar form throughout a canopy, as exhibited above, is shown to be unreliable in the case of Rivox, if somewhat more applicable in the case of Amiro (1990*b*). These considerations are much more important for scalar co-spectra as discussed below (section 6.3.2).

6.3 SCALAR SPECTRA

Power spectra of scalar quantities above and within plant canopies have been published on only a few occasions. The most comprehensive study was conducted by Amiro (1990*b*) for temperature in three forest types: black spruce, pine, and aspen for heights above the canopy through to the forest floor (1.21*h* to 0.13*h*). The power and co-spectral densities of CO_2 and H_2O, have only been reported in a systematic way above a deciduous forest by Anderson *et al.* (1986) and above a wheat field by Ohtaki (1985). Power and co-spectra of CO_2 have been reported, in the context of transfer function correction of CO_2 fluxes, at the floor of a deciduous forest by Baldocchi and Meyers (1991), above a wheat field by Leuning and King (1992) and above Sorghum, by Suyker and Verma (1993).

The scalar power and co-spectra measured using infra red gas analysers, thin wire thermocouples, or sonic anemometer/thermometers, are all subject to signal losses at specific frequencies which can be corrected by derived transfer functions (section 2.3). Scalar power spectral densities presented here were calculated for instruments with response times sufficiently fast to ensure that the corrections were negligible, i.e. E009 IRGAs, sonic thermometers and a CA27 thin-wire thermocouple (Table 3.2.3). All scalar power spectra are thus presented without transfer function corrections in section 6.3.1. Scalar co-spectral densities through the canopy are also presented in section 6.3.2 without transfer function corrections, as no reliable co-spectral models could be obtained at 0.7*h* or 0.1*h*. The CO_2 co-spectra from the E009 and Li6252 IRGAs at 1.2*h* are used to test the validity of the transfer function

corrections applied to CO_2 fluxes at $1.2h$ in section 6.3.2.

The problems with data contamination were once again evident in many of the scalar spectra. On day J213 no CO_2 or H_2O power or co-spectral information could be salvaged as the noise strength greatly outweighed the signal. Also on J213 no temperature power or co-spectra were obtainable at $0.1h$ and similarly there was no temperature co-spectrum at $0.7h$. A full set of power and co-spectra were obtained for the J207/ J191/ J198 data set for: CO_2, temperature and H_2O at $1.2h$ and $0.1h$ and temperature at $0.7h$.

6.3.1 Scalar Power Spectra

The power spectra of temperature correspond well for the two days when a comparison was possible as shown in Figures 6.3.1 and 6.3.2. At heights $1.2h$ and $0.1h$ on J207/ J198/ J191 the responses of all three scalars also correspond closely (Figures 6.3.1*a* and 6.3.1*c*).

At $1.2h$ the correspondence of the three scalars is extremely close at the start of the inertial sub-range, with all of the spectra displaying a slope close to -2/3. The peak frequencies exhibit rather more variability, with the CO_2 and H_2O spectra apparently peaking at lower frequencies than temperature. The peak frequency of the temperature signal corresponds to that of the horizontal velocity power spectra (Figures 6.2.1 and 6.2.2). Above a wheat crop, Ohtaki (1985) observed a peak and a sub-peak in temperature, CO_2 and H_2O power spectra. This result was attributed to both horizontal and vertical velocity fluctuations contributing to the fluctuations of the scalar quantities. The main peak was postulated to be a result of horizontal velocity fluctuations and the sub-peak, at a higher frequency, of vertical velocity fluctuations. The scalar spectra did show a slight increase in power around a normalised frequency of 0.07, which lies between the horizontal and velocity peak frequencies, and may be a combined maximum contribution from the u, v and w velocity motions.

The $1.2h$ CO_2 power spectra displays an upturn in the high frequencies, as does the temperature spectra. The upturn in the temperature spectra has a slope of about +1, indicative of the presence of spikes in the data. The CO_2 signal has an upturn with a lesser slope and is very likely the instrumental noise noted by Moncrieff *et al.* (1992), from E009 sensors during the FIFE experiment in 1989. This white noise in their power spectral response was attributed to instabilities in the electronics of the analysers.

The rapid roll off in the signals from the IRGA at the highest frequencies is a result of the electronic low-pass filters, which have a cut off frequency, n_c, of 7.4 Hz,

(thus for Figure 6.3.1*a* $n_c(h-d)/\overline{U} \sim 5.7$). As the filters operate on the signals prior to their being digitised by the A/D board, where the contamination originated, signals displaying some downturn due to the filters are unlikely to have been affected by data contamination. Thus the noise evident in the CO_2 signal, which does display downturn is probably attributable to the instrument and not contamination of the data. It is interesting to note that the H_2O signal from the same analyser shows no such noise.

In the canopy crown the power spectra of temperature shows the typical upturn, with slope + 1, due to data contamination. The lower frequency response, however, mirrors the velocity spectral responses at this height, with a roll-off much steeper than -2/3. The spectral peak is less well defined than for the velocity power spectra, but would appear to occur at a slightly lower frequency than the velocity power spectral peaks at 0.7*h*, Figures 6.3.1 and 6.3.2.

In the trunk space, the three scalar spectra correspond well in the low- and mid-frequencies. The temperature signal in the higher frequencies has a slope greater than -2/3, whereas the CO_2 and H_2O signals fall away more rapidly than -2/3. It is unlikely that the temperature signal at high frequencies is due to noise spikes as the slope is not +1. The fall off above normalised frequencies greater than about 1 in the IRGA power spectra is probably a result of losses from averaging over the IRGA sensor path, see section 2.3.6. At 0.1*h* the scalar power spectra again have less distinct peaks than the velocity spectra at 0.1*h*, occurring at a somewhat lower frequency. There is also a suggestion of a secondary peak in all of the scalar power spectra at 0.1*h*, similar to that observed in the horizontal velocity power spectra although much less distinct. If the scalar fluctuations are driven by a combination of horizontal and vertical velocity fluctuations, as postulated by Ohtaki (1985), this would explain the less prominent 'dip' and 'hump' in the spectra, as the *w* motions would 'fill in' the energy gap in the *u* and *v* spectra.

The three scalars at 1.2*h* and 0.1*h* have very similar power spectra and thus we could assume that they share the same physical transport processes. Any differences between the power spectra are attributable either to differing frequency losses of the individual instruments or corrupt data.

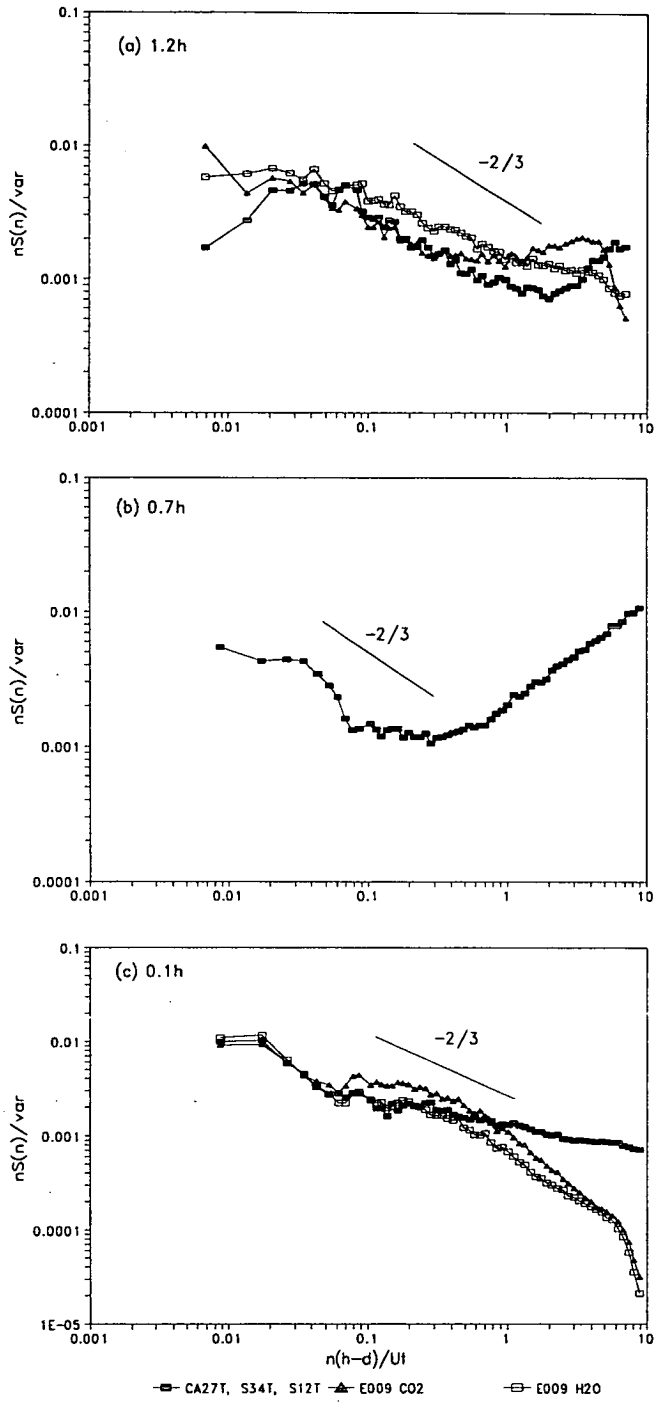

Fig. 6.3.1 J207/ J191/ J198 normalised power spectral densities $nS_\alpha(n)/\sigma_\alpha^2$, where α denotes the scalars Temperature, CO_2 and H_2O, plotted against normalised frequency, $n(h-d)/\overline{U}$, at heights: (*a*) 1.2*h*; (*b*) 0.7*h*; and (*c*) 0.1*h*. The legend refers to the instruments deployed, see Table 3.2.3. [$\overline{U}$ = 3.1 m s^{-1} for J198/ J191 and 2.5 m s^{-1} for J207, and (*h* - *d*) ~ 2.4 m.]

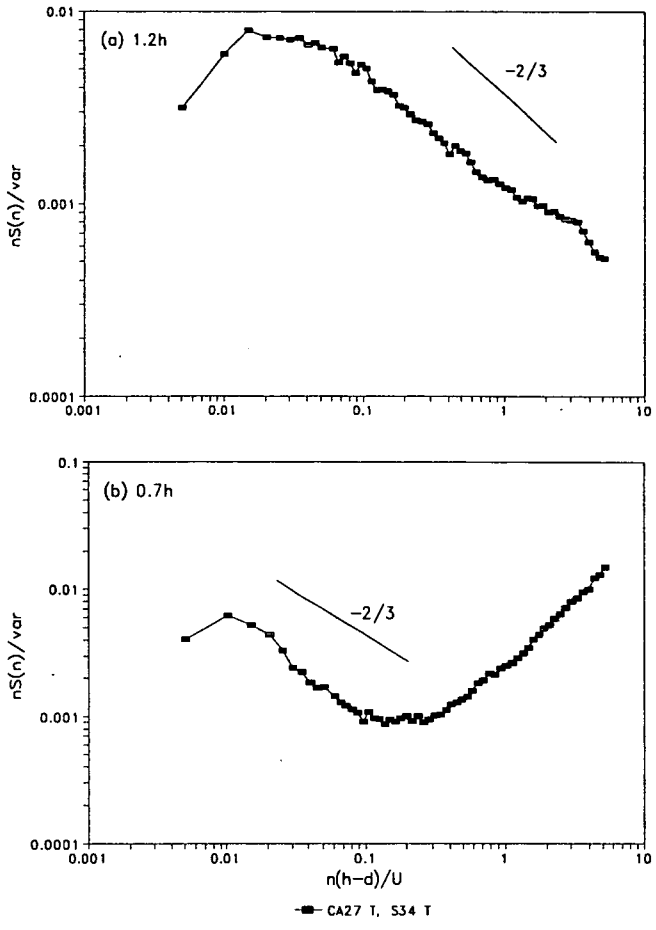

Fig. 6.3.2 J213 normalised temperature power spectral densities $nS_T(n)/\sigma_T^2$, against normalised frequency, $n(h-d)/\overline{U}$, at heights: (*a*) 1.2*h*; and (*b*) 0.7*h*. The legend refers to the instruments deployed, see Table 3.2.3. [$\overline{U}$ = 4.2 m s^{-1} and (h - d) ~ 2.4 m.]

6.3.1.1 CO_2 Power Spectra from Open and Closed Path IRGAs

Figure 6.3.3 shows the comparison of the power spectral response of the E009 open path IRGA and the Li6252 closed path IRGA at 1.2*h*, shows the signal attenuation with frequency predicted by the transfer functions in section 2.3. Both the instruments display noise at high frequencies, and a downturn due to the low-pass electronic filters, (n_c ~ 7.4 Hz). The noise in the Li6252 above 1 Hz is not unexpected as all actual signal has probably been attenuated, leaving only noise thereafter.

Both the sensors are subject to signal losses from the acquisition system, the digital recursive filtering and the low-pass filtering (section 2.3). Individually, the open path instrument has losses due to sensor path averaging and its own frequency

response, (nominally a sample rate of 33 Hz). The closed path IRGA suffers losses from tube sampling and a slower frequency response (approximately 2 Hz response to stepped changes). Although the losses from sampling down a tube and from the slower response are clearly significant, if these losses are relatively well predicted by the transfer functions, then the agreement in corrected CO_2 flux will be good as in the CO_2 intercomparison experiment in section 3.2.4. A similar spectral comparison between an E009 and a Li-6251 analyser was reported by Leuning and King (1992).

The ability to correct fluxes from a closed path instrument properly are further discussed in section 6.3.2 with respect to the actual co-spectral responses.

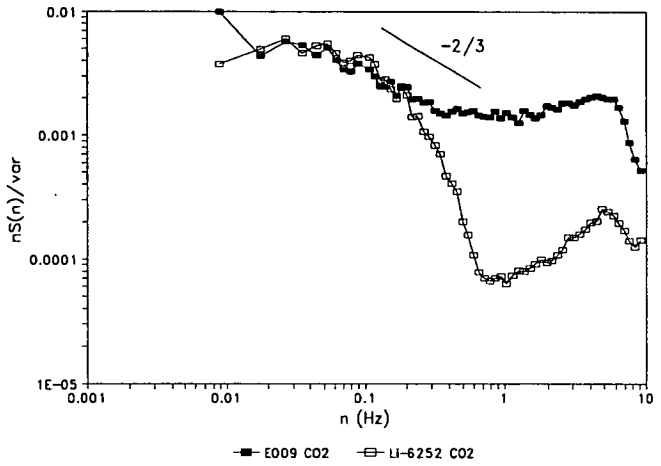

Fig. 6.3.3 Power spectral response, $nS_{\rho c}(n)/\sigma_{\rho c}^2$, of an E009 open path and a Li6252 closed path IRGA to CO_2 density with natural frequency n at $1.2h$.

6.3.2 Scalar Co-Spectra

6.3.2.1 Verification of Transfer Functions for CO_2 Response

The appropriate correction schemes for the E009 and the Li6252 IRGAs are given in section 4.2.1, where the two situations (*i*) and (*ii*) refer to the open path E009 and the closed path Li6252 respectively. The CO_2 co-spectral response function, given in section 4.2.1, was obtained by fitting the Kaimal *et al.* (1972) function, equation 2.3.39, to the low and mid-frequency E009 CO_2 data, i.e. at frequencies up to about 1 Hz. The transfer functions applicable to the E009 IRGA indicate that attenuation of co-spectral signals takes place above this frequency and that attenuation at lower frequencies will be negligible. The fitted function, extrapolated to higher frequencies, gives a good approximation to a 'perfect' unattenuated co-spectral response for CO_2.

Co-spectra for both the E009 and Li6252 show markedly different attenuation with frequency (Figure 6.3.4) as did their respective power spectra (Figure 6.3.3). As a test of the effectiveness of the transfer functions described in Chapter 2 in recreating the lost signal, the combined transfer functions for cases (*i*) and (*ii*) are shown in Figure 6.3.4 attenuating the fitted CO_2 function (shown as 'FIT'). The resulting curves correspond well to the attenuated portions of the two data sets. The area beneath the 'FIT' curve in Figure 6.3.4, less the areas underneath the 'FIT×T(*i*)' or the 'FIT×T(*ii*)' curves, equals the flux loss fractions presented in section 4.2.1 for the two cases, where T(*i*) and T(*ii*) represent the appropriate transfer functions for cases (*i*) and (*ii*), respectively.

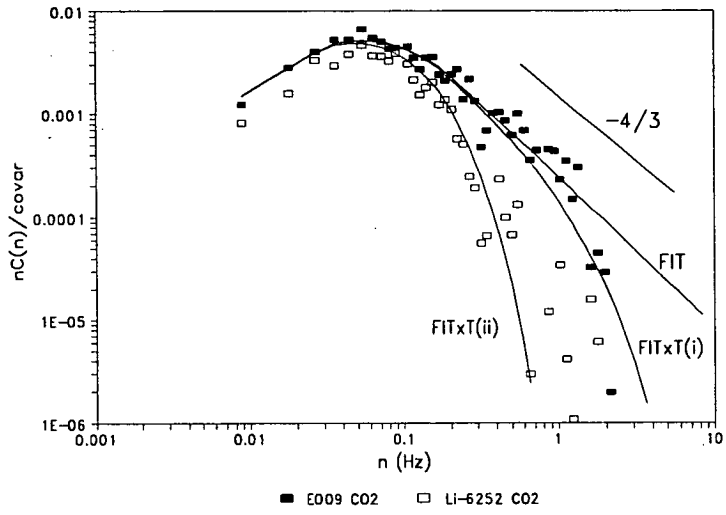

Fig. 6.3.4 Comparison of J207/ J191/ J198 normalised CO_2 co-spectral densities, $nC_{w\alpha}(n)/\overline{w'\alpha'}$, where α denotes the E009 and Li6252 CO_2 signals, plotted against natural frequency, n, at height 1.2h. The fitted model is as described in section 4.2.1. Solid lines are the fitted model (FIT), the product of the model with the total transfer functions of case (*i*) and (*ii*), (FIT×T(*i*) and FIT×T(*ii*), respectively).

Similar instances have been reported of the successful correction of fluxes from open and closed path IRGAs by Leuning and King (1992) and Suyker and Verma (1993), using the same transfer functions. Leuning and King (1992) applied the transfer functions to spectral data gathered above a wheat crop, and found that the sensible heat co-spectral model of Kaimal *et al.* (1972) adequately represented the CO_2 co-spectral response. Similarly, Suyker and Verma (1993) applied the corrections to spectra from measurements above a Sorghum crop, which again were

represented by the sensible heat model of Kaimal *et al.* (1972).

Transfer function corrections were not applied to within canopy or trunk space co-spectral densities, as reliable co-spectral functions could not be derived. The problems relating to correction of within canopy scalar co-spectra are discussed below with the relevant spectra.

6.3.2.2 Scalar Co-spectral Response Above and Within the Canopy

The co-spectral response of temperature, CO_2 and water vapour will be examined here at the three measurement heights. All the CO_2 and H_2O data analysed for presentation comes from the E009 IRGAs at $1.2h$ and $0.1h$. The temperature data at $1.2h$ comes from the fast response thermocouple, CA27, and at $0.7h$ and $0.1h$ from sonic temperature measurements from the Solent anemometers, S34 and S12. Full details of instruments deployed were given in Table 3.2.3

The scalar co-spectra above the canopy are very similar for all the scalar quantities with peak response occurring at a normalised frequency of ~ 0.05, Figures 6.3.5*a* and 6.3.7. At height h in a deciduous forest Anderson *et al.* (1986) reported very similar co-spectra of temperature, CO_2 and H_2O with peak normalised frequencies of 0.1 At $1.3h$ above a pine forest Bergström and Högström (1989) reported very similar co-spectra of temperature and water vapour with a common peak frequency of 0.015 Hz.

The fit to the CO_2 co-spectral data in Figure 6.3.5*a* is that given in section 4.2.1 and in Figure 6.3.4, shown in linear-log, rather than log-log, form. The inertial sub-range slopes of the $1.2h$ co-spectra have the expected -4/3 value up to a normalised frequency of 0.6, (n ~ 1 Hz), thereafter the signals are attenuated and roll-off rapidly, Figure 6.3.4. At this frequency the normalised co-spectral density falls to ~ 7 % of the peak value. At normalised frequencies > 1, the normalised co-spectral density falls to less than 1 % of the peak value.

Within the canopy, much more scatter was evident in the co-spectral densities, probably as a result of the correlations between w and the scalar densities often being very small compared to the values at $1.2h$. At $0.7h$, in the canopy crown, the co-spectra for temperature shows a large low frequency peak occurring at a lower normalised frequency than the peak at $1.2h$, namely ~ 0.025 (Figure 6.3.5*b*). The roll-off after this peak is extremely rapid, with a significant negative overshoot, followed by a noisy zero signal (Figure 6.3.7*b*). The co-spectral peak corresponds well to that of the momentum co-spectra at $0.7h$, Figures 6.2.5*b* and 6.2.6*b*, although the roll-off is more rapid here than for either of the momentum co-spectra. The co-spectra at $0.1h$ show a similar response to that in the canopy crown, with low

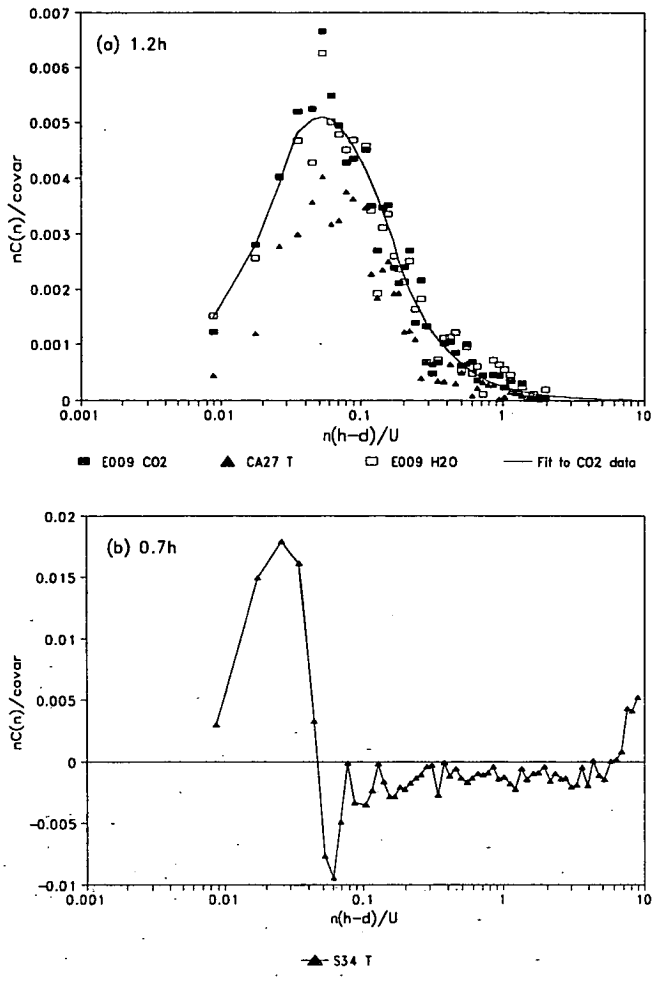

Fig. 6.3.5 J207/ J191/ J198 normalised co-spectral densities, $nC_{w\alpha}(n)/\overline{w'\alpha'}$, where α denotes the scalars: Temperature; CO_2; and H_2O; plotted against normalised frequency, $n(h-d)/\overline{U}$, at heights: (*a*) 1.2*h*; and (*b*) 0.7*h*. [$\overline{U}$ = 3.1 and 2.5 m s^{-1} for J191/ J198 and J207, respectively, and $(h - d) \sim 2.4$ m.]

frequency components rolling off very rapidly into what appears to be a noisy zero response in the mid- and high frequencies (Figure 6.3.5). At 0.1*h* the scalar power spectrum had a similar response to the *u* and *v* power spectra which differed from that of *w*. This mismatching of response may explain some of the scatter in the scalar co-spectra at 0.1*h*.

Temperature co-spectra reported by Amiro (1990*b*) in spruce, pine, and Aspen forests all had forms similar to those above the canopy and to the momentum co-spectra at the same heights. They exhibited entirely positive normalised co-spectral densities and recognisable inertial sub-range slopes with values around -1.

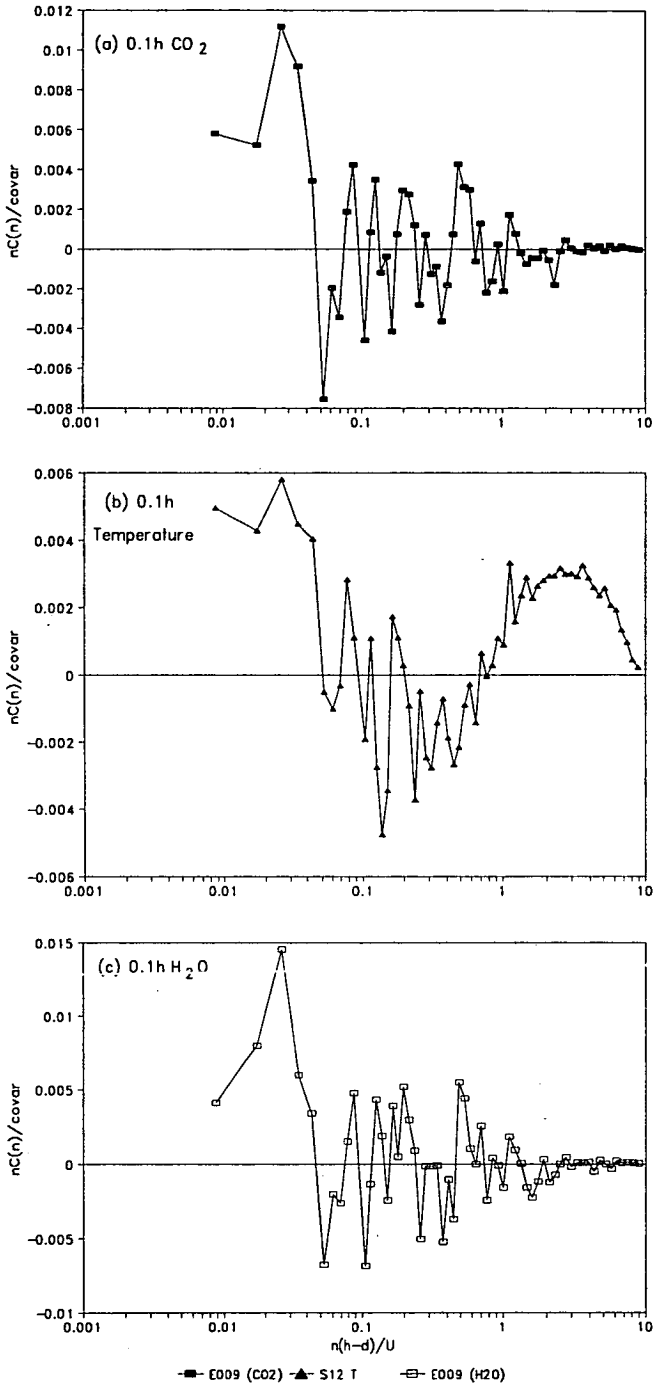

Fig. 6.3.6 J207/ J191/ J198 normalised co-spectral densities, $nC_{w\alpha}(n)/\overline{w'\alpha'}$, where α denotes the scalars: (*a*) CO_2; (*b*) Temperature; and (*c*) H_2O; plotted against normalised frequency, $n(h-d)/\overline{U}$, at height 0.1*h*. [$\overline{U}$ = 3.1 and 2.5 m s^{-1} for J191/ J198 and J207, respectively, and (h - d) ~ 2.4 m.]

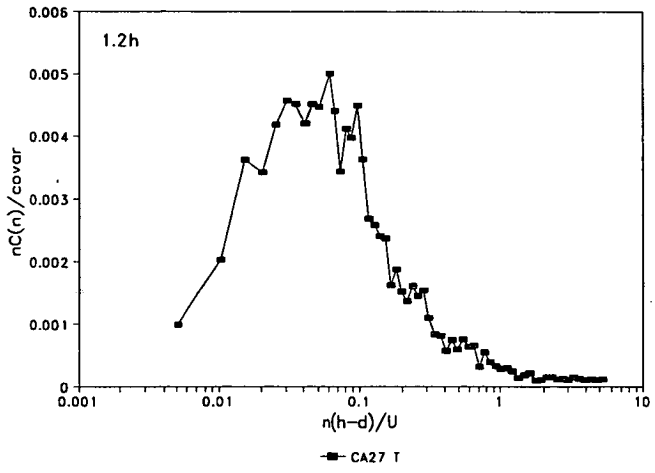

Fig. 6.3.7 J213 normalised co-spectral densities, $nC_{wx}(n)/\overline{w'x'}$, where x denotes the scalar Temperature, plotted against normalised frequency, $n(h-d)/\overline{U}$, at height 1.2h. Where $\overline{U}$ = 4.2 m s^{-1}, and (h - d) ~ 2.4 m.

The sub-canopy co-spectra present a serious problem, in that they are uncorrected by appropriate transfer functions for two reasons: firstly, the derived transfer functions for scalar and velocity path averaging and sensor separation do not apply in the sub-canopy as Taylor's Hypothesis is invalid; secondly, no well defined co-spectral model can be obtained from the scalar co-spectra at 0.1h as shown in Figure 6.2.6.

Consequently, the sub-canopy co-spectra presented here for the scalar quantities, as discussed in section 6.2 for momentum, have an unknown flux loss with frequency. In the case of the scalar co-spectra, the expected losses are much greater, as losses now occur due to IRGA and sonic path averaging (i.e. E009), sensor separation and tube smearing. As the derived transfer functions relate to a flow where Taylor's hypothesis is valid, they cannot be applied and, as in the case of momentum co-spectra, we cannot assume that the scalar co-spectral models above the canopy apply below. This may well be the case for the spruce, pine, and Aspen forests of Amiro (1990*b*) but is seen not to be the case for Rivox.

The implication for making eddy covariance measurements is important, in that we have no means for testing whether we are successfully sampling the scalar fluxes. Presented with co-spectra such as those in Figure 6.3.5, we cannot tell whether high frequency flux components are zero because no eddies with these frequencies exist, or as a result of the inability of our instruments to resolve them. With the very low wind speeds found on average in the trunk space, (0.4 - 0.6 m s^{-1} on J207 and

J213), the errors due to path averaging of scalar and velocity measurements, and the sensor separation loss, would be expected to be very much larger than in higher wind speeds, and cannot be ignored.

6.4 SUMMARY AND CONCLUSIONS

(i) Velocity power spectra at $1.2h$ had slopes close to the -2/3 value predicted from similarity arguments outlined in section 2.1.9. Horizontal velocity spectra peaked at lower frequencies than w velocity power spectra, indicating the dominance of larger scale motions in the horizontal flow.

In the canopy crown, the velocity power spectra had slopes steeper than -2/3 indicating a cascade of turbulent energy from large to small motions as the flow interacts with the trees.

In the forest trunkspace at $0.1h$ the horizontal velocity power spectra displayed a primary peak at similar low frequencies as at $0.7h$ and $1.2h$ but also a secondary peak in higher frequencies. The vertical velocity power spectrum had a much diminished low frequency peak and a larger main peak corresponding with the secondary peak in the u and v power spectra. The cross-correlation analysis of Chapter 5 identified that mainly horizontal gusts were able to penetrate to the trunk space when the sub-canopy was well coupled to the atmosphere above the forest, whereas w fluctuations in the trunk space were much weaker and linked to pressure gradient forces associated with the gusts. The large low frequency peak in the u and v power spectra at $0.1h$, may represent gust/ejection structures penetrating to the trunk space while the w spectral densities at this frequency are much smaller as they arise from pressure gradient forces associated with the gust. The interaction of the large horizontal motions with the tree trunks may also account for the secondary peak in the u and v power spectra.

(iii) The length scales of the dominant motions at $1.2h$ were estimated, assuming Taylor's hypothesis, from the u and w spectral peaks to be $L_u \sim 4$ - $14h$ and $L_w \sim 1$ - $3h$. These dominant eddy length scales are approximately a factor of ten larger than the integral Eularian time scales presented in section 5.3.

(iv) The flow at $1.2h$, $0.7h$ and $0.1h$ was found to be locally anisotropic as the ratios of velocity power spectral densities $S_v(n)/S_u(n)$ and $S_w(n)/S_u(n)$ did not approach -4/3 in the frequencies of the inertial subranges.

(vi) Momentum co-spectra at $1.2h$ had inertial subrange slopes close to -4/3 as predicted by similarity arguments (section 2.1.9). The momentum co-spectra in the canopy at $0.7h$ and $0.1h$ showed significantly steeper slopes indicating efficient absorption of momentum by the canopy. The co-spectral peaks occurred at similar

frequencies at all three heights. Assuming Taylor's hypothesis these peak frequencies implied that the dominant events in the transport of momentum were of order $5h$ at $1.2h$, and of order h at $0.7h$ and $0.1h$, respectively.

(vii) The scalar power spectra of temperature, CO_2 and H_2O showed fewer distinct features than the velocity power spectra and more instrumental noise. At $1.2h$ and $0.1h$ the three scalars corresponded well indicating common transport processes. At $0.7h$ the temperature power spectra had a rapid roll-off of spectral density similar to the velocity power and co-spectra at $0.7h$ as discussed above.

In general, scalar spectral peaks occurred at slightly lower frequencies than the corresponding velocity power spectra, although the peaks were less distinct. At $0.1h$ there was a suggestion of the secondary peak observed in the u and v power spectra at $0.1h$ although it was less prominent.

(viii) The attenuation of the CO_2 power and co-spectra with frequency was seen to be as predicted by the transfer functions in section 2.3. A fitted function to the E009 open path IRGA CO_2 low- and mid-frequency co-spectral densities was used to approximate an unattenuated co-spectral response. The appropriate transfer functions were applied to this model to produce attenuated co-spectral densities for the E009 and Li6252 IRGAs which corresponded well with the calculated densities.

(vi) Scalar co-spectra of temperature, CO_2 and H_2O had similar forms above the canopy at $1.2h$ with a common spectral peak at normalised frequency ~ 0.05, and slopes close to -4/3 up to a normalised frequency ~ 0.6. Above this frequency, the co-spectra exhibited the expected attenuation with frequency predicted by the transfer functions section 2.3.

Scalar co-spectra within the canopy showed more scatter and variability in the sign of the normalised co-spectral densities. This can perhaps be attributed to the low covariances found below the canopy, especially at $0.1h$. All the within canopy co-spectra had low frequency peaks with a very rapid roll-off of co-spectral densities in mid-range frequencies with very noisy signals there after.

The lack of reliable within canopy scalar co-spectra has important consequences for making eddy covariance measurements of scalar fluxes inside canopies. Without such co-spectra we have no means of testing whether we are successfully sampling the scalar fluxes and cannot obtain a co-spectral model to allow us to apply transfer function corrections to the measured fluxes.

CHAPTER 7
QUADRANT ANALYSIS

7.1 INTRODUCTION

Quadrant analysis of turbulent velocity fluctuations above and within a canopy reveals processes contributing to the overall fluxes of momentum and scalars in the system. The technique was developed from laboratory studies of smooth and rough wall boundary layers (Lu and Willmarth, 1973; Raupach, 1981) and enables information about the structure of turbulent transport to be deduced from conditionally sampled turbulence measurements at a single point.

The quadrants represent either negative momentum fluxes, i.e. $Q2$ ('ejections' or 'bursts') and $Q4$ ('gusts' or 'sweeps'), or positive momentum fluxes, i.e. $Q1$ ('outward interactions') and $Q3$ ('inward interactions') as discussed previously in section 2.1.6, (Lu and Willmarth, 1973; Moritz, 1989). Using the concept of 'normal' and 'extreme' momentum events, we can obtain a phenomenological description of the flow. The transition between normal and extreme events is taken here to occur at a hole size $H = 4$, i.e. where the instantaneous momentum flux is equal to four times $\overline{u'w'}$, the half hour mean value at that level.

Care must be taken to refer processes revealed through quadrant analysis to the actual mean fluxes at all levels. At the lowest heights in the canopy, mean fluxes can be very small, with comparatively very large instantaneous values of opposing signs. These instantaneous covariances appear to be highly extreme in relation to the mean flux, but are in fact still small when compared to events above the canopy. In any situation where positive and negative events are evenly balanced to give a small net flux, almost all events appear to be extreme.

The quadrant analysis results presented here were obtained in a momentum quadrant frame, and partitioning of scalar fluxes of sensible heat and CO_2 was carried out into these momentum quadrants. The instantaneous momentum flux, $u'w'$, was added to the appropriate momentum stress fraction, $S_{Q.H}$, and the instantaneous scalar flux, $w'\rho_c'$, was added to the scalar flux fraction, $R_{Q.H}$, according to the values of u' and w', both using the same values of Q and H. Scalar flux fractions for CO_2 and temperature were formed in this way. At the end of a half hour period, the flux fractions were normalised by the absolute value of the mean half hour flux, thus all momentum and scalar flux fractions summed to ± 1 depending on the sign of the mean flux.

All results presented here are averages over the quadrant analysis from several half hour periods. Problems are encountered when averaging over periods which have

mean fluxes in opposing directions as the flux fractions over the half hour periods sum to a mixture of +1 or -1. The average flux fractions obtained from these mixed direction periods do not themselves necessarily sum to ± 1. This situation arose for sensible heat fluxes at $0.7h$ for J207 and CO_2 fluxes at $0.1h$ for J213. The fluxes had no consistent flux direction and were highly variable and were considered unreliable.

7.2 QUADRANT ANALYSIS RESULTS

Results are presented for three days: J198, 1991 at heights $1.2h$ and $0.1h$, J207 at $0.7h$ and $0.1h$, and J213, 1991 at heights $1.2h$, $0.7h$ and $0.1h$. The data periods analysed from the three days were: J198 (13:30 - 17:00), J207 (13:30 - 17:00) and J213 (13:30 - 17:00). To aid interpretation of the quadrant analysis results, mean statistics over the three data sets are given in Table 7.2.1.

Julian Day	Height	$\overline{U}$ (m s^{-1})	$\overline{u'w'}$ (m^2 s^{-2})	H (W m^{-2})	F_a (mg m^{-2} s^{-1})
J198	$1.2h$	3.2	-0.631	106	-0.27
	$0.7h$	—	—	—	—
	$0.1h$	0.4	0.013	37	0.06
J207	$1.2h$	2.4	-0.190	—	—
	$0.7h$	0.1	-0.003	0	—
	$0.1h$	0.3	0.000	2	-0.04
J213	$1.2h$	4.2	-0.524	65	-0.52
	$0.7h$	1.0	0.011	13	—
	$0.1h$	0.6	0.000	16	—

Table 7.2.1 Mean values of wind speed $\overline{U}$, Reynolds stress $\overline{u'w'}$, sensible heat H and CO_2 flux, F_a, over the data sets J198, J207 and J213, 1991, at heights $1.2h$, $0.7h$ and $0.1h$.

The CO_2 flux fractions are presented uncorrected for WPL effects. The WPL correction factor is additive to the mean flux and could not be distributed across the quadrants. At $1.2h$ the WPL correction factor reduces the magnitude of the negative CO_2 flux on J198 and J213 but does not change the flux direction. At $0.1h$ the WPL correction was negligible on J207 (due to very small sensible heat fluxes) but was large on J198, and changes the flux direction of some of the half hour period fluxes. Consequently, CO_2 data from J198 at $0.1h$ is not presented here.

All CO_2 flux data came from open path E009 IRGAs (details of the instruments deployed were given in Table 3.2.3).

When mean half hour flux values are small, the flux fractions are rather sensitive to changes in the mean flux and also to measurement errors. This is true of all sensible heat flux fractions from the J207 data set, for all CO_2 flux fractions at $0.1h$ and momentum fractions at $0.7h$ from J207 and at $0.1h$ from J207 and J213. These results must necessarily be treated with some caution.

7.2.1 Above the Canopy

In the roughness sublayer above the canopy we have a conceptually simple model of turbulent exchange. Net momentum flux is directed down towards the canopy, with the dominant events having large length scales of the order of tree height, as discussed in sections 5.3 and 6.2.2. We might expect that sensible heat flux would by day be directed away from the forest canopy, which is warmed by solar radiation, and that CO_2 flux would be directed into the canopy as CO_2 is depleted in the canopy crown as a result of photosynthesis.

The fractions of time spent in each quadrant at $1.2h$ on J198 and J213 for momentum events with different hole sizes are shown in Figures 7.2.1*a* and 7.2.2*a*. Both these figures show that more events occurred in $Q2$ and $Q4$ (the 'gust/ejection quadrants') than in $Q1$ and $Q3$ ('interaction quadrants'), and that normal events were more frequent than extreme ones. The fraction of time accounted for by extreme events was 5.4 % and 12.0 % for J198 and J213, respectively. Simplifying these figures into normal and extreme momentum event classes, then over all events, ejections occurred slightly more frequently than gusts in both cases, Figures 7.2.3*a* and 7.2.4*a*.

The corresponding momentum stress fractions (Figures 7.2.1*b*, 7.2.2*b*, 7.2.3*b* and 7.2.4*b*) show the actual flux contributions associated with the time fractions discussed above. The flux contributions from the gust/ejection quadrants greatly dominated those of the interaction quadrants, resulting in a large negative momentum flux to the forest. The ratio of momentum flux fractions in the interaction and gust/ejection quadrants, $(S_{1,0} + S_{3,0})/(S_{2,0} + S_{4,0})$, was -0.2 for both J198 and J213, respectively (Table 7.2.2). At $1.2h$ above a pine forest, Bergström and Högström (1989) reported a value of this ratio of -0.3 (see their Fig. 10), while Baldocchi and Meyers (1988*a*) reported a range of values of -0.3 - -0.8 between $1.5h$ - $0.1h$ in a deciduous forest.

The overall contribution from extreme events was 49.3 % and 56.4 % of the negative net mean momentum flux on J198 and J213, respectively. The limit for

extreme events of $H \geq 4$ seems reasonable as these events transport ~ 50 % of the net momentum flux whilst occurring only ~ 5 - 12 % of the time.

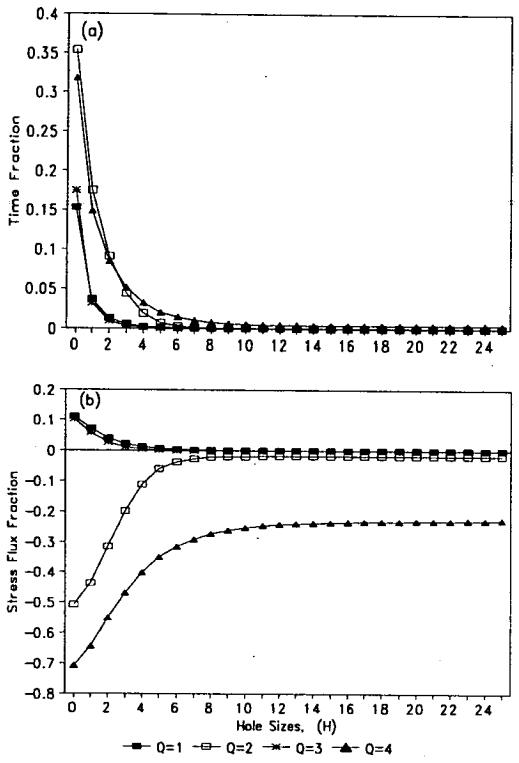

Fig. 7.2.1 Time and momentum stress fractions from J198, 1991, at 1.2*h* at Rivox, shown in (*a*) and (*b*) respectively.

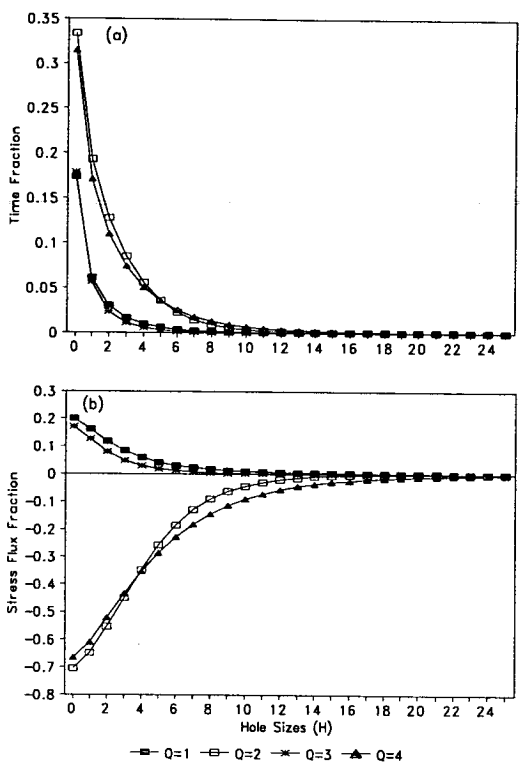

Fig. 7.2.2 Time and momentum stress fractions from J213, 1991, at 1.2*h* at Rivox, shown in (*a*) and (*b*) respectively.

The observation that extreme, infrequent events account for a disproportionate amount of momentum flux above and within plant canopies has been reported previously in wheat (Finnigan, 1979*b*), in corn (Shaw *et al.*, 1983), in an almond orchard (Baldocchi and Hutchison, 1987), in deciduous forests, (Baldocchi and Meyers, 1988*b*; Moritz, 1989), above a pine forest (Bergström and Högström, 1989), and in an artificial plant canopy (Raupach *et al.*, 1986). At 1.1*h* above a pine forest Bergström and Högström (1989) reported that ~ 50 % of the net momentum flux was accounted for by events with hole sizes greater than 4 to 5, which occurred only 7 - 11 % of the time.

The momentum flux fraction at 1.2*h* by gusts (in *Q*4) was larger than that transported by ejections (in *Q*2) on J198, while the reverse is true on J213. (Indeed the momentum flux fraction in *Q*4 on J198 shown in Figure 7.2.1*b* indicates that a large

fraction of the momentum stress occurred for hole sizes $H \geq 25$). The ratios of $S_{4,0}/S_{2,0}$ were 1.4 and 0.9 on J198 and J213, respectively. Above a pine forest, Bergström and Högström (1989) reported a value of $S_{4,0}/S_{2,0}$ of ~ 1.1 at 1.2h, while Moritz (1989) reported a value of 1.2 at 1.2h above an Oak forest, and Raupach *et al.* (1986) reported a value of 1.0 at 1.13h above an artificial canopy in a wind tunnel experiment.

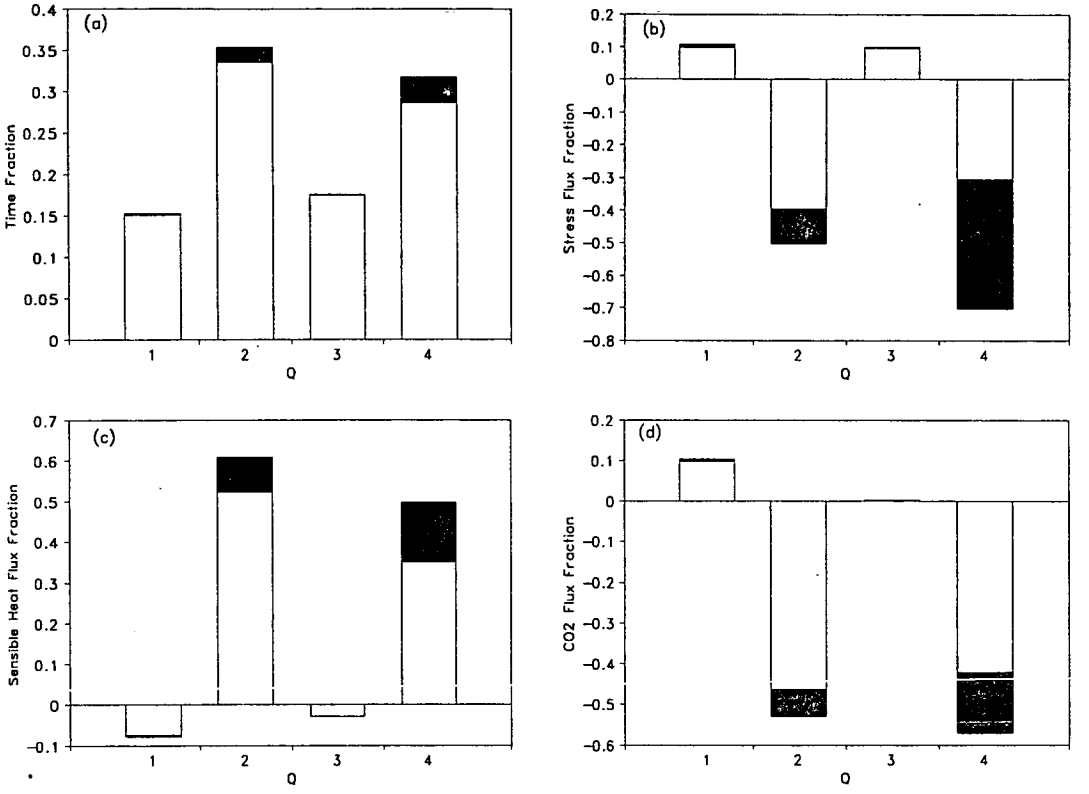

Fig. 7.2.3 Time, momentum stress, sensible heat and CO_2 flux fractions from J198, 1991, at 1.2h at Rivox, shown as (*a*), (*b*), (*c*) and (*d*) respectively. Dark shading denotes extreme events, i.e. $H \geq 4$.

The corresponding fluxes of sensible heat in the momentum quadrants show similar dominance of gusts and ejections over the interaction quadrants, with $Q2$ and $Q4$ containing large positive sensible heat fluxes (Figures 7.2.3*c* and 7.2.4*c*). Ejections dominated gusts for sensible heat transport on both days with sensible heat contributions in $Q2$ of 61.0 % and 59.0 % for J198 and J213, respectively. A similar result was reported for sensible heat flux fractions at 1.2h above an Oak forest (Moritz, 1989) with a 60 % contribution to net mean flux from the ejection quadrant,

Q2. Contributions of sensible heat flux associated with extreme momentum events were 23.0 % and 44.4 % of the sensible heat flux on J198 and J213, respectively.

Most of the CO_2 flux directed downward was contained in the gust\ejection quadrants (Figures 7.2.3*d* and 7.2.4*d*). On both days, gust contributions dominated the CO_2 flux compared to that from ejections, and this may be tentatively explained by the presence of high CO_2 concentrations in the lower canopy as a result of within canopy respiration fluxes. Ejections from the lower parts of the canopy would be transporting air rich with respired CO_2, out to the atmosphere through the crown, where the air would have been depleted of CO_2 by photosynthesis, rather than simply the CO_2 depleted air from the crown. Gusts moving down through the plane at 1.2*h* would still be transporting air downwards which is rich in CO_2 compared to that in the canopy crown. The contributions to the negative net mean CO_2 flux associated with extreme momentum events were 21.3 % and 47.0 % on J198 and J213, respectively.

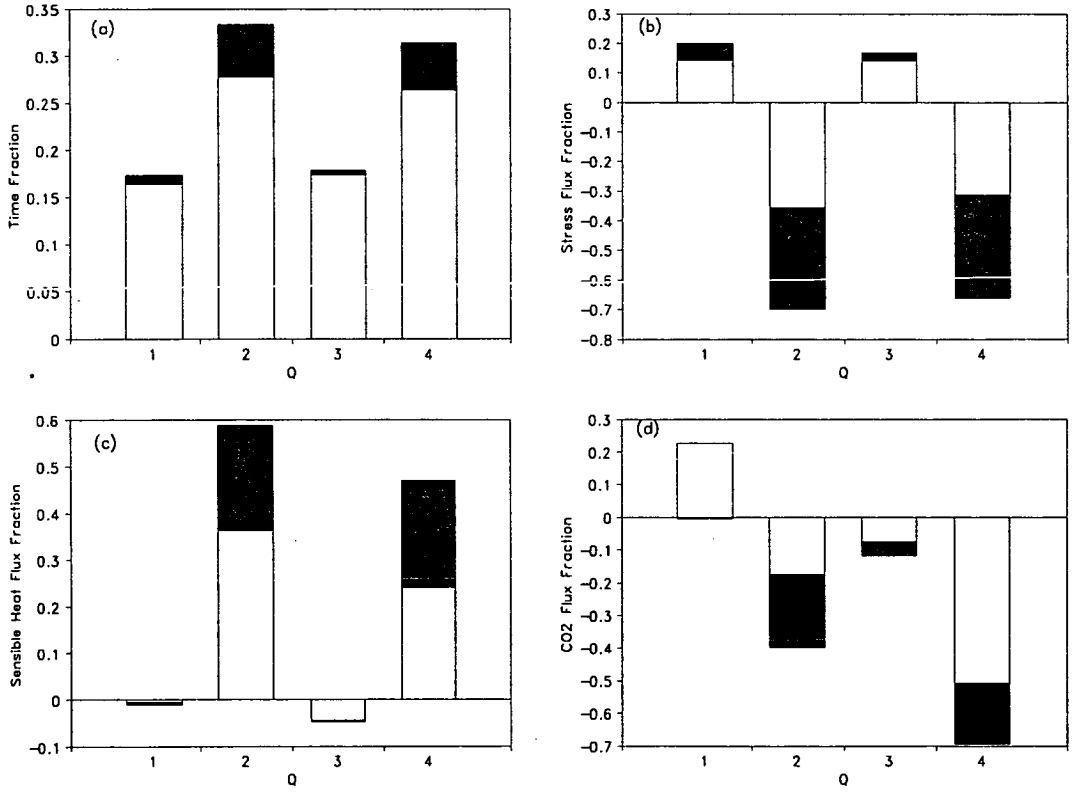

Fig. 7.2.4 Time, momentum stress, sensible heat and CO_2 flux fractions from J213, 1991, at 1.2*h* at Rivox, shown as (*a*), (*b*), (*c*) and (*d*) respectively. Dark shading denotes extreme events, i.e. $H \geq 4$.

The interaction quadrant contributions on J213 showed more variability in the direction of the associated CO_2 flux. The normal contribution to the CO_2 flux in $Q1$ was positive and represented 22.7 % of the net mean flux, while the extreme contribution was negative and 0.4 % of the net mean flux Figure 7.2.4*d*, although this is not obvious from the figure.

	J198		J207		J213	
Height	$(S_{1,0}+S_{3,0})/(S_{2,0}+S_{4,0})$	$S_{4,0}/S_{2,0}$	$(S_{1,0}+S_{3,0})/(S_{2,0}+S_{4,0})$	$S_{4,0}/S_{2,0}$	$(S_{1,0}+S_{3,0})/(S_{2,0}+S_{4,0})$	$S_{4,0}/S_{2,0}$
1.2*h*	-0.2	1.4	—	—	-0.2	0.9
0.7*h*	—	—	-0.7	1.5	-1.8	1.3
0.1*h*	0.1	0.9	-0.9	0.8	-0.9	1.1

Table 7.2.2 Ratios of total momentum flux in the interaction and gust/ejection quadrants, $(S_{1,0}+S_{3,0})/(S_{2,0}+S_{4,0})$, and ratios of total momentum flux in $Q4$ and $Q2$, $S_{4,0}/S_{2,0}$, for J198, J207 and J213, respectively.

7.2.2 In the Canopy Crown

Results at 0.7*h* come from J207, and J213, 1991. The time fractions in the momentum quadrants from the two data sets showed different distributions (Figures 7.2.5*a* and 7.2.6*a*). In the data set from J207, the largest time fraction was in the ejection quadrant with the other quadrants having roughly similar values (Figure 7.2:7*a*). On J213 the interaction quadrants had larger contributions than the gust/ejection quadrants (Figures 7.2.9*a*). In general, for both these data sets the time fractions had closer values between the quadrants than at 1.2*h*. The attenuation of momentum in the canopy crown by form drag on tree elements creates turbulent wakes which would be expected to increase the occurrence of interaction momentum events. At 0.7*h*, extreme events occurred 39.1 % and 29.3 % of the time on J207 and J213, respectively, compared with only 5 - 12 % at 1.2*h* on J198 and J213, respectively.

The momentum stress fractions from the two data sets reflected the differences in the time fractions (Figures 7.2.5*b* and 7.2.6*b*). Both momentum stress distributions showed a high contribution from extreme events, with 95.9 % and 86.7 % of the mean momentum stress accounted for by extreme events on days J207 and J213, respectively. This is a result of the upward and downward momentum contributions at 0.7*h* being more evenly balanced about a much smaller net flux than at 1.2*h*, as discussed in section 7.2. The ratios of interaction to gust/ejection momentum

fractions, $(S_{1,0} + S_{3,0})/(S_{2,0} + S_{4,0})$, were -0.7 and -1.8 for J207 and J213, respectively (Table 7.2.2).

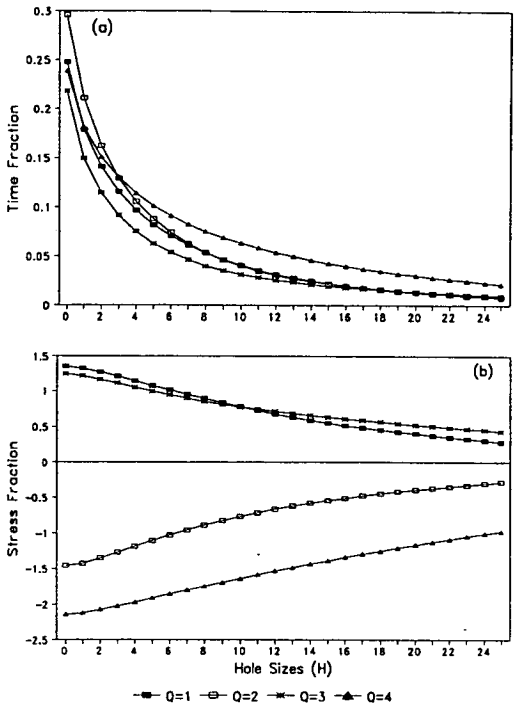

Fig. 7.2.5 Time and momentum stress fractions from J207, 1991, at 0.7*h* at Rivox, shown as (*a*) and (*b*) respectively.

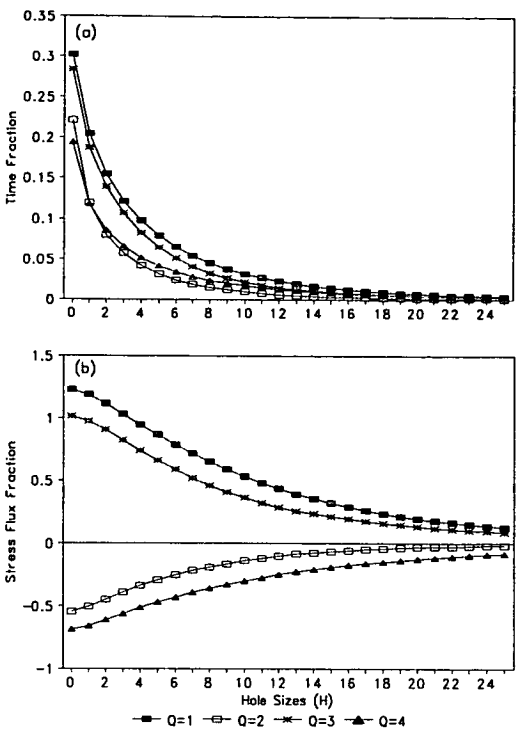

Fig. 7.2.6 Time and momentum stress fractions from J213, 1991, at 0.7*h* at Rivox, shown as (*a*) and (*b*) respectively.

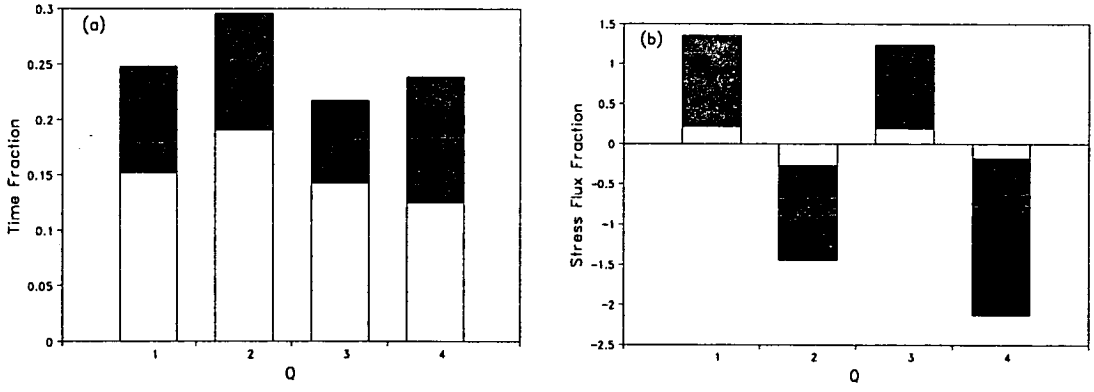

Fig. 7.2.7 Time and momentum stress fractions from J207, 1991, at 0.7*h* at Rivox, shown as (*a*) and (*b*) respectively. Dark shading denotes extreme events, i.e. $H \geq 4$.

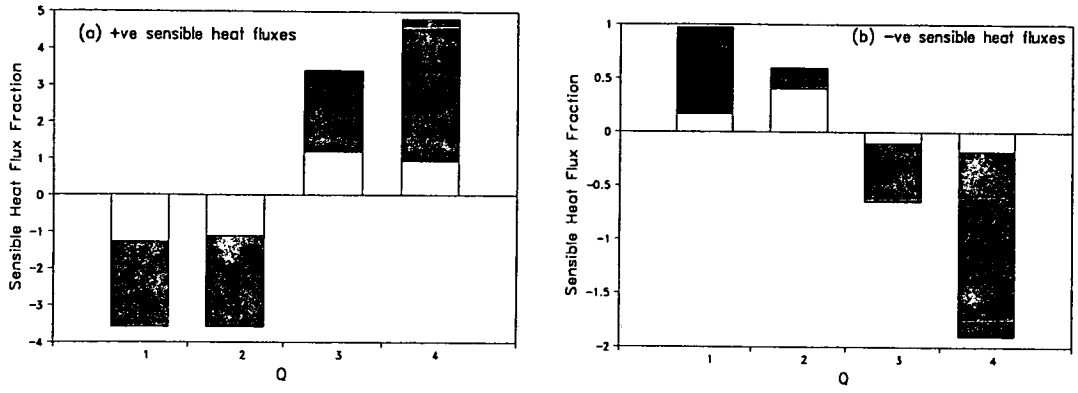

Fig. 7.2.8 Sensible heat flux fractions averaged over periods with (*a*) positive and (*b*) negative mean half hour sensible heat fluxes, from J207, 1991, at 0.7*h* at Rivox. Each average is over four half hour periods. Dark shading denotes extreme events, i.e. $H \geq 4$.

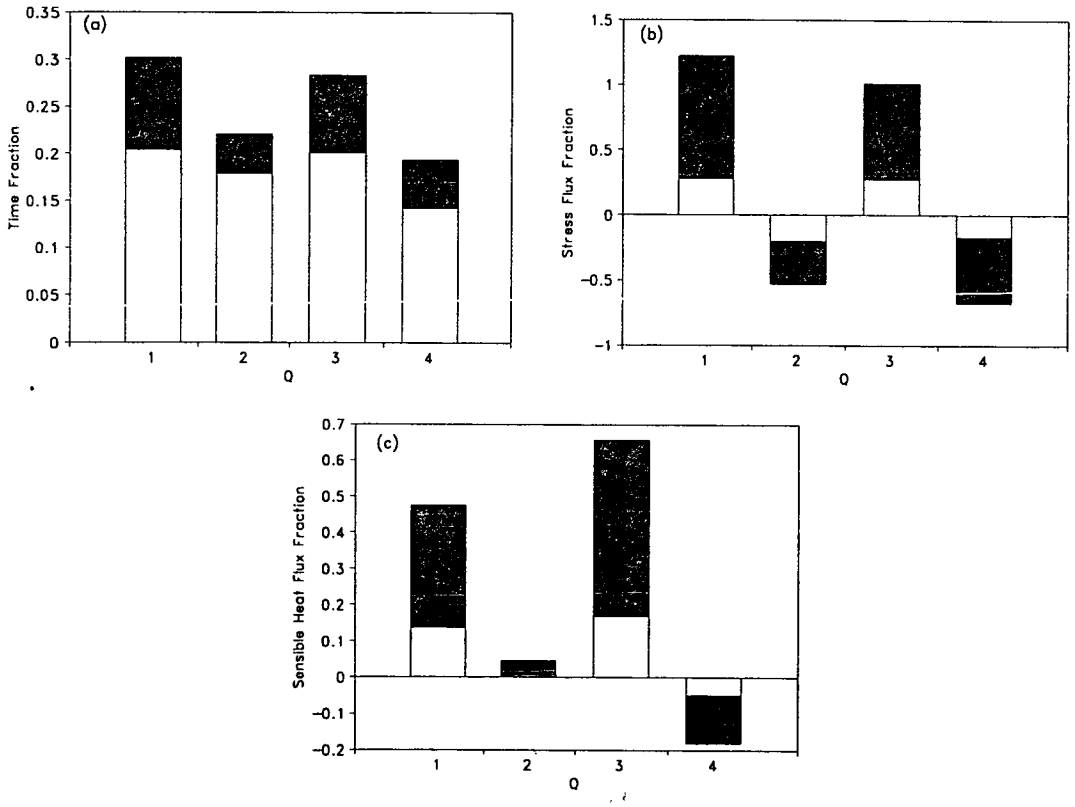

Fig. 7.2.9 Time, momentum stress and sensible heat flux fractions from J213, 1991, at 0.1*h* at Rivox, shown as (*a*), (*b*) and (*c*) respectively. Dark shading denotes extreme events, i.e. $H \geq 4$.

The magnitudes of the mean momentum stresses at $0.7h$ were only about 2 to 3 % of the values of the net momentum flux at $1.2h$ on days J207 and J213, respectively (Table 7.2.1). The overall net flux of momentum on J207 was negative, whilst it was positive on J213 as discussed earlier. Considering the gust/ejection quadrants, gusts made a larger contribution to the downward flux than ejections, where the ratio $S_{4,0}/S_{2,0}$ was 1.5 and 1.3 for J207 and J213, respectively. Previously reported values of $S_{4,0}/S_{2,0}$ in forest canopy crowns were ~ 1.4 at $0.5h$ in an Almond orchard (Baldocchi and Meyers, 1987) and 1.7 at $0.5h$ in an Oak forest (Moritz, 1989). In an artificial plant canopy in a wind tunnel experiment, Raupach *et al.* (1986) reported values of $S_{4,0}/S_{2,0}$ of 1.3 and 1.2 at $0.8h$ and $0.5h$, respectively. Our values would seem to broadly agree with the results from quite different forest types, with the general observation that gusts dominate ejections in the canopy crown. However, the usefulness of such comparisons is doubtful as all the canopies produced a much less rapid attenuation of momentum than was found at Rivox.

The mean sensible heat fluxes over the eight half hour periods on J207 had an even mixture of positive and negative fluxes. Average fractional flux contributions were calculated from the two groups (Figure 7.2.8). The two sets of sensible heat flux fractions had different directions in all quadrants. The average sensible heat flux over the J207 data set was 0 ± 0.9 W m^{-2}, Table 7.2.1, (the error being one standard deviation). With such small mean fluxes this data can not be considered reliable.

The half hourly calculated sensible heat fluxes on J213 were all positive, with an average value of 16 W m^{-2}. The sensible heat flux fractions from the interaction quadrants were much larger than those from the gust/ejection quadrants, (Figure 7.2.9*c*). Extreme momentum events were associated with 73.7 % of the net mean sensible heat flux on J213 compared to only 44.4 % at $1.2h$.

7.2.3 In the Trunkspace

Results at $0.1h$ came from days J198, J207 and J213, 1991. Time fraction results from J198 at $0.1h$ indicated a dominance of events occurring in the interaction quadrants, with mostly normal events occurring in all quadrants (extreme events occurred only 28.1 % of the time), (Figures 7.2.10 and 7.2.13). The time fraction contributions on J207 and J213 at $0.1h$ are approximately equal in all quadrants and extreme events occurred 62.0 % and 71.5 % of the time on J207 and J213, respectively, (Figures 7.2.11, 7.2.12, 7.2.14 and 7.2.15). The net mean momentum fluxes at $0.1h$ of the data periods from days J207 and J213 were between 3 to 4 % of the value at $0.1h$ on J198, Table 7.2.1. The stronger mean momentum flux from J198 seemed to result from a dominance of the interaction quadrants over the gust/ejection

quadrants, with the weaker momentum flux periods having a more even distribution of occurrences in all quadrants.

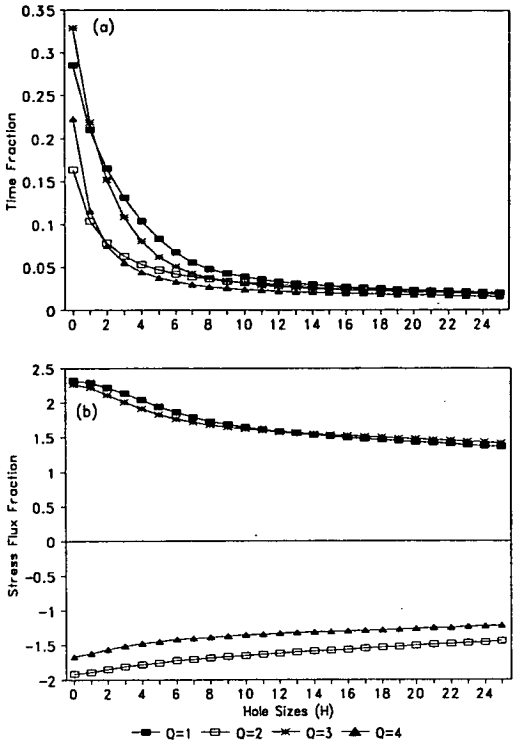

Fig. 7.2.10 Time and momentum stress fractions from J198, 1991, at 0.1h at Rivox, shown as (a) and (b) respectively.

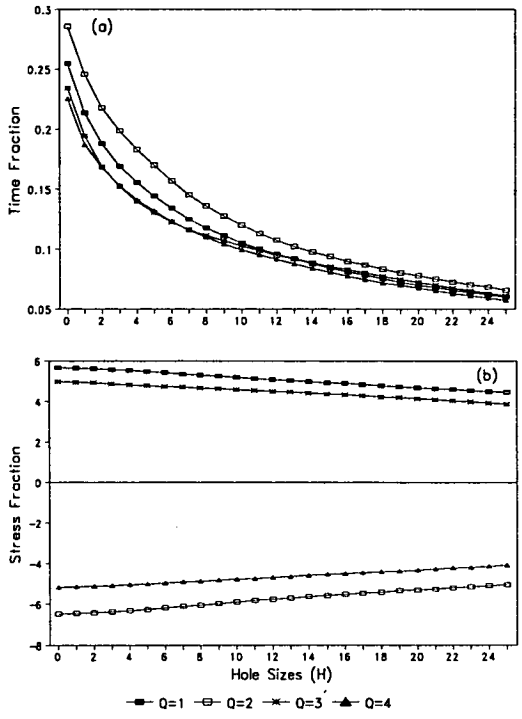

Fig. 7.2.11 Time and momentum stress fractions from J207, 1991, at 0.1h at Rivox, shown as (a) and (b) respectively.

The corresponding momentum stress contributions for the three data sets were evenly balanced between positive and negative quadrant fractions. The ratios of interaction to gust/ejection momentum fractions, $(S_{1,0} + S_{3,0})/(S_{2,0} + S_{4,0})$, was -1.3 for J198 and -0.9 for J207 and J213 (Table 7.2.2). The individual quadrant momentum fractions were as high as ± 8, i.e. 800 % of the net mean flux at 0.1h on J213, but even a figure of 8 times this net flux represents only ~ 0.7 % of the net flux at 1.2h (Table 7.2.1). The actual net mean flux magnitudes were very small for the data sets from J207 and J213 and must be treated with some caution, (Table 7.2.1).

Extreme events predominated in all three data sets at 0.1h due to the small net mean momentum flux, with extreme events accounting for 69.1 %, 100.6 % and 100.0 % of the net mean flux for J198, J207 and J213, respectively, (normal events on J207 accounted for 0.6 % of the net mean flux, in the opposing direction). The ratio

between gust and ejection events for the three data sets, $S_{4,0}/S_{2,0}$ was 1.1, 0.8 and 1.1 for J198, J207 and J213, respectively. Previously reported results at $0.1h$ in an Oak forest trunkspace (Moritz, 1989), had $S_{4,0}/S_{2,0} \sim 1.1$ to 1.4 and at $0.14h$ in an Almond orchard, Baldocchi and Meyers (1987) reported $S_{4,0}/S_{2,0} \sim 0.9$. The results for our forest indicate that at $0.1h$ gusts/ejection events and also interaction events are evenly balanced in magnitude.

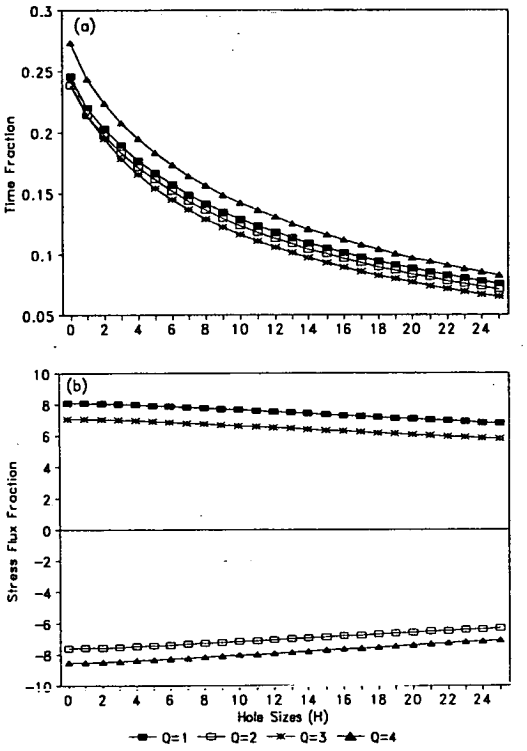

Fig. 7.2.12 Time and momentum stress fractions from J213, 1991, at $0.1h$ at Rivox, shown as (*a*) and (*b*) respectively.

As discussed in section 4.4 and 6.3.2, the lack of predictable scalar co-spectral responses at $0.1h$ casts some doubt over the reliability of these fluxes. The small mean fluxes of sensible heat and CO_2 at $0.1h$ compared to those above the forest result in flux fractions that are more sensitive to instrumental errors than those calculated at $1.2h$. The sensible heat and CO_2 flux fractions at $0.1h$ show somewhat more variability when the fluxes are very small and this is particularly true at $0.1h$ on J207.

The associated sensible heat flux contributions in the momentum quadrants were similar for the data from J198 and J213, but the results from the J207 data were quite different, showing variability in the directions of the normal and extreme contributions in $Q3$. The sensible heat data from J207 is probably unreliable due to the very small heat flux measured over this period (Table 7.2.1). Sensible heat

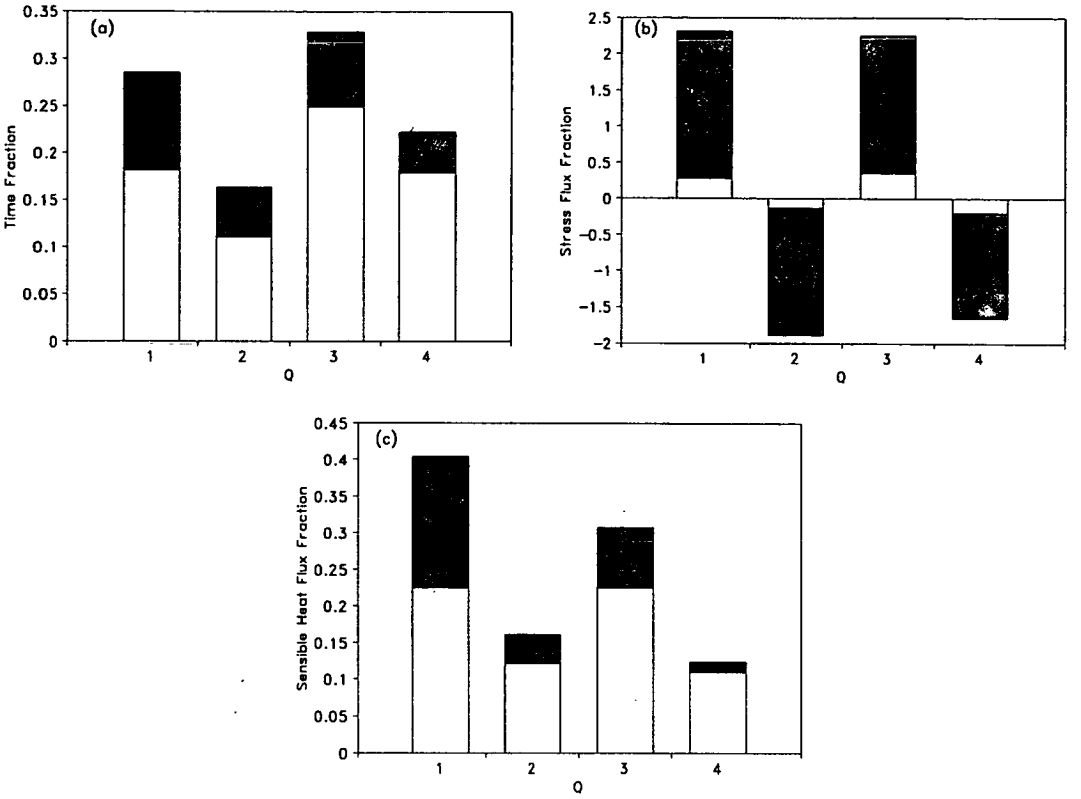

Fig. 7.2.13 Time, momentum stress and sensible heat flux fractions from J198, 1991, at 0.1*h* at Rivox, shown as (*a*), (*b*) and (*c*) respectively. Dark shading denotes extreme events, i.e. $H \geq 4$.

contributions in the momentum quadrants on J198 and J213 were dominated by positive interaction quadrant contributions (Figures 7.2.13*c* and 7.2.15*c*). The gust/ejection quadrants had an associated upward positive sensible heat flux concurrent with a downward negative momentum flux. Physically, this implies that gusts were transporting cooler air into the trunkspace and ejections were carrying warmer air out of the trunkspace. Extreme events accounted for 31.9 % and 85.5 % of net mean sensible heat flux on J198 and J213, respectively.

The CO_2 fluxes for periods from J207 also had small net mean fluxes which were uniformly negative. The averaged quadrant flux fractions are given in Figure 7.2.14*d*. The gust/ejection quadrants' contribution to the total flux was larger than that from the interaction quadrants, with the ejection quadrant contribution dominating all the others. The inward interaction quadrant, $Q3$, displayed a normal and extreme component in opposing directions which indicates a degree of directional variability in the transport. Extreme events accounted for 90.8 % of the negative net mean CO_2 flux at 0.1*h* on J207.

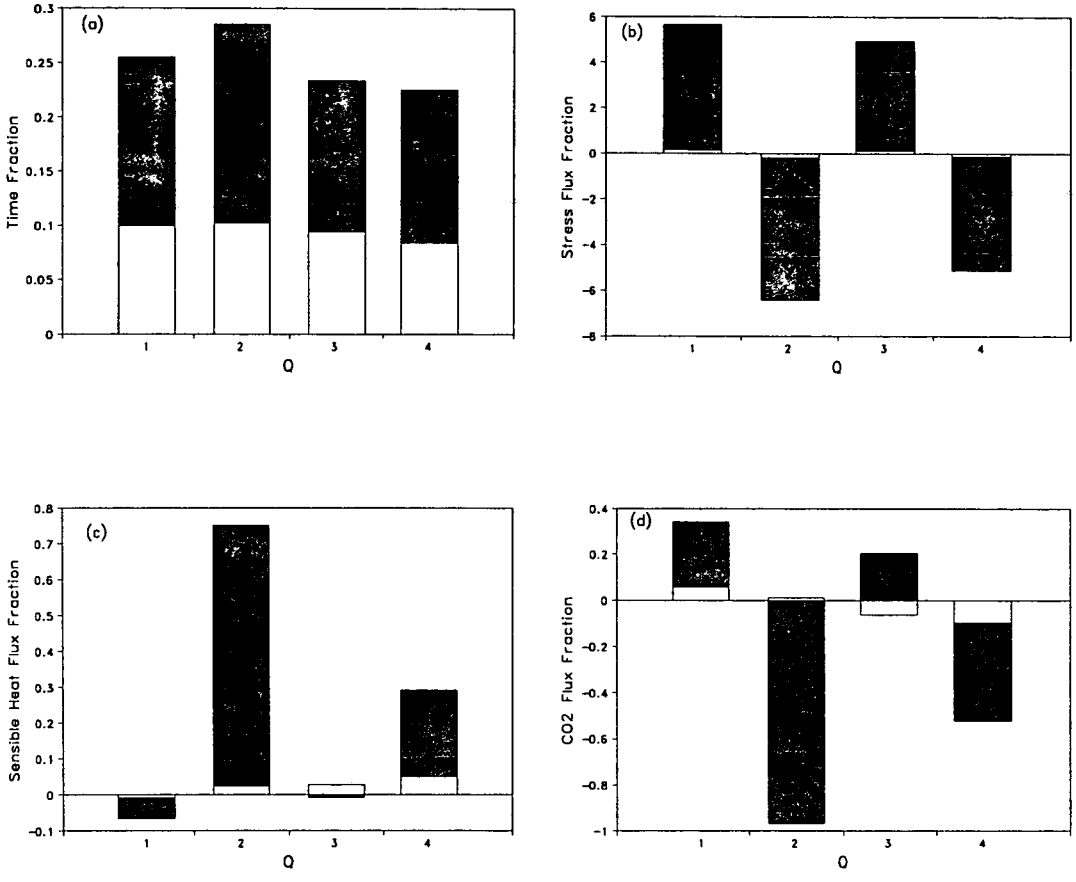

Fig. 7.2.14 Time, momentum stress, sensible heat flux and CO_2 flux fractions from J207, 1991, at $0.1h$ at Rivox, shown as (*a*), (*b*), (*c*) and (*d*) respectively. Dark shading denotes extreme events, i.e. $H \geq 4$.

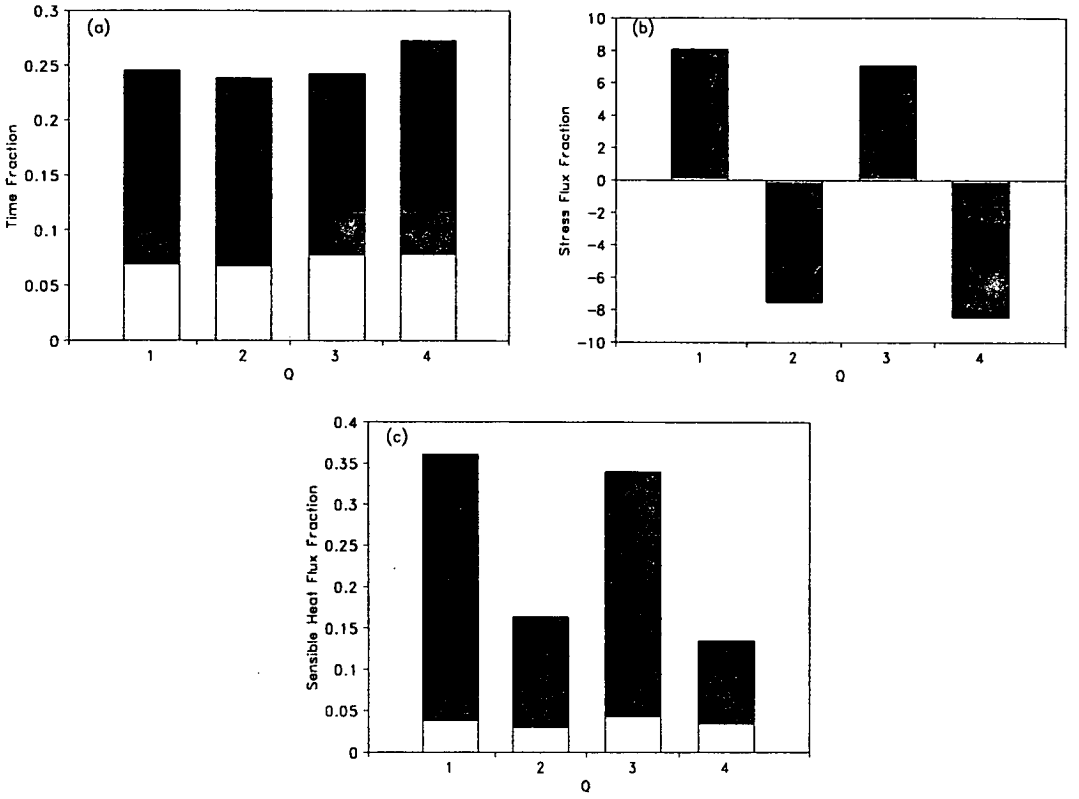

Fig. 7.2.15 Time, momentum stress and sensible heat flux fractions from J213, 1991, at $0.1h$ at Rivox, shown as (*a*), (*b*) and (*c*) respectively. Dark shading denotes extreme events, i.e. $H \geq 4$.

7.3 SUMMARY AND CONCLUSIONS

(i) Above the canopy more momentum events occurred in the gust/ejection quadrants $Q2$ and $Q4$ than in the interaction quadrants $Q1$ and $Q3$, with ejections occurring slightly more frequently than gusts. Taking all quadrants together, extreme momentum events occurred only 5 - 12 % of the time.

(ii) At $1.2h$ extreme events accounted for 49 - 56 % of the negative momentum flux, 23 - 44 % of the positive sensible heat flux and 21 - 47 % of the negative CO_2 flux across this plane despite only occurring 5 - 12 % of the time. The definition of extreme events above the canopy at $H \geq 4$ seems reasonable as these events occur intermittently yet transport a high proportion of the momentum and scalar fluxes. These extreme events are significantly more energetic than the mean flow and are thus able to penetrate deeply into the canopy, where they exchange momentum and scalars. In terms of the momentum and scalar fluxes into and out of the forest system these intermittent energetic events are clearly of great importance.

(iii) At $0.7h$, in the canopy crown there was a more even frequency of occurrence across the quadrants, with a larger time fraction in the interaction quadrants, than at $1.2h$. The momentum flux fractions in the interaction quadrants were also larger than at $1.2h$ and there was a higher proportion of extreme events in all quadrants.

The increase in the time and momentum stress fractions of the interaction quadrants would be expected in the canopy crown as a result of the creation of turbulent wakes. The small net fluxes of momentum resulting from large opposed components in the gust/ejection and interaction quadrants increases the contribution of extreme events as more events occur at very large hole sizes. Extreme events at $0.7h$ occurred 29 - 39 % of the time, transporting 86 - 96 % of the mean momentum flux and 74 % of the sensible heat flux.

(iv) In the trunkspace at $0.1h$ the distribution of time fractions across the quadrants was again more even than at $1.2h$, occasionally with a dominance by the interaction quadrants. The net momentum fluxes at $0.1h$ were extremely small compared to those at $1.2h$. The contributions from the gust/ejection and interaction quadrants were large in comparison to the net flux and evenly balanced in magnitude.

(v) The ratio $S_{4,0}/S_{2,0}$ of the momentum flux transported by gusts to that of ejections for $H = 0$ has often been quoted in the literature to indicate which of these physical processes dominates the momentum transfer. The values of this ratio from our analysis, (shown in Table 7.2.2), showed no clear domination of gusts over ejections at $1.2h$ or $0.1h$ and a probable domination of gusts over ejections at $0.7h$. However, the ratio of total positive and negative momentum fractions, $(S_{1,0} + S_{3,0})/(S_{2,0} + S_{4,0})$, showed that the gust/ejection quadrants did indeed dominate at $1.2h$ but that there was no clear pattern within the canopy as momentum transport was occasionally dominated by the interaction quadrants.

CHAPTER 8
CONCLUSIONS AND RECOMMENDATIONS

8.1 INTRODUCTION

The aim of this research was to investigate the turbulent exchange of mass, energy and momentum in a northern hemisphere coniferous forest, with special attention to the exchange of carbon dioxide. The eddy covariance technique was considered to be the best method of examining these exchanges.

The research also examined the turbulent transfer processes in the forest with reference to turbulence statistics and with the techniques of spectral analysis, velocity space-time cross-correlations and quadrant analysis.

This thesis reports eddy covariance measurements of CO_2, and supporting heat and momentum fluxes, above and within a coniferous forest canopy in south west Scotland. The nature of the turbulent flow regimes at each measurement height were also examined. The correction to fluxes for frequency-limited losses were estimated and the eddy covariance technique evaluated in the different regimes above and below the canopy. The examination of the flow regimes tells us much about the transport processes which dominate exchanges within and above the forest. This information will aid the planning, implementation and interpretation of future eddy covariance experiments.

8.2 SUMMARY AND CONCLUSIONS

8.2.1 The Forest/Atmosphere Momentum Exchange

Measurements were made of the turbulent air flow above and within a dense plantation of Sitka spruce (*Picea Sitchensis* (Bong.) Carr.) with an array of sonic anemometers at three heights.

The canopy was found to be extremely efficient at attenuating momentum compared to more open plant canopies (Raupach, 1988). At $0.7h$, in the lower part of the canopy crown, momentum fluxes were 2 - 3 % of the magnitude of the downward flux at $1.2h$ and were on occasions directed upwards. This momentum attenuation is a result of the action of plant elements on the flow. Power spectra of u, v and w velocities had inertial sub-range slopes at $1.2h$ close to the -2/3 value predicted by Kolmogorov similarity arguments (Stull, 1988); however, at $0.7h$ the spectral slopes were considerably steeper. These steep slopes indicate that the flow is doing work against form drag of the plant elements. Large scale motions in the flow are thus broken down into motions with length scales of the order of the plant elements which

then quickly dissipate. Similarly, spectral slopes of momentum co-spectra in the lower crown had much steeper slopes than the -4/3 slopes predicted by similarity theory and observed at 1.2h above the canopy.

A quadrant analysis of the momentum fluxes showed that the negative (downward) momentum flux quadrants $Q2$ and $Q4$ dominated the positive flux quadrants $Q1$ and $Q3$ above the canopy. At heights 0.7h and 0.1h, however, the distribution of momentum between the quadrants was more even, indicating the production of turbulent wakes within the canopy as the downward moving elements were attenuated. On occasion, in the crown at 0.7h and in the trunkspace at 0.1h, the 'interaction' quadrants dominated, resulting in positive net momentum fluxes.

Much evidence to support the existence of the large, intermittent and energetic structures which dominate the transfer of momentum from the atmosphere to plant canopies has been reported in the literature (e.g. Finnigan, 1979*b*; Denmead and Bradley, 1985; Raupach *et al.*, 1989), and this view is confirmed by this study. Integral Eularian length scales calculated from autocorrelations of u and w velocities at 1.2h were $L_u \sim h$ and $L_w \sim 0.2h$ confirming that canopy height, h, is the primary length scale for canopy turbulence (Raupach, 1988; Raupach *et al.*, 1989). The normalised velocity power and co-spectra had low frequency peaks at all levels above and within the canopy. Assuming the validity of Taylor's hypothesis, these peak frequencies indicated dominant motions at 1.2h with length scales $L_u \sim 4$ - $14h$ and $L_w \sim 1$ - $3h$. Momentum co-spectral peaks at 1.2h indicated dominant events with a length scale $\sim 5h$. Quadrant analysis of momentum transport at 1.2h showed that about 50 % of the momentum flux into the canopy was accounted for by events occurring only about 5 - 12 % of the time.

Cross-correlations in time of velocity components at 1.2h with those within the canopy, showed that streamwise velocity fluctuations at 0.7h and 0.1h lagged those at 1.2h. This indicates the passage of an inclined structure of canopy scale 'leaning with the shear' through the canopy (Raupach *et al.*, 1989). Vertical velocity fluctuations occurred simultaneously throughout the canopy, i.e. with zero lag. This result indicates that pressure waves or gradients associated with large gust structures produce w fluctuations within the canopy (this is not observed above the canopy where the effect is swamped by the gusts).

8.2.2 The Forest/Atmosphere CO_2 Exchange

Measurements of CO_2 flux and supporting measurements of sensible and latent heat fluxes were made with eddy covariance systems at 1.2h above the forest,

and at $0.1h$ in the dead branch trunkspace. CO_2 fluxes were calculated taking into account the WPL density effect and losses due to imperfect frequency response of the system.

At $1.2h$ the net CO_2 flux across the upper system boundary, F_a, showed a strong diurnal cycle with maximum influx to the forest occurring around midday. The 48 hour data period (J199 - J201, 1990), presented in Chapter 4, was warm, sunny and dry and had a maximum influx of -0.8 mg m^{-2} s^{-1}. During an intercomparison of CO_2 sensors (J195, 1990), conditions were cooler with a smaller vapour pressure deficit, and maximum influxes of -1.4 mg m^{-2} s^{-1}. Night time respiration fluxes out of the forest on J199 - J201 were around 0.1 mg m^{-2} s^{-1}.

The main controlling environmental variable on F_a was found to be photosynthetically active photon flux, I_P. No evidence was found during the J199 - 201 data period of a strong dependence of F_a on either D or air temperature, T_{air}. This may be attributed to the small range of vapour pressure deficits over the period and the relatively small amount of data (96 half hour average fluxes). Net CO_2 flux into the system was found to vary with I_P in a form well represented by a rectangular hyperbola. Curves of this form were fitted to the data from J199 - 201 and to a smaller data set from J207, 1991 when conditions were overcast. These curves predicted quantum requirements of 43 and 23 photons (molecule CO_2 fixed)$^{-1}$, dark respiration fluxes of 0.12 and 0.17 mg m^{-2} s^{-1}, saturation net influxes of 1.3 and 1.2 mg m^{-2} s^{-1}; and compensation points of 130 and 104 μmol m^{-2} s^{-1} for sunny and overcast periods, respectively.

The CO_2 flux data reported above the forest were biased to dry weather conditions which are not typical for the site which has an annual rainfall of ~ 1800 mm. To obtain a better understanding of the long term exchanges of this forest with the atmosphere, further measurements must be made in all weathers.

At $0.1h$ CO_2 fluxes were presented for 45 hours from J205, 1990, uncorrected for the WPL density effect and for frequency losses as no LE fluxes were measured and no reliable co-spectral function for CO_2 response was obtainable. The uncorrected CO_2 flux showed little diurnal pattern and much scatter with average value around 0.06 mg m^{-2} s^{-1}. Estimates of the likely correction for WPL effects indicated the raw fluxes were in error by ~ 50 %; however, the error due to frequency losses could not be estimated and little reliability can be placed on these flux values. The problems of making eddy covariance measurements in the conditions found at $0.1h$ at Rivox are discussed below.

A quadrant analysis of momentum transport in the canopy showed the relationship of scalar transport of CO_2 and sensible heat to momentum events. Above

the canopy at 1.2*h* the scalar flux transport was dominated by intermittent and energetic events in a similar manner to the momentum fluxes. Momentum events which occurred for about 5 -12 % of the time transported about 50 % of the momentum flux, about 21 - 47 % of the CO_2 flux, and about 23 - 44 % of the sensible heat flux at 1.2*h*. These events at 1.2*h* were mostly gust/ejection structures which sweep into and out of the canopy crown and were clearly very efficient at exchanging momentum and scalars with the atmosphere above the forest. Within the canopy at 0.7*h* and 0.1*h* the flow appeared almost entirely extreme in the quadrant analysis due to the very small net momentum fluxes comprised of large opposing components. No clear picture of scalar exchange emerges from this analysis in the lower levels of the canopy where scalar fluxes where very small and highly variable.

8.2.3 Evaluation of Eddy Covariance technique in the forest system

Measurement of mass fluxes using the eddy covariance technique is ideally suited to work in plant canopies where measurements can be made *in situ* in relatively undisturbed and representative terrain. Certain problems arise with the technique, most of which can be overcome.

The successful use of transfer function corrections for frequency losses (Moore, 1986) at 1.2*h* above this forest depended upon obtaining an accurate representation of the CO_2 co-spectral response function. The model for sensible heat co-spectral response in unstable conditions of Kaimal *et al.* (1972) has often been used in the literature to represent the CO_2 response. Over field crops, deciduous forest canopies, or prairie, this function often corresponds well to calculated co-spectral densities, but in the dense conifer canopy at Rivox this was not the case. A representative co-spectral response for Rivox was obtained by fitting curves of the form of the co-spectral models of Kaimal *et al.* (1972) to CO_2 co-spectral densities calculated from data at 1.2*h*.

In the canopy trunkspace at Rivox, the flow regime was very different to that above the canopy. A cross-correlation analysis of velocity fluctuations at 0.1*h*, with reference to 1.2*h*, showed that on some days the trunkspace was effectively de-coupled from the atmosphere above the forest (Figure 5.4.3). On other days the trunkspace was well correlated with the flow at 1.2*h* with large horizontal structures penetrating to 0.1*h* with vertical velocities apparently driven by pressure forces associated with these structures. Spectral analysis of the air flow in the trunkspace also showed that the horizontal and vertical velocities exhibited different behaviour (Figures 6.2.1*c* and 6.2.2*c*). The accuracy of eddy covariance measurements of scalars such as CO_2 is difficult to evaluate in these conditions. Scalar co-spectra at 0.1*h* were

scattered and variable and showed none of the characteristics of the co-spectra above the canopy. At $0.1h$ the scalar power spectrum had a similar response to the u and v power spectra, where the w power spectrum had a different form. This mismatching of response between w and scalar fluctuations may explain some of the scatter in the scalar co-spectra at $0.1h$. It was not possible to verify a suitable co-spectral response function so that frequency loss corrections could be applied.

In other, more open, canopies, measurements of CO_2 fluxes in the trunk spaces of forests have been reported where CO_2 co-spectra had a form similar to that above the forest (Baldocchi *et al.*, 1986; Baldocchi and Meyers, 1991). In a dense Black spruce forest, Amiro (1990*b*) also reported scalar co-spectra (temperature) in the trunkspace with a form similar to that above the forest. At Rivox, in the absence of a stable co-spectral response, the CO_2 fluxes at $0.1h$ on the days presented could not be relied on.

8.3 RECOMMENDATIONS FOR FUTURE WORK

To gain a better picture of the size and form of the large structures that dominate exchanges between the forest and the atmosphere, an extended instrument array is needed. Anemometer arrays in two dimensions of the flow (i.e. in the yz plane) would allow cross-correlations of velocity fluctuations in both time and space. These large structures have been identified in this way as 'double-roller' eddies by Raupach *et al.* (1989) in a wind tunnel wheat canopy (and by others in smooth wall boundary layer experiments). Raupach *et al.* (1989) postulated that these double-roller structures are a universal form above all canopies, and further work is required in varied real canopy types to confirm this.

The routine monitoring of CO_2 exchanges between forests and the atmosphere would be helpful to those attempting to address the global effects of changes in CO_2 concentrations. The adaptation of eddy covariance systems to all weather and low maintenance operation is consequently an important area for future effort.

To increase our understanding of the internal CO_2 fluxes of the forest system further experiments measuring fluxes within the canopy are necessary. As the flow regimes within the forest are very different to that above the canopy careful evaluation of the data will be required. Eddy covariance instruments in the canopy trunkspace are sampling air from a very different and probably much smaller area than those placed above the canopy. Rather than single instrument systems at each height, several systems might give a better area average of the flux, perhaps sampled over a longer time than above the canopy to avoid problems of stationarity in highly skewed intermittent flows.

REFERENCES

Allen L. H. Jr.: (1968), 'Turbulence and wind speed spectra within a Japanese larch plantation', *J. App. Meteorol.*, **7**, 73-78.

Amiro B.D., Davis P.A.: (1988), 'Statistics of atmospheric turbulence within a natural black spruce forest canopy', *Boundary-Layer Meteorol.*, **44**, 267-283.

Amiro B.D.: (1990*a*), 'Comparison of turbulence statistics within three boreal forest canopies', *Boundary-Layer Meteorol.*, **51**, 99-121.

Amiro B.D.: (1990*b*), 'Drag coefficients and turbulent spectra within three boreal forest canopies', *Boundary-Layer Meteorol.*, **52**, 227-246.

Anderson D.E., Verma S.B., Clement R.J.: (1986), 'Turbulence spectra of CO_2, water vapour, temperature and velocity over a deciduous forest', *Agric. Forest Meteorol.*, **38**, 81-99.

Anderson D.E., Verma S.B., Rosenberg N.J.: (1984), 'Eddy correlation measurements of CO_2, latent heat and sensible heat over a crop surface', *Boundary-Layer Meteorol.*, **29**, 263-272.

Antonia R.A., Brown L.W.B., Bisset D.K.: (1988), 'Effects of Reynolds number on the organised motion in a turbulent boundary layer', *Proceedings of the Zaric Memorial Internetional Seminar on Wall Turbulence*, Dubrovnik, Yugoslavia, 16-20 May 1988.

Baldocchi D.D, Verma S.B., Matt D.R., Anderson D.E.: (1986), 'Eddy-correlation measurements of carbon dioxide efflux from the forest floor of a deciduous forest', *J. Appl. Ecology*, **23**, 967-975.

Baldocchi D.D, Hicks B.B., Meyers T.P.: (1988), 'Measuring biosphere-atmosphere exchanges of biologically related gases with micrometeorological methods', *Ecology*, **69**, 1331-1340.

Baldocchi D.D., Hutchison B.A.: (1987), 'Turbulence in an almond orchard: vertical variations in turbulent statistics', *Boundary-Layer Meteorol.*, **40**, 127-146.

Baldocchi D.D., Hutchison B.A.: (1988), 'Turbulence in an almond orchard: spatial variations in spectra and coherence', *Boundary-Layer Meteorol.*, **42**, 293-311.

Baldocchi D.D., Meyers T.P.: (1988*a*), 'Turbulence structure in a deciduous forest canopy', *Boundary-Layer Meteorol.*, **43**, 345-365.

Baldocchi D.D., Meyers T.P.: (1988*b*), 'A spectral and lag-correlation analysis of turbulence in a deciduous forest canopy', *Boundary-Layer Meteorol.*, **45**, 31-58.

Baldocchi D.D., Meyers T.P.: (1991), 'Trace gas exchange above the floor of a deciduous forest. 1 Evaporation and efflux', *J. Geophys. Research*, **96**, No. D4, 7271-7285.

Bergström H., Högström U.: (1989), 'Turbulent exchange above a pine forest. II Organized structures', *Boundary-Layer Meteorol.*, **49**, 231-263.

Biscoe P.V., Saffell R.A., Smith P.D.: (1977), 'An apparatus for calibrating soil heat flux plates', *Agric. Meterol.*, **18**, 49-54.

Bottemanne F.A.: (1976), 'Eddy correlation measurements above a maize crop using a simple cruciform hot-wire anemometer', *Agric. Meteorol.*, **20**, 397-410.

Businger J.A., Wyngaard J.C., Izumi Y., Bradley E.F.: (1971), 'Flux profile relationships in the atmospheric surface layer', *J. Atmos. Sciences.*, **28**, 181-189.

Campbell G.S., Unsworth B.D: (1979), 'An inexpensive sonic anemometer for eddy correlation', *J. Appl. Meteorol.*, **18**, 1072-1077.

Chen F.: (1990), 'Turbulent characteristics over a rough natural surface. Part I: Turbulent structures', *Boundary-Layer Meteorol.*, **52**, 151-175.

Coppin P.A., Taylor K.J. (1983), 'A three component sonic anemometer/thermometer for general micrometeorological research', *Boundary-Layer Meteorol.*, **27**, 27-42.

Crowther J.M., Hutchings N.J.: (1985), 'Correlated vertical wind speeds in a spruce canopy. In B.A. Hutchinson and B.B. Hicks (eds), *Forest-Atmosphere Interactions*', D. Reidel Pub. Co., Dordrecht, 543-562.

D'Arrigo R., Jacoby G.C., Fung I.Y.: (1987), 'Boreal forests and atmosphere-biosphere exchange of carbon dioxide', *Nature*, **329**, 321-323.

Denmead O.T., Bradley E.F.: (1985), 'Flux-gradient relationships in a forest canopy. In B.A. Hutchinson and B.B. Hicks (eds), *Forest-Atmosphere Interactions*', D. Reidel Pub. Co., Dordrecht, 421-442.

Denmead O.T., Bradley E.F.: (1989), 'Eddy-correlation measurement of the CO_2 flux in plant canopies', *Proc. of the Fourth Australian Conf. on Heat and Mass Transfer*, Christchurch, New Zealand.

Denmead O.T.: (1969), 'Comparative micrometeorology of a wheat field and a forest of *Pinus Radiata*, *Agric. Meteorol.*, **6**, 357-371.

Dyer A.J., Garratt J.R., Francey R.J., McIlroy I.C., Bacon N.E., Bradley E.F., Denmead O.T., Tsvang L.R., Volkov Y.A., Koprov B.M., Elagina L.G., Sahashi K., Monji N., Hanafusa T., Tsukamoto O., Frenzen P., Hicks B.B., Wesely M., Miyake M., Shaw W.: (1982), 'An international turbulence comparison experiment', *Boundary-Layer Meteorol.*, **24**, 181-209.

Dyer A.J., Hicks B.B., King K.M: (1967), 'The Fluxatron, a revised approach to the measurement of eddy fluxes in the lower atmosphere', *J. Appl. Meteorol.*, **6**, 408-413.

Dyer A.J., Hicks B.B.: (1970), 'Flux-gradient relationships in constant flux layer', *Quart. J. R. Met. Soc.*, **98**, 206-212.

Dyer A.J., Pruitt W.O.: (1962), 'Eddy-flux measurements over a small, irrigated area', *J. Appl. Meteorol.*, **1**, 471-473.

Dyer A.J., Maher F.J.: (1965), 'Automatic eddy-flux measurement with the evapotron', *J. Appl. Meteorol.*, **4**, 622-625.

Dyer A.J.: (1961), 'Measurement of evaporation and heat transfer in the lower atmosphere by an automatic eddy-covariance technique', *Quart. J. R. Met. Soc.*, **87**, 401-412.

Dyer A.J.: (1981), 'Flow distortion by supporting structures', *Boundary-Layer Meteorol.*, **20**, 243-251.

Dyer A.J.: (1982), 'Reply', *Boundary-Layer Meteorol.*, **22**, 267-268.

Eckert E.R.G., Drake R.M.: (1959), '*Heat and mass transfer*', McGraw-Hill, New York, pp 530.

Fan S.M., Wofsey S.C., Bakwin P.S., Jacob D.J.: (1990), 'Atmosphere-Biosphere exchange of CO_2 and O_3 in a central amazonian forest', *J.Geo Phys. Research*, No. D10, **95**, 16851-16864.

Finnigan J.J.: (1979*a*), 'Turbulence in waving wheat, I: Mean statistics and Honami', *Boundary-Layer Meteorol.*, **16**, 181-211.

Finnigan J.J.: (1979*b*), 'Turbulence in waving wheat, II: Structure of momentum transfer', *Boundary-Layer Meteorol.*, **16**, 213-236.

Finnigan J.J: (1985), 'Turbulent transport in flexible plant canopies. In B.A. Hutchinson and B.B. Hicks (eds), *Forest-Atmosphere Interactions*', D. Reidel Pub. Co., Dordrecht, 443-480.

Gao W., Shaw R.H. and Paw U K.T.: (1989), 'Observation of organised structure in turbulent flow within and above a forest canopy', *Boundary-Layer Meteorol.*, **47**, 349-377.

Gardiner B.A.: (1993), 'WindFlow and forces in a plantation spruce forest', *submitted to Boundary-Layer Meteorol.*

Griffiths J.H.: (1983), 'Field investigation of CO_2 uptake in sitka spruce', unpubl. M. Phil. thesis, I.E.R.M., Edinburgh university.

Gurvich A.S.: (1962), 'The pulsation spectra of the vertical component of wind velocity and their relation to micrometeorological conditions', *Isv. Atmos. Oceanic Phys.* **4**, 101-136.

Holland J.Z.: (1989), 'On pressure-driven wind in deep forests', *J. App. Meteorol.*, **28**, 1349-1355.

Hollinger D.Y., Kelliher F.M., Byres J.N., Hunt J.E., McSeveny T.M., Weir P.L: (1993), 'Carbon dioxide exchange between an undisturbed old-growth temperate forest and the atmosphere', *Ecology*, in press.

Horst T.W., Weil J.C.: (1992), 'Footprint estimation for scalar flux measurements in the atmospheric surface layer', *Boundary-Layer Meteorol.*, **59**, 279-296.

Horst T.W.: (1973), 'Spectral transfer functions for a three-component sonic anemometer', *J. Appl. Meteorol.*, **12**, 1072-1075.

Hyson P., Hicks B.B.: (1975), 'A single-beam infra-red hygrometer for evaporation measurement', *J. Appl. Meteorol.*, **14**, 301-307.

Irwin H.P.A.H.: (1979), 'Cross-spectra of turbulence velocities in isotropic turbulence', *Boundary-Layer Meteorol.*, **16**, 237-243.

Jarvis P.G., James G.B., Landsberg J.J.: (1976), 'Coniferous forest. In: Monteith J.L. (ed.), *Vegetation and the atmosphere*, Vol. 2', Academic Press, London, 171-240.

Jarvis P.G., Miranda H.S., Muetzelfeldt R.I.: (1985), 'Modelling Canopy Exchanges of Water Vapour and Carbon Dioxide in Coniferous Forest Plantations. In B.A. Hutchinson and B.B. Hicks (eds), *Forest-Atmosphere Interactions*', D. Reidel Pub. Co., Dordrecht, 521-542.

Jarvis P.G., Sandford A.P.: (1985), 'The measurement of carbon dioxide in air. In: Marshall B. and Woodward F.I (eds.), Instrumentation for Environmental physiology', *Cambridge University Press*, Cambridge, UK, pp 242.

Jarvis P.G.: (1987), 'Water and carbon fluxes in ecosystems. In: Schulze E.D. and Zwolfer H.Z., (eds.), *Ecological studies, Vol. 61*', Springer-Verlag Pub. Co., Berlin, 50-67.

Jarvis P.G.: (1993), 'Resource capture by coniferous forest - a case study', *presented at the 52nd Easter School, University of Nottingham, Sutton Bonington, to be published in 'Resource Capture by Crops', ed. Monteith J.L, Scott R.K. and Unsworth M.H.,* in press.

Kaimal J.C, Wyngaard J.C., Haugen D.A.: (1968), 'Deriving power spectra from a three-component sonic anemometer', *J. Appl. Meteoerol.*, 7, 827-834.

Kaimal J.C., Wyngaard J.C., Izumi Y., Cote O.R.: (1972), 'Spectral characteristics of surface-layer turbulence', *Quart. J. R. Met. Soc.*, **98**, 563-589.

Kaimal J.C., Businger J.A.: (1963), 'A continuous wave sonic anemometer-thermometer', *J. Appl. Meteorol.*, **2**, 156-164.

Kaimal J.C., Finnigan J.J.: (1993), ' Atmospheric boundary layer flows', *Oxford University Press*, In press.

Kaimal J.C., Gaynor E.: (1991), 'Another look at sonic thermometry', *Boundary-Layer Meteorol.*, **56**, 401-410.

Kaimal J.C.: (1978), 'Sonic anemometer measurement of atmospheric turbulence', *Procs. Dynamic Flow Conf.*, 1978, Skovlunde, Denmark, 551-565.

Kaufman M., Seidman A.H. (eds.): (1979), 'Handbook of electronics calculations for engineers and technicians', *McGraw-Hill*, London, pages 19-30 - 19-33.

Kim J., Verma S.B.: (1990), 'Carbon dioxide exchange in a temperate grassland ecosystem', *Boundary-Layer Meteorol.*, **52**, 135-149.

Leclerc M.Y., ThurtellG.W.: (1990), 'Footprint prediction of scalar fluxes using a Markovian analysis', *Boundary-Layer Meteorol.*, **52**, 247-258.

Lee A.C.L.: (1981), 'Smoothing of meteorological data', *The Meteorological magazine*, vol. 110, No. 1306, 115-132.

Lenshow D.H., Raupach M.R.: (1991), 'The attenuation in fluctuations in scalar concentrations through sampling tubes', *J. Geophys. Res.*, **96**, 15259-15268.

Leuning R., Denmead O.T., Lang A.R.G., Ohtaki E.: (1982), 'Effects of heat and water vapour transport on eddy covariance measurements of CO_2 fluxes', *Boundary-Layer Meteorol.*, **23**, 209-222.

Leuning R., King K.M.: (1992), 'Comparison of eddy-covariance measurements of CO_2 fluxes by open- and closed-path CO_2 analysers', *Boundary-Layer Meteorol.*, **59**, 297-311.

Leuning R., Moncrieff J.B.: (1990), 'Eddy-covariance CO_2 flux measurements using open and closed path CO_2 analysers: corrections for analyser water vapour sensitvity and damping of fluctuations in air sampling tubes', *Boundary-Layer Meteorol.*, **53**, 63-76.

Lloyd C.R., Shuttleworth J.H.,Gash J.H.C., Turner M.: (1984), 'A micro-processer system for eddy correlation', *Agric. Forest Meteorol.*, **33**, 67-80.

Lu S.S., Willmarth W.W.: (1973), 'Measurements of the structure of the Reynolds stress in a turbulent boundary layer', *J. Fluid Mech.*, **60**, 481-511.

Ludlow M.M., Jarvis P.G.: (1971), 'Photosynthesis in Sitka spruce (*Picea sitchensis* (Bong.) Carr.). I General characteristics', *J Appl. Ecol.*, **8**, 925-953.

Lumley J.L., Panofsky H.A.: (1964). '*The structure of atmospheric turbulence*', Wiley-Interscience, New York, pp 239.

Massman W.J.: (1991), 'The attenuation of concentration fluctuations in turbulent flow through a tube', *J. Geophys. Res.*, **96**, No. D8, 15269-15273.

McMillen R.T.: (1986), 'A basic program for eddy correlation in non-simple terrain', National Oceanic and Atmospheric Administration, USA, *NOAA Technical Memorandum ERL ARL-147*, Air Resources Lab., Maryland.

Milne R., Brown T.A.: (1990), 'Tree stability and form', *Institute of Terrestrial Ecology Final Report to CEC/NERC Contract No. MA-0061-UK(BA)*, pp 96.

Moncrieff J.B., Verma S.B. and Cook D.R.: (1992), 'Intercomparison of eddy correlation carbon dioxide sensors during FIFE 1989', *J.Geo Phys. Research*, **97**, No. D17, 18725-18730.

Monteith J.L., Unsworth M.H.: (1990), 'Principles of environmental physics', 2nd edition, *Edward Arnold*, London, pp 291.

Moore C.J.: (1986), 'Frequency response corrections for eddy correlation systems', *Boundary-Layer Meteorol.*, **37**, 17-35.

Moritz E.: (1989), 'Heat and momentum transport in an oak forest canopy', *Boundary-Layer Meteorol.*, **49**, 317-329.

Ohtaki E. Matsui T.: (1982), 'Infrared device for simultaineous measurement of fluctuations of atmospheric carbon dioxide and water vapour', *Boundary-Layer Meteorol.*, **24**, 109-119.

Ohtaki E. Oikawa T.: (1991), 'Fluxes of carbon dioxide and water vapour above paddy fields', *Int. J. Biometeorology*, **35**, 187-194.

Ohtaki E.: (1980), 'Turbulent transport of carbon dioxide over a paddy field', *Boundary-Layer Meteorol.*, **19**, 315-336.

Ohtaki E.: (1984), 'Application of an infrared carbon dioxide and humidity instrument to studies of turbulent transport', *Boundary-Layer Meteorol.*, **29**, 85-107.

Ohtaki E.: (1985), 'On the similarity in atmospheric fluctuations of carbon dioxide, water vapour and temperature over vegetated fields', *Boundary-Layer Meteorol.*, **32**, 25-37.

Panofsky H.A., Dutton J.A.: (1984), 'Atmospheric Turbulence: Models and Methods for Engineering Applications', John Wiley and Sons, New York, pp 397.

Philip J.R.: (1963*a*), 'The theory of dispersal during laminar flow in tubes. I', *Aust. J. Phys.*, **16**, 287-299.

Philip J.R.: (1963*b*), 'The theory of dispersal during laminar flow in tubes. II', *Aust. J. Phys.*, **16**, 300-310.

Philip J.R.: (1963*c*), 'The damping of fluctuating concentration by continuous sampling through a tube', *Aust. J. Phys.*, **16**, 454-463.

Press W.H, Flannery B.P., Teukolsky S.A., Vetterling W.T.: (1989), 'Numerical Recipes in Pascal: The Art of Scientific Computing', Cambridge University Press Pub. Co., Cambridge, UK, pp 759.

Price D.T., Black T.A.: (1990), 'Effects of short-term variation in weather on dirurnal canopy CO_2 flux and evapotranspiration of a juvenile Douglas-fir stand', *Agric. and Forest Meteorol.*, **50**, 139-158.

Price D.T., Black T.A.: (1991), 'Effects of summertime changes in weather and root-zone soil water storage on canopy CO_2 flux and evapotranspiration of two juvenile Douglas-fir stands', *Agric. and Forest Meteorol.*, **53**, 303-323.

Pruitt W.O., Morgan D.L., Lourence F.J.: (1973), 'Momentum and mass transfer in the surface boundary layer', *Quart. J. R. Met. Soc.*, **99**, 370-386.

Raupach M.R., Coppin P.A., Legg B.J.: (1986), 'Experiments on scalar dispersion within a model plant canopy. Part I: The turbulence structure', *Boundary-Layer Meteorol.*, **35**, 21-52.

Raupach M.R., Finnigan J.J., Brunet Y.: (1989), 'Coherent eddies in vegative canopies', *Proc. of the Fourth Australian Conference on Heat and Mass Transfer*, 9-12 May, Christchurch, New Zealand.

Raupach M.R., Shaw R.H.: (1982), 'Averaging procedures for flow within vegetation canopies', *Boundary-Layer Meteorol.*, **22**, 79-90.

Raupach M.R., Thom A.S., Edwards I.: (1980), 'A wind tunnel study of turbulent flow close to regularly arrayed rough surfaces', *Boundary-Layer Meteorol.*, **18**, 373-397.

Raupach M.R., Legg B.J.: (1984), 'The uses and limitations of flux-gradient relationships in micrometeorology', *Agric. Water Management*, **8**, 119-131.

Raupach M.R., Thom A.S: (1981), 'Turbulence in and above plant canopies', *Ann. Rev. Fluid Mech.*, **13**, 97-129.

Raupach M.R.: (1981), 'Conditional statistics of Reynolds stress in rough-wall and smooth-wall boundary layers', *J. Fluid Mech.*, **108**, 363-382.

Raupach M.R.: (1988), 'Canopy transport processes. In: Steffen W.L and Denmead O.T. (eds.), Flow and transport in the natural environment: Advances and applications', Springer-Verlag Pub. Co., London, pages 95-127.

Ross J.: (1975), 'Radiative Transfer in Plant Communities. In: Monteith J.L. (ed.), *Vegetation and the atmosphere*, Vol. 1', Academic Press, London, 13-56.

Schotanus P., Nieuwstadt F.T.M., De Bruin H.A.R.: (1983), 'Temperature measurement with a sonic anemometer and its application to heat and moisture fluxes', *Boundary-Layer Meteorol.*, **26**, 81-93.

Schuepp P.H., Leclerc M.Y., MacPherson J.I., Desjardins R.L.: (1990), 'Footprint prediction of scalar fluxes from analytical solutions of the diffusion equation', *Boundary-Layer Meteorol.*, **50**, 355-373.

Seginer I., Mulhearn P.J., Bradley E. F., Finnigan J.J.: (1976), 'Turbulent flow in a model plant canopy', *Boundary-Layer Meteorol.*, **10**, 423-453.

Shaw R.H., Silversides R.H.,Thurtell G.W.: (1974), 'Some obervations of turbulence and turbulent transport within and above plant canopies', *Boundary-Layer Meteorol.*, **5**, 429-449.

Shaw R.H., Tavangar J., Ward D.P.: (1983), 'Structure of the Reynolds stress in a canopy layer', *J. Climate Appl. Meteorol.*, **22**, 1922-1931.

Shaw R.H., Zhang X.J.: (1992), 'Evidence of pressure-forced turbulent flow in a forest', *Boundary-Layer Meteorol.*, **58**, 273-288.

Shaw R.H., Kidd G., Thurtell G.W.: (1973), 'A miniature three-dimensional anemometer for use within and above canopies', *Boundary-Layer Meteorol.*, **3**, 359-4380.

Shaw R.H., Seginer I.: (1987), 'Calculation of velocity skewness in real and artificial plant canopies', *Boundary-Layer Meteorol.*, **39**, 315-332.

Shuttleworth W.J.: (1988), 'Corrections for the effect of background concenration change and sensor drift in real-time eddy correlation systems', *Boundary-Layer Meteorol.*, **42**, 167-180.

Shuttleworth W.J.: (1991), 'I. Insight from large-scale observational studies of land/atmosphere interactions', *Surveys in Geophysics*, **12**, 3-30.

Silverman B.A.: (1968), 'The effect of spatial averaging on spectrum estimation', *J. Appl. Meteorol.*, **7**, 168-172.

Sinclair T.H., Allen (Jr) L.H., Lemon E.R.: (1975), 'An analysis of errors in the calculation of energy flux densities above vegetation by a Bowen-ratio profile method', *Boundary-Layer Meteorol.*, **8**, 129-139.

Stewart J.B, Thom A.S.: (1973), 'Energy budjets in pine forest', *Quart. J. R. Met. Soc.*, **99**, 154-170.

Stull R.B.: (1988), 'An introduction to boundary layer meteorology', Kluwer Academic Publishers, London, pp 666.

Suyker A.E., Verma S.B: (1993), 'Eddy correlation measurement of CO_2 flux using a closed-path sensor - Theory and field tests against an open-path sensor', *submitted to Boundary-Layer Meteorol.*

Swinbank W.C: (1951), 'The measurement of vertical transfer of heat and water vapour by eddies in the lower atmosphere', *J. Meteorol.*, **8**, 135-145.

Tans P.P, Fung I.Y., Takahashi T.: (1990), 'Observational constraints on the global atmospheric CO_2 budget', *Science*, **247**, 1431-1438.

Taylor G.I.: (1938), 'The spectrum of turbulence', *Proc. Roy. Soc.*, **A164**, 476-490.

Taylor G.I.: (1953), 'Dispersion of soluble matter in solvent flowing slowly through a tube', *Proc. Roy. Soc.*, **A219**, 186-203.

Taylor G.I.: (1954), 'The dispersion of matter in turbulent flow through a pipe', *Proc. Roy. Soc.*, **A223**, 446-468.

Thom A.S.: (1975), 'Momentum, heat and mass exchange of plant communities. In: Monteith J.L. (ed), Vegetation and the atmosphere, Vol. 1', Academic Press, London, pp 278.

Vallentini R., Scarascia Mugnozza G.E., De Angelis P., Bimbi R.: (1991), 'An experimental test of the eddy correlation technique over a Mediteranean macchia canopy', *Plant, Cell and Environment*, **14**, 987-994.

Verma S.B, Rosenberg N.J: (1975), 'Accuracy of lysimetric, energy balance and stability-corrected aeordynamic methods of estimating above-canopy flux of CO_2', *Agronomy Journal.*, **67**, 699-704.

Verma S.B., Baldocchi D.D., Anderson D.E., Matt D.R., Clement R.J.: (1986), 'Eddy fluxes of CO_2, water vapour and sensible heat over a deciduous forest', *Boundary-Layer Meteorol.*, **36**, 71-81.

Webb E.K., Pearman G.I., Leuning R.: (1980), 'Correction of flux measurements for density effects due to heat and water vapour transfer', *Quart. J. R. Met. Soc.*, **106**, 85-100.

Webb E.K.: (1970), 'Profile relationships: the log-linear range and extension to strong stability', *Quart. J. R. Met. Soc.*, **96**, 67-90.

Wilson J.D., Thurtell G.W., Kidd G.E.: (1981), 'Numerical simulation of particle trajectories in inhomogeneous turbulence, I: Systems with constant turbulent velocity scale', *Boundary-Layer Meteorol.*, **21**, 295-313.

Wilson J.D., Ward D.P., Thurtell G.W., Kidd G.E.: (1982), 'Statistics of atmospheric turbulence within and above a corn canopy', *Boundary-Layer Meteorol.*, **24**, 495-519.

Wilson J.D., Swaters G.E.: (1991), 'The source area influencing a measurement in the planetary boundary layer: The "Footprint" and the "distribution of contact distance"', *Boundary-Layer Meteorol.*, **55**, 25-46.

Wyngaard J.C., Coté O.R: (1972), 'Cospectral similarity in the atmospheric surface layer', *Quart. J. R. Met. Soc.*, **98**, 590-603.

Wyngaard J.C.: (1982), 'Comments on flow distortion by supporting structures', *Boundary-Layer Meteorol.*, **22**, 263-265.

Zeller K., Massman W., Stocker D., Fox D.G., Stedman D., Hazlett D.: (1989), 'Initial results from the Pawnee eddy correlation system for dry acid deposition research', US Dept. Agric. (Forest Service), Research paper RM-282, Fort Collins, Colorado 80526.

APPENDIX A.1
BUTTERWORTH LOW-PASS FILTERS

A1.1 INTRODUCTION

As discussed in section 3.2.2, to examine a sampled time series in the frequency domain with spectral analysis we must be aware of the phenomenon of "aliasing'. To resolve a wave in a signal we must have a minimum of two measurements or data points per wavelength or period. With only one data point per cycle we cannot determine the wavelength correctly as many waves can contain the same signal at that time. The Nyquist frequency, n_0, is defined as half the sample frequency, n_s, (Stull, 1988; Kaimal and Finnigan, 1993):

$$n_0 = \frac{n_s}{2} \qquad \text{(A1.1.1)}$$

Spectral power at frequencies above n_0 is folded back around n_0 and added to that at lower frequencies, this phenomenon is called aliasing or 'spectral folding'.

Aliasing can be eliminated by sampling at a frequency such that $n_0 > 0.5 n_s$ and low-pass filtering the voltage signals from the instruments with electronic filters which have a frequency cut off lower than n_0. For our data acquisition system a sample rate of 18.2 Hz was chosen, i.e. Δt = 0.055 s and n_0 = 9.1 Hz, and voltage signals were low-pass filtered with electronic filters with a 3 dB cut-off frequency of 7.4 Hz.

A1.2 FILTER DESIGN AND MANUFACTURE

The Butterworth filter is a very common choice for meteorological applications and is efficient at separating sinusoidal signals at low and high frequencies (Lee, 1981). The filters were designed following the guidelines in Kaufman and Seidman (1979) to have a nominal 3 dB cut-off of 8 Hz. A fifth order design was chosen with circuit as shown in Figure A2.2.1. The op-amps were powered from zero and 5 V power lines from the A/D board, inverted by a 7660 inverter chip to ± 5 V. The input voltage range for the filters was 0 - 5 V.

Using 10 kΩ resistors, (0.5 W standard carbon film resistors with tolerances of 3 %), and 35 V dipped Tantalum capacitors the optimum and the actual available capacitance values were as shown in Table A2.2.1.

The filters were manufactured on epoxy glass boards with the printed circuit board copper etch method. Four filter circuits were etched onto each 150 - 235 mm photoresist board, the circuit transparency used in the etching processes is attached as

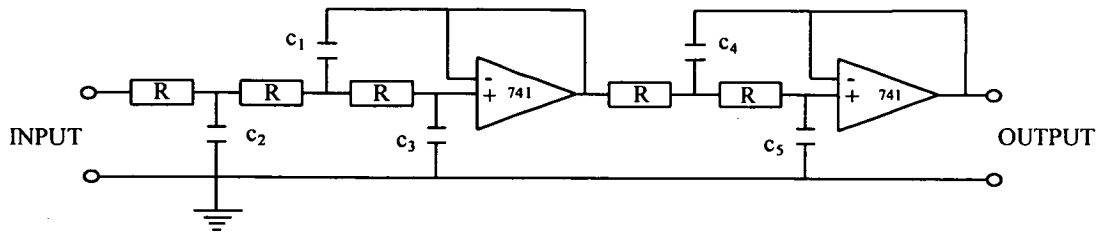

Fig. A1.2.1 Schematic circuit diagram for a fifth order Butterworth low-pass filter. All op-amps are standard 741 chips.

Plate A2.2.1. The photoresist was irradiated with UV for 3.5 minutes, developed in sodium hydroxide solution (~ 1 minute) and the excess copper removed in ferric chloride ($FeCl_3$) solution (~ 20 minutes depending on solution strength and temperature).

capacitor	optimum capacitance (μF)	Actual capacitance (μF)
c_1	3.49	3.3 + 0.22 = 3.52
c_2	2.69	2.2 + 0.47 + 0.22 = 2.89
c_3	0.84	0.68 + 0.15 = 0.83
c_4	6.4	6.8
c_5	0.615	0.68

Table A2.2.1 Capacitance values for optimum and actual fifth order Butterworth low-pass filters.

A1.3 FILTER RESPONSE

The gain response of the filters was measured experimentally with an input from a sine wave oscillator. Input signal was a 2.0 V peak to peak sine wave with frequencies between 1.0 - 19.6 Hz as measured on an oscilloscope.

A response function was fitted to the data that could be used to predict the signal losses of the filter. The response function is shown, with the data, in Figure A1.3.1, and is given by:

$$T_B(n) = \left[1 + \left(\frac{n}{7.4}\right)^{12}\right]^{-\frac{1}{2}} \qquad \text{(A1.3.1)}$$

where $T_B(n)$ is the gain or transfer function for the filters.

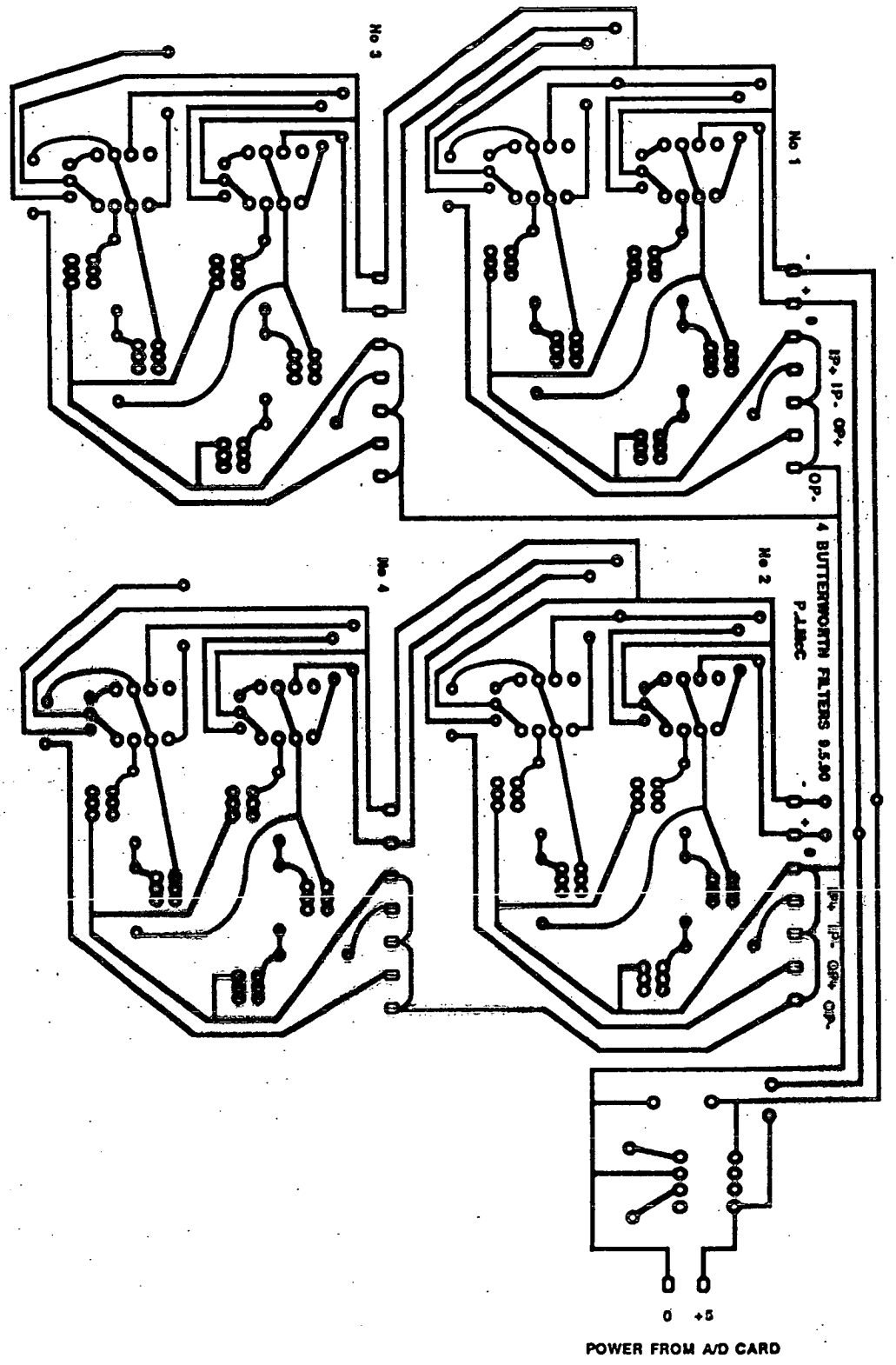

Plate A2.2.1 Transparency of filter circuit board for four fifth order Butterworth filters for use with copper etch printed circuit board manufacture process.

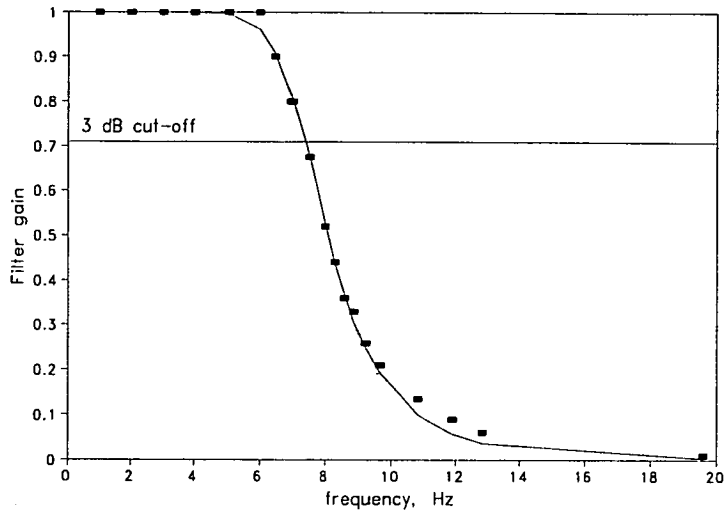

Fig. A1.3.1 Measured filter gain response with frequency, where symbols are the data points and the line is the fitted response function given by equation A1.3.1. The 3 dB cut-off for the filters is 7.4 Hz.

APPENDIX A.2
VELOCITY CO-ORDINATE ROTATION ROUTINES

A2.1 INTRODUCTION

Co-ordinate rotation of three dimensional wind velocity measurements is essential to correctly calculate the Reynolds stress at a given site (McMillen, 1986). The co-ordinate rotation orients the u velocity component into the mean wind direction thus removing streamline distortion effects from the velocity data and any calculated eddy covariance fluxes. Within plant canopies, where distinct flow streamlines are not obvious, generally only one rotation is performed pointing the streamwise velocity into the direction of the mean horizontal velocity.

Three rotations are performed above canopies such that u points along the mean wind vector, $\overline{v}$ is zero and the cross stream stress is minimised, i.e. $\overline{v'w'} \rightarrow 0$. The mathematical procedures are discussed below with reference to a Turbo Pascal Unit, ROTATION.TPU, which contains code that carries out the co-ordinate rotation. The general method given below follows that of McMillen (1986) but corrects several errors in the trigonometry which were included in that report. The Turbo Pascal routines presented here are based substantially on the BASIC program listed in McMillen (1986).

A2.2 THE FIRST TWO ROTATIONS

The initial velocities are u, v and w in the x, y and z Cartesian directions. This frame represents the orientation of the anemometer in the field. In the first rotation, illustrated in Figure A2.2.1, the streamwise velocity u is rotated to point in the direction of the mean horizontal velocity, thus the new streamwise velocity component u_1 is given by:

$$u_1 = \left(u^2 + v^2\right)^{1/2}, \qquad \text{(A2.1)}$$

this velocity is equivalent to $\overline{U}$, as defined in the main body of the thesis. The velocities after the first rotation are u_1, $v_{1/2}$ and w in the x_1, $y_{1/2}$ and z directions and are given by:

$$\begin{aligned} u_1 &= u\cos\varepsilon + v\sin\varepsilon \\ v_{1/2} &= -u\sin\varepsilon + v\cos\varepsilon \\ w &= w \end{aligned} \qquad \text{(A2.2)}$$

by resolving the vectors u and v into the x_1 and $y_{1/2}$ directions..

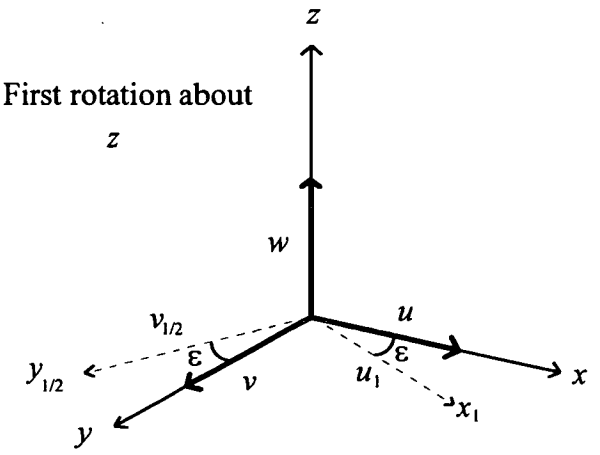

Fig. A2.2.1 Diagram illustrating the first rotation of the co-ordinate rotation of angle ε about axis z. The original velocity components are u, v and w in the x, y and z directions. The once rotated velocities are u_1, $v_{1/2}$ and w in the x_1, $y_{1/2}$ and z directions.

Similarly in the second rotation, illustrated in Figure A2.2.2, the streamwise velocity component is rotated into the direction of the mean flow velocity component, u_2 which is given by:

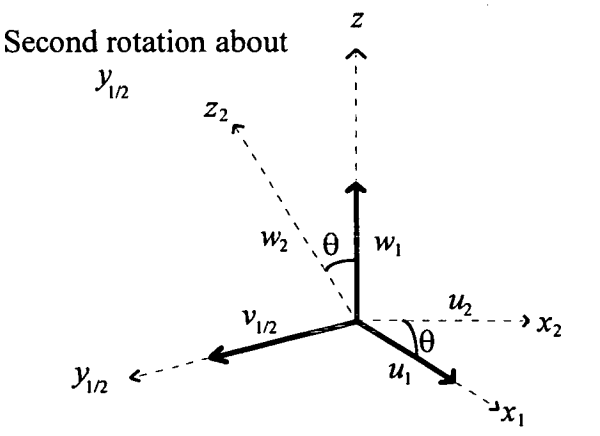

Fig. A2.2.2 Diagram illustrating the second rotation of the co-ordinate rotation of angle θ about axis $y_{1/2}$. The previous rotation velocity components are u_1, $v_{1/2}$ and w in the x_1, $y_{1/2}$ and z directions. The twice rotated velocities are u_2, $v_{1/2}$ and w_2 in the x_2, $y_{1/2}$ and z_2 directions.

$$u_2 = \left(u^2 + v^2 + w^2\right)^{1/2}. \qquad \text{(A2.3)}$$

The twice rotated velocities are now u_2, $v_{1/2}$ and w_2 in the x_2, $y_{1/2}$ and z_2 directions where and are given by:

$$\begin{aligned} u_2 &= u\cos\varepsilon\cos\theta + v\sin\varepsilon\cos\theta + w\sin\theta \\ v_{1/2} &= v_{1/2} \\ w_2 &= w\cos\theta - u\cos\varepsilon\sin\theta - v\sin\varepsilon\sin\theta \end{aligned} \qquad \text{(A2.4)}$$

by resolving the vectors u_1 and w into the x_2 and z_2 directions.

We can now describe the first two co-ordinate rotations by the matrix M_{2R} as:

$$\begin{pmatrix} u_2 \\ v_{1/2} \\ w_2 \end{pmatrix} = \begin{pmatrix} \cos\varepsilon\cos\theta & \sin\varepsilon\cos\theta & \sin\theta \\ -\sin\varepsilon & \cos\varepsilon & 0 \\ -\cos\varepsilon\sin\theta & -\sin\varepsilon\sin\theta & \cos\theta \end{pmatrix} \begin{pmatrix} u \\ v \\ w \end{pmatrix} \qquad \text{(A2.5)}$$

$$M_{2R}.$$

A2.3 THE THIRD ROTATION

The third co-ordinate rotation minimises the transverse momentum flux $\overline{v'w'}$

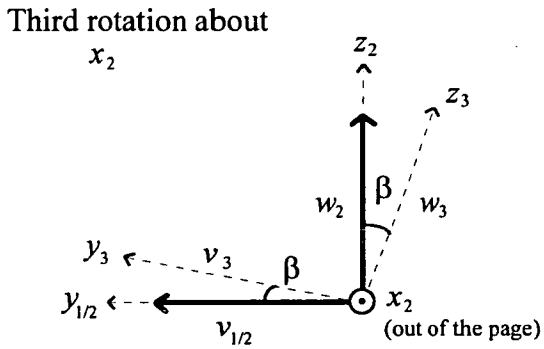

Fig. A2.3.1 Diagram illustrating the third rotation of the co-ordinate rotation of angle β about axis x_2. The previous rotation velocity components are u_2, $v_{1/2}$ and w_2 in the x_2, $y_{1/2}$ and z_2 directions. The thrice rotated velocities are u_2, v_3 and w_3 in the x_2, y_3 and z_3 directions.

such that $\overline{v_3' w_3'} \to 0$. The rotation is illustrated in Figure A2.3.1 where the final velocities are u_2, v_3 and w_3 in the x_2, y_3 and z_3 directions.

The thrice rotated velocity components are given by the transformation with matrix M_{3R}:

$$\begin{pmatrix} u_3 \\ v_3 \\ w_3 \end{pmatrix} = \begin{pmatrix} 1 & 0 & 0 \\ 0 & \cos\beta & \sin\beta \\ 0 & -\sin\beta & \cos\beta \end{pmatrix} \begin{pmatrix} u_2 \\ v_{1/2} \\ w_2 \end{pmatrix} \qquad \text{(A2.6)}$$

$$M_{3R},$$

or in full:

$$\begin{pmatrix} u_3 \\ v_3 \\ w_3 \end{pmatrix} = \begin{pmatrix} \cos\varepsilon\cos\theta & \sin\varepsilon\cos\theta & \sin\theta \\ -\sin\varepsilon\cos\beta - \cos\varepsilon\sin\theta\sin\beta & \cos\varepsilon\cos\beta - \sin\varepsilon\sin\theta\sin\beta & \cos\theta\sin\beta \\ \sin\varepsilon\sin\beta - \cos\varepsilon\sin\theta\cos\beta & -\cos\varepsilon\sin\beta - \sin\varepsilon\sin\theta\cos\beta & \cos\theta\cos\beta \end{pmatrix} \begin{pmatrix} u \\ v \\ w \end{pmatrix} \qquad \text{(A2.7)}$$

This transformation applies in an identical way to fluctuating velocity components, (i.e. u') and mean velocity components ($\overline{u}$) as to instantaneous velocities (u). Applying M_{2R} and M_{3R} to u, v and w, the covariance $\overline{v_3' w_3'}$ is given by:

$$\begin{aligned} v_3' w_3' &= (v_{1/2}' \cos\beta + w_2' \sin\beta)(-v_{1/2}' \sin\beta + w_2' \cos\beta) \\ &= -\sin\beta\cos\beta v_{1/2}' v_{1/2}' + \sin\beta\cos\beta w_2' w_2' + (\cos^2\beta - \sin^2\beta) v_{1/2}' w_2' \\ &= -\sin\beta\cos\beta(v_{1/2}' v_{1/2}' + w_2' w_2') + (1 - 2\sin^2\beta) v_{1/2}' w_2' \end{aligned} \qquad \text{(A2.8)}$$

Thus for $\overline{v_3' w_3'} \to 0$ then:

$$\sin\beta\cos\beta(v_{1/2}' v_{1/2}' + w_2' w_2') \to (1 - 2\sin^2\beta) v_{1/2}' w_2'. \qquad \text{(A2.9)}$$

If we define K as:

$$K = \frac{v_{1/2}' w_2'}{(v_{1/2}' v_{1/2}' + w_2' w_2')}, \qquad \text{(A2.10)}$$

then we have a quadratic equation in $\sin^2\beta$ for the solution with $\overline{v_3' w_3'} = 0$, i.e.:

$$2K\sin^2\beta + \sin\beta\cos\beta - K = 0. \qquad \text{(A2.11)}$$

The solution to this quadratic equation is:

$$\sin\beta = \frac{-\cos\beta \pm \left(\cos^2\beta + 8K^2\right)^{1/2}}{4K}, \qquad \text{(A2.12)}$$

where we must take the positive sign solution so that $|\sin\beta| \leq 1$.

This minimisation is carried out in the computer code by an iterative process which makes use of equation A2.12 and the identity $\cos\beta = \left(1 - \sin^2\beta\right)^{1/2}$. By computing the value of $\cos\beta$ from the identity, for each iterative value of β, and then computing the value of $\sin\beta$ from equation A2.12, an approximate value of β is found such that $\overline{v_3' w_3'} \rightarrow 0$. The iterative loop ends when both $\sin\beta$ and $\cos\beta$ differ from their previous value by less than 1×10^{-5}.

A2.4 THE ROUTINES IN TURBO PASCAL

The Turbo Pascal Unit containing the code to perform co-ordinate rotation on velocity data is called ROTATION.TPU and is listed in section A2.6. The unit contains routines to rotate mean covariances at the end of a sample period on input of mean sample period velocities $\bar{u}$, $\bar{v}$ and $\bar{w}$. The unit also contains routines which rotate velocity fluctuation data line by line, on input of the rotation angles calculated previously for a sample period. I will concern myself here solely with the co-ordinate rotation of mean covariances by the procedure CALCWXXC in ROTATION.TPU.

The code operates on a covariance tensor, input to the program as WXX and output rotated as WXXC. These tensors have three rows corresponding to the velocity components and eight columns corresponding to calculated covariances. The tensor WXX is shown as input to the unit:

$$\mathrm{WXX}[i,j] = \begin{bmatrix} u'u' & u'v' & u'w' & u'T' & u'\rho_c' & u'\rho_v' & u'\mathrm{misc1} & u'\mathrm{misc2} \\ v'u' & v'v' & v'w' & v'T' & v'\rho_c' & v'\rho_v' & v'\mathrm{misc1} & v'\mathrm{misc2} \\ w'u' & w'v' & w'w' & w'T' & w'\rho_c' & w'\rho_v' & w'\mathrm{misc1} & w'\mathrm{misc2} \end{bmatrix} \qquad \text{(A2.13)}$$

where i refers to rows and j refers to columns, T is air temperature and ρ_c' and ρ_v' refer to densities in air of CO_2 and water vapour, respectively. Columns j = 7 and 8 are miscellaneous input channels for sensors 'misc1' and 'misc2'. The tensor WXXC is identical to WXX in equation A2.13 when the velocity fluctuations u', v' and w' are replaced with the rotated fluctuations u_3', v_3' and w_3'. The covariances for momentum

flux, after rotation, would thus be given by WXXC[1, 3] or WXXC[3,1] and for CO_2 flux by WXXC[1, 5].

A2.5 EFFECT OF THE THREE CO-ORDINATE ROTATIONS

An example of the effect of the three rotations on typical data gathered at $1.2h$ at Rivox on J207, 1991 is shown in Figure A2.5.1.

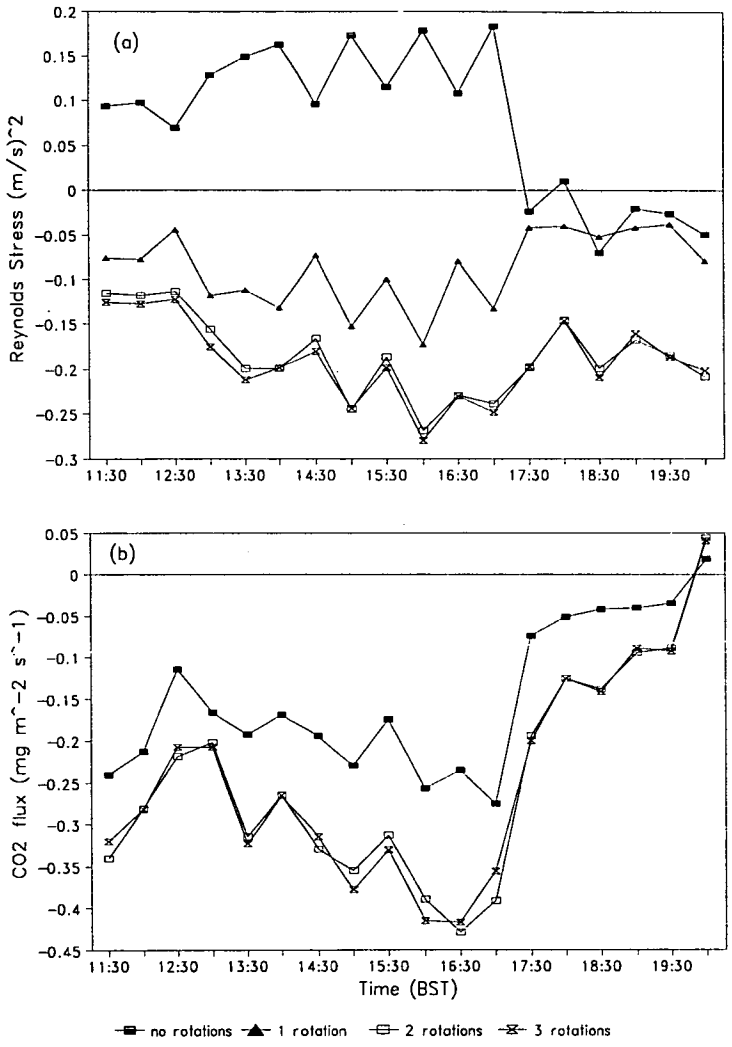

Fig. A2.5.1 The effect on calculated Reynold's stress (*a*) and CO_2 flux (*b*) of applying no rotations, one, two and three rotations. The once rotated CO_2 flux data is identical to the unrotated data as w is unchanged by the first rotation. Data is from $1.2h$ at Rivox from J207, 1991. [$\overline{U}$ = 2.4 m s^{-1} and $z - d = 5.4$ m].

The application of the rotations changes the Reynold's stress from a positive value to a negative one, with the first and second rotations having a larger effect than the third rotation in this instance. The CO_2 flux is also more negative after rotation, again with the third rotation having a lesser effect than the second one. These results agree well with those reported by McMillen (1986) and indicate that above a plant surface, co-ordinate rotation is essential for the correct calculation of eddy fluxes.

A2.6 LISTING OF PASCAL ROUTINE

The turbo pascal unit, ROTATION.TPU is reproduced below.

```
unit Rotation;

{ June 1990 }
{ Unit containing co-ordinate rotation procedures for calcs on u,v,w wind  }
{ data from a 3 component sonic anemometer. Requires Covariance Tensor     }
{ WXX[3,8] (for 8 instruments) to be input as well as the aritmetic        }
{ means of u,v,w (here called Ch_Means[n]).                                }
{ For theory see my technical memo (includes discussion of the code below.) }
{ By P.J.McCracken 15.3.90 ,MicroMet ,F&NR ,Univ. Edinburgh               }
{*************************************************************************}
{3.12.90                                                                   }
{ Modified to do rotations on single lines of data for input to   }
{ conditional sampling routines in procedure 'Quadrant'.          }
{ proc Coord_1rot does a 1d rotation for below canopy data (Baldocchi &}
{  Hutchinson, 1987, BLM 40, 127-146).                                     }
{ proc Coord_3rots is full rotation line by line for above canopy.     }
{*************************************************************************}
{29.6.91                                                                   }
{ Now called ROTATION a derivative of Quad_rot. The changes are an addition }
{ of a procedure to write WXX arrays to avoid the hard wiring in EDDY & QUAD}
{ called CreateWXX                                                         }
{*************************************************************************}
{ 12.11.91                                                                 }
{ Now also procs for 2 rotations both for WXXC and for fluctuations called.  }
{ CalcWXXC_2rots and Calc_2rots respectively                               }
{ FOUND MISTAKES IN CALCWXXC AND CALCWXXC_2ROTS, }
{ CORRECTIONS MARKED WITH DATE}
{ - MISTAKES IN WXXB[3,3] & WXXC[1,2]                                      }
{ Also in coord_3rots                                                      }
{*************************************************************************}
interface

type
   Ch_Data = array[1..16] of double;          {to try to solve precision}
   CovarTensor = array[1..3,1..16] of double;  {problem with Sk & K }

var Ch_Means,UnRotated_Data,Rotated_data : Ch_Data;
   TW,WS,SE,CE,ST,CT,SB,CB  : single;
   WXX,WXXC    : CovarTensor;
```

```
procedure CalcWXXC(var Ch_Means : Ch_Data; var index : integer;
            var WXX : CovarTensor;  var WXXC :CovarTensor;
            var Num_Instr :integer;
            var TW,WS,SE,CE,ST,CT,SB,CB : single);

procedure CalcWXXC_1rot(var Ch_Means : Ch_Data; var index : integer;
                var WXX : CovarTensor;  var WXXC :CovarTensor;
                var Num_Instr :integer;
                var WS,SE,CE : single);

procedure CalcWXXC_2rots(var Ch_Means : Ch_Data; var index : integer;
                var WXX : CovarTensor;  var WXXB :CovarTensor;
                var Num_Instr :integer;
                var TW,WS,SE,CE,ST,CT : single);

procedure Coord_3rots(var UnRotated_Data,Rotated_data : Ch_Data;
              var index : integer;
              var SE,CE,ST,CT,SB,CB : single);

procedure Coord_1rot(var UnRotated_Data,Rotated_data : Ch_Data;
             var index : integer;
             var SE,CE : single);

procedure Coord_2rots(var UnRotated_Data,Rotated_data : Ch_Data;
              var index : integer;
              var SE,CE,ST,CT : single);

procedure CreateWXX(var WhichWXX :CovarTensor;
            var fluct : Ch_Data;
            var index : integer;
            ch_no_T,ch_no_CO2,ch_no_H2O,ch_no_misc1
              ,ch_no_misc2 : integer);


implementation

{-------------------------------------------------------------------------}
procedure CalcWXXC(var Ch_Means : Ch_Data; var index : integer;
            var WXX : CovarTensor;  var WXXC :CovarTensor;
            var Num_Instr :integer;
            var TW,WS,SE,CE,ST,CT,SB,CB : single);
var
   K,OSB,OCB : single;
   WXXB : CovarTensor;
   J,IJ : integer;

{first calc Total (TW) and Horizontal (WS) mean Wind speeds }
{ Ch_Means[1] = u, Ch_Means[2] =v, Ch_Means[3] = w                    }

begin
    TW := sqrt(sqr(Ch_Means[index+1])+sqr(Ch_Means[index+2])+
                                  sqr(Ch_Means[index+3]));
    WS := sqrt(sqr(Ch_Means[index+1])+sqr(Ch_Means[index+2]));

    if (TW = 0) or (WS = 0) then
     begin
```

```
      for J := 1 to num_instr do
       begin
        for IJ := 1 to 3 do
         WXXC[IJ,J] := WXX[IJ,J];
       end;
      exit;
     end;

{ now calc cosine and sine of first two rotation angles Eta & Theta ie CE, ST etc}

    CE := Ch_Means[index +1]/WS;
    SE := Ch_Means[index +2]/WS;
    CT := WS/TW;
    ST := Ch_Means[index +3]/TW;

{1ST & 2ND ROTATION - ie rotate WXX thru Eta & Theta to WXXB }

    WXXB[1,1] := WXX[1,1]*SQR(CT)*SQR(CE)+WXX[2,2]*SQR(CT)*SQR(SE)+
            WXX[3,3]*SQR(ST)+2*WXX[1,2]*SQR(CT)*CE*SE+
            2*WXX[3,1]*CT*ST*CE+2*WXX[3,2]*CT*ST*SE;
    WXXB[2,2] := WXX[2,2]*SQR(CE)+WXX[1,1]*SQR(SE)-2*WXX[1,2]*CE*SE;
    WXXB[3,3] := WXX[3,3]*SQR(CT)+WXX[1,1]*SQR(ST)*SQR(CE)+
                              {12.11.91, 2 - for +}
            WXX[2,2]*SQR(ST)*SQR(SE)-2*WXX[3,1]*CT*ST*CE-
            2*WXX[3,2]*CT*ST*SE+2*WXX[1,2]*SQR(ST)*CE*SE;
    WXXB[3,1] := WXX[3,1]*CE*(SQR(CT)-SQR(ST))-2*WXX[1,2]*CT*ST*SE*CE+
            WXX[3,2]*SE*(SQR(CT)-SQR(ST))-WXX[1,1]*CT*ST*SQR(CE)-
            WXX[2,2]*CT*ST*SQR(SE)+WXX[3,3]*CT*ST;
    WXXB[1,3] := WXXB[3,1];
                                  {12.11.91, CE for SE}
    WXXB[1,2] := WXX[1,2]*CT*(SQR(CE)-SQR(SE))+WXX[3,2]*ST*CE-
            WXX[3,1]*ST*SE-WXX[1,1]*CT*CE*SE+WXX[2,2]*CT*CE*SE;
    WXXB[2,1] := WXXB[1,2];
    WXXB[3,2] := WXX[3,2]*CT*CE-WXX[3,1]*CT*SE-WXX[1,2]*ST*(SQR(CE)-SQR(SE))
    .           +WXX[1,1]*ST*CE*SE-WXX[2,2]*ST*CE*SE;
    WXXB[2,3] := WXXB[3,2];

    for J := 4  to Num_Instr do
     begin
         WXXB[1,J] := WXX[1,J]*CT*CE+WXX[2,J]*CT*SE+WXX[3,J]*ST;
         WXXB[2,J] := WXX[2,J]*CE-WXX[1,J]*SE;
         WXXB[3,J] := WXX[3,J]*CT-WXX[1,J]*ST*CE-WXX[2,J]*ST*SE;
      end; {for}

    if (WXXB[2,2] = WXXB[3,3]) or (WXXB[3,2] = 0) then      {this avoids the}
     begin                                                  {possibility of}
      for IJ := 1 to 3 do                                    {K or SB = infinity}
       begin
        for J := 1 to num_instr do
           WXXC[IJ,J] := WXXB[IJ,J];
       end;
       exit;
     end;

 { ITERATION FOR BETA - 3rd ROTATION }
```

```
   K := WXXB[3,2]/(WXXB[2,2]-WXXB[3,3]);
   CB := 1;                                    {cos Beta}
   SB := 0;                                    {sin Beta}
   repeat
    OSB := SB;
    OCB := CB;
    SB := (-CB+SQRT(SQR(CB)+8*SQR(K)))/(4*K);
    if (SQR(SB) > 1) then
     begin
      for IJ := 1 to 3 do
       begin
        for J := 1 to num_instr do          { avoids case of }
         WXXC[IJ,J] := WXXB[IJ,J];          { CB = infinity  }
       end;
       exit;
     end;
    CB := SQRT(1-SQR(SB));
   until (ABS(OSB-SB) < 0.00001) and (ABS(OCB-CB) < 0.00001);

{ NOW CONSTRUCT FINAL COVAR TENSOR WXXC FOR ROTATION THRU BETA, }
{ABOUT NEW x AXIS }

   WXXC[2,2] := WXXB[2,2]*SQR(CB)+2*WXXB[3,2]*CB*SB+WXXB[3,3]*SQR(SB);
   WXXC[3,3] := WXXB[3,3]*SQR(CB)-2*WXXB[3,2]*CB*SB+WXXB[2,2]*SQR(SB);
   WXXC[3,1] := WXXB[3,1]*CB-WXXB[1,2]*SB;
   WXXC[1,3] := WXXC[3,1];
   WXXC[1,2] := WXXB[1,2]*CB+WXXB[3,1]*SB;
   WXXC[2,1] := WXXC[1,2];
   WXXC[3,2] := WXXB[3,2]*(SQR(CB)-SQR(SB))+WXXB[3,3]*CB*SB
           -WXXB[2,2]*CB*SB;
   WXXC[2,3] := WXXC[3,2];
   WXXC[1,1] := WXXB[1,1];

   for J := 4 to Num_Instr do
    begin
       WXXC[1,J] := WXXB[1,J];
       WXXC[2,J] := WXXB[2,J]*CB+WXXB[3,J]*SB;
       WXXC[3,J] := WXXB[3,J]*CB-WXXB[2,J]*SB;
    end; {for}
end;  { CalcWXXC }
{-------------------------------------------------------------------------}
procedure CalcWXXC_1rot(var Ch_Means : Ch_Data; var index : integer;
            var WXX : CovarTensor;  var WXXC :CovarTensor;
            var Num_Instr :integer;
            var WS,SE,CE : single);
var
   J,IJ : integer;

{ THIS PROC IS FOR ROTATING BELOW CANOPY SONIC DATA PURELY INTO THE }
{  HORIZONTAL MEAN WIND DIRN                                        }

{first calc  Horizontal (WS) mean Wind speed }
{ Ch_Means[1] = u, Ch_Means[2] =v, Ch_Means[3] = w                  }

begin
    WS := sqrt(sqr(Ch_Means[index+1])+sqr(Ch_Means[index+2]));
```

```
    if WS = 0 then
     begin
      for J := 1 to num_instr do
       begin
        for IJ := 1 to 3 do
         WXXC[IJ,J] := WXX[IJ,J];
       end;
      exit;
     end;

{ now calc cos and sine of first rotation angle Eta ie CE,SE etc}

    CE := Ch_Means[index +1]/WS;
    SE := Ch_Means[index +2]/WS;

  WXXC[1,1] := WXX[1,1]*SQR(CE) + WXX[2,2]*SQR(SE) + 2*WXX[1,2]*SE*CE;
  WXXC[2,2] := WXX[1,1]*SQR(SE) + WXX[2,2]*SQR(CE) - 2*WXX[1,2]*SE*CE;
  WXXC[3,3] := WXX[3,3];
  WXXC[1,2] := WXX[2,2]*SE*CE - WXX[1,1]*SE*CE + WXX[1,2]*(SQR(CE)-SQR(SE));
  WXXC[1,3] := WXX[1,3]*CE + WXX[2,3]*SE;
  WXXC[2,3] := WXX[2,3]*CE - WXX[1,3]*SE;
  WXXC[2,1] := WXXC[1,2];
  WXXC[3,1] := WXXC[1,3];
  WXXC[3,2] := WXXC[2,3];

  for J := 4  to Num_Instr do
      begin
          WXXC[1,J] := WXX[1,J]*CE+WXX[2,J]*SE;
          WXXC[2,J] := WXX[2,J]*CE-WXX[1,J]*SE;
          WXXC[3,J] := WXX[3,J];
       end; {for}

end; { CalcWXXC_1rot}
{-------------------------------------------------------------------------}
procedure CalcWXXC_2rots(var Ch_Means : Ch_Data; var index : integer;
                  var WXX : CovarTensor;  var WXXB :CovarTensor;
                  var Num_Instr :integer;
                  var TW,WS,SE,CE,ST,CT : single);
var
   K,OSB,OCB : single;
   J,IJ : integer;

{first calc Total (TW) and Horizontal (WS) mean Wind speeds }
{ Ch_Means[1] = u, Ch_Means[2] =v, Ch_Means[3] = w                    }

begin
    TW := sqrt(sqr(Ch_Means[index+1])+sqr(Ch_Means[index+2])+
                                  sqr(Ch_Means[index+3]));
    WS := sqrt(sqr(Ch_Means[index+1])+sqr(Ch_Means[index+2]));

    if (TW = 0) or (WS = 0) then
     begin
      for J := 1 to num_instr do
       begin
        for IJ := 1 to 3 do
```

```
        WXXC[IJ,J] := WXX[IJ,J];
       end;
      exit;
     end;

{ now calc cos and sine of first two rotation angles Eta & Theta ie CE,ST etc}

    CE := Ch_Means[index +1]/WS;
    SE := Ch_Means[index +2]/WS;
    CT := WS/TW;
    ST := Ch_Means[index +3]/TW;

{1ST & 2ND ROTATION - ie rotate WXX thru Eta & Theta to WXXB }

    WXXB[1,1] := WXX[1,1]*SQR(CT)*SQR(CE)+WXX[2,2]*SQR(CT)*SQR(SE)+
            WXX[3,3]*SQR(ST)+2*WXX[1,2]*SQR(CT)*CE*SE+
            2*WXX[3,1]*CT*ST*CE+2*WXX[3,2]*CT*ST*SE;
    WXXB[2,2] := WXX[2,2]*SQR(CE)+WXX[1,1]*SQR(SE)-2*WXX[1,2]*CE*SE;
    WXXB[3,3] := WXX[3,3]*SQR(CT)+WXX[1,1]*SQR(ST)*SQR(CE)
                          {12.11.91, 2 - for +}
            WXX[2,2]*SQR(ST)*SQR(SE)-2*WXX[3,1]*CT*ST*CE-
            2*WXX[3,2]*CT*ST*SE+2*WXX[1,2]*SQR(ST)*CE*SE;
    WXXB[3,1] := WXX[3,1]*CE*(SQR(CT)-SQR(ST))-2*WXX[1,2]*CT*ST*SE*CE+
            WXX[3,2]*SE*(SQR(CT)-SQR(ST))-WXX[1,1]*CT*ST*SQR(CE)-
            WXX[2,2]*CT*ST*SQR(SE)+WXX[3,3]*CT*ST;
    WXXB[1,3] := WXXB[3,1];
                          {12.11.91,CE for SE}
    WXXB[1,2] := WXX[1,2]*CT*(SQR(CE)-SQR(SE))+WXX[3,2]*ST*CE-
            WXX[3,1]*ST*SE-WXX[1,1]*CT*CE*SE+WXX[2,2]*CT*CE*SE;
    WXXB[2,1] := WXXB[1,2];
    WXXB[3,2] := WXX[3,2]*CT*CE-WXX[3,1]*CT*SE-WXX[1,2]*ST*(SQR(CE)-SQR(SE))
            +WXX[1,1]*ST*CE*SE-WXX[2,2]*ST*CE*SE;
    WXXB[2,3] := WXXB[3,2];

    for J := 4  to Num_Instr do
     begin
        WXXB[1,J] := WXX[1,J]*CT*CE+WXX[2,J]*CT*SE+WXX[3,J]*ST;
        WXXB[2,J] := WXX[2,J]*CE-WXX[1,J]*SE;
        WXXB[3,J] := WXX[3,J]*CT-WXX[1,J]*ST*CE-WXX[2,J]*ST*SE;
     end; {for}

    if (WXXB[2,2] = WXXB[3,3]) or (WXXB[3,2] = 0) then      { this avoids }
     begin                                  { possibility of}
      for IJ := 1 to 3 do                   { K or SB = infinity}
       begin
        for J := 1 to num_instr do
          WXXC[IJ,J] := WXXB[IJ,J];
       end;
      exit;
     end;
end; {CalcWXXC_2rots}
{-------------------------------------------------------------------------}
procedure Coord_3rots(var UnRotated_Data,Rotated_data : Ch_Data;
            var index : integer;
            var SE,CE,ST,CT,SB,CB : single);
```

```
begin
 Rotated_Data[index+1] := UnRotated_data[index+1]*CE*CT +
            UnRotated_data[index+2]*SE*CT + UnRotated_data[index+3]*ST;
 Rotated_Data[index+2] := -UnRotated_data[index+1]*CB*SE +
         UnRotated_data[index+2]*CB*CE - UnRotated_data[index+1]*SB*CE*ST
       - UnRotated_data[index+2]*SB*SE*ST {12.11.91, ST for SE}
       + UnRotated_data[index+3]*SB*CT;
 Rotated_data[index+3] := UnRotated_data[index+1]*SB*SE -
         UnRotated_data[index+2]*SB*CE - UnRotated_data[index+1]*CB*CE*ST
       - UnRotated_data[index+2]*CB*SE*ST + UnRotated_data[index+3]*CB*CT;
end;{ Coord_3rots }
{-------------------------------------------------------------------------}
procedure Coord_1rot(var UnRotated_Data,Rotated_data : Ch_Data;
              var index : integer;
              var SE,CE : single);
begin

 Rotated_Data[index+1] := UnRotated_data[index+1]*CE +
                          UnRotated_data[index+2]*SE;
 Rotated_Data[index+2] := UnRotated_data[index+2]*CE -
                          UnRotated_data[index+1]*SE;
 Rotated_Data[index+3] := UnRotated_Data[index+3];

end; { Coord_1rot }
{-------------------------------------------------------------------------}
procedure Coord_2rots(var UnRotated_Data,Rotated_data : Ch_Data;
               var index : integer;
               var SE,CE,ST,CT : single);
begin

 Rotated_Data[index+1] := UnRotated_data[index+1]*CE*CT +
                  UnRotated_data[index+2]*SE*CT +
                  UnRotated_data[index+3]*ST;
 Rotated_Data[index+2] := UnRotated_data[index+2]*CE -
                  UnRotated_data[index+1]*SE                ;
 Rotated_Data[index+3] := UnRotated_Data[index+3]*CT -
                  UnRotated_data[index+1]*CE*ST -
                  UnRotated_data[index+2]*SE*ST;

end; { Coord_2rots }
{-------------------------------------------------------------------------}
procedure CreateWXX(var WhichWXX :CovarTensor;
              var fluct : Ch_Data;
              var index:integer;
              ch_no_T,ch_no_CO2,ch_no_H2O,
              ch_no_misc1,ch_no_misc2 : integer);

var iij,ij : integer;

(* create WXX[3,8] array :-

    1       2       3       4       5       6       7       8

 1 u'u'    u'v'    u'w'    u'      etc
 2 v'u'    v'v'    v'w'    v'
 3 w'u'    w'v'    w'w'    w'T'   w'CO2'   w'H2O'   w'misc1   w'misc2'
```

```
If any of the instruments are not relevent or not used ie misc ch's, then
array is filled with zeros.
*)

begin
   for iij := 1 to 3 do
    begin
     for ij := 1 to 3 do
      begin
       WhichWXX[iij,ij] := WhichWXX[iij,ij] + fluct[iij+index]*fluct[ij+index];
      end;
     if ch_no_T = 0 then WhichWXX[iij,4] := 0 else
      WhichWXX[iij,4] := WhichWXX[iij,4] + fluct[iij+index]*fluct[ch_no_T];
     if ch_no_CO2 = 0 then WhichWXX[iij,5] := 0 else
      WhichWXX[iij,5] := WhichWXX[iij,5] + fluct[iij+index]*fluct[ch_no_CO2];
     if ch_no_H2O = 0 then WhichWXX[iij,6] := 0 else
      WhichWXX[iij,6] := WhichWXX[iij,6] + fluct[iij+index]*fluct[ch_no_H2O];
     if ch_no_misc1 = 0 then WhichWXX[iij,7] := 0 else
      WhichWXX[iij,7] := WhichWXX[iij,7] + fluct[iij+index]*fluct[ch_no_misc1];
     if ch_no_misc2 = 0 then WhichWXX[iij,8] := 0 else
      WhichWXX[iij,8] := WhichWXX[iij,8] + fluct[iij+index]*fluct[ch_no_misc2];
    end;


end; {proc}
{------------------------------------------------------------------------}
end.  { UNIT }
```